THERMODYNAMICS AND KINETICS OF PHASE TRANSITIONS DURING SUPERCOOLING AND SUPERHEATING: A THEORETICAL AND COMPUTATIONAL INVESTIGATION IN MODEL LENNARD-JONES SYSTEMS

A Dissertation
Presented to
The Academic Faculty

by

Xianming Bai

In Partial Fulfillment
of the Requirements for the Degree
Doctor of Philosophy in the
School of Materials Science and Engineering

Georgia Institute of Technology
December 2006

THERMODYNAMICS AND KINETICS OF PHASE TRANSITIONS DURING SUPERCOOLING AND SUPERHEATING: A THEORETICAL AND COMPUTATIONAL INVESTIGATION IN MODEL LENNARD-JONES SYSTEMS

Approved by:

Dr. Mo Li, Advisor
School of Materials Science and Engineering
Georgia Institute of Technology

Dr. Andrei G. Fedorov
School of Mechanical Engineering
Georgia Institute of Technology

Dr. Thomas H. Sanders, Jr.
School of Materials Science and Engineering
Georgia Institute of Technology

Dr. Martha A. Gallivan
School of Chemical & Biomolecular Engineering
Georgia Institute of Technology

Dr. Christopher J. Summers
School of Materials Science and Engineering
Georgia Institute of Technology

Date Approved: October 25, 2006

ACKNOWLEDGEMENTS

First of all, I would like to sincerely thank my academic advisor, Dr. Mo Li, for his academic guidance and financial support during my PhD study. From him, I have learned how to build models, develop creative ideas, organize research, and analyze results. I believe what I have learned from him will greatly benefit me in my future career. I also would like to sincerely thank each of my committee members, Dr. T. H. Sanders, Dr. C. J. Summers, Dr. A. Fedorov, and Dr. M. A. Gallivan, for their precious time and very helpful suggestions.

Thanks are extended to all current and former members in our group: Dr. Q. K. Li, Mr. T. Xu, Dr. J. Payman, Dr. G. P. Zheng, Mr. H. Wang, and Mr. H. M. Li. Without their help, I would meet more difficulties in my research.

I am very grateful to my parents, Zengxian Bai and Guiqin Zhang, who have supported me both financially and spiritually continously. I am also grateful to my sisters and brothers for their encouragements and concerns.

Most importantly, I am very grateful to my wife, Zheng Lin, who always encourages me, cares me, and supports me continuously and unconditionally. Especially during the most difficult time of my study, her encouragements and supports help me greatly to overcome the difficulties.

This work was supported by the National Science Foundation (Grant No. NSF-0296163), the Structural Amorphous Metals Program of DARPA (ARO contract number DAAD19-01-1-0525), and Georgia Tech.

TABLE OF CONTENTS

Page

ACKNOWLEDGEMENTS iii

LIST OF TABLES ix

LIST OF FIGURES x

LIST OF ABBREVIATIONS xxvi

SUMMARY xxvii

CHAPTER

1 INTRODUCTION 1

2 MOLECULAR DYNAMICS SIMULATION TECHNIQUES AND BULK PROPERTIES OF A LENNARD-JONES SYSTEM 12

2.1. Molecular Dynamics Simulations in Different Ensembles 13

2.1.1. MD Simulation in an NVE Ensemble 13

2.1.2. MD Simulation in NPE Ensemble 14

2.1.3. MD Simulation in NPT Ensemble 16

2.2. Lennard-Jones Potential 18

2.3. Examples of Calculating the Physical Properties 21

2.3.1. System Temperature 21

2.3.2. Pair Distribution Function 22

2.3.3. Diffusion Coefficient 24

2.3.4. Elastic Constants 25

2.4. Computing Facilities 31

3 TEST OF CLASSICAL NUCLEATION THEORY FOR LIQUID SUPERCOOLING AND COMPUTING SOLID-LIQUID INTERFACIAL FREE ENERGY 33

3.1. Theory, Model, and Method 36

3.1.1. Classical Nucleation Theory 36

3.1.2. Simulation Techniques 39

3.1.3. Model of a Solid Nucleus Embedded in a Supercooled Liquid 40

3.2. Results and Discussion 46

3.2.1. Determining the Equilibrium Melting Temperature 46

3.2.2. Bulk Properties of Solid and Liquid Phases 48

3.2.3. Determining the Critical Temperature of the Composite System 50

3.2.4. Statistical Nature Near the Coexistence Temperature 55

3.2.5. Crystal Growth 57

3.2.6. Extracting the Average Interfacial Free Energy from the Inverse Relation between r^* and ΔT^* 61

3.2.7. Finite Size Effects 69

3.2.8. Temperature Dependence of Interfacial Free Energy 71

3.2.9. Anisotropic Interfacial Free Energy 73

3.3. Conclusions and Discussion 80

4 TEST OF CLASSICAL NUCLEATION THEORY FOR SOLID SUPERHEATING VIA A SOLID- LIQUID COEXISTENCE MODEL 82

4.1. Theory, Model, and Method 84

4.1.1. Theory 84

4.1.2. Simulation Method 86

4.1.3. Creating the Coexistence Model for Solid Superheating 86

4.2. Results 91

4.2.1. Surface Melting 91

4.2.2. Calculation of the Solid Shear Modulus and Liquid Bulk Modulus 93

4.2.3. Determining the Critical Temperature of the Composite System 95

4.2.4. Statistical Nature at the Critical Temperature 98

4.2.5. Relation between the Liquid Droplet Radius and the Critical Temperature 100

4.2.6. Our Proposed Theory for Solid Superheating 107

4.2.7. Liquid growth from Disk Nuclei 115

4.2.8. Kinetic Differences between Solid Superheating and Liquid Supercooling 121

4.3. Discussion and Conclusions 124

5 TEMPERATURE, FACE, AND SIZE DEPENDENCES OF STEADY-STATE CRYSTALLIZATION RATES 127

5.1. Theory of Crystal Growth 131

5.2. Models and Method 137

5.2.1. Model Configurations 137

5.2.2. Molecular Dynamics Simulations 139

5.2.3. Measuring Interface Moving Velocities via Energy Profiles 141

5.3. Results 146

5.3.1. Crystal-melt Interface Structures of (100) and (111) 146

5.3.2. Crystal Growth Morphologies from (100) and (111) Interfaces 157

5.3.3. Face-Dependent Crystal Growth Rates 166

5.3.4. Relaxation Time of Crystal Growth 176

5.3.4.1. Definition of the Relation Time 176

5.3.4.2. Face-Dependent Relaxation Time 180

5.3.4.3. Temperature-Dependent Relaxation Time 182

5.3.4.4. Size-Dependent Relaxation Time 184

5.3.5. Finite-Size Effects on Crystallization Rates 186

5.3.6. Our Proposed Theory for the Crystallization Rate 192

5.4. Discussion and Conclusions 202

6 NUCLEATION AND MELTING FROM NANOVOIDS 206

6.1. Models and Method 210

6.1.1. Creating a Nanovoid at the Center of a Crystal 210

6.1.2. Molecular Dynamics Simulations 211

6.2. Results 215

6.2.1. Four Stages of Void Melting 215

6.2.2. The Relation between T_m^A and r_0 227

6.2.3. The Relation between T_m^B and r_0 234

6.3. Discussion and Conclusions 243

7 HOMOGENEOUS MELTING AND RING DIFFUSION AT THE UPPER LIMIT OF SUPERHEATING 248

7.1. Gradual Heating and Isothermal Heating 252

7.2. Instability Theories and Melting Criteria 258

7.2.1. Born Shear Instability Theory 258

7.2.2. Lindemann Vibrational Instability Theory 260

7.2.3. Interstitial Instability Theory 262

7.2.4. Relation between the Crystal Enthalpy at T_m^S and Liquid Enthalpy at T_m^E 264

7.2.5. Number of the First Nearest Neighbors 267

7.3. Ring Diffusion in a Superheated Crystal 270

7.3.1. Mean Square Displacement during the Isothermal Heating 270

7.3.2. Ring Diffusion in a Superheated Crystal 273

7.3.3. Melting Caused by the Ring Diffusion 277
7.4. First-Order and Second-Order Transitions 290
7.4.1. Definition of the First-Order and Second-Order Transitions 290
7.4.2. Heat Capacity 291
7.4.3. Bond-Orientational Order 293
7.4.4. Symmetry Parameter 297
7.5. Discussion and Conclusions 299
REFERENCES 301

LIST OF TABLES

Page

Table 2.1: The Voigt notation. 28

Table 3.1: Statistics for nucleus growth and shrinkage around the coexistence temperature of a composite system with 683 solid atoms and 31 317 liquid atoms. 56

Table 3.2: Calculated solid-liquid interfacial energies by different theoretical approaches. In order to make comparisons, all the results are converted to the LJ units. Due to the lack of the attractive potential in hard-sphere systems, the calculated interfacial energies of hard-sphere systems are about 10% larger than those of the LJ systems [87]. 63

Table 4.1: The evolution (either shrinking or growing) of the liquid sphere. The probability of the growth or shrinkage is about 50%. 100

Table 5.1: The total 16 different configurations of the simulation systems. The simulation box is rectangular. The x direction is [100] for (100) interface, and [111] for (111) interface. Note a_0 is the lattice constant of the fcc crystal. 138

Table 5.2: The comparisons between the experimental crystallization rates and the theoretical predictions. The theoretical predictions are calculated with our model, $v_{\max}^{100} = 1.36 + 2541.43\left(a_0 / L\right)^{3/2}$ [Eq. (5.14a)], where $a_0 = 0.53$ nm. 201

LIST OF FIGURES

Page

Figure 2.1: Illustration of the interaction between one atom (in blue) and its surrounding atoms (in black). The interatomic interaction is analogous to an elastic spring. 13

Figure 2.2: Illustration of periodic boundary conditions. The green area represents the original simulation system, and the blue areas represent its periodic boundary conditions. 18

Figure 2.3: The Lennard-Jones potential as a function of interatomic distance r. 20

Figure 2.4: The desired system temperature (red) and the calculated system temperature (blue). 21

Figure 2.5: Illustration of a shell between r and r+dr originating from a central atom i. 22

Figure 2.6: The pair distribution function at different temperatures and states: T=0.5 ε / k_B (blue line); T=0.739 ε / k_B, before melting (red line); T=0.739 ε / k_B, after melting (green line). 23

Figure 2.7: The diffusion coefficient of a LJ liquid as a function of temperature. 25

Figure 2.8: The elastic constants as functions of the simulation time at T = 0.33 ε / k_B (40K). 29

Figure 2.9: Temperature dependent elastic constants. The left and bottom scales show the reduced LJ units, and the right and top scales show the standard units. The symbols are calculated from MD calculations, and the lines are linear fits to the data. T_m^s represents the upper limit of superheating. 30

Figure 2.10: Parallel computing clusters. Thunder (left): 96-node clusters; Apollo (right): 64-node clusters. 32

Figure 3.1: Illustration of the classical nucleation theory for homogeneous nucleation. (a) Model of homogeneous nucleation. A solid sphere of radius r forms in a supercooled liquid. (b) The changes of the interfacial free energy and the volume free energy in homogeneous nucleation. The critical radius and nucleation barrier are given in Eqs. (3.4) and (3.5). 37

Figure 3.2: The classical way of creating a crystal-melt interface. Three independent runs are usually required. 42

Figure 3.3: Schematic illustration of creating a composite system with a crystal nucleus embedded in a supercooled liquid. The outer matrix follows the path A→C→D→E→F, and the solid sphere follows the path A→G→B→G→C. At temperature T', the potential depth of the solid sphere is changed from 4ε to 1ε (G→C). See text for details. 43

Figure 3.4: Cross-section snapshots during the process of creating the composite system. (a) Initial configuration (at point A in Figure 3.3). (b) At the superheating limit $T_s^{1\varepsilon}$, the outer matrix becomes liquid. (c) At T' in Figure 3.3, the coexistence sample is created after the potential depth of the inner solid sphere is changed from 4ε to 1ε. 43

Figure 3.5: Determining the equilibrium melting temperature with a flat interface. (a) At T =$0.618\,\varepsilon/k_B$, the flat interface stays stationary. (b) At T <$0.618\,\varepsilon/k_B$, crystallization of the liquid makes the interface move from left to right. (c) At T >$0.618\,\varepsilon/k_B$, the interface moves from right to left. Melting of the crystal can be seen. 46

Figure 3.6: The hysteretic loops of the heating and cooling processes of a homogeneous bulk system. (a) The density loop. (b) The enthalpy loop. The arrows indicate the spontaneous crystallization point. The polynomial fits to the data are given in Eq. (3.7) – (3.10). 49

Figure 3.7: The volume changes at different temperatures for a sample of 683 solid atoms embedded in a liquid matrix of 31 317 atoms. The liquid matrix crystallizes at $T \le 0.559$, and does not change when $T \ge 0.560$. Thus the coexistence temperature is approximately at $T = 0.559$. 50

Figure 3.8: Visualization of the cross-section snapshots of the atomic configurations. (a) At $T = 0.555$, the liquid matrix crystallizes, and the solid sphere still keeps its original shape. Some defects can be clearly seen inside the crystal. (b) At $T = 0.565$, the solid sphere disappears. The solid atoms diffuse into the liquid and become liquid atoms. 53

Figure 3.9: The enthalpy changes of the solid sphere and the liquid matrix. (a) At $T = 0.555$, the enthalpy of the liquid matrix decreases to that of the solid sphere. (b) At $T = 0.565$, the enthalpy of the solid sphere increases to that of the liquid matrix. 55

Figure 3.10: Snapshots of the crystal growth from a solid nucleus at $T = 0.557\,\varepsilon/k_B$. We use the coloring scheme described in the text to differentiate the solid and liquid atoms. The color continuously changes from bright green (for solidlike atoms) to dark purple (for

liquidlike atoms). (a) The initial sample of 683 solid atoms embedded in 31 317 liquid atoms. The interface atoms are less bright. (b) After 80 000 MD steps (0.4ns), solid sphere grows. The newly grown crystals have some parts whose crystallographic orientations are different from the initial solid sphere. The growth pattern is close to spherical although small irregular shape is seen. (3) After 3 million MD steps (15ns), most grains disappear and the polycrystal almost becomes a single crystal. A few small grains still exist but would disappear if the simulation time is long enough. 58

Figure 3.11: Illustration of the free energy levels of different phases. The structural change during the solidification process is often assumed as liquid $\rightarrow$ bcc $\rightarrow$ fcc. 60

Figure 3.12: The inverse relation between the critical nucleus size r^* and the critical undercooling temperature ΔT^*. The solid line in (a) is a fit to Eq. (3.4). The linear fit in (b) yields the value of k in Eq. (3.6). 62

Figure 3.13: (a) The theoretical prediction of the nucleation rates with different interfacial free energies as inputs. (b) The spontaneous crystallization of a pure supercooled liquid. 67

Figure 3.14: Size dependence of the lag time before massive crystallization. The larger sample has a much longer lag time than the smaller sample ($\tau_2 \approx 3\tau_1$). 70

Figure 3.15: A comparison of the driving force used in CNT relation (solid circles) and calculated from Gibbs-Helmholtz relation (solid squares). The data of CNT relation are calculated from Eq. (3.3), and the data of Gibbs-Helmholtz relation are calculated from Eq. (3.13) and (3.14). 71

Figure 3.16: Temperature dependence of interfacial free energy. A positive temperature coefficient is found. Turnbull's empirical relation is shown for comparison. 73

Figure 3.17: Nuclei of different geometric shapes. (a) and (b): A cubic nucleus with {100} planes on the surface. The edge length of the cubic nucleus is a. (c) and (d): A bipyramidal nucleus with {111} planes on the surface. The edge length is b. (e) and (f): A spherical nucleus of radius r. 74

Figure 3.18: The shrinkage of a cubic nucleus in a supercooled liquid. (a) Initially, a cubic nucleus is embedded in a supercooled liquid. (b) After some time, the corners start to collapse. (c) Finally, the cubic nucleus dissolves into the liquid. 77

Figure 3.19: The shrinkage of a cubic nucleus in a supercooled liquid. (a) Initially, a cubic nucleus is embedded in a supercooled liquid. (b) After some

time, the corners start to collapse. (c) Finally, the cubic nucleus dissolves into the liquid. 77

Figure 3.20: Crystal growth from non-spherical nuclei. The crystal growth prefers to occur at the locally flat interface regions. (a) The crystal growth from a cubic nucleus. (b) The crystal growth from a bipyramidal nucleus. 78

Figure 3.21: The linear relation between $(n/\rho_s)^{1/3}$ and $1/\Delta T$ for crystal nuclei with different crystal planes on their interfaces. 79

Figure 4.1: A spherical liquid droplet embedded in a superheated solid model. 84

Figure 4.2: Unproven CNT relation between the critical nuclei size and the superheating temperature. 85

Figure 4.3: Schematic illustration of creating a liquid droplet in a superheated solid. The inner sphere goes along the path A→B→C→D→E, and the outer matrix goes along the path A→F→G. See text for details. 88

Figure 4.4: Cross-section snapshots of the atomic configurations. (a) Initial configuration (at point A in Figure 4.3). (b) At the superheating limit $T_s^{0.6\varepsilon}$, the inner sphere becomes a liquid. (c) At T' in Figure 4.3, the coexistence sample is created after the potential depth of the inner liquid sphere is changed from 0.6ε to 1ε. 88

Figure 4.5: Melting starts from the free surface. (a) At $T < T_m^E$. (b) At $T \geq T_m^E$. 91

Figure 4.6: The shear modulus of the solid (μ) and the bulk modulus of the liquid (K_l). The bulk modulus (K_S) and another shear modulus (C_{44}) of the solid are also shown. 94

Figure 4.7: The total volume change as a function of time at different temperatures. 95

Figure 4.8: The cross-sectional snapshots at T=$0.688\,\varepsilon/k_B$ after the potential is switched. (a) Initially, the liquid droplet is embedded in the crystal matrix. (b) After 0.1 ns, the liquid starts to crystallize. (c) After 0.15 ns, the liquid droplet becomes one part of the crystal. 96

Figure 4.9: The cross-sectional snapshots at T=$0.691\,\varepsilon/k_B$ after the potential is switched. (a) Initially, the liquid droplet is embedded in the crystal matrix. (b) After 0.1 ns, the liquid grows. (c) After 0.175 ns, the liquid droplet grows further. 96

Figure 4.10: The statistical nature at the critical temperature. The evolution of the liquid sphere is listed in Table 4.1. 99

Figure 4.11: The r^* vs. ΔT relation in supercooling and superheating processes. CNT (the solid line at the left-hand side) represents the classical nucleation theory. 101

Figure 4.12: Cross-sectional snapshots of the supercooling and superheating models. (a) Supercooling model: a solid sphere is embedded in a supercooled liquid. (b) Superheating model: a liquid droplet is embedded in a superheated crystal. 102

Figure 4.13: The interface pressures in the liquid supercooling and solid superheating models. The sign of the compressive pressure is positive and the sign of the tensile pressure is negative. 104

Figure 4.14: The enthalpy changes of the liquid droplet (blue line) and the crystal matrix (pink line). (a) At T=0.690 ε / k_B, the melting occurs. The enthalpy of the crystal matrix increases to the liquid value. (b) At T=0.689 ε / k_B, the liquid sphere disappears. The enthalpy of the liquid droplet decreases to the crystal value. 105

Figure 4.15: Schematic drawing of (a) a liquid droplet nucleating in a superheated solid, and (b) a curved solid-liquid interface. The disorder in the solid close to the interface is shown. 107

Figure 4.16: Schematic diagram of the free energies of solid and liquid phases as functions of the temperature. The solid lines marked by G_l and G_s are the free energies of the solid and liquid phases without the elastic energy. Their intersection gives the equilibrium melting temperature Tm. The dashed and dash-dotted lines marked by $(G_l + E_l)$ and $(G_s - E_s)$ are the free energies of the solid and liquid after including the elastic energies. Their intersection gives the homogeneous melting temperature $T_m^{\mathrm{hom}o}$. T_m^s is the ultimate superheating temperature. The forbidden nucleation region is $\Delta T_{gap} = T_m^{\mathrm{hom}o} - T_m$. 110

Figure 4.17: The relation between critical solid (liquid) nucleus radius r^* and supercooling (superheating) temperature ΔT^*. Samples of different sizes were used. The solid line in supercooling region is fitted to the relation, $r^* \cong (2\gamma_{sl} T_m / \Delta L_v) / \Delta T$. For superheating, finite-size effect is shown. The theoretical prediction [Eq. (4.8)] is plotted as the blue solid line. The results from the largest system tested (N=256 000) are in excellent agreement with the theory. The nucleation forbidden gap $\Delta T_{gap} = 0.044$ is indicated by the dotted line. At the superheating limit, the size of the liquid droplet is about 19 atoms. 112

Figure 4.18: Brener et al.'s model [122] of the liquid growth morphology from a disk nucleus in a superheated crystal. Their model predicts that the disk nucleus prefers to grow in the horizontal direction. 116

Figure 4.19: The cross-sectional snapshot of a liquid nucleus of a disk shape and the outer crystal matrix. The enlarged view of the liquid nucleus is shown at the right-hand side. 116

Figure 4.20: The cross-sectional snapshots of the liquid growth from a disk nucleus. (a) Initial configuration. (b) After 0.25 ns. (c) After 0.4ns. (d) After 0.65ns. 117

Figure 4.21: Illustration of the liquid growth morphology from a disk nucleus. The liquid prefers to grow from the interface of small curvature such as k1. 119

Figure 4.22: Comparison between the disk nucleus and spherical nucleus. The total number of atoms in the system is 108 000 in both systems. 119

Figure 4.23: Finite size effects in the liquid growth from disk nuclei. The curve shifts upwards when the system size increases. 121

Figure 4.24: The flat interface model for calculating the interface moving velocities at the superheating and superheating regimes. The horizontal direction is [100] in this example system. (a) At $T = T_m$, the interface is stable. (b) At $T < T_m$, crystallization occurs. The interface is moving from the crystal side to the liquid side. (c) At $T > T_m$, melting occurs. The interface is moving from the liquid side to the crystal side. 122

Figure 4.25: Interface moving velocities at different supercooling and superheating. 123

Figure 5.1: The temperature-dependent diffusion coefficient of a Lennard-Jones system. 132

Figure 5.2: Two typical models of crystal growth from the undercooled melt. Crystals are at the left-hand side and liquids are at the right-hand side. (a) The diffusion-controlled model: atoms travel from the faraway liquid to the crystalline sites at the interface. (b) The collision-controlled model: the vicinity atoms "collide" on the interface and become a part of the crystal. 133

Figure 5.3: Comparison of the different crystallization rates between the diffusion-controlled [Eq. (5.1)] and collision-controlled [Eq. (5.3)] models. The units of the left and bottom axes are reduced LJ units, and those of the right and top axes are real units. 135

Figure 5.4: The 3D view of the rectangular flat-interface model. The green and red spheres represent crystal and liquid atoms respectively. The edge

length in x direction is longest, while the lengths in y and z directions are same. The interface is at the middle of the x direction. 137

Figure 5.5: The evolution of three box lengths with simulation time in a system of 32 000 atoms and with a (100) interface. The left y-axis is for LX and the right y-axis is for LY and LZ. 141

Figure 5.6: A sample is sliced evenly into N thin slices along the crystal growth (horizontal) direction. The thickness of each slice is d. 142

Figure 5.7: Three snapshots at different time and the corresponding enthalpy profiles at T = 0.51 ε / k_B. The system has 32 000 atoms and two (100) interfaces. (a) The snapshot of the initial configuration. (b) After 20 000 MD steps. (c) After 40 000 MD steps. (d) The corresponding enthalpy profiles for (a), (b), and (c). The constant E* is the critical enthalpy for discriminating the solid and liquid slices. 144

Figure 5.8: The linear decrease of the liquid length with the time at different temperatures. The system consists of 32 000 atoms and two crystal-melt interfaces normal to the [100] direction. The slope of each linear fit (divided by 2) is the steady-state interface moving velocity at the corresponding temperature. 146

Figure 5.9: Illustration of Gibbs dividing interface and diffuse (real) interface. 147

Figure 5.10: The density profile along the [100] direction. (a) The overall density profile of the sample with two crystal-melt interfaces. (b) The detailed density profile of the region surrounded by the rectangle in (a). The numbers indicate the atomic layers. The transition (interface) region is from layer 3 to layer 9. 148

Figure 5.11: The 2-D projections of nine atomic layers at the (100) interface. (a) The side view of nine layers. (b) The projection of layer 1 (red circles) and layer 2 (blue dots). Layer 1 and layer 2 are alternatively shown in (c)-(i) as reference layers. (c)-(i): The projections of layer 3 to layer 9. Red circles represent the atoms of the present layer. The blue crosses represent the atoms of layer 1 in (c), (e), (g), and (i), and of layer 2 in (d), (f), and (h). 151

Figure 5.12: The density profile along the [111] direction. (a) The overall density profile of the sample with two crystal-melt interfaces. (b) The enlarged density profile of the interface region. The numbers in (b) indicate the corresponding atomic layers. The interface region is from layer 4 to layer 8. 152

Figure 5.13: The 2-D snapshots of eight atomic layers at the (111) interface. (a) The side view of eight layers. (b)-(i) The projections of layer 1-8 (red

circles). The close-packed regions are indicated by the pink polygons. Some other types of ordering are also indicated. 155

Figure 5.14: The side view of a crystal grown from a (100) interface. The red and green spheres represent the atoms originally in liquid state and solid state, respectively. A thin slice of 3-layer width [bounded by the blue rectangle] is picked from the newly formed crystal for detailed investigation in Figure 5.15. 157

Figure 5.15: The detailed in-plane structure of the thin slice as indicated in Figure 5.14. (a) The side view of the 3-layer slice. (b) Projection of layer 1. (c) Projections of layer 1 and layer 2. (d) Projections of layer 1, layer 2, and layer 3. Red circles - Layer 1; Green spheres - layer 2; Blue crosses - layer 3. 158

Figure 5.16: The side view of a crystal grown from a (111) interface. The red and green spheres represent the atoms originally in liquid state and solid state, respectively. Three crystal slices, A, B, and C, each of them is 3-layer wide, are picked from the newly formed crystal for detailed investigation in Figures 5.17-5.19. 160

Figure 5.17: The detailed in-plane structure of slice A [in Figure 5.16]. (a) The side view of the 3-layer slice. (b) Projection of layer 1. (c) Projections of layer 1 and layer 2. A vacancy is indicated by the blue square. (d) Projections of layer 1, layer 2, and layer 3. The atoms in layer 3 are directly on the top of layer 1, indicating the structure of this slice is an hcp structure. Red circles - Layer 1; Green spheres - layer 2; Blue crosses - layer 3. 161

Figure 5.18: The detailed in-plane structure of slice B [in Figure 5.16]. (a) The side view of the slice. (b) Projection of layer 1. (c) Projections of layer 1 and layer 2. A vacancy is indicated by the pink square. (d) Projections of layer 1, layer 2, and layer 3. A vacancy is indicated by the pink square. The atoms in layers 2 and 3 lie alternatively in the interstices of layer 1, indicating the structure of this slice is an fcc structure. Red circles - Layer 1; Green spheres - layer 2; Blue crosses - layer 3. 162

Figure 5.19: The detailed in-plane structure of slice C [in Figure 5.16]. (a) The side view of the 3-layer slice. (b) Projection of layer 1. A vacancy is indicated by the blue square. (c) Projections of layer 1 and layer 2. Two dislocations are indicated. (d) Projections of layer 1, layer 2, and layer 3. Some atoms in layer 3 lie in hcp sites (bounded by the pink polygons), and some atoms in layer 3 lie in fcc sites (unbounded region). The structure of this slice is a hybrid (fcc+hcp) structure. Red circles - Layer 1; Green spheres - layer 2; Blue crosses - layer 3. 163

Figure 5.20: The temperature-dependent interface moving velocities of (100), (110), and (111) faces. The number of atoms is 32,000, 33,600, and 33,600 for the sample with a (100), (110), and (111) interface, respectively. Red filled circles – (100); Blue filled squares – (110); Green filled triangles – (111). 167

Figure 5.21: The snapshots of atoms in a thin liquid slice [bounded by a blue rectangle] at different temperatures during the crystallization. The sample contains a (100) interface. (a) The original liquid slice. (b) At T=0.27. (c) At T=0.41. (d) At T=0.55. Big pink spheres – atoms in the liquid slice; Small red spheres – original liquid atoms; Medium green spheres – original crystal atoms. 170

Figure 5.22: The snapshots of atoms in a thin liquid slice [bounded by a blue rectangle] at different temperatures during the crystallization. The sample contains a (111) interface. (a) The original liquid slice. (b) At T=0.27. (c) At T=0.41. (d) At T=0.55. Big pink spheres – atoms in the liquid slice; Small red spheres – original liquid atoms; Medium green spheres – original crystal atoms. 171

Figure 5.23: The fitting of the collision-controlled model [Eq. (5.3), dotted line] and diffusion-controlled model [Eq. (5.1), dashed line] to the growth rate of the (111) interface. The prefactor f_0 is 0.12 for the collision-controlled model and 0.40 for the diffusion-controlled model. 175

Figure 5.24: A snapshot of a sample with a thin liquid slice. The liquid slice is used for investigating the relaxation time. Green spheres – original crystal atoms; Red spheres – original liquid atoms; Yellow spheres – atoms in the liquid slice. 176

Figure 5.25: Two types of "mean-square-displacements" (MSD) of the atoms in the thin liquid slice. The left y-axis is for the cumulative MSD, and the right y-axis is for the dynamic MSD. The respective relaxation time measured from the two types of MSD, τ_{CMSD} and τ_{DMSD}, are indicated. The snapshots at time A, B, and C are shown in Figure 5.26. 178

Figure 5.26: The snapshots of the sample at time A, B, and C as indicated in Figure 5.25. (a) At time A, the crystal-melt interface just arrives at the liquid slice. (b) At time B, the interface just passes through the thin slice. (c) At time C, the thin slice is completely crystallized. Green spheres – original crystal atoms; Red spheres – original liquid atoms; Yellow spheres – atoms in the original liquid slice. 179

Figure 5.27: The comparison of the relaxation time between a (100) interface and a (111) interface at the same temperature and of roughly same system size. 182

Figure 5.28: The comparison of the relaxation time at different temperatures for the same sample. The sample consists of 32 000 atoms and a (100) interface. 183

Figure 5.29: The size-dependent relaxation time. Three different size samples are used for comparison: N = 32 000, 64 000, and 128 000. Each sample has a (100) interface. 184

Figure 5.30: Comparison of the relaxation time in different size systems by using the cumulative MSD (CMSD). 185

Figure 5.31: The (100) interface moving velocities of different size systems at different temperatures. The data points are calculated with our MD simulations. The diffusion-controlled model [Eq. (5.1)] and the collision-controlled model [Eq. (5.3)] are shown as dashed line and dotted line respectively. The solid lines are the fittings of our proposed theory in section 5.3.6 [Eq. (5.11)] to the simulation data. The reduced LJ unit of the velocity is $(\varepsilon / m)^{1/2} \approx 158$ m/s. 187

Figure 5.32: The (111) interface moving velocities of different size systems at different temperatures. The data points are calculated with our MD simulations. The diffusion-controlled model [Eq. (5.1)] and the collision-controlled model [Eq. (5.3)] are shown as dashed line and dotted line respectively. The solid lines are the fittings of our proposed theory in section 5.3.6 [Eq. (5.11)] to the simulation data. The reduced LJ unit of the velocity is $(\varepsilon / m)^{1/2} \approx 158$ m/sec. 188

Figure 5.33: The temperature-dependent homogeneous nucleation rate of an undercooled LJ liquid. The bottom x-axis represents the undercooling ΔT, and the top x-axis represents the temperature T. The arrow indicates the critical undercooling/temperature for the spontaneous nucleation. 191

Figure 5.34: The volume fluctuations during the crystallization process in three size systems: N = 32 000, 64 000, and 128 000. Each blue dashed line indicates the corresponding average value of the fluctuations. (a) Size-dependent volume fluctuations. The smaller system has the larger fluctuations. (b) The normalized volume fluctuations by multiplying a factor of $\sqrt{N}$. The normalized volume fluctuations in the three size systems are almost identical. 194

Figure 5.35: The linear relation between the volume fluctuation and the reciprocal of the square root of the system size. The data points are the average volume fluctuations in different size systems. 196

Figure 5.36: The linear fits of f_2 to $1/\sqrt{N}$ for (100) and (111) interfaces. 198

Figure 5.37: The rescaled interface moving velocities by multiplying a factor $\sqrt{N}$. The data points are calculated from simulations. The solid lines are plotted with the product of Eq. (5.11) and $\sqrt{N}$. (a) The (100) interface. (b) The (111) interface. 199

Figure 6.1: Illustration of the relation between the melting temperature of a void-containing system and the void radius. r^* is the critical radius beyond which the melting temperature reaches a plateau. 208

Figure 6.2: Cross-sectional projection of a crystal sample containing a void. In this figure the total number of atoms in this sample (before creating a void) is N = 108 000 and the number of atoms removed for creating the void is n = 1 505 (or r_0 = 0.73nm). 210

Figure 6.3: An example of the simulation procedure. See the text for details. 212

Figure 6.4: Comparison between the gradual heating (GH) and isothermal heating (IH) method. The gradual heating shows a strong hysteresis effect on the melting temperature. 214

Figure 6.5: The time evolution of the average volume per atom at different temperatures. The snapshots at the four stages are given in Figure 6.6. The circle indicates a bump in stage III. Stage I: T = 0.590; Stage II: T = 0.630; Stage III: T = 0.645; Stage IV: T = 0.670. 215

Figure 6.6: The cross-sectional snapshots of the four stages (shown in Figure 6.5) during void melting. (a) Stage I: at $T < T_m^E$, the solid-vapor void surface is stable. (b) Stage II: at $T_m^E \le T < T_m^A$, a thin liquid layer nucleates around void surface. (c)-(e) Stage III: at $T_m^A \le T < T_m^B$, the thin liquid layer grows [(c)]; after some MD runs the liquid atoms fills the void completely [(d)]; the liquid droplet stops growing and the radius does not change even after very long MD runs [(e)]. (f) Stage IV: at $T > T_m^B$, the sample melts completely. See the text for the definition of the notations T_m^E, T_m^A, and T_m^B. 216

Figure 6.7: The free energy diagram of stage I ($T < T_m^E$) in the void melting. See the text for details. 217

Figure 6.8: The cross-sectional snapshots of the sample at different simulation time in stage I. (a) Initial snapshot at T = 0.590. The surface atoms are slightly disordered. (b) After 200 000 isothermal runs, the void surface is still stable. 218

Figure 6.9: The free energy diagram of stage II ($T_m^E \le T < T_m^A$) in the void melting. See the text for details. 219

Figure 6.10: The cross-sectional snapshots of the sample at different simulation time in stage II. (a) Initial snapshot at T = 0.630. A thin liquid layer (represented by the disordered atoms) forms at this temperature. (b) After 200 000 isothermal runs, the thin liquid layer only changes slightly. 220

Figure 6.11: The stable coexistence between the liquid droplet (disordered region) and the crystal matrix. (a) Initial snapshot at T = 0.645. (b) After 130 000 isothermal runs, the thin liquid droplet only changes slightly. 221

Figure 6.12: The free energy diagram of stage III ($T_m^A \le T < T_m^B$) and stage IV ($T \ge T_m^B$) in the void melting. See the text for details. 224

Figure 6.13: The model for estimating the final liquid droplet radius r_A at temperature T_m^A. All the crystal atoms in the shell between r_0 and r_A become liquid atoms that form a liquid droplet of radius r_A. 225

Figure 6.14: The procedure of using visualization to determine T_m^A. Here N = 108 000 and n = 1 505. (a) At T = 0.636, the thin liquid layer is stable after 200 0000 MD runs. (b) At T = 0.637, the void is filled up by the molten material. 228

Figure 6.15: The internal melting temperature from the void surface (T_m^A) as a function of the void radius (r_0). Three sample sizes are used and the finite size effect is not strong. The equilibrium melting temperature T_m^E=0.618 ε / k_B is indicated by the dashed line. 229

Figure 6.16: Three types of solid-vapor interfaces. (a) A nanoparticle of a positive surface curvature. (b) A flat surface of a zero surface curvature. (c) A void of a negative surface curvature. 231

Figure 6.17: The effective radius of the solid-liquid interface in the void melting. r_0 is the initial void radius, and dr is the thickness of the solid-liquid interface (or the thin liquid layer). The effective radius is thus $r_0 + dr$. 231

Figure 6.18: The effective interfacial free energy γ_{eff} as a function of the void radius. γ_{eff} increases with the increasing void radius (or with the decreasing temperature) and has a trend to approach the solid-liquid interfacial free energy. 232

Figure 6.19: Determining T_m^B by using the visualization of the snapshots. Here N = 108 000 and n=1 505. (a) At T=0.662, the liquid droplet is stable after 200 0000 MD runs. (b) At T=0.663, the system melts completely. 235

Figure 6.20: The total volume changes of systems with different void sizes during the melting. The circled region indicates the cavity effect when the void size is large. The snapshots at moments A-D are given in Figure 6.21. 236

Figure 6.21: The snapshots at moments A-D indicated in Figure 6.20. (a) At moment A, the liquid grows from the void surface. (b) At moment B, the liquid front reaches the crystal boundaries but the void is still not completely filled. (c) At moment C, the void is filled, but the crystal can be seen at the corners. (d) At moment D, the system becomes a liquid. 237

Figure 6.22: The complete melting temperature T_m^B as a function of the void radius r_0. A strong finite size effect is shown. In all size systems, $T_m^B > T_m^E$. 239

Figure 6.23: The critical condition under which the elastic energy will not show up. (a) Illustration of the critical condition. If the radius of liquid droplet at T_m^A, r_A, reaches the boundaries of the simulation box, the elastic energy will not show up. (b) A snapshot of a system with a critical liquid droplet at T_m^A. The radius of the critical liquid droplet is half the edge length of the simulation box. (c) A snapshot of a system with an unfilled space when the liquid reaches the boundaries at T_m^A. 241

Figure 6.24: The complete melting temperature T_m^B as a function of the volume fraction of the void. The finite size effects are removed compared to Figure 6.22. The critical volume fraction for reaching the plateau is estimated to be 5-6%. 242

Figure 7.1: The melting in the gradual heating method. The number of atoms in the system is 4 000. The melting occurs at the upper superheating limit $T_m^S = 0.76\,\varepsilon / k_B$. (a) The change of the volume per atom with the increasing temperature. (b) The change of the enthalpy per atom with the increasing temperature. 253

Figure 7.2: The evolution of the volume per atom with the simulation time in the isothermal heating method. The melting occurs at $0.739\,\varepsilon / k_B$. The number of atoms in the system is 4 000. The snapshots at A, B, and C are shown in Figure 7.3. 254

Figure 7.3: The snapshots at time A, B, and C [indicated in Figure 7.2]. (a) Time A, T = 0.3 ε / k_B. (b) Time B, T = 0.739 ε / k_B, before melting. (c) Time C, T = 0.739 ε / k_B, after melting. 256

Figure 7.4: The size-dependent melting temperature obtained from the isothermal heating method. The melting temperature approaches 0.740 at large sample sizes. The bottom axis is plotted with the logarithmic scale. 257

Figure 7.5: Temperature-dependent elastic moduli of a LJ crystal. The equilibrium melting temperature T_m^E and the superheating limit T_m^S are indicated by the dashed lines. The linear decrease of the elastic moduli indicates the crystal is softening with increasing temperature. The shear modulus C' still has finite value at the superheating limit T_m^S. The arrow indicates the temperature at which the extrapolation of C' approaches zero (Born shear instability). Bottom and left scales: in reduced LJ units; Right and top scales: in real units (GPa and K). 259

Figure 7.6: Mean square displacement (MSD) of atoms as a function of temperature. The arrow indicates the critical MSD at which melting occurs. 261

Figure 7.7: Two types of interstitial sites in an fcc crystal. The distance between an interstitial site (filled circle in green) and an atom (filled circle in black) is indicated by a dashed line in each figure. (a) Octahedral site. (b) Tetrahedral site. 262

Figure 7.8: The evolution of the shortest interatomic distance with the simulation time. The system contains 500 atoms. The system temperature is increased from 0.2 to 0.725 and held at 0.725 isothermally. The gradual heating and isothermal heating periods are separated by the dotted line. The ideal distance between an octahedral interstitial site and a neighboring atom is indicated by $r_{oct-atom}$, and that between a tetrahedral interstitial site and a neighboring atom is indicated by $r_{tet-atom}$. 264

Figure 7.9: The enthalpy per volume as a function of the temperature during the heating-cooling process. The crystal enthalpy per volume at the superheating limit T_m^S is not equal to the liquid enthalpy per volume at the equilibrium melting temperature T_m^E (indicated by the dashed line). 267

Figure 7.10: The evolution of the average number of the first nearest neighbors during the melting process. At T=0.46 ε / k_B, the number deviates from twelve. At T=0.739 ε / k_B, the number drops from 11 to 8.6 upon the

melting. The distributions of the number of the first nearest neighbors at time A-E are shown in Figure 7.11. 268

Figure 7.11: The distributions of the number of the first nearest neighbors at different stages. The stages A-E are indicated in Figure 7.10. See the text for details. 270

Figure 7.12: The time-dependent mean square displacement at the isothermal temperature T = 0.738. The MSD is larger than the critical value of 0.12 but the sample does not melt. 271

Figure 7.13: The distribution of the atomic displacements at T = 0.738 at different simulation time. The horizontal axis represents the atomic displacement. The two arrows indicate the first and second nearest neighbor distances respectively. 273

Figure 7.14: The atom hopping in a superheated crystal of 500 atoms at T=0.739 ε / k_B. The blue spheres represent the equilibrium sites of the atoms. (a) The equilibrium atom positions. (b) Clusters formed by the atom hopping. The hopping atoms are represented by large spheres. The arrow heads represent the new atom positions. 274

Figure 7.15: Illustration of two types of diffusion loops. (a) A close diffusion loop. (b) An open diffusion loop. 276

Figure 7.16: The snapshots of forming a close diffusion loop. The blue spheres represent original equilibrium sites. The red spheres represent the hopping atoms. The vectors represent the atom displacements. (a) Initial. (b) After 320 MD steps (1.6 ps). (c) After 880 MD steps (4.4 ps). (d) After 1 220 MD steps (6.1 ps). 276

Figure 7.17: Snapshots of close-pair atoms and displaced atoms during the formation of the diffusion loops. The close-pair atoms are represented by red spheres. The blue spheres represent the original equilibrium sites of atoms. The vectors represent the atom displacements. (a) Initial stage when melting occurs. (b) After 1 400 MD steps. (c) After 1 800 MD steps. (d) After 1 840 MD steps. 278

Figure 7.18: Snapshots of defective atoms and displaced atoms during the formation of the diffusion loops. An atom is defective if the number of its first nearest neighbors is less than eight. The defective atoms are represented by red spheres. The vectors represent the atom displacements. (a) Initial stage when melting occurs. (b) After 1 400 MD steps. (c) After 1 800 MD steps. (d) After 1 840 MD steps. 280

Figure 7.19: The enthalpy change of each atom during the formation of the diffusion loops. The enthalpy level is represented by the color of the

spheres. The green is for solidlike atoms (lower enthalpy) and the dark purple is for liquidlike atoms (higher enthalpy). The vectors represent the atom displacements. (a) Initial stage when melting occurs. (b) After 1 400 steps. (c) After 1 800 steps. (d) After 1 840 steps. 282

Figure 7.20: The 3D snapshots of the diffusion loops during the melting process. Different loops are distinguished by different colors. (a) Initial stage when melting occurs. (b) After 1 400 MD steps. (c) After 1 800 MD steps. (d) After 1 840 MD steps. 284

Figure 7.21: Illustration of the melting sequence. The temperature scale is for a LJ model system. 285

Figure 7.22: The open diffusion loops in a system of 4 000 atoms at two different temperatures. The loops are discriminated by different colors. (a) At T=$0.739\,\varepsilon / k_B$. The melting occurs at this temperature. (b) At T=$0.738\,\varepsilon / k_B$. The melting does not occur at this temperature. 286

Figure 7.23: (a) The number of the open loops as a function of time at two different temperatures. The crystal contains 4 000 atoms. (b) The enlarged graph of the transition period enclosed in the blue rectangular. 288

Figure 7.24: The upper and lower bounds of the critical densities in each size system. The bottom axis (total number of atoms in the system) is plotted with the logarithmic scale. 289

Figure 7.25: The difference in the entropy between (a) the first-order transition, and (b) the second-order transition [156]. 290

Figure 7.26: The difference in the heat capacity between (a) the first-order transition, and (b) the second-order transition [156]. 291

Figure 7.27: The heat capacity as a function of temperature. The melting occurs at the discontinuous point. 292

Figure 7.28: The quadratic invariants Q_4 and Q_6 as functions of time during the melting. Both Q_4 and Q_6 drop to zero at the superheating limit, indicating the melting is an order-to-disorder transition. 295

Figure 7.29: The third-order invariants W_4 and W_6 as functions of time during the melting. Both W_4 and W_6 jump to zero when melting occurs. 296

Figure 7.30: The symmetry parameters in X, Y, and Z directions. The rapid increase of the symmetry parameters indicates the crystal loses its symmetry. 298

LIST OF ABBREVIATIONS

CMSD	Cumulative Mean Square Displacement
CNT	Classical Nucleation Theory
DFT	Density Functional Theory
DMSD	Dynamic Mean Square Displacement
EAM	Embedded Atom Method
EML	Electromagnetic Levitation
ESL	Electrostatic Levitation
GH	Gradual Heating
IH	Isothermal Heating
LJ	Lennard-Jones
MC	Monte Carlo
MD	Molecular Dynamics
MSD	Mean Square Displacement
NPE	Constant Number of atoms, Constant Pressure, and Constant Enthalpy
NPT	Constant Number of atoms, Constant Pressure, and Constant Temperature
NVE	Constant Number of atoms, Constant Volume, and Constant Enthalpy
NVT	Constant Number of atoms, Constant Volume, and Constant Temperature
PBC	Periodic Boundary Condition
PDF	Pair Distribution Function
PRMD	Parrinello-Rahman Molecular Dynamics
RMSD	Root Mean Square Displacement
RDF	Radial Distribution Function

SUMMARY

The phase transitions between solid and liquid are the fundamental processes in nature. Although extensive studies have been performed in the past century, many problems, especially the microscopic mechanisms of the transition, are still not fully understood. In the work presented in this dissertation, we have used extensive molecular dynamics simulations to investigate the thermodynamics and kinetics over a wide range of supercooling and superheating temperatures in a Lennard-Jones model system.

Usually the crystallization process requires some supercooling. If impurities are removed, a liquid can be supercooled twenty percent below the melting point without solidifying. If the surface melting is properly suppressed, melting can occur internally at an elevated temperature higher than the melting point. Most researchers assumed that superheating is simply a reverse process of supercooling, and the classical nucleation theory was directly applied for estimating the nucleation rates of melting at superheating. In this work, we have demonstrated that classical nucleation theory well describes the crystal nucleation in liquid supercooling, but fails for solid superheating. The elastic energy associated with the liquid nucleation and the interface disordering play significant roles in affecting the liquid nucleation in superheating regime. A new nucleation theory is developed in this work, which can quantitatively describe the homogenous nucleation in superheated crystals.

The crystal-melt interfacial free energy is a fundamental parameter in solid-liquid transition. Due to its small magnitude, the interfacial free energy is difficult to obtain in both experiments and simulations. We have developed a new method based on the

classical nucleation theory to accurately determine the crystal-melt interfacial energy and its anisotropy. The interfacial free energy obtained in this work is very close to Turnbull's experimental result.

The face, temperature, and size dependences on the crystallization rate are carefully investigated in this work. We have found that the crystallization rate decreases with the increasing system size. The two prevailing models for crystal growth, diffusion-controlled model and collision-controlled model, both fail to interpret our results. We have found that the atomic site acceptance ratio, which is treated as an invariant in those models, should be both temperature and size dependent. Based on the collision-controlled model, we have developed a new theory to describe the size- and temperature- dependent crystallization rate.

The melting from the internal nanovoids has been investigated in this work. We have found that the melting mechanism of void melting is quite different from bulk melting and nanoparticle melting. There are four different stages and three local melting temperatures in void melting. The complex melting sequence is caused by the interplay among the interfacial free energies, the negative void surface curvature, and the elastic energy associated with density change during the void melting.

The homogenous melting at the upper limit of superheating has been investigated in this work. We have found that ring diffusion takes place in superheated crystals when the heating rate is slow. The prevailing instability theories are not suitable to describe the melting caused by the ring diffusion. It is found that the open diffusion loop causes the instability to the system. The critical density of the open loops for triggering the melting is about 0.5%-1%.

CHAPTER 1

INTRODUCTION

Melting and crystallization are two fundamental processes in nature. A good example of the two processes is the transition between water and ice. Although the solid-liquid transition has been studied extensively for centuries, many problems, especially the microscopic mechanisms of the transition, are still not fully understood [1-3]. One of those problems is the asymmetry between melting and crystallization processes. For crystallization process, i.e., the transformation from a liquid phase to a solid phase, small amount of supercooling (the temperature is below the equilibrium melting point) is always required to provide the driving force for solidification [1-3]. Generally, the amount of the achievable supercooling is small, because the heterogeneous nucleation is usually predominant in a supercooled liquid [1-3]. However, as Turnbull and Cech [4] showed in 1950, if impurities or any other external nucleation catalysts are excluded, liquid metals can be supercooled tens to hundreds of degrees below their equilibrium melting temperatures without solidifying [4-6]. The crystal nuclei must forms homogeneously through the thermal fluctuations. Based on numerous sophisticated experiments, the classical nucleation theory for homogeneous and heterogeneous nucleation had been proposed and applied for interpreting many crystallization phenomena [1-6].

Unlike crystallization process that always requires some undercooling, melting usually occurs at the normal melting temperature without any superheating [1]. One explanation is that the free surface (solid-vapor interfaces) of a solid has very small

energy barriers for heterogeneous nucleation of liquid phase [1,7]. At melting point, melting always starts from the free surface to lower the interface free energy. The absorbed energy from outside is used to melt the solid at the interface. Therefore, the solid superheating is rarely observed in regular melting. In certain materials, a few layers of surface atoms have even been observed to become liquid-like atoms and form quasi-liquid layers at temperatures below the melting point [8,9].

However, if the surface melting is properly suppressed, the solid superheating also can be achieved. Daeges *et al.* [10] performed an innovative experiment to achieve superheating. In order to suppress the surface initiated melting of silver (Ag), they coated a thin layer of gold (Au) on the surface of a silver sphere. Since the melting point of Au (1 338 K) is about 100 degree higher than that of Ag (1 234 K), the inner silver sphere can become a liquid while the outer gold layer is still a solid. The crystal structures of Ag and Au are both fcc structures and the lattice constants of Ag ($4.09A^0$) and Au ($4.08\ A^0$) are very close at the room temperature. The linear thermal expansion coefficients of Ag ($1.86\times10^{-5}/C^0$) and Au ($1.42\times10^{-5}/C^0$) are very close, too. Therefore, the surface of the silver sphere is effectively "erased". When the composite sample was heated to high temperatures, the accompanying internal hydrostatic pressure, which is induced by the difference in the thermal expansion coefficients between Ag and Au, was released in their experiment by careful annealing. They observed that the silver sphere could be superheated up to 25 K for a time period of about one minute. This work told us that superheating is possible if the surface nucleation is suppressed. Superheating can also be achieved by ultra-short pulsed laser irradiations [11-12]. Due to the ability of focusing a laser light on a small area or even inside the solid, the laser-irradiated materials can be

heated internally. As a result, a significant amount of superheating has been observed in those experiments.

Although it is hard to prepare surface-free systems in experiment, it is very easy to produce the surface-free system in computer simulations by applying the periodic boundary conditions (PBCs) [13]. With PBCs, the simulation system is equivalent to be embedded in an infinite system. Consequently, the free surface is "removed" and the melting can start from within. The maximum superheating is usually about 20% above the equilibrium melting temperature [14]. The interpretations for melting at superheating, fell into several categories of instability theories [15-20]: (1) Born shear instability [15], (2) Lindemann vibrational lattice instability [16-18], and (3) Fecht and Johnson's inverse entropy catastrophe [19,20]. The main idea of Born shear instability is that melting is preempted by the vanishing of the shear modulus at high temperatures [15]. Lindemann vibrational instability theory argues that melting occurs when the root-mean-square displacement (RMSD) of atoms in a superheated crystal reaches a critical fraction of the nearest neighbor distance [16-18]. Fecht & Johnson's entropy catastrophe theory proposes that the entropy of a superheated solid increases because of the presence of various defects such as vacancies at high temperatures [19-20]. However, the solid entropy cannot increase indefinitely, because a liquid always has higher entropy than does a solid. The entropy catastrophe or melting occurs when the solid entropy is equal the liquid entropy. This theory is a close analogy of Kautzmann's paradox for glass transition [21].

The above theories mainly focus on the static instability limits of metastable superheating, or the highest possible melting temperatures at superheating. Little has

been done to investigate thermodynamics and kinetics of melting in a wide range of superheating temperatures. Many researchers simply viewed superheating as a reverse process of supercooling [22-25]. Some theories [14] have been proposed but without any direct supports from either experiments or simulations. The nucleation rates and the upper limits of superheating were estimated based on the classical nucleation theory [22-25]. However, the fundamental question is whether one can apply the classical nucleation theory directly for the superheating process. So far, there is no decisive evidence to support this assumption.

Similarly, many researchers focused on the thermodynamics and kinetics at deep undercooling [26-29], at which the critical nuclei are small and easy to form via thermal fluctuations. Very few people have studied the homogeneous nucleation in a wide range of supercooling temperatures, especially at shallow and moderate undercooling where critical nuclei are large and, therefore, hard to form spontaneously through the thermal fluctuations [28].

The solid-liquid interfacial free energy is a very important parameter in the solid-liquid transition [1-6]. However, the interfacial free energy is extremely difficult to obtain in experiments, because the solid-liquid interface is buried in two condensed phases [30]. Moreover, the crystal-melt interfacial free energy is very weak (typically in the order of 10^{-3} J/m^2) [1-6]. Thus, it is difficult to measure it accurately. Turnbull and coworkers [4-6] extracted the crystal-melt interfacial free energies for various metals by measuring the homogeneous nucleation rates at deep undercooling. From the experimental data, they proposed an empirical linear correlation between the interfacial free energy and the latent heat. To date, this empirical correlation is still used extensively to predict the solid-liquid

interfacial free energy. However, in Turnbull's homogeneous nucleation experiments [4-6], the impurity effects were still strong. Recently the electromagnetic levitation (EML) and electrostatic levitation (ESL) have been used to investigate homogenous nucleation [31]. In such experiments, the liquid droplets can be levitated in an electromagnetic field. Significant amount of supercooling can be achieved via such containerless processing. In computer simulations, it is also very difficult to extract the weak solid-liquid interfacial free energy accurately from the large thermal fluctuations. Broughton and Gilmer [30] used an "energy-integration" method to calculate the solid-liquid interfacial energy of a Lennard-Jones (LJ) system. The key idea of this method is to integrate the *reversible* work in forming a flat crystal-melt interface. Hoyt et al. [32] used "fluctuation method" to estimate the solid-liquid interfacial energy of a pure nickel. In their method, the interface stiffness can be extracted by monitoring the thermal fluctuations of the flat solid-liquid interface profile. Both methods yield reasonable results. However, it seems that the calculated interfacial free energy is about 10% higher than Turnbull's empirical estimation. Since the nucleation rate is a function of $\exp(-A\gamma_{SL}^3)$, such small discrepancy can cause substantial decrease in the nucleation rate [1-3].

The temperature and orientation dependence of interface energy is another interesting topic. In classical nucleation theory, the interface energy is assumed to be a constant [1-6]. However, this assumption may not be valid in certain conditions. Based on Turnbull's experimental data of homogeneous nucleation rates at different temperatures [6], Spaepen [33] extracted the temperature-dependent interfacial energy of mercury. He found that the interfacial energy increases almost linearly with the increasing temperature up to the melting point. The anisotropy in the crystal-melt

interfacial free energy was investigated with different approaches [30,32]. Generally, the interfacial free energy is found to be isotropic in many systems [30,32].

The steady-state crystallization rate is very important for understanding the kinetics of crystallization process. Generally, the crystal growth of many materials exhibits a thermally activated behavior [34]. Wilson [35] and Frenkel [36] showed that the crystal growth rate is determined by the diffusion coefficient of the supercooled liquid. In other words, the crystal growth is diffusion-controlled [34]. Since the diffusion coefficient can be represented by the Arrhenius equation [1], the diffusion coefficient decays exponentially with the decreasing temperature. At half the melting point, it almost approaches zero [34]. Therefore the crystal growth rate is expected to be very slow at low temperatures. However, Turnbull and coworkers found that the crystallization rates of pure liquid metals are still very fast even at very low temperatures [37]. As a result, the pure metals are not glass formers [34,37]. Therefore, for monatomic systems, the crystal growth may not be a thermally activated process. Turnbull and Bagley [37] argued that the crystal growth of a monatomic system should be a collision-controlled process, in which the crystallization rate is determined by the frequencies of the near interface liquid atoms colliding on the interface. Using molecular dynamics simulations of a Lennard-Jones model system, Broughton and coworkers [34,38] showed that the crystal growth of (100) plane is more like a collision-controlled process, while that of (111) plane is more like a diffusion-controlled one.

Although the growth mechanism has been investigated extensively, the finite size effects on the crystallization rate are seldom investigated. In Broughton et al.'s work [34], the maximum crystallization rate of (100) face was found to be as large as 80 m/s in their

simulations. The similarly high growth rates were found in other simulations as well [39-42]. In many experiments of rapid solidification, the measured crystal growth rates are about 5m/s [43-50]. Therefore, it appears to be a general result that the velocities in simulation studies are much larger than those observed in experiments, implying that the computer simulation overestimates the growth rate. Unfortunately, this large discrepancy between the experimental results and the theoretical predictions has not been resolved. The underlying physical origins for this discrepancy, therefore, still remain veiled to date.

Moreover, the crystallization rate may be face dependent [38]. This may be related to the interface structures of different crystallographic planes. In theoretical models, the solid-liquid interface is always considered to be atomically sharp (Gibbs dividing interface) [34,38-42]. In reality, the interface is usually atomic rough (diffuse interface) and the transition from liquid to solid usually takes place over a few atomic layers [51,52]. Although some advances in investigating the interface structures have been achieved recently [51,52], the detailed understanding of the microscopic interface structures, the mechanisms of ordering during the crystallization, and the kinetics associated with the interface moving is still limited.

Usually, the superheating phenomenon is investigated with a perfect crystal system [17,53]. However, in reality, many materials contain various kinds of internal defects such as grain boundaries, stacking faults, voids, etc [19,54]. Those defects can provide heterogeneous nucleation sites for melting. Therefore, the liquid prefers to initiate from these defective regions (if the outer surface melting is suppressed). As a result, the magnitude of superheating can be lowered. In the past decades, some researchers [55-59] have investigated the melting from inner voids. They found that at the

initial stage the melting temperature decreases rapidly with the increasing void size. After the void size is larger than a critical value, the melting temperature becomes leveled and approaches a plateau. They treated this plateau temperature as the equilibrium melting temperature at which a bulk solid and a bulk liquid can coexist with a flat interface. However, by far the mechanism of void melting is still lacking and the theoretical basis for its unusual melting behavior is still unknown [55]. Therefore, this conclusion is rather superficial, because no detailed understanding of the microscopic mechanisms or in-depth thermodynamic considerations have been provided to support this argument.

In superheating experiments, the sample is heated to a very high temperature with picosecond laser irradiations [11,12]. The heating rate is very fast, typically of 10^{12} *K*/s. In computer simulations, the heating rate is of the same order [17]. Recently, the femtosecond electron pulses are also used to achieve superheating [60]. However, such high heating rate may suppress the relaxation of atoms. As a result, the thermodynamic nucleation of liquid may be not observable. The catastrophic melting behavior [20] usually manifests at the upper limit of superheating. If we bring a surface-free sample to a temperature slightly below the upper superheating limit and hold the system temperature isothermally, can melting occur through the spontaneous nucleation? To date, this problem is rarely investigated.

The overall goal of this research is to understand the fundamental problems associated with the solid-liquid transition in both superheating and supercooling regimes. Molecular dynamics simulations have been performed with a Lennard-Jones model system. In Chapter 2, the molecular dynamics simulation techniques are introduced. Several examples are given to illustrate how to calculate the physical quantities from the

atomic trajectories. In Chapter 3, the crystal-melt interfacial free energy is calculated via classical nucleation theory. The temperature and orientation dependences of the interfacial free energy are discussed. In Chapter 4, the classical nucleation theory is tested for melting at superheating. In Chapter 5, the size, face, and temperature dependences of the crystallization rate are investigated. In Chapter 6, the mechanism of void melting is studied. In Chapter 7, the homogenous melting at temperatures close to the upper superheating limit is investigated. We have obtained the following significant results:

- A new method is developed for creating various kinds of solid-liquid coexistence systems [61]. This method efficiently circumvents the atom-overlapping problems in the conventional method [Chapter 3].
- A new method based on the classical nucleation theory is developed for calculating the crystal-melt interfacial free energy and its anisotropy [61,62]. Compared to other methods, the interfacial free energy calculated with this method is more close to Turnbull's experimental results. The interfacial free energy is found to be isotropic and increase slightly with the increasing temperature. The classical nucleation theory is found to be valid for liquid supercooling within its assumption [Chapter 3].
- The classical nucleation theory is found to be not suitable or at least incomplete for describing solid superheating [63,64]. Thus, the solid superheating cannot be viewed as a simple reverse process of liquid supercooling. The elastic energy induced by the density difference between the solid and liquid phases plays a significant role in affecting the liquid nucleation. A nucleation forbidden gap is found in the superheating regime. If the temperature is within this forbidden gap,

melting only can occur from the free-surfaces or the grain boundaries. The liquid growth from disk nuclei is also investigated. It is found that the liquid growth from disk nuclei is easier (requires less superheating) than spherical nuclei. The disk nuclei tend to grow into liquid spheres rather than more oblate disks [Chapter 4].

- It is found that the crystallization rate decreases with the increasing system size [65]. For monatomic system, the crystal growth from both (100) face and (111) face is more like a collision-controlled process rather than a diffusion-controlled one. A modified collision-controlled model is proposed in which the atom acceptance ratio is both temperature and size dependent. The interface thickness of (111) interface is slightly thinner than that of (100) interface. The growth morphology from (111) interface is found to have more defects than that from (100) interface [Chapter 5].
- The void melting is found to be quite different from nanoparticle melting [66]. It is found that the void melting has four distinct stages and three local melting temperatures. In each of the stages, the melting is governed by a unique thermodynamic mechanism. The void melting is determined by the interplay among the surface curvature, the solid-liquid interfacial free energy, and the elastic energy induced by the solid-liquid density difference. The plateau region of the melting temperature appears when the elastic energy is absent. The solid-vapor interfacial free energy controls the liquid nucleation from the void surface, while the solid-liquid interfacial free energy determines the subsequent liquid growth (or the local melting temperature) [Chapter 6].

- It is found that the homogenous melting is possible at temperatures slightly below the upper superheating limit. The ring-diffusion is found in the superheated crystals. The prevailing instability theories such as Born shear instability, Lindemann vibrational instability, and entropy catastrophe may be not invalid when ring-diffusion occurs. The ring-diffusion forms two types of diffusion loops: open loops and close loops. The open loops cause the instability to the system. The aggregation of the open loops is a kind of thermodynamic nucleation. The critical density of the open loops is between 0.5%-%1 when melting occurs. The melting at superheating is still a first-order transition [Chapter 7].

CHAPTER 2

MOLECULAR DYNAMICS SIMULATION TECHNIQUES AND BULK PROPERTIES OF A LENNARD-JONES SYSTEM

Over the past fifty years, molecular dynamics (MD) simulations have been successfully used to investigate the atomic-level details of the materials properties under different physical conditions [13]. The MD simulation provides an alternative way for studying some physical processes that are difficult to access in experiment. The governing principle of MD simulation is Newton's second law. In MD simulations, each atom interacts with its neighboring atoms via an atomic potential. The interaction potential is similar to an "elastic spring" [Figure 2.1] that provides a force (the first derivative of the interaction potential) in the negative direction of the atomic displacement. Thus, the motion of each atom affects its neighboring atoms cooperatively. The net force on each atom is the summation of the forces over its surrounding atoms. The equation of motion of each atom is determined by Newton's second law. By solving the equations of motion of all atoms, one can get the trajectories (time-dependent atom positions and velocities) of all atoms. The discrete atomic configurations and the continuous macroscopic physical properties are connected via the statistical mechanics. Thus, various physical quantities such as enthalpy, temperature, stress, and diffusion coefficient can be obtained from the MD simulation. In this chapter, I will introduce the detailed algorithms of the MD simulation in different ensembles. Some examples of calculating the physical properties in the MD simulation are also illustrated.

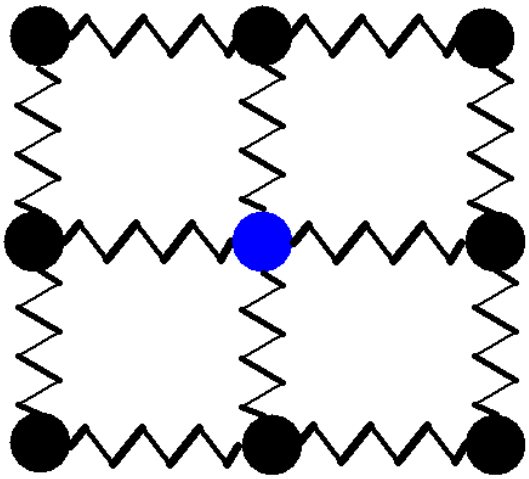

Figure 2.1. Illustration of the interaction between one atom (in blue) and its surrounding atoms (in black). The interatomic interaction is analogous to an elastic spring.

2.1. Molecular Dynamics Simulations in Different Ensembles

2.1.1. MD Simulation in an NVE Ensemble

The simplest type of MD simulations is performed in an NVE ensemble, in which the particle number N, the system volume, and the total energy (enthalpy) E remain constant throughout the simulation [13]. The NVE ensemble is a microcanonical ensemble. For a system containing N particles, the Lagrangian of the system is

$$L = \sum_{i=1}^{N} \frac{1}{2} m_i \dot{\vec{r}}_i^{\,T} \dot{\vec{r}}_i - \sum_{i=1}^{N} \sum_{j>i}^{N} \phi(r_{ij}), \tag{2.1}$$

where *i* represents the *i*th particle, m_i represents the atomic mass of the *i*th particle, $\dot{\vec{r}}_i$ is a vector and represents the velocity of the *i*th particle, $\dot{\vec{r}}_i^{\,T}$ represents the transpose of $\dot{\vec{r}}_i$, r_{ij} is a scalar and represents the interatomic distance between the *i*th particle and the *j*th particle, and $\phi(r_{ij})$ represents the interaction potential between two particles of a distance

r_{ij}. From Eq. (2.1) and the relation $\frac{d(\partial L/\partial \dot{\vec{r}})}{dt} = \frac{\partial L}{\partial r_{ij}}$, one can derive the equation of motion for each particle,

$$\ddot{\vec{r}}_i = -\frac{1}{m_i}\sum_{j\neq i}\frac{\phi'(r_{ij})}{r_{ij}}(\vec{r}_i - \vec{r}_j), \tag{2.2}$$

where $\phi'(r_{ij})$ is the first derivative of the interaction potential. Since the volume and enthalpy are fixed in an NVE ensemble, it is suitable for studying the system in equilibrium conditions. However, most systems are in non-equilibrium conditions and the system pressure and temperature are changing. Thus, the NVE MD is incapable to adjust these changes.

2.1.2. MD Simulation in NPE Ensemble

In order to adjust the system volume with different physical conditions, Anderson [67] developed a new MD algorithm in which an external hydrostatic pressure can be applied to change the edge length of the cubic simulation box. However, the simulation box must be kept at the cubic shape in this method. Parrinello and Rahman [68] extended Anderson's method so that both the volume and the shape of the MD box can change in order to accommodate different physical conditions. Moreover, not only an external hydrostatic pressure but also an external anisotropic stress can be coupled to the system. This is the well-known Parrinello-Rahman molecular dynamics (PRMD). The PRMD generates a constant number of atoms, constant pressure, and constant enthalpy (NPE or NPH) ensemble. In PRMD, a 3×3 shape matrix $h=(a,b,c)$ is introduced to the simulation algorithm, where *a*, *b*, and *c* are the respective vectors of the three box edges.

All particle coordinates are scaled with this shape matrix. Thus the values of the coordinates are in the range from 0 to 1. If we use q_i to represent the scaled coordinate of the i th particle, then its real position is $r_i = hq_i$, and the velocity is $\dot{r}_i = h\dot{q}_i$. The purpose of using the matrix h is to vary the shape and volume of the box in respond to the changes of the pressure, temperature, or potential energy. The physical picture of this method is using a virtual "piston" to squeeze or stretch the system. Thus, In PRMD the Lagrangian of the system is

$$L = \sum_{i=1}^{N} \frac{1}{2} m_i \dot{q}_i^T G \dot{q}_i - \sum_{i=1}^{N} \sum_{j>i}^{N} \phi(r_{ij}) + \frac{1}{2} W \cdot Tr(\dot{h}^T \dot{h}) - PV \ , \tag{2.3}$$

where $G = h^T h$ is a metric tensor, W is the mass of the fictitious "piston", Tr is an operator which sums the diagonal components of a matrix, P is the hydrostatic pressure, and $V = \det(h)$ is the volume of the MD box. The equations of motion for q_i and h derived from Eq. (2.3) are,

$$\ddot{q}_i = -\frac{1}{m_i} \sum_{j \neq i} \frac{\phi'(r_{ij})}{r_{ij}} (q_i - q_j) - G^{-1} \dot{G} \dot{q}_i \ , \tag{2.4}$$

and

$$\ddot{h} = \frac{1}{W} (\Pi - P) A \ , \tag{2.5}$$

where $A = Vh^{-T}$ (h^{-T} is the transverse transpose of h) is an area tensor, and Π is the microscopic stress tensor which has the following form:

$$\Pi = \frac{1}{V} \sum_{i=1}^{N} m_i \dot{\vec{r}}_i \cdot \dot{\vec{r}}_i^T - \frac{1}{V} \sum_{i=1}^{N} \sum_{j>i} \frac{\phi'(r_{ij})}{r_{ij}} \vec{r}_{ij} \cdot \vec{r}_{ij}^T \ . \tag{2.6}$$

Eq. (2.5) is valid only when an external hydrostatic pressure is applied. If an external stress σ is applied to the system, Eq. (2.5) is not applicable. Suppose a symmetric tensor

Γ is related to the external stress σ and the reference matrix (or undeformed shape matrix) h_0 by

$$\Gamma = h_0^{-1}(\sigma - P)h_0^{-T}V_0 . \tag{2.7}$$

where $V_0 = \det(h_0)$ is the reference volume. In this case, Eq. (2.5) is replaced by

$$\ddot{h} = \frac{1}{W}(\Pi - P)A - h\Gamma . \tag{2.8}$$

When the system is under a pressure or a stress, the shape of the simulation system changes, which induces a strain. The strain tensor can be written as

$$\varepsilon = \frac{1}{2}(h_0^{-T}Gh_0^{-1} - 1) . \tag{2.9}$$

Although the system volume can be adjusted in respond to the external stress or pressure, the system temperature cannot be controlled. If the system is stressed or pressurized, the accompanying energy causes an increase of the system temperature. Unfortunately, the temperature change in PRMD cannot be controlled.

2.1.3. MD Simulation in NPT Ensemble

In many circumstances, we need to keep the system temperature and pressure at desired values. In other words, the system should be kept in an *NPT* ensemble. This can be done with two methods. The first one is to rescale the atomic velocities by multiply a factor [13]. The other one is using Nose's scaling method [13,69]. Both methods can keep the temperature constant. In Nose's method, a scaling variable s is introduced to the atom velocities. The velocity of the *i*th particle is rewritten as $\dot{r}_i = h\dot{q}_i s$. In order to couple this Nose variable to the system, a new fictitious "mass" Q is introduced. The

physical picture of the Nose method is to adjust the system temperature through an external thermostat. In an *NPT* ensemble with the Nose variable in use, the Lagrangian changes to the new form:

$$L = \sum_{i=1}^{N} \frac{1}{2} m_i s^2 \dot{q}_i^T G \dot{q}_i - \sum_{i=1}^{N} \sum_{j>i}^{N} \phi(r_{ij}) + \frac{1}{2} W \cdot Tr(\dot{h}^T \dot{h}) - PV$$

$$+ \frac{1}{2} Q \dot{s}^2 - (3N+1) k_B T_{eq} \ln s \,. \tag{2.10}$$

The new equation of motion of q_i in the *NPT* ensemble can be represented by

$$\ddot{q}_i = -\frac{1}{m_i s^2} \sum_{j \neq i} \frac{\phi'(r_{ij})}{r_{ij}} (q_i - q_j) - G^{-1} \dot{G} \dot{q}_i - \frac{2 \dot{s} \dot{q}_i}{s} \,. \tag{2.11}$$

The equation of motion of h [Eq. (2.5) or Eq. (2.8)] does not change. However, the microscopic stress tensor Π [Eq. (2.6)] has a new form:

$$\Pi = \frac{1}{V} \sum_{i=1}^{N} m_i s^2 (h \dot{q}_i \dot{q}_i^T h^T) - \frac{1}{V} \sum_{i=1}^{N} \sum_{j>i} \frac{\phi'(r_{ij})}{r_{ij}} \vec{r}_{ij} \cdot \vec{r}_{ij}^{\,T} \,. \tag{2.12}$$

The equation of motion of the Nose variable is represented by

$$\ddot{s} = \frac{1}{Q} \sum_{i=1}^{N} m_i s (\dot{q}_i^T G \dot{q}_i) - \frac{(3N+1)}{Q} k_B T_{eq} \frac{1}{s} \,. \tag{2.13}$$

Sometimes an *NVT* ensemble (constant number of atoms, constant volume, and constant temperature) is of the interest. This ensemble can be constructed by introducing the Nose variable to an NVE ensemble, i.e., the combination of Eq. (2.2) and Eq. (2.13).

Due to the limited computational capacity, usually the upper limit of the number of atoms included in the system is of several millions. Such a small system has a large surface to volume ratio that strongly affects the stability of the system. In order to get rid of the surface effects, periodic boundary conditions (PBCs) [13] are usually applied in all directions in computer simulations. As illustrated in Figure 2.2, the original system is

surrounded by its periodic boundary images. As a result, the system is equivalent to a small bulk part of an infinite system. Using this method, the surface effects can be suppressed. However, in some cases PBCs cannot be applied. For example, the PBCs should be disabled when one investigates the properties of nanoparticles.

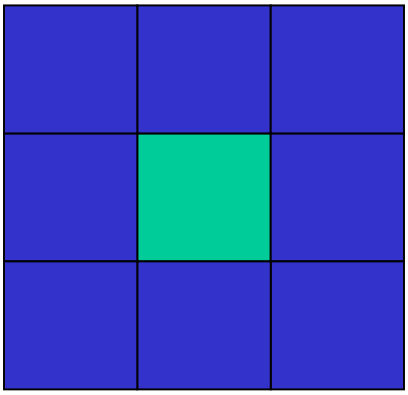

Figure 2.2. Illustration of periodic boundary conditions. The green area represents the original simulation system, and the blue areas represent its periodic boundary conditions.

The atom positions and velocities can be obtained by solving (or integrating) the equations of motion. The predict-correct algorithm [13] is usually used for solving these second-order differential equations. In order to minimize the integration errors, we use the fifth-order Gear predict-correct algorithm [13] to solve the differential equations in this work.

2.2. Lennard-Jones Potential

The interatomic potential is an essential element in MD simulations. Various potential models have been developed for different materials. For example, a simple

Lennard-Jones (LJ) potential is usually used to describe argon. For metals and metallic alloys, the embedded-atom-method (EAM) potentials [70,71] are frequently used. For ionic interaction systems such as metal oxides [72], the Coulomb potentials are more suitable. In this work, we use a monatomic Lennard-Jones system as a model system to investigate some universal thermodynamic and kinetic theories. Since the LJ model system has been extensively investigated over the past 30 years, a lot of data are available for comparison. Moreover, unlike some empirical potentials only works well at room temperatures, the LJ potential works well for both crystal and liquid phases.

The Lennard-Jones potential has a simple 12-6 form, which can be expressed as

$$\phi(r) = \begin{cases} 4\varepsilon[(\frac{\sigma}{r})^{12} - (\frac{\sigma}{r})^{6}] & (r \le r_c) \\ 0 & (r > r_c) \end{cases}, \qquad (2.14)$$

where ε is the energy well depth, σ is a length parameter, r is the interatomic distance, and r_c is the cutoff distance. For solid argon, ε / k_B = 119.8K, where k_B is Boltzmann's constant and σ = 3.405 $\overset{0}{A}$ [13]. The relation between $\phi(r)$ and r is shown in Figure 2.3. At the equilibrium distance, the potential energy has a minimum. If the interatomic distance is less than the equilibrium distance, the interaction is repulsive. If the interatomic distance is larger than the equilibrium distance, the interaction is attractive. If two atoms are far away from each other, the interaction energy $\phi(r)$ is very small and the interaction is neglectable. Thus, one can define a cutoff distance r_c beyond which no interaction is considered. In our work, we define $r_c = 2.5\sigma$. By using the cutoff distance, the long-range interaction is not included and a lot of computation time can be saved.

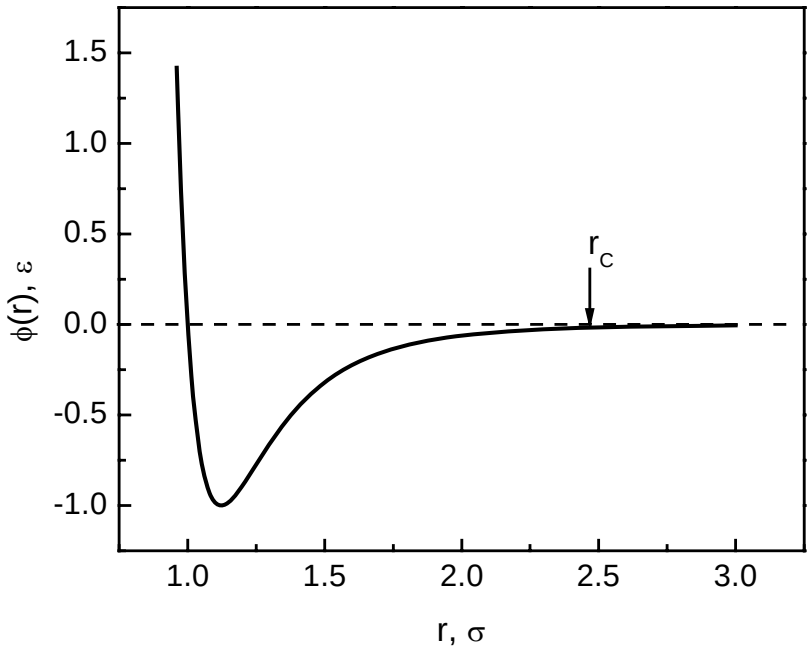

Figure 2.3. The Lennard-Jones potential as a function of interatomic distance *r*.

At low temperatures, the LJ system is in crystal state and has a face-center-cubic (fcc) structure. Initially all atoms in the system are arranged in an fcc lattice. The initial atom velocities assigned with a Gauss distribution. Standard reduced units [13] are used in this work: the mass unit is set as the weight of one argon atom, m = 39.95 amu = 66.3398×10^{-27} kg, length unit is in $\sigma \approx 0.3405$ nm, energy unit is in $\varepsilon \approx 1.654\times10^{-21}$ *J*, time unit is in $\tau = (m\sigma^2/\varepsilon)^{1/2} \approx 2.1561\times10^{-12}$ s, temperature unit is in $\varepsilon/k_B \approx$ 120 K. The time step is set as 0.002319τ, which is about 5×10^{-15} second.

2.3. Examples of Calculating the Physical Properties

2.3.1. System Temperature

Many physical properties can be calculated from the trajectories of the atoms. A simple example is that the system temperature is related to the atom velocities by

$$\sum_{i=1}^{N} \frac{1}{2} m_i v_i^2 = \frac{3}{2} N k_B T \ . \qquad (2.15)$$

Figure 2.4 shows a heating-cooling process. The desired system temperature and the calculated temperature [based on Eq. (2.15)] are shown with different colors. Clearly, the two temperatures coincide with each other so that the red line is hardly seen.

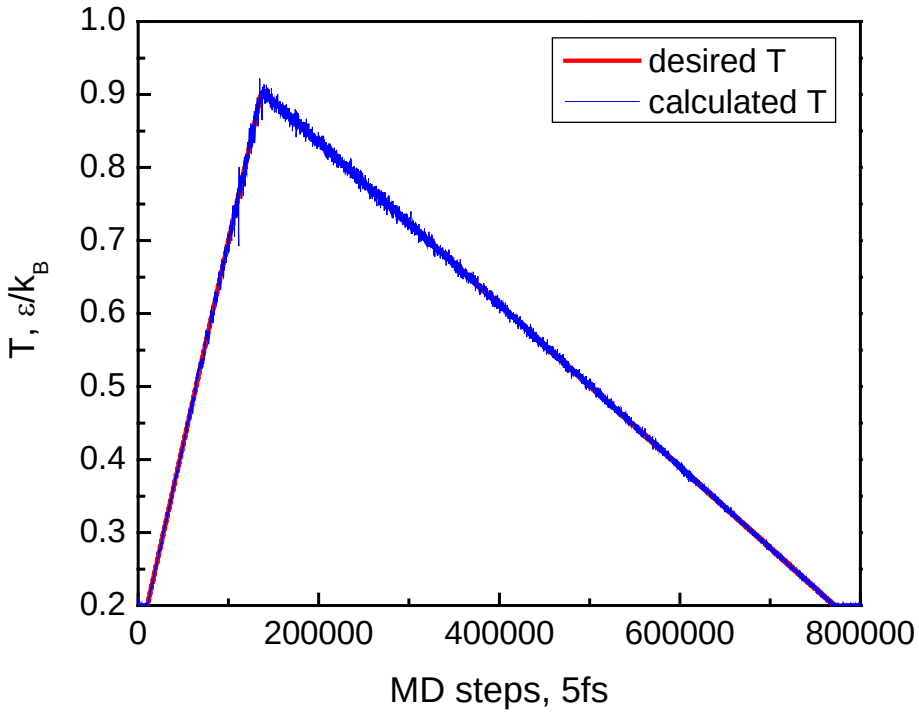

Figure 2.4. The desired system temperature (red) and the calculated system temperature (blue).

2.3.2. Pair Distribution Function

Pair distribution function (PDF), also called radial distribution function (RDF), is a useful technique for characterizing the structure of materials [13]. Suppose there are N atoms in the system, and the volume of the system is V. Originating from a center atom i (i=1, N), the number of atoms enclosed in the shell between r and $r+dr$ [Figure 2.5] is $\Delta N_i(r)$. If $\Delta N_i(r)$ is averaged over all the atoms, one can get

$$\langle \Delta N(r) \rangle = \frac{1}{N} \sum_{i=1}^{N} \Delta N_i(r), \tag{2.16}$$

and the density in the spherical shell r to $r+dr$ is

$$\rho(r) = \frac{\langle \Delta N(r) \rangle}{4\pi r^2 dr} = \frac{1}{4\pi N r^2 dr} \sum_{i=1}^{N} \Delta N_i(r). \tag{2.17}$$

The pair distribution function is the ratio of this average density at r to the average density of the whole system, which is $\overline{\rho} = N/V$. So the pair distribution function $g(r)$ is

$$g(r) = \frac{\rho(r)}{\overline{\rho}} = \frac{V}{N^2 4\pi r^2 dr} \sum_{i=1}^{N} \Delta N_i(r). \tag{2.18}$$

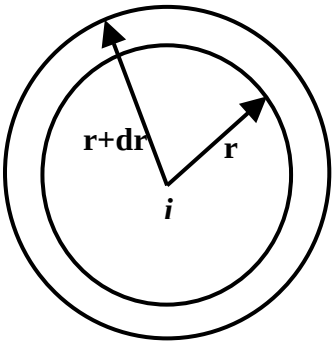

Figure 2.5. Illustration of a shell between r and r+dr originating from a central atom *i*.

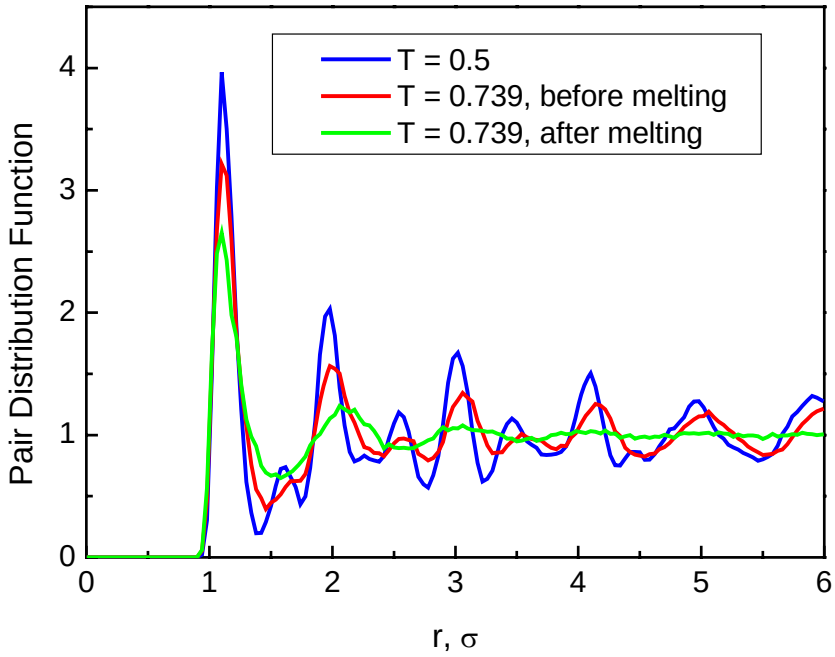

Figure 2.6. The pair distribution function at different temperatures and states: T=0.5 ε / k_B (blue line); T=0.739 ε / k_B, before melting (red line); T=0.739 ε / k_B, after melting (green line).

From Eq. (2.18), one can calculate the pair distribution function from the atomic coordinates. Figure 2.6 shows the pair distribution functions of a LJ crystal system at different temperatures. The LJ system is heated from a low temperature to a high temperature. At T=0.739 ε / k_B, the crystal becomes a liquid. At low temperatures, the system is a well-ordered crystal. At T=0.5 ε / k_B, the PDF shows many sharp peaks. The first minimum of PDF at this temperature occurs at r = 1.35 σ which corresponds the first nearest neighbor distance. At the melting temperature (T=0.739 ε / k_B) but before melting occurs, the peaks of the PDF are not as sharp as those at low temperatures. However, the system still maintains the crystal structure. After melting occurs at this

temperature, only the first two peaks can be clearly seen and other peaks disappear. At large *r*, the PDF is close to 1.0, indicating the system is in liquid state.

2.3.3. Diffusion Coefficient

The diffusion coefficient is related to the atomic displacements over a certain time period. Assume the initial position of atom i at $t = 0$ is $\vec{r}_i(0)$, and at time t the new position is $\vec{r}_i(t)$, then the instantaneous square displacement of atom i is $\left|\vec{r}_i(t) - \vec{r}_i(0)\right|^2$. For a very long time t, the diffusion coefficient D in the 3D space is [13]

$$D = \lim_{t\to\infty}\left(\frac{1}{6Nt} \sum_{i=1}^{N} \left\langle \left|\vec{r}_i(t) - \vec{r}_i(0)\right|^2 \right\rangle \right), \tag{2.19}$$

where the average $\langle \cdots \rangle$ is over all atoms. Equation (2.19) is also called "Einstein relation" [13]. It is worth noting that the periodic boundary conditions should be disabled for calculating the atomic displacements. Otherwise, the shifting from the real atom position to its periodic image causes an artificial increase in the displacement. In molecular dynamics simulations, the time-dependent atomic positions (or trajectories) can be easily traced. Thus, one can use Eq. (2.19) to calculate the diffusion coefficient. Figure 2.7 shows the calculated diffusion coefficients of a liquid at different temperatures. The diffusion coefficient decreases very fast with the decreasing temperature. The diffusion coefficient at T=0.9 ε / k_B is almost 20 times larger than that at T=0.5 ε / k_B. Actually, the diffusion coefficient decreases exponentially with the temperature: $D \sim \exp(-Q / k_B T)$, where Q is the activation energy associated with the diffusion [1].

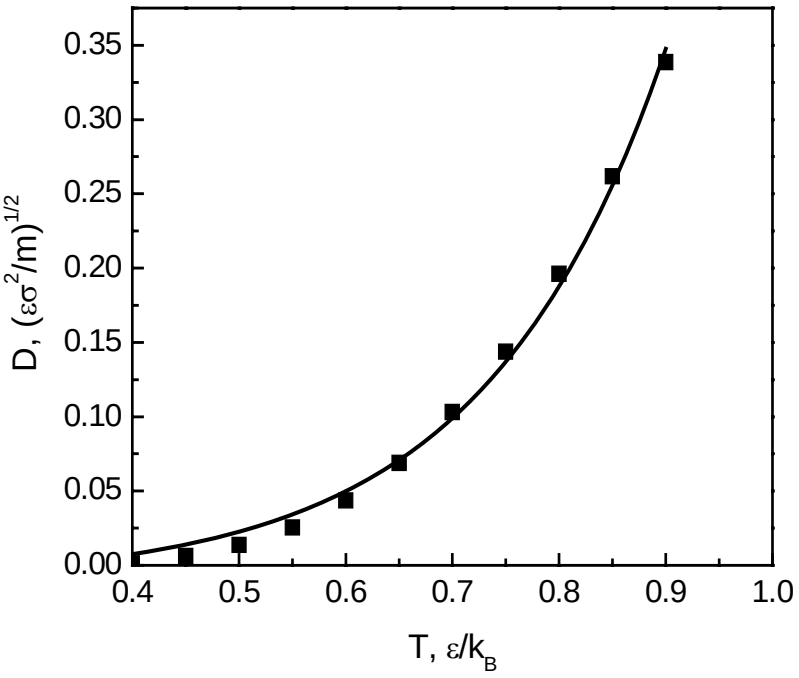

Figure 2.7. The diffusion coefficient of a LJ liquid as a function of temperature.

2.3.4. Elastic Constants

The elastic constants of solids are closely related to the stability and stiffness of materials. Over the past 30 years, several methods have been developed for calculating the elastic constants of solids in computer simulations. A direct method [73] is to apply a tension on the sample and calculate the corresponding strain. From the strain-stress relationship, one can determine the elastic constants. This method is simple and convenient. However, the results are generally less accurate. Moreover, it is difficult to calculate some off-diagonal components of the elastic constants. Rahman and Parrinello [74] developed a fluctuation method to calculate the elastic energy. In this method, the

strain fluctuations are directly related to the adiabatic compliance tensor $S_{ij,kn}$, as shown by

$$< \varepsilon_{ij}\varepsilon_{kl} > - < \varepsilon_{ij} >< \varepsilon_{kl} >= \frac{k_B T}{V_0} S_{ijkl}, \tag{2.20}$$

where ε_{ij} is the strain component and can be calculated with Eq. (2.9). The fluctuation method also can be used in Monte Carlo (MC) simulations [75,76], although the convergence is very slow. One advantage of this method is that the derivatives of the potential are not needed. Therefore this method is useful when the potential has a complicated form. However, from my own experience, Eq. (2.20) generates poor results of the elastic constants. This is primarily due to the presence of some artificial fluctuations in the system. Moreover, since the fluctuations are directly related to the system size by $\Delta\varepsilon_{ij} / \varepsilon_{ij} \sim 1/\sqrt{N}$, Eq. (2.20) may yield a finite-size dependence on the elastic constants.

Elastic constants also can be calculated from the first and second order derivatives of the potential [67,77,78]. In this method, MD should be performed in an NVE ensemble. The form for calculating the adiabatic elastic constants under zero pressure in an NVE ensemble is proposed by Ray and Rahman [77,78],

$$C_{ijkl} = -\frac{V_0}{k_B T}(< P_{ij}P_{kl} > - < P_{ij} >< P_{kl} >) + \frac{2Nk_B T}{V_0}(\delta_{il}\delta_{jk} + \delta_{ik}\delta_{jl})$$

$$+ \left\langle \frac{1}{V_0} \sum_{a=1}^{N-1} \sum_{b=a+1}^{N} \left[\phi'' - \frac{\phi'}{r_{ab}} \right] \frac{x_{abi} x_{abj} x_{abk} x_{abm}}{r_{ab}^2} \right\rangle, \tag{2.21}$$

where P_{ij} is the internal stress tensor which has the same form as Π_{ij} in Eq. (2.6), V_0 is the equilibrium volume under zero external pressure, ϕ' and ϕ'' are the first and second

order derivatives of the pair potential respectively, δ_{ij} has a value of 1 if $i=j$ and 0 otherwise, x_{ab} is the vector joining particle a and b of length r_{ab}, and x_{abi} is the projection of x_{ab} in the i th direction. The first term on the right-hand side in Eq. (2.21) is called fluctuation term, the second term is called temperature correction term or kinetic term, and the third term is called Born term [77,78]. As shown latter, the main contribution of the elastic constants is from Born term. In Eq. (2.21), ϕ is a pair potential. If the interaction potential is not a pair potential such as embedded-atom-method (EAM) function, Eq. (2.21) must be modified in order to include the contribution of many-body effects [79,80]. Since the atom velocities are zero at $T = 0$, the first two terms in Eq. (2.21) are zero and the elastic constant is only determined by the Born term [81].

In order to prepare an NVE ensemble, the system ensemble needs to be changed in the following order: $\text{NPT} \rightarrow \text{NVT} \rightarrow \text{NVE}$. First the NPT MD is performed for 20,000 MD steps to equilibrate the system at a desired temperature T. In the next 20,000 MD steps the reference (or equilibrium) shape matrix $h_0(T) = \langle h(T) \rangle$ and reference volume $V_0(T) = \left| \langle h(T) \rangle \right|$ are obtained by taking the statistical averages of the two quantities. After that, the NPT ensemble is changed to an NVT ensemble by fixing the shape matrix with $h(T) = h_0(T)$. After the system equilibrates for 20,000 MD steps in the NVT ensemble, the Nose thermostat is removed from the system. As a result, the system changes from an NVT to an NVE ensemble. In the NVE ensemble, the system equilibrates for 20,000 MD steps. In the next 60,000 MD steps, we use Eq. (2.21) to calculate the elastic constants. The $3 \times 3 \times 3 \times 3$ matrix C_{ijkl} can be changed to the 9×9 matrix C_{mn} by using Voigt

notation [82], in which the suffixes $ij \to m$, and $kl \to n$. The mapping properties of the Voigt notation are shown in Table 2.1.

Table 2.1: The Voigt notation.

Tensor notation	11	22	33	23, 32	13, 31	12, 21
Matrix notation	1	2	3	4	5	6

For cubic crystals, the elastic constants have the following symmetry:

$$C_{ij} = \begin{pmatrix} C_{11} & C_{12} & C_{12} & 0 & 0 & 0 \\ C_{12} & C_{11} & C_{12} & 0 & 0 & 0 \\ C_{12} & C_{12} & C_{11} & 0 & 0 & 0 \\ 0 & 0 & 0 & C_{44} & 0 & 0 \\ 0 & 0 & 0 & 0 & C_{44} & 0 \\ 0 & 0 & 0 & 0 & 0 & C_{44} \end{pmatrix}. \tag{2.22}$$

Using Eq. (2.21), we calculated all the 36 components of C_{ij} at a given temperature. For example, at T = $0.33\,\varepsilon / k_B$ (40K), the 36 components (in unit GPa) are

$$C_{ij} = \begin{pmatrix} 3.07 & 1.79 & 1.80 & 0.02 & -0.01 & -0.01 \\ 1.79 & 3.07 & 1.79 & -0.03 & 0.01 & 0.02 \\ 1.80 & 1.79 & 3.09 & -0.03 & 0.00 & 0.00 \\ 0.02 & -0.03 & -0.03 & 1.56 & -0.02 & 0.02 \\ -0.01 & 0.01 & 0.00 & -0.02 & 1.60 & -0.01 \\ -0.01 & 0.02 & 0.00 & 0.02 & -0.01 & 1.62 \end{pmatrix}.$$

Clearly, C_{11}, C_{22}, and C_{33} are almost of the same value, which is close to 3.08GPa; $C_{12}(=C_{21})$, $C_{13}(=C_{31})$, and $C_{23}(=C_{32})$ are almost of the same value, which is close to 1.79GPa; C_{44}, C_{55}, and C_{66} are almost of the same value, which is close to 1.59Gpa. The other components are close to zero. Thus, the symmetry of the calculated elastic constants is in very good agreement with Eq. (2.22).

The elastic constants as functions of the time are shown in Figure 2.8. Clearly, only after about 20000 time steps, the nine components reach good convergences. The convergences in this work are faster than those in the Monte Carlo simulations [75,76].

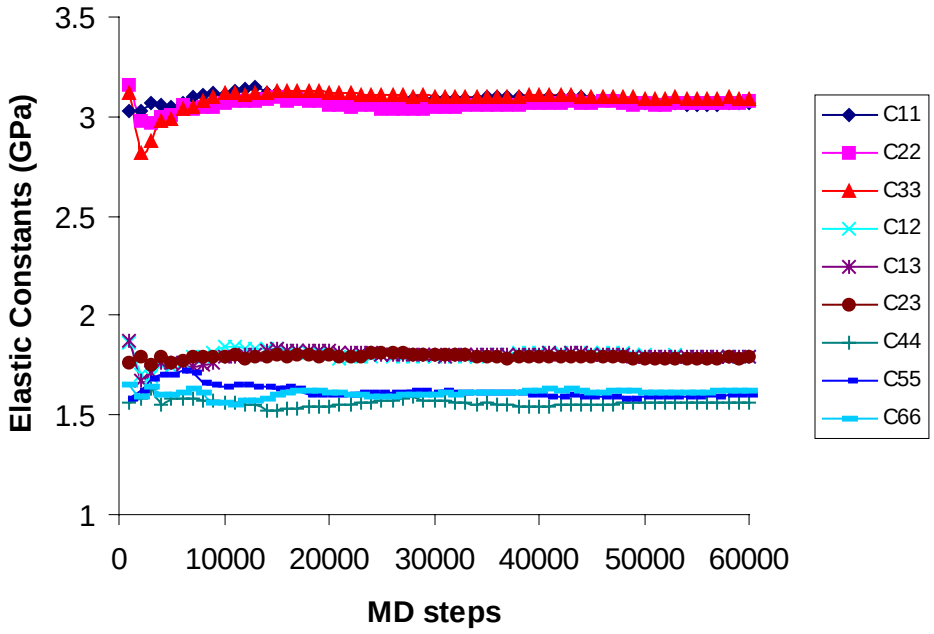

Figure 2.8. The elastic constants as functions of the simulation time at T = 0.33 ε / k_B (40K).

Due to the cubic symmetry [Eq. (2.22)], we can use the average values to represent C_{11}, C_{12}, and C_{44}: $C_{11}=\frac{C_{11}+C_{22}+C_{33}}{3}$, $C_{12}=\frac{C_{12}+C_{13}+C_{23}}{3}$, and $C_{44}=\frac{C_{44}+C_{55}+C_{66}}{3}$. The bulk modulus B_s is related to C_{11} and C_{12} by $B_s=\frac{C_{11}+2C_{12}}{3}$. The shear modulus is $C'=(C_{11}-C_{12})/2$. At different temperatures, we repeat the above calculations and get the temperature-dependent elastic constants, which are shown in Figure 2.9.

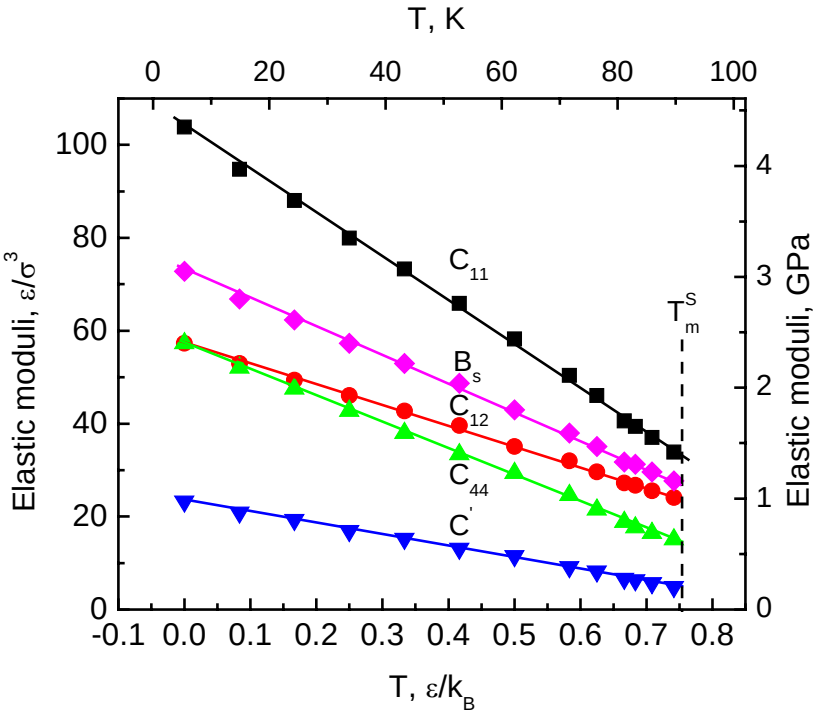

Figure 2.9. Temperature dependent elastic constants. The left and bottom scales show the reduced LJ units, and the right and top scales show the standard units. The symbols are calculated from MD calculations, and the lines are linear fits to the data. T_m^s represents the upper limit of superheating.

Clearly, the elastic constants C_{11}, C_{12}, C_{44}, B_s, and C' decrease almost linearly with the increasing temperature. This is because the fluctuation term in Eq. (2.21) yields a negative value to the respective elastic constant. As temperature increases, the thermal fluctuation also increases. Moreover, the total volume also increases with the increasing temperature. As a result, both the kinetic term and Born term decrease. The total outcome is that the elastic constants decrease with the increasing temperature. At low temperatures, C_{12} and C_{44} are very close to each other. At T=0, $C_{12}=C_{44}$. This is in agreement with the Cauchy relation [83]: for a crystal with central forces (e.g., a LJ potential), in which all atoms are in the center of symmetry (e.g., a perfect cubic crystal at T=0), the relation $C_{12}=C_{44}$ is satisfied. If the temperature is nonzero, C_{44} decreases faster than C_{12} with the increasing temperature. Thus, we have $C_{12}>C_{44}$. The linear fits in Figure 2.9 yield the temperature-dependent elastic constants, as shown in Eq. (2.23a)-(2.23e):

$$C_{11} = 103.72 - 93.27 \times T , \quad (2.23a)$$

$$C_{12} = 57.17 - 44.26 \times T , \quad (2.23b)$$

$$C_{44} = 57.08 - 56.91 \times T , \quad (2.23c)$$

$$B_s = 72.62 - 60.25 \times T , \quad (2.23d)$$

$$C' = 23.27 - 24.51 \times T . \quad (2.23e)$$

2.4. Computing Facilities

In order to handle large systems, the parallel computing is used in this work. Using the parallel computing, we can split one job into several sub-jobs and each of them

is executed in an individual cpu. Currently, we have two major parallel computing clusters: Thunder and Apollo. Thunder clusters have 96 nodes that are connected by Gbit communication cables. The cpu speed of each node is of 2.8-GHz. Apollo clusters have 64 nodes that are connected by optical fibers for Myrinet communication. The cpu speed of each node is of 2.2-GHz. Figure 2.10 shows the two clusters in our lab. Most simulations in this work were performed at those clusters.



Figure 2.10. Parallel computing clusters. Thunder (left): 96-node clusters; Apollo (right): 64-node clusters.

CHAPTER 3

TEST OF CLASSICAL NUCLEATION THEORY FOR LIQUID SUPERCOOLING AND COMPUTING SOLID-LIQUID INTERFACIAL FREE ENERGY

The interfacial free energy, which is generated by the structural differences between two different phases, is a fundamental thermodynamic parameter governing phase transformations [1-6]. For example, the free energy of the crystal-melt interface plays an important role in nucleation and growth of new phases at different supercooling temperatures [1-6]. Unfortunately, interfacial free energies are very weak and extremely difficult to obtain experimentally for systems with two condensed phases such as solid-liquid systems [30]. Turnbull [4] extracted the solid-liquid interfacial free energies for various materials from the homogeneous nucleation rates at temperatures close to their maximum undercoolings. He proposed an empirical relation between the latent heat of fusion and interfacial free energy, which can be expressed as

$$\gamma_{SL} = \alpha \rho^{2/3} (\Delta H_f / N_a), \tag{3.1}$$

where ρ is the atom number density of crystal, ΔH_f is gram atomic heat of fusion, N_a is Avogadro's number (therefore, $\Delta H_f / N_a$ is the enthalpy per atom), and α is a coefficient whose value is approximately 0.45 for most metals and 0.32 for most nonmetals. In order to minimize the heterogeneous nucleation introduced by impurities and other types of catalysts in experiments, Turnbull [5,6] and Cech [5] broke the metal specimen into a large number of small droplets (10 to 100 micron diameter). The

catalysts might be localized in a small fraction of particles so that the crystal nucleation could take place homogeneously. Although impurities may still play a role in affecting the crystal nucleation in the experiment, along with other difficulties in generating and maintaining the droplets of different types of materials, Turnbull's technique had been proved to be effective in suppressing heterogeneous nucleation and made it possible to extract the solid-liquid interfacial energies from crystal nucleation [4]. As we show later, our work is inspired by this experimental approach. An analogous method is developed for atomistic simulation so that the solid-liquid interface free energy could be obtained.

In computer simulations, impurities can be effectively excluded, but calculating the solid-liquid interfacial free energies is still difficult, because the solid-liquid interfacial energies are too small to be accurately retrieved from thermal fluctuations. Several numerical approaches have been developed in the past two decades [30,84-87]. Broughton and Gilmer [30] used a "free energy integration" method by applying an external "cleaving potential" to estimate the anisotropic solid-liquid interfacial energies of a Lennard-Jones system. The basic idea of this method is to integrate the reversible work when two isolated slabs of solid and liquid are joined together to form a flat solid-liquid interface. Davidchack and Laird [84] extended this method to a hard-sphere system by constructing two movable hard-sphere walls at the interface. Although this method can lead to some satisfactory results, it is relatively complicated and not straightforward to implement. For example, in Broughton's work, a lot of efforts were needed to deal with creating a stable interface, and periodic boundary conditions were applied and removed back and forth at the interface. The external cleaving potential must be chosen carefully to make sure the integration process is reversible. Hoyt *et al.* [32,85], on the

other hand, used the "interface fluctuation method" to estimate the anisotropic solid-liquid interfacial energies of several fcc and bcc metals. In their method, the interfacial stiffness (which is the interfacial energy plus its second order derivative) was extracted by monitoring the fluctuations of the solid-liquid interface profile. Since the interfacial stiffness is more sensitive to the anisotropy than interfacial energy itself, this method best suits studying the anisotropy of interfacial energies. However, some difficulties may still be encountered in this method. First, the solid-liquid interface is not easy to be identified, because it always has a transient thickness. Second, the accuracy of identifying the solid and liquid atoms is strongly dependent on the criterion of one's choice. Third, although in principle the thermal fluctuations of the interface profile are directly related to the stiffness of the interface, in computer simulation the fluctuations may mix with other types of fluctuations from finite-size effects, shape fluctuations of simulation box, etc. These kinds of fluctuations may bring difficulties for extracting accurate interfacial energies that are relatively small for most of materials - a small artificial variation of the interfacial energy may cause a large variation of its second order derivative (hence the anisotropy of interface energies). Furthermore, in the above two methods, the system should be kept at the equilibrium melting temperature so that the two phases coexist and the solid-liquid interface stays stationary. Therefore only the interfacial energy at the equilibrium melting temperature can be obtained. In order to consider the temperature dependence of interfacial energy [33,88], a new method is needed for a wide range of temperatures. Recently other theoretical calculations based on density-function theory (DFT) [86,87] have been developed to provide an alternative for estimating the interfacial energy. Unfortunately the results from these approaches are strongly dependent on the

approximations used in constructing DFT models. Hence a relatively simple and accurate method for calculating solid-liquid interfacial energy is still needed.

In this Chapter, we describe a straightforward and easy-to-implement method for calculating the solid-liquid interfacial free energy. As compared with other methods in which the calculations were mainly performed at the equilibrium melting temperatures for flat crystal-melt interfaces, our calculations were performed for a wide range of temperatures and with different sizes of crystal nuclei. Following Turnbull's work, we apply the classical nucleation theory in a wide range of undercooling temperatures and use it to directly estimate the weak interfacial free energy. The temperature dependence of interfacial energy can be calculated with this method as well. Although this work is performed with a standard Lennard-Jones system, the method for creating reliable crystal-melt interfaces can be easily extended to other types of interaction systems.

3.1. Theory, Model, and Method

3.1.1. Classical Nucleation Theory

According to the classical nucleation theory (CNT) [1], to form a small solid sphere of radius *r* in a supercooled liquid [Figure 3.1(a)], the change in Gibbs free energy can be expressed as

$$\Delta G_r = -\frac{4}{3}\pi r^3 \Delta G_V + 4\pi r^2 \gamma_{SL}, \tag{3.2}$$

where γ_{SL} is solid-liquid interfacial energy, and ΔG_V is the Gibbs free energy difference per unit volume between solid and liquid phases at the same temperature. Figure 3.1(b)

shows the relation between the interface free energy term and volume free energy term in Eq. (3.2). In CNT, ΔG_V can be approximated as

$$\Delta G_V \cong L_V \frac{\Delta T}{T_m}, \tag{3.3}$$

where L_V is the latent heat of fusion per unit volume at the equilibrium melting temperature, T_m is the equilibrium melting temperature, and $\Delta T (= T_m - T)$ is undercooling temperature. The critical nucleus radius is obtained from Eq. (3.2),

$$r^* = \frac{2\gamma_{SL}}{\Delta G_V} \cong \left(\frac{2\gamma_{SL} T_m}{L_V}\right)\frac{1}{\Delta T}, \tag{3.4}$$

and the critical nucleation barrier is

$$\Delta G^* = \frac{16\pi\gamma_{SL}^3}{3(\Delta G_V)^2} \cong \left(\frac{16\pi\gamma_{SL}^3 T_m^2}{3L_V^2}\right)\frac{1}{(\Delta T)^2}. \tag{3.5}$$

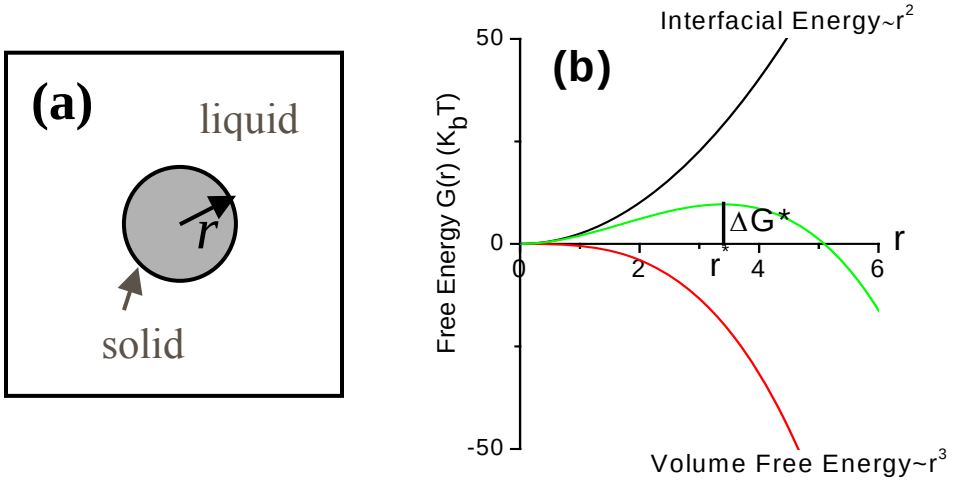

Figure 3.1. Illustration of the classical nucleation theory for homogeneous nucleation. (a) Model of homogeneous nucleation. A solid sphere of radius *r* forms in a supercooled liquid. (b) The changes of the interfacial free energy and the volume free energy in homogeneous nucleation. The critical radius and nucleation barrier are given in Eqs. (3.4) and (3.5).

For a given undercooling temperature, there exists a critical radius r^*, which is associated with maximum excess free energy (or nucleation barrier), as shown in Figure 3.1(b). If $r < r^*$, the solid sphere shrinks in order to lower the free energy of the system; If $r > r^*$, it grows to lower the free energy; If $r = r^*$, solid sphere can be in equilibrium (but unstable) with its surrounding liquid. This relation is very useful in helping rationalize the results from homogeneous nucleation experiments of small metal droplets [4,6]. Turnbull and Cech [5] found that the nucleation rates of critical nuclei governed by the activation energy [Eq. (3.5)] were extremely sensitive to the undercooling temperatures from which he successfully extracted the interfacial energy [4].

This fact motivates us to apply CNT to calculate the interface energy from a different point of view. In our simulations, instead of finding the critical nucleus radius at a given undercooling temperature, we try to find the critical undercooling temperature for a given critical nucleus radius. Namely, for a given critical nucleus radius, r^*, if $\Delta T < \Delta T^*$, the solid sphere dissolves into its surrounding liquid; if $\Delta T > \Delta T^*$, the solid sphere grows; if $\Delta T = \Delta T^*$, solid sphere is in equilibrium (but unstable) with the supercooled liquid. For each given r^*, we can find a corresponding critical undercooling temperature, ΔT^*. By varying the critical sphere size at different ΔT^*, we can obtain a series of corresponding critical undercooling temperatures. Since the critical nucleus radius is proportional to the reciprocal of undercooling temperature [Eq. (3.4)], we can plot a curve of r^* vs. $1/\Delta T^*$ and find its slope k. From Eq. (3.4), we can obtain

$$k = \frac{2\gamma_{SL} T_m}{L_V}. \tag{3.6}$$

The equilibrium melting temperature T_m can be calculated by finding the coexistence temperature of the bulk solid and liquid. The latent heat of fusion can be obtained by comparing the enthalpy difference between the bulk liquid and solid phases at T_m. So the interfacial energy r_{SL} can be calculated from Eq. (3.6) directly. It is worth noting that r_{SL} in Eq. (3.6) is an averaged value over different crystallographic orientations and a wide range undercooling temperatures. As in CNT, for the time being we assumed it as a quantity independent of temperature and orientation. However, these assumptions might not be always true [88,89]. We will discuss these dependences later in this paper.

3.1.2. Simulation Techniques

In this work, we performed the molecular dynamics (MD) simulation in a *NPT* ensemble (where *N* is the number of atoms, *P* is pressure, and *T* is temperature). The Parrinello–Rahman method [68] was employed to control the external hydrostatic pressure (in this work, the external pressures was set to zero), and Nose thermostat [69] was used for controlling the system temperature. The atomic interaction potential used in this work is a Lennard-Jones (LJ) potential, $\phi(r) = 4\varepsilon[(\frac{\sigma}{r})^{12} - (\frac{\sigma}{r})^{6}]$, where σ=3.405Å, ε / k_B= 119.8K, and k_B is Boltzmann constant. One of the reasons for using a LJ system is that it has been studied extensively in the past several decades. Thus a lot of data are available for comparison. Furthermore, the potential can be easily tuned by changing the two parameters. The cutoff distance is set to 2.5σ. The initial lattices structure was face-center-cubic (fcc). To get rid of the surface effects, period boundary conditions were applied in all directions. The number of atoms in the system ranges from 32,000 to

128,000. Standard reduced LJ units [13] are used in this work: the mass unit is in the weight of one argon atom, length unit in σ, energy unit in ε, time unit in $\tau = \sqrt{m\sigma^2/\varepsilon}$, and temperature unit in ε/k_B. The MD time step is set as 0.002319τ, which is about 5×10^{-15} second. In order to handle large systems, parallel computing was used in this work.

3.1.3. Model of a Solid Nucleus Embedded in a Supercooled Liquid

If impurities are effectively excluded from the system, the homogeneous nucleation process dominates during crystallization. As indicated by Turnbull's experiment of cooling mercury droplets [6], the heating and cooling processes generate a large hysteretic loop. The large hysteretic loop also means that solid and liquid phases can coexist for a wider range of temperatures. At equilibrium melting temperature, bulk solid and liquid phases have the same Gibbs free energy. For homogeneous nucleation, the solid nuclei form spontaneously via the thermal fluctuations at deep undercoolings. The critical nuclei usually include less than a few hundred atoms [90]. At shallow or moderate undercoolings, according to Eq. (3.4), the critical nuclei are too large to form spontaneously. In computer simulations, as pointed out by Frenkel *et. al.* [27], spontaneous nucleation is extremely difficult at shallow or moderate undercoolings due to the limitation in computing time. Here we give a rough estimation. The nucleation rate *I* has the unit of $[cm^3]^{-1}[second]^{-1}$. For a system of one million (LJ) atoms and the total simulation time of 100 nanoseconds (ns), which is at the upper limit of the capacity for most modern computers, *I* is in the range of $10^{20\text{-}26}$ $[cm^3]^{-1}[second]^{-1}$, which depends on the size or the number of atoms in the critical nucleus. It is the minimum measurable

nucleation rate in computer simulations. If I is below this value, which is often the case for many materials, one cannot observe nucleation events at all unless the simulation time is on the order of $10^{15\text{-}20}$ seconds or more, which is clearly impossible to achieve. This time barrier has been known to prevent detailed nucleation process from being seen in atomistic simulations in shallow and moderate undercooling. As a result, simulations of homogeneous nucleation are often performed at deep undercooling.

Although it is impossible to form large crystal nuclei spontaneously at shallow or moderate undercoolings, we can artificially insert a "pre-formed" spherical solid nucleus of radius r in a supercooled liquid and create a coexisting system of two phases. At shallow or moderate undercoolings, we can insert nuclei of large sizes. At deep undercoolings, we can insert nuclei of relatively small sizes. By watching how these nuclei change at different temperatures, we could, therefore, study the thermodynamics and kinetics of nucleation in a wide range of supercooling temperatures. The time-barrier limitation [27] described above in MD simulations could be effectively circumvented. However, by doing so, we exclude the possibility of observing the evolution of critical nucleus. The critical nucleus in the spontaneous nucleation could form through complex pathways, either evolving from a single sub-critical solidlike cluster or through merging and dissolving of multiple sub-critical clusters of various sizes and shapes [91]. The nuclei usually exhibit structure, shape, surface morphology, and temporal behaviors different from those assumed in the CNT. In a simplified model as we did in this work, we sacrificed the morphological complexities of the evolving nuclei during homogeneous nucleation in order to focus on the thermodynamic and kinetic behaviors.

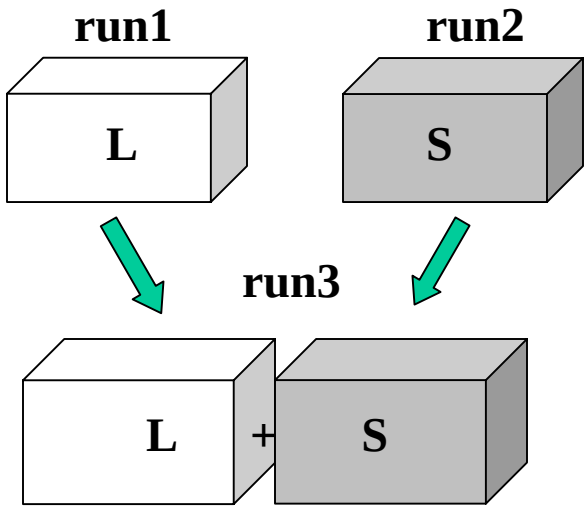

Figure 3.2. The classical way of creating a crystal-melt interface. Three independent runs are usually required.

In many simulation studies [30,84,85], crystal-melt interfaces were created by bringing liquid and solid phases together, as shown in Figure 3.2. Two independent computer runs generated solid and liquid phases separately, and then the liquid and solid slabs were joined together to form a flat crystal-melt interface. However, when the solid and liquid slabs are joined together, the atoms at or near the interfaces may be too close or even overlap with each other. The overlapping could not be eradicated by relaxation, which may introduce strong repulsive forces and cause collapse of the simulation system. For example, Broughton and Gilmer [30] put a lot of efforts to deal with the boundary problems at the interface. In this work, we use only one single computer run to create a "composite" system of a crystal nucleus embedded in a supercooled liquid without such burdens at the interface.

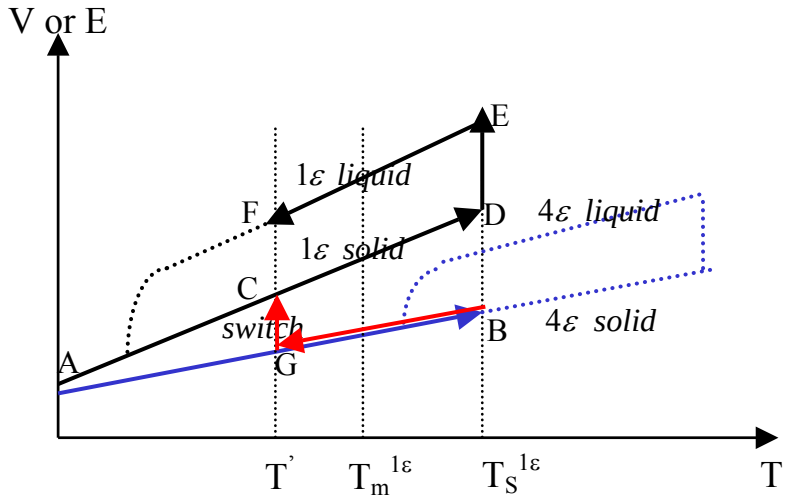

Figure 3.3. Schematic illustration of creating a composite system with a crystal nucleus embedded in a supercooled liquid. The outer matrix follows the path A→C→D→E→F, and the solid sphere follows the path A→G→B→G→C. At temperature T', the potential depth of the solid sphere is changed from 4ε to 1ε (G→C). See text for details.

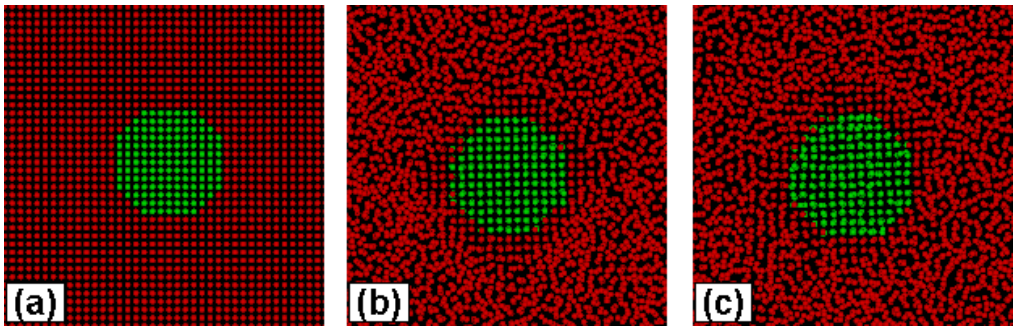

Figure 3.4. Cross-section snapshots during the process of creating the composite system. (a) Initial configuration (at point A in Figure 3.3). (b) At the superheating limit $T_s^{1\varepsilon}$, the outer matrix becomes liquid. (c) At T' in Figure 3.3, the coexistence sample is created after the potential depth of the inner solid sphere is changed from 4ε to 1ε.

Figure 3.3 schematically illustrates this method. Initially, as shown in Figure 3.4(a), the atoms are arranged in an fcc lattice. The system is divided into two parts. One is a cubic matrix, and the other one is a solid sphere embedded in this matrix. The interaction potential of the system is LJ potential. At the beginning, both the sphere and matrix are fcc crystals as indicated by point A in Figure 3.3. The matrix and the sphere have the same atom diameters ($\sigma_1 = \sigma_2 = \sigma$). However, the matrix consists of atoms with the Lennard-Jones potential depth ($\varepsilon_1 = \varepsilon$), and the atoms inside the solid sphere have a larger potential depth ($\varepsilon_2 = 4\varepsilon$). At the interface region, the potential depth for different species of atoms is taken the value of $\sqrt{\varepsilon_1 \varepsilon_2}$. So the sphere has a higher melting point than its surrounding matrix. Due to different thermal expansions of the sphere and the matrix, when the system is heated up, the average enthalpy or volume (per atom) of the sphere follows the line A→G→B while the matrix follows the line A→C→D, as shown in Figure 3.3. If the temperature is higher than the superheating limit of matrix ($T_s^{1\varepsilon}$, where the superscript 1ε represents a standard LJ system), the matrix becomes liquid (D→E) whereas the center sphere still remains in crystalline state (point B). The corresponding snapshot at this temperature is shown in Figure 3.4(b). After a short time period of equilibration and relaxation, the system is cooled down to a temperature T', which is below the equilibrium melting point of the matrix ($T_m^{1\varepsilon}$). At this step, the average enthalpy or volume (per atom) of the matrix follows the line E→F, and that of the solid sphere goes back along the line B→G. At temperature T', the liquid matrix becomes a supercooled liquid (with potential depth ε) while the central sphere is still crystal (still with potential depth of 4ε). As indicated in Figure 3.3, the heating-cooling

process generates a hysteretic loop in the supercooling and superheating regions. If the temperature is within this loop, solid and liquid phases with the *same* chemical composition can coexist. For example, point C and point F represent solid and liquid phases respectively at the same temperature.

At temperature T', we gradually change the potential depth of atoms in the solid sphere to that of the matrix material (i.e., $4\varepsilon \rightarrow \varepsilon$). So the average enthalpy or volume (per atom) of the solid sphere increases gradually from G→C while that of liquid matrix remains at position F. The final outcome is that we create a crystal sphere (point C) embedded in the supercooled liquid (point F) and they have the *same* interaction potential ($\varepsilon_1 = \varepsilon_2 = \varepsilon$). The corresponding snapshot of the atomic configuration is given in Figure 3.4(c). Since there is no atom overlapping problems in this method, the crystal-melt interface looks like a naturally formed one. Therefore, we use only one single computer run and effectively bypass the difficulties of dealing with atom overlapping problems [30] at the interface. Using this method, we can also easily create the flat interface model, superheating model of a liquid nucleus embedded in crystal matrix [63,64], or nuclei of various geometric shapes such as disks, needles, etc. Furthermore, this method can be easily extended to other interaction systems.

Using this approach we can bring the "composite" sample to different undercoolings. Depending on the undercooling temperatures, the nucleus either grows or shrinks. Thus we can find a critical "coexistence" undercooling temperature ΔT^*, within a certain range of errors: if $\Delta T < \Delta T^*$, the solid sphere dissolves in the liquid; if $\Delta T \geq \Delta T^*$, the solid sphere grows. We can create a series of solid nuclei of different radii

r^*, and determine their corresponding ΔT^*'s. More details are given in the next several sections.

3.2. Results and Discussion

3.2.1. Determining the Equilibrium Melting Temperature

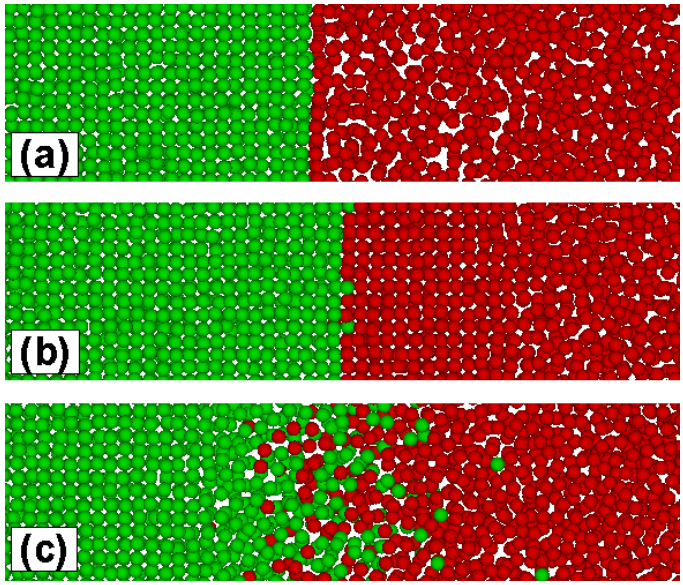

Figure 3.5. Determining the equilibrium melting temperature with a flat interface. (a) At T =0.618 ε / k_B, the flat interface stays stationary. (b) At T <0.618 ε / k_B, crystallization of the liquid makes the interface move from left to right. (c) At T >0.618 ε / k_B, the interface moves from right to left. Melting of the crystal can be seen.

The equilibrium melting temperature of the model LJ system is a crucial reference point for studying the supercooling or superheating phenomena. Due to the applied periodic boundary conditions, the surface melting is suppressed so that the solid can be

superheated to temperatures above the equilibrium melting point $T_m^{1\varepsilon}$ without melting, as shown in Figure 3.3. Eventually at $T_s^{1\varepsilon}$, the solid becomes liquid. $T_s^{1\varepsilon}$ is the upper limit of superheating. Our calculation shows that $T_s^{1\varepsilon} = 0.76\varepsilon / k_B$. It worth noting that $T_s^{1\varepsilon}$ cannot be used in the place of the equilibrium melting point ($T_m^{1\varepsilon}$). The experimental melting point of solid argon ($\approx$83.8 K, about $0.7\,\varepsilon / k_B$) [92] cannot be used as the melting point of LJ system either, because the LJ model system differs from the real argon. In order to determine the equilibrium melting point of the LJ model system ($T_m^{1\varepsilon}$), we try to find the temperature at which a flat liquid-solid interface stays stationary, because liquid and solid phases can coexist with a flat interface at the equilibrium melting temperature. We first use the method described in last section to create the flat solid-liquid interface. The total number of atoms in this system is 32 000. Some snapshots of this system are shown in Figure 3.5. The initial potential depth of the left side is 2ε, and that of the right is 1ε. The external pressure *P* for the entire system is kept at zero in the *NPT* ensemble MD. After the system is heated to a temperature that is above the upper superheating limit ($T_s^{1\varepsilon}$), the right side becomes liquid but the left side is still solid [Figure 3.5(a)]. Then the temperature is cooled down to a lower temperature and the potential depth of the left side is gradually changed from 2ε to 1ε. Afterward we monitor the movement of the flat interface. If the interface moves towards the liquid side [crystallization of liquid, Figure 3.5(b)], we then slightly increase the temperature. Or if the interface moves towards solid side [melting of solid, Figure 3.5(c)], we then decrease the temperature slightly. After a series of trial and error, we found that the flat interface became stationary at T=$0.618\,\varepsilon / k_B$ (about 74.2 K). Thus we can determine that the

equilibrium melting point of the LJ system is $0.618\,\varepsilon/k_B$ at *P*=0. This value is in good agreement with Broughton and Gilmer's result ($T_m^{1\varepsilon}$=$0.617\,\varepsilon/k_B$ at *P*=0) [30], Morris and Song's ($T_m^{1\varepsilon}$=$0.620\,\varepsilon/k_B$ at *P*= $-0.01\,\varepsilon/\sigma^3$) [93], and slightly smaller than Agrawal and Kofke's ($\approx 0.63\varepsilon/k_B$ at $P = 0$) [94]. Note that the value of equilibrium melting temperature is strongly dependent on the choices of simulation parameters such as the cutoff distance of the potential, external pressure, etc. For example, Shen and Oxtoby [95] found the triple point of a LJ system was at $0.67\varepsilon/k_B$. In this work, we use the same set of simulation parameters for all simulations for self-consistency.

3.2.2. Bulk Properties of Solid and Liquid Phases

The bulk properties of solid and liquid phases can be determined from homogeneous crystal or liquid samples. First we heat a single-phase crystalline sample consisting of 32 000 atoms from a lower temperature of $0.2\,\varepsilon/k_B$ to a higher temperature of 0.9 ε/k_B at a heating rate of 1.333×10^{11} *K*/sec. The potential is the standard LJ potential and periodic boundary conditions are applied in all directions. The sample becomes liquid at the upper superheating limit $T_s^{1\varepsilon} = 0.76\varepsilon/k_B$. When the temperature reaches 0.9 ε/k_B, the system is cooled down to a lower temperature of $0.2\,\varepsilon/k_B$ at a much slower cooling rate of 3.333×10^{9} *K*/sec. At temperatures around $0.41\,\varepsilon/k_B$, the liquid starts to crystallize. We record the number densities and enthalpies of solid and liquid phases at different temperatures, which can be seen in Figure 3.6.

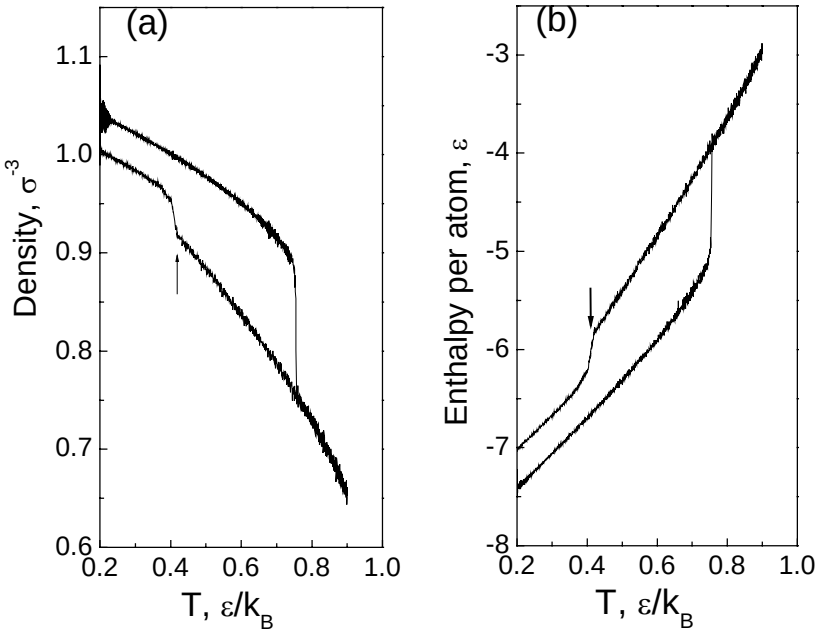

Figure 3.6. The hysteretic loops of the heating and cooling processes of a homogeneous bulk system. (a) The density loop. (b) The enthalpy loop. The arrows indicate the spontaneous crystallization point. The polynomial fits to the data are given in Eq. (3.7) – (3.10).

By fitting the data in the temperature range from 0.41 to $0.76\,\varepsilon/k_B$, the temperature-dependent densities and enthalpies of solid and liquid phases can be approximated by the 3rd order polynomial functions. The number density of the bulk solid phase at a temperature T is

$$\rho_s(T) = 1.2566 - 1.24352T + 2.09829T^2 - 1.45575T^3, \tag{3.7}$$

and the number density of the bulk liquid phase is

$$\rho_l(T) = 1.14956 - 0.77309T + 0.76469T^2 - 0.57129T^3. \tag{3.8}$$

The enthalpy per solid atom is

$$E_s(T) = -8.33233 + 5.43011T - 5.46738T^2 + 5.28305T^3, \quad (3.9)$$

and the enthalpy per liquid atom is

$$E_l(T) = -8.37089 + 7.21323T - 3.97902T^2 + 2.93256T^3. \quad (3.10)$$

At the equilibrium melting temperature $T_m^{1\varepsilon}(=0.618\varepsilon/k_B)$, we can determine the latent heat of fusion $L_V = [E_l(T) - E_s(T)] \times \rho_s(T)\big|_{T=T_m^{1\varepsilon}} = 1.024\varepsilon/\sigma^3$.

3.2.3. Determining the Critical Temperature of the Composite System

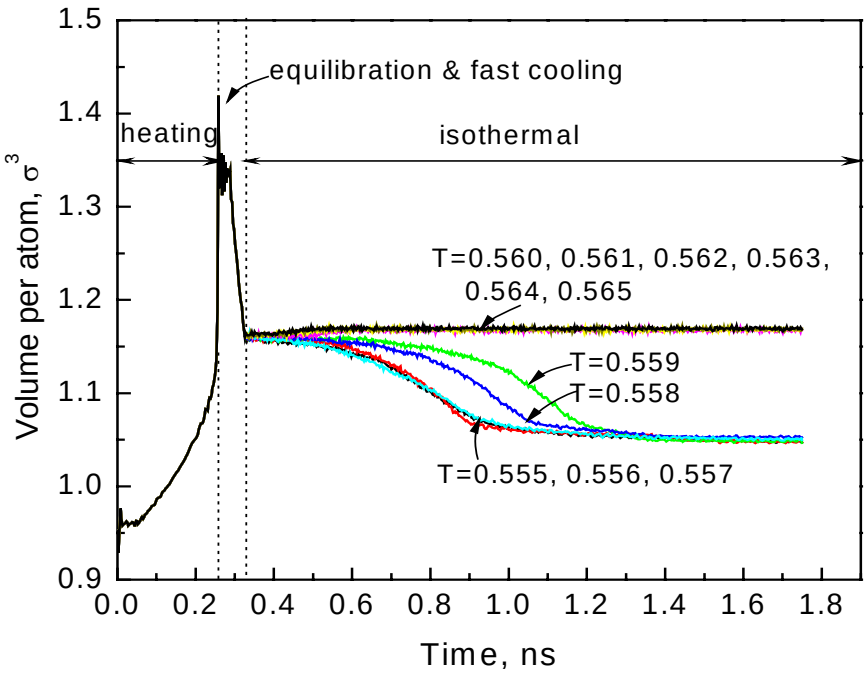

Figure 3.7. The volume changes at different temperatures for a sample of 683 solid atoms embedded in a liquid matrix of 31 317 atoms. The liquid matrix crystallizes at $T \le 0.559$, and does not change when $T \ge 0.560$. Thus the coexistence temperature is approximately at $T = 0.559$.

We use two different size systems containing 32 000 and 128 000 atoms respectively in this work. The purpose of using different size systems is to check whether the system size would affect our simulation results. The initial configuration of the composite system, which is a solid sphere embedded in a matrix, has been described in the section 3.1.3. The initial potential depth of the central sphere is 4ε, and that of the outer matrix is 1ε (the regular LJ potential). The external pressure is kept at zero. MD runs are carried out at an initial temperature of $0.2\,\varepsilon/k_B$ and run for 10 000 MD steps (10 000 steps × 5 fs/step = 50 ps) to equilibrate the system. Then the system is heated up at a rate of increasing 0.5K ($\approx 0.00417\,\varepsilon/k_B$) every 300 MD steps (the heating rate is 3.3×10^{11} K/sec). The heating process is stopped at a temperature of $0.80\,\varepsilon/k_B$. Since the superheating limit of the standard LJ system ($T_s^{1\varepsilon}$) is $0.76\,\varepsilon/k_B$, the outer matrix is in liquid state already at this temperature. However, the sphere is still solid. After being equilibrated for 5 000 MD runs (25 ps) at this temperature, the system is quickly cooled down to a desired temperature T' which is below the equilibrium melting temperature of the matrix $T_m^{1\varepsilon}$ (= $0.618\,\varepsilon/k_B$) at a cooling rate of 6.6×10^{-11} K/sec. The cooling process should be fast in order to avoid the pre-mature crystallization induced by the solid. At temperature T', the potential depth of atoms inside the sphere is changed gradually from 4ε to 1ε in 3 000 MD steps (15 ps). During this step, cautions are taken to make sure no large and abrupt disturbance arises in volume, energy and temperature of the system. After the potential is changed, the atoms in solid sphere have the same potential as those in the liquid matrix. Due to the different thermal expansions between 4ε-solid and 1ε-solid, the volume of the solid sphere expanded about 8% after the potential of the sphere was changed to the regular LJ potential. Since we use constant pressure-constant

temperature molecular dynamics (*NPT* MD) simulation, the system can effectively adjust the change of volume during this procedure.

After the potential was changed, we held the temperature isothermally at T' [Figure 3.7] for additional 200 000 ─ 900 000 MD steps (1ns ─ 4.5ns) and observe the structural and thermodynamic evolutions of the solid sphere. It has three possible outcomes: (a) if the undercooling temperature $\Delta T = \Delta T^*$, the solid sphere and liquid coexist but in an unstable equilibrium, (b) if $\Delta T < \Delta T^*$, the solid sphere dissolves in the liquid, and (c) if $\Delta T > \Delta T^*$, the solid crystal grows. Since the coexistence of the solid sphere and supercooled liquid is unstable and a small thermal fluctuation can break this equilibrium, the solid sphere either shrinks or grows. Therefore, it is difficult to determine the exact value of the coexistence temperature. Practically, we define the critical undercooling ΔT^* as the *minimum* undercooling at or above which the solid sphere can grow. In other words, the solid sphere of radius r has a high probability to grow at undercooling $\Delta T \geq \Delta T^*$ and shrink at $\Delta T < \Delta T^*$. Here we give an example to explain how we determined ΔT^*, as shown in Figure 3.8. We created a composite system with a solid sphere of 683 atoms embedded in a liquid matrix of 31 317 atoms. In the first run we cooled the system to T =0.555 (or ΔT = 0.063) and held the temperature isothermally for 200 000 time steps (1ns). We found that the system crystallized and the solid sphere still kept its original shape at the center of the newly formed crystal [Figure 3.8(a)]. In the second run we cooled the system to a slightly higher temperature T =0.565 (or ΔT =0.053) and held the temperature isothermally for 200 000 time steps (1ns). We found that the solid sphere collapsed and the atoms in the solid sphere diffused to the surrounding liquid [Figure 3.8(b)]. Thus, we can determine that the coexistence

temperature is somewhere between 0.555 and 0.565. In the next several runs we cooled the system to a series of temperatures between 0.555 and 0.565. For each run we changed the temperature with an increment or decrement of 0.001. And finally, as shown in Figure 3.7, we found that if $T \le 0.559$, the system crystallized; If $T > 0.559$, the solid sphere disappeared and became part of the liquid. Thus, by gradually narrowing the bounds we determined that the coexistence temperature is close to $T^* = 0.559$ or $\Delta T^* = T_m^{1\varepsilon} - T^* = 0.059$.

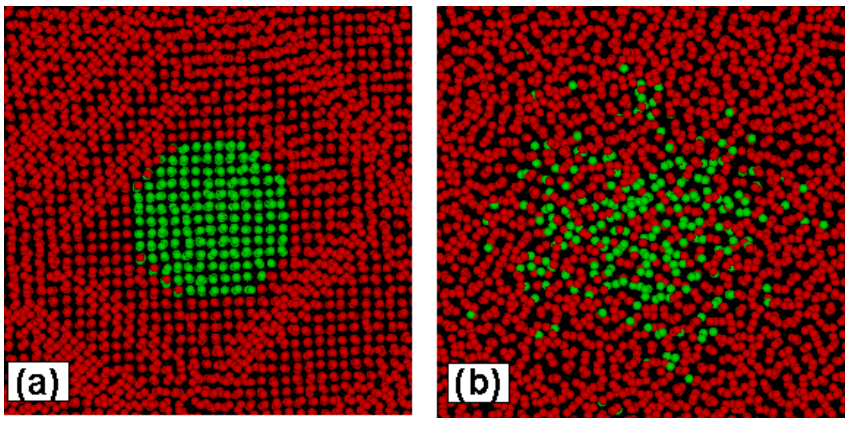

Figure 3.8. Visualization of the cross-section snapshots of the atomic configurations. (a) At $T = 0.555$, the liquid matrix crystallizes, and the solid sphere still keeps its original shape. Some defects can be clearly seen inside the crystal. (b) At $T = 0.565$, the solid sphere disappears. The solid atoms diffuse into the liquid and become liquid atoms.

We use the following three methods to monitor and determine the evolution of the composite system: (1) Calculating the average volume per atom of the total system. If the volume does not change, or increases slightly, the liquid matrix does not crystallize, or the solid sphere may dissolve in the liquid. As shown in Figure 3.7, at T=0.560, 0.561,

0.562, 0.563, 0.564, and 0.565, the matrix is still in liquid state. If the volume decreases significantly, which can be clearly seen at T=0.555, 0.556, 0.557, 0.558, and 0.559, the liquid matrix crystallizes. (2) Visualizations of the atomic snapshots. We save the atomic configurations and observe the structural change of the system. Figure 3.8(a) shows that the system crystallizes at T=0.555. The solid sphere still keeps its original shape and structures after the crystallization. Figure 3.8(b) shows that the sphere dissolves into the surrounding liquid at $T = 0.565$. The atoms in the solid sphere diffuse into the liquid and become liquid atoms. (3) Calculating the respective enthalpies of the solid sphere and the liquid matrix. As shown in Figure 3.9(a), when $T = 0.555$, the enthalpy of solid sphere does not change, but that of liquid matrix decreases significantly. Thus, the liquid crystallizes. Upon crystallization, the small difference in enthalpy is due to the presence of defects such as grain boundaries, vacancies, and stacking faults in the newly formed crystal, which can be clearly seen in Figure 3.8(a). If the system equilibrates for a long time, these defects could be effectively removed. We will discuss this interesting problem in the next section. On the other hand, as shown in Figure 3.9(b), when T=0.565, the enthalpy of the liquid matrix does not change, but that of the solid sphere increases and finally reaches the same level of the liquid. It indicates that the solid sphere dissolves in the surrounding liquid and becomes part of it. Using the above three methods, the solid-liquid evolution and final state of the system can be determined unambiguously.

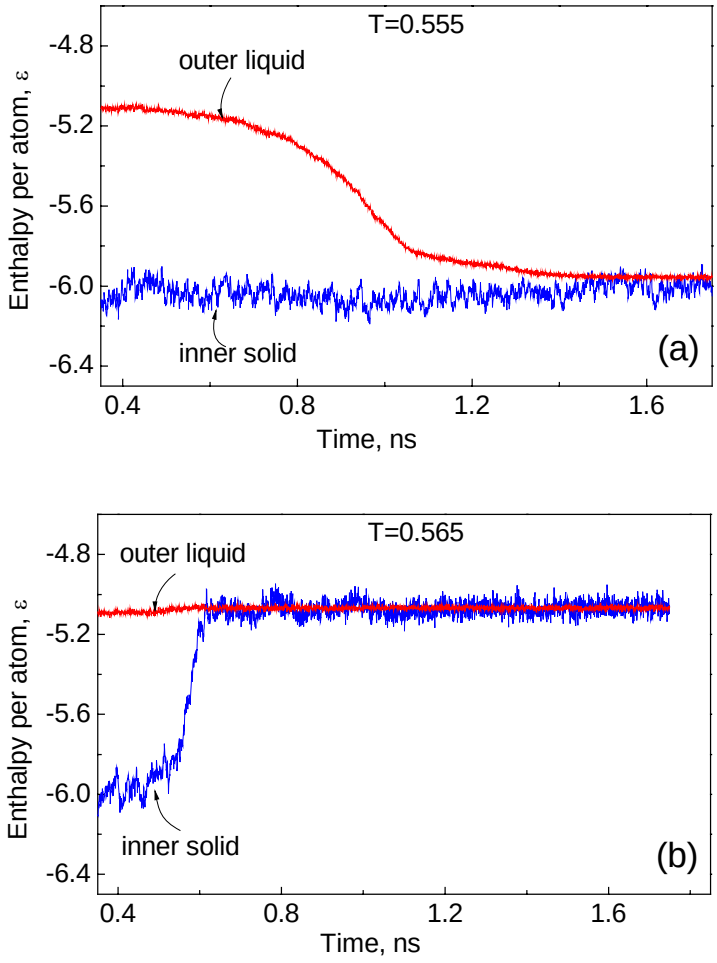

Figure 3.9. The enthalpy changes of the solid sphere and the liquid matrix. (a) At $T = 0.555$, the enthalpy of the liquid matrix decreases to that of the solid sphere. (b) At $T = 0.565$, the enthalpy of the solid sphere increases to that of the liquid matrix.

3.2.4. Statistical Nature Near the Coexistence Temperature

Since the exact coexistence temperature is between $0.559\,\varepsilon / k_B$ and $0.560\,\varepsilon / k_B$ for the composite system described above, the errors of our estimation are within 0.001 ε / k_B. We can improve the precision of our results further if needed.

Table 3.1: Statistics for nucleus growth and shrinkage around the coexistence temperature of a composite system with 683 solid atoms and 31 317 liquid atoms.

T (ε / k_B)	0.559231	0.559232	0.559233	0.559234	0.559235
Evolution of solid sphere	growth	growth	growth	shrinkage	shrinkage
T (ε / k_B)	0.559236	0.559237	0.559238	0.559239	0.559240
Evolution of solid sphere	growth	growth	shrinkage	shrinkage	shrinkage

When the temperature is within the narrow range bounded between 0.559 and 0.560, some uncertainties manifest due to thermal fluctuations around the coexistence temperature. It should be noted that it is impossible to locate the exact coexistence temperature, because the coexistence of a solid sphere in a supercooled liquid is in an unstable equilibrium so that even a small thermal fluctuation could break this equilibrium. Due to this reason, as we mentioned above, we took the lower bound (which is 0.559 in the above example) of the narrow temperature range as the critical coexistence temperature T^*. The uncertainty of locating the exact coexistence temperature reflects the statistical nature of the nucleation process. If the radius of the nucleus is slightly smaller than the critical radius, i.e., $r_-^* < r^*$, the nucleus should shrink according to classical nucleation theory. However, due to the thermal fluctuations, it also has a (smaller) chance to grow. Similarly, if $r_+^* > r^*$, the solid sphere has a probability to shrink as well as growing, although the former has a larger probability than the later. One

can therefore estimate the statistics, or fluctuation property of nucleation by monitoring the change (slightly increasing or shrinking) of the nucleus radius of different sizes at a given temperature [96], or by monitoring the temperatures to which a nucleus of a given radius is brought [62]. In this work, as shown in the last section, we keep the nucleus radius constant but vary the undercooling temperatures. Within the narrow bound of the temperatures of $0.00001\,\varepsilon/k_B$, the probability for the nucleus growing or shrinking is found close to 50% in the system of 683 solid atoms embedded in the liquid matrix with 31 317 atoms. Table 3.1 shows the test results of this case. Within the narrow temperature range between 0.559231 and 0.559240, the solid nucleus can grow at high temperatures (such as 0.559237) and shrink at low temperatures (such as 0.559234). The probability for growing or shrinking is close to 50%. Out of this narrow range, the evolution of the nucleus becomes more deterministic: at low temperatures, solid nucleus grows with higher probability; at high temperatures, solid nucleus shrinks with higher probability. In our work, the errors of the estimation for ΔT^* are within 0.001. Each time we approach ΔT^* from above and below with an increment or decrement of 0.001, and we make sure that the nucleus shrinks if $\Delta T < \Delta T^*$ and grows if $\Delta T \geq \Delta T^*$ with correct probability. Although we can improve the precision of ΔT^*, it is not necessary to do so because that does not change our results qualitatively.

3.2.5. Crystal Growth

If we bring a homogeneous liquid to a deep undercooling at an appropriate cooling rate, the spontaneous nucleation could happen. For a LJ system, we have found that the spontaneous nucleation happens at $T = 0.410$ or $\Delta T = 0.208$ [Figure 3.6]. Since

the spontaneous nucleation proceeds with the formation of solidlike clusters of various sizes and shapes, the spherical crystal nucleus formation and growth as assumed in the CNT, are seldom observed. The discrepancies are often cited as evidences for non-classical nucleation.

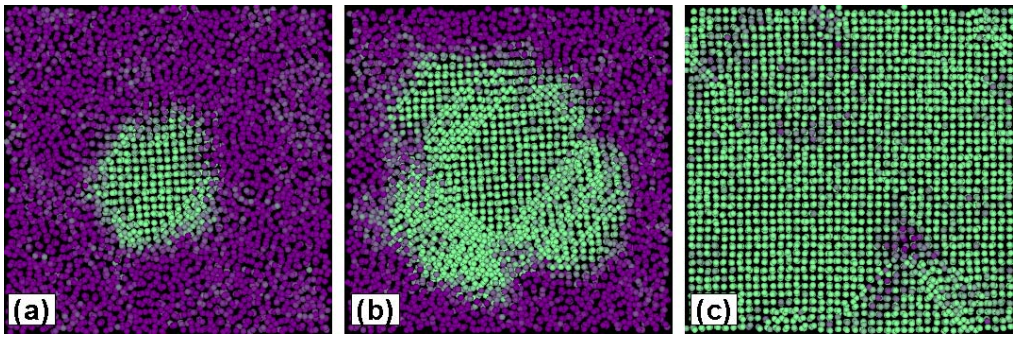

Figure 3.10. Snapshots of the crystal growth from a solid nucleus at $T = 0.557\,\varepsilon / k_B$. We use the coloring scheme described in the text to differentiate the solid and liquid atoms. The color continuously changes from bright green (for solidlike atoms) to dark purple (for liquidlike atoms). (a) The initial sample of 683 solid atoms embedded in 31 317 liquid atoms. The interface atoms are less bright. (b) After 80 000 MD steps (0.4ns), solid sphere grows. The newly grown crystals have some parts whose crystallographic orientations are different from the initial solid sphere. The growth pattern is close to spherical although small irregular shape is seen. (3) After 3 million MD steps (15ns), most grains disappear and the polycrystal almost becomes a single crystal. A few small grains still exist but would disappear if the simulation time is long enough.

At deep undercoolings, the spontaneously formed nuclei could emerge everywhere in the supercooled liquid with different orientations and geometric shapes. These nuclei of different orientations form various small crystalline grains. Thus, the crystals always exhibit polycrystalline structure. At moderate undercoolings, the spontaneous homogeneous nucleation becomes very difficult due to the limitations in

computing time. But we can observe the crystal growth from a pre-formed crystal nucleus, as shown in Figure 3.8(a). Since the atomic planes in the nucleus are slightly distorted and oriented in different crystallographic directions, the newly formed crystal around the nucleus grows in different orientations. Consequently, it also grows into polycrystalline structure. Now the questions are what shape the inserted crystalline sphere could grow into and whether other nucleus morphologies are more preferable.

In both cases, the crystal nucleation and growth morphologies are difficult to be observed clearly from direct visualization of the snapshots. We developed a simple technique to differentiate the solidlike or liquidlike atoms: From a homogeneous sample, we can calculate the enthalpies of solid atom (E_s) and liquid atom (E_l) at each undercooling temperature [Eqs. (3.9) and (3.10)]. For each atom i in the composite system, we average its enthalpy E_i over $\tau = 2\,000$ time steps to get the average enthalpy $< E_i >$ at a temperature. Then we define a parameter $\alpha = (E_l - < E_i >)/(E_l - E_s)$ as a measure of the magnitude of crystallization. If α is close to 0, the atom is liquidlike; if α is close to 1, the atom is solidlike. We then color the atoms continuously from dark purple to light green when α is changing from 0 to 1. Figure 8 shows the growth morphology. Clearly, in Figure 3.10(a) and 3.10(b), the crystal growth pattern is close to spherical although the polycrystalline structure is shown. Note the time τ needs to be longer than the characteristic diffusion time of the atoms at the given temperature.

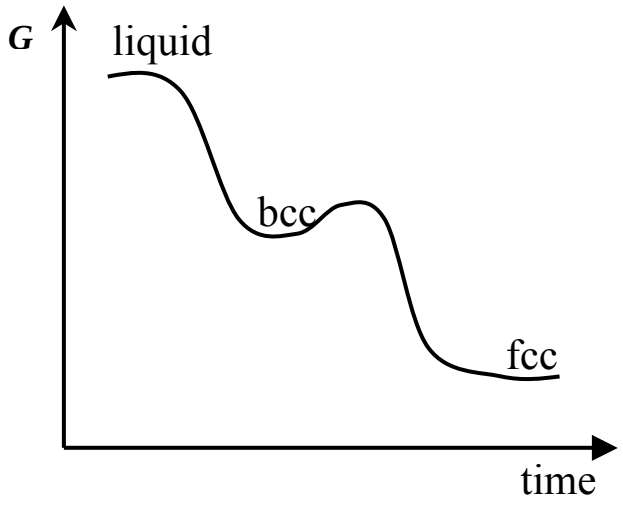

Figure 3.11. Illustration of the free energy levels of different phases. The structural change during the solidification process is often assumed as liquid $\rightarrow$ bcc $\rightarrow$ fcc.

The presence of polycrystalline structure of the new crystal is due to the distortion and different orientations of the atomic planes in the crystal nucleus. It seems that this is a necessary transient process during crystal growth. Based on Ostwald's rule of stages [97], Some authors [98,99] claimed that during crystallization, the least stable structure such as metastable bcc structure should form first and transform to stable fcc structure thereafter [Figure 3.11]. In our work, we have not found any evidence to support this hypothesis. As shown in Figure 3.10(b), we only find the polycrystalline fcc structure with a lot of defects (mainly vacancy, stacking fault, and dislocations) during the crystal growth. The enthalpy difference between the polycrystal and single fcc crystal is small (about 0.1ε per atom). The polycrystalline structure is metastable and it is a transient state. Thus, it may be more suitable to replace the bcc structure in Figure 3.11 with the polycrystalline structure. This polycrystalline structure is a metastable state. If we hold

the temperature isothermally for a long time period, the polycrystalline structure disappears and the system becomes a single crystal. Figure 3.10(c) gives a typical example. After the system is equilibrated for 3 million time steps (15ns), the polycrystal becomes almost a single crystal.

3.2.6. Extracting the Average Interfacial Free Energy from the Inverse Relation between r^* and ΔT^*

In section 3.2.3, we give an example to illustrate how we determine the critical undercooling temperature for a solid nucleus of a given radius r^*. By varying the radius r^* of the solid nucleus, i.e., changing the number of solid atoms enclosed in the solid sphere, and repeating the same procedures described in section 3.2.3, one can find their corresponding critical undercooling temperatures. Thus, the relation between the critical nucleus size r^* and critical undercooling temperature ΔT^* can be derived. In order to check whether the system size played a role in this relation, we performed simulations for two systems with 32 000 and 128 000 atoms respectively. The number of atoms enclosed in the solid sphere ranges from 43 to 12 215. The radius of a solid sphere can be calculated using $r^* = \left[3n / 4\pi\rho_s(T)\right]^{1/3}$, where $\rho_s(T)$ is given in Eq. (3.7). Figure 3.12(a) shows the relation of r^* vs. ΔT^*. Apparently, the data calculated from the two different size systems follow the same curve, indicating that the system size does not affect the relation between r^* and ΔT^*.

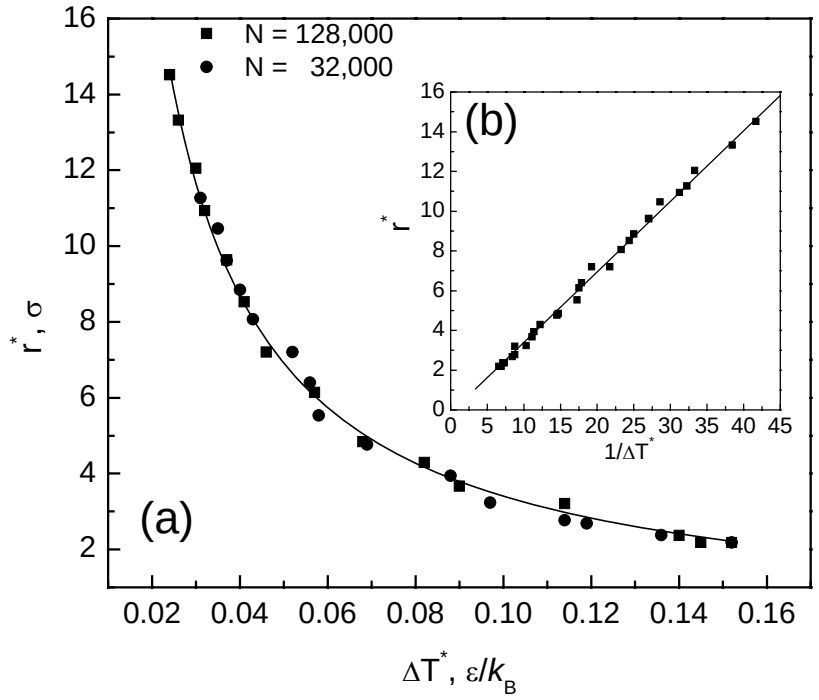

Figure 3.12. The inverse relation between the critical nucleus size r^* and the critical undercooling temperature ΔT^*. The solid line in (a) is a fit to Eq. (3.4). The linear fit in (b) yields the value of k in Eq. (3.6).

As pointed out by Kelton and Greer [100,101], although nucleation has been extensively studied, critical experimental tests of CNT are still lacking in getting the detailed atomic mechanisms of nucleation, as well as other thermodynamic properties, because the required interfacial energies and atom attachment frequencies are not directly measurable. Our simulation result shows a direct numerical support for the validity of the classical nucleation theory in a wide range of undercooling temperatures.

Table 3.2: Calculated solid-liquid interfacial energies by different theoretical approaches. In order to make comparisons, all the results are converted to the LJ units. Due to the lack of the attractive potential in hard-sphere systems, the calculated interfacial energies of hard-sphere systems are about 10% larger than those of the LJ systems [87].

	Method	$\gamma\sigma^2/\varepsilon$
This work	CNT approach, LJ, MD	0.302±0.002
Turnbull [4]	Empirical estimation from experiments	0.330 [a]
Broughton and Gilmer [30]	Reversible work integration, LJ, MD	0.35±0.02[b]
Davidchack and Laird [102]	Reversible work integration, LJ, MD	0.360±0.002[b]
Morris and Song [93]	Interface fluctuation method, LJ, MD	0.362±0.002[b]
Davidchack and Laird [84]	Reversible work integration, hard-sphere, MD	0.376±0.006[b,c]
Auer and Frenkel [103]	Umbrella sampling, hard-sphere, MC	0.38[b,c]
Marr and Gast [86]	DFT[d], hard-sphere, MC	0.389±0.01[c]
Curtin [87]	DFT[d], hard sphere, MD	0.398[b, c]

[a]For nonmetals, the interfacial energies can be empirically expressed as $\gamma_{sl} = 0.32\Delta L_n \rho_s^{2/3}$ (Ref. 1), here the $\Delta L_n = 1.075\varepsilon$ is the latent heat per atom, and $\rho_s = 0.94/\sigma^3$ is the number density of crystal.

[b]Interfacial free energy is averaged over (100), (110), and (111) orientations.

[c]The unit of interfacial energy for hard-sphere systems, $k_B T/\sigma^2$, is converted to the standard Lennard-Jones unit ε/σ^2 by Barker and Henderson's method [104,105]: an effective hard-sphere diameter σ_{eff} can be expressed in terms of the LJ potential $u_{lj}(r)$, $\sigma_{eff} = \int_0^{\sigma_{lj}} (1 - e^{-u_{lj}(r)/kT}) dr$.

[d]DFT – Density Functional Theory; MC – Monte Carlo simulation; MD – Molecular Dynamics simulation.

With all the aforementioned tests done to make sure that the model we adopted can faithfully represent CNT, we are ready to extract the solid-liquid interface free energies. According to classical nucleation theory, the critical nucleus size r^* is proportional to the reciprocal of critical undercooling temperature ΔT^*, i.e., $r^* \propto 1/\Delta T^*$ [Eq. (3.4)]. It is more convenient to plot r^* vs. $1/\Delta T^*$, which is shown in Figure 3.12(b). From the least squares fitting to the data to the equation $r^* = k/\Delta T^*$, we found k=0.364. From Eq. (3.6), we can get $k = \frac{2\gamma_{SL} T_m}{L_V}$=0.364. Here L_V=1.024, which was calculated from homogeneous crystalline phase [section 3.2.2], and T_m=0.618, so $\gamma_{SL} = k \cdot L_V / (2 \cdot T_m) = 0.302\, \varepsilon/\sigma^2$ ($\approx 3.58\ mJ/m^2$). In order to compare this value with the results of other authors' work, we list in Table 3.2 the interfacial free energies calculated by various theoretical approaches. It can be seen that our result is in good agreement with Turnbull's estimate ($\approx 0.330\varepsilon/\sigma^2$) [4]. But the value of γ_{SL} in our work is lower than those calculated previously, which are listed in Table 3.2. The possible origins of the discrepancies are addressed below.

First, the interfacial energies calculated early were from flat crystal-melt interfaces at the equilibrium melting temperature, while our result was obtained with curved interfaces and averaged over a wide range of temperatures. Second, either NVT or NVE ensemble MD was used in previous works. As shown in Eq. (10) of Broughton's paper [30], the *PV* term was neglected from the contribution of the interfacial free energy. Contrast to the authors' assumption that the sample volume is constant, the system volume may change (or the pressure may not be always at zero) during the process of

changing the cleaving potential. Moreover, since the flat interface was formed by combining two separate bulk solid and liquid slabs, the rigidly formed interface needs to be relaxed. This could lead to volume change (expansion associated with the relaxation), which was not considered in NVT and NVE ensemble MD. Therefore a higher value of interface energy is expected. In our method, we created fully relaxed crystal/melt interfaces in a NPT ensemble MD. The interface energy calculated from our work is an average over not only all crystallographic planes, but also over all temperatures (the previous work was at fixed temperature). As we shown in section H, there is a slight decrease of the interface energy with decreasing temperature. Therefore, the lower value is expected. Although our value is lower than the previous calculations, it is in fact closer to Turnbull's experimental value [4].

In the classical nucleation theory, the interfacial free energy is assumed to be isotropic for all orientations. For example, anisotropic properties of interface free energies were not considered in Turnbull's work [4]. It is also the case in our work. However, it should be noted here that this assumption might not always be true. It was found that the anisotropy in interfacial free energies could be the main factor accounted for the dendrite growth [106]. Some previous numerical works [30,84,85,93,102] and experimental works [89,107,108] considered the anisotropy in interface free energies for different atomic planes. But for the Lennard-Jones [30,93,102] and hard-sphere systems [84,97,103], the interfacial free energy are nearly isotropic for (100), (110), and (111) planes within the simulation errors. Therefore our assumption of isotropic interfacial energies is quite reasonable. However, we also can use our method to calculate the interfacial energies for different atomic planes. We should mention that instead of using a

spherical nucleus, we could insert a nucleus with all (100), (110) or (111) planes as the interface to calculate the interfacial energies for a specific atomic plane. We will present the calculations of anisotropic interfacial energies in a separate publication.

Furthermore, the interfacial free energy may be curvature dependent. The γ value should be affected at small nucleus size. However, so far this issue has not been settled yet, either from experimental or theoretical aspects. The most well known theory for curvature dependent interfacial free energy is by Tolman (although its validity is still questionable): $\gamma = \gamma_\infty /(1+\frac{\delta}{r})$, where δ is Tolman length. Typically, δ is of the order of the first nearest neighbor length [90]. According to the theory, the curvature dependence becomes significant only when the size of the nucleus is less than 100 atoms. This estimation is checked by Frenkel et al. [109,110]. An alternative theory by McGraw and Laaksonen [111,112] predicts that γ for the critical cluster has a correction inversely proportional to the interface area *A*, i.e., $\gamma = \gamma_\infty + \frac{C(T)}{A}$ or $\gamma = \gamma_\infty + \frac{C'(T)}{r^2}$ for spherical nuclei, where *C* is an arbitrary function and could be negative [111,112]. Therefore, compared to Tolman's theory, it predicts that the curvature correction is less significant even though the nucleus size is much smaller. Thus, McGraw and Laaksonen concluded that CNT correctly predicts the critical nucleus size, but not the nucleation barrier. This theory is in good agreement with Wolk et al.'s experiments of homogenous nucleation of H_2O and D_2O [113,114]. It appears valid even when the cluster size is less than 10 (atoms). Using Monte Carlo simulations, Kathmann and Hale [115] showed that the cluster size could be as small as 5-10. Our data points [Figure 3.12] fit well to the CNT down to the nucleus size as small as 43 for a LJ system, which is in good agreement with

those results. In our work, the nucleus size ranges from 43 to 12 215. Most (about 90%) of the nucleus sizes are larger than 100 atoms. According to either of the above two theories, these nucleus sizes are still too large to contribute a significant corrections to the interfacial free energy. Even if the curvature correction was significant at small nucleus radii, its effect could be marginalized, because we fitted the data over a large range of nucleus sizes.

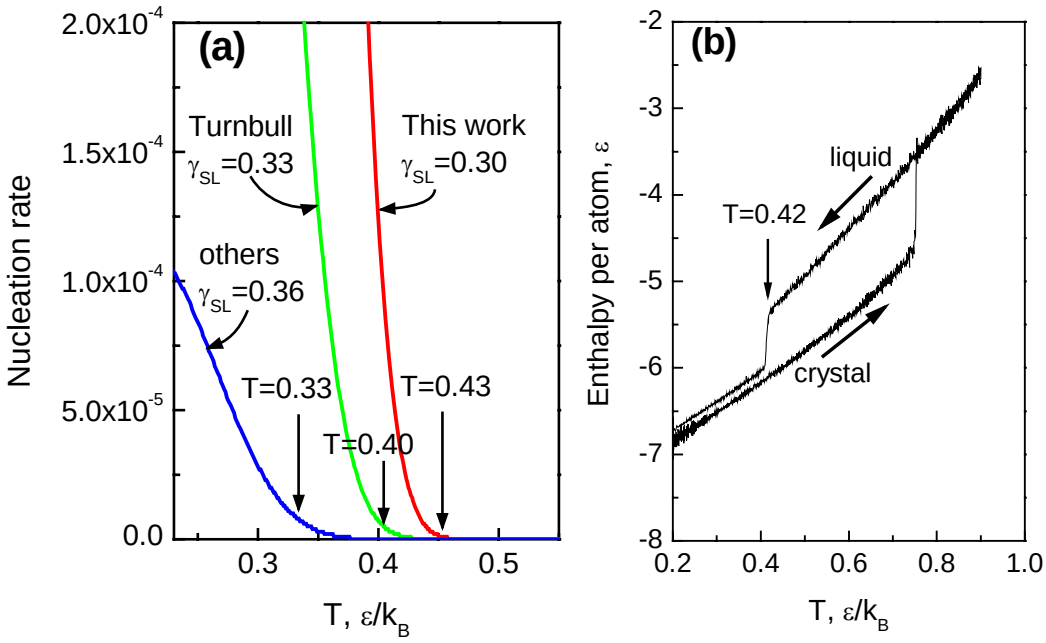

Figure 3.13. (a) The theoretical prediction of the nucleation rates with different interfacial free energies as inputs. (b) The spontaneous crystallization of a pure supercooled liquid.

We can use the theoretical prediction of the nucleation rate to determine which approach gives more accurate interfacial free energy. According to the classical nucleation theory, the homogenous nucleation rate can be expressed as [1],

$$I \sim \exp(-\Delta G^*_{\text{hom}} / k_B T), \tag{3.11}$$

where the homogeneous nucleation barrier can be calculated with the following equation,

$$\Delta G^*_{\text{hom}} = \left(\frac{16\pi \gamma_{SL}^3 T_m^2}{3L_V^2} \right) \frac{1}{(\Delta T)^2}. \tag{3.12}$$

Clearly, the critical nucleation barrier is related to the undercooling ΔT and the interfacial free energy γ_{SL}. Since Eq. (3.11) decays exponentially with the increasing γ_{SL}^3, a slight increase of γ_{SL} can cause the nucleation rate decrease significantly. For LJ system, the latent heat per volume $L_V = 1.024\ \varepsilon/\sigma^3$, and $T_m = 0.618\ \varepsilon/k_B$ [61]. We choose three typical interfacial free energies in Table 3.2 for inputs: our calculated value of $0.30\ \varepsilon/\sigma^2$ [61], Turnbull's empirical estimation of $0.33\,\varepsilon/\sigma^2$ [4], and $0.36\,\varepsilon/\sigma^2$ which is the approximate value of other approaches [30,93,102]. Putting all above parameters into Eq. (3.12), we can use Eq. (3.11) to estimate the nucleation rate as a function of the temperature. Figure 3.13(a) shows the temperature-dependent nucleation rates with different interfacial free energy as inputs. The sudden increase in the nucleation rate fingers the temperature at which the massive nucleation or spontaneous crystallization occurs. If the input is our calculated interfacial free energy, the critical temperature is about $0.43\,\varepsilon/k_B$; If the input is Turnbull's empirical estimation, the critical temperature is about $0.40\,\varepsilon/k_B$; If the input is others' calculated value, the critical temperature is about $0.33\,\varepsilon/k_B$. Then another test was performed. We slowly cooled a pure liquid (without any crystal seed) from a high temperature to a low temperature. The spontaneous crystallization occurs at about $0.42\,\varepsilon/k_B$, as shown in Figure 3.13(b). This crystallization should be achieved through the spontaneous nucleation. It is worth noting

that the cooling of the pure liquid is an independent test. In this test, we did not assume whether the classical nucleation theory is valid or not. Thus, this test can be viewed as an independent "experimental" result. From Figure 3.13(a) and (b), one can find that the inputs of our calculated interfacial free energy and Turnbull's empirical estimation yield correct critical temperatures that are very close to that obtained in the independent test. Contrastively, the input of the interfacial free energy from other approaches yields the critical temperature faraway from the "experimental" value. Thus, our calculated interfacial free energy and Turnbull's empirical estimation may be more accurate.

It is worth noting that our method for calculating the interfacial free energy is not appropriate in the superheating range. When a liquid droplet forms in the superheated crystal, the rising elastic energy due to the volume expansion of liquids plays a significant role in affecting the relation between r^* and ΔT^* [63,64]. The simple relation between r^* and $1/\Delta T^*$ is no longer valid for homogeneous nucleation of melting at superheating. Therefore this method may not be directly applied in superheating range. In Chapter 4, we will discuss the relation between r^* and ΔT^* in the superheating regime. In Chapter 6, we will use the void melting to calculate the interfacial free energy in the superheating regime.

3.2.7. Finite Size Effects

Although the system size does not affect the $r^* \sim \Delta T^*$ relation as shown in Figure 3.12, we find that the larger system has a much longer period of time of solid-liquid coexistence than the smaller system. This coexistence time before the massive crystal growth is a different kind of lag time. Here we give an example. We prepared two

different size samples consisting 31 317 and 107 317 liquid atoms respectively, and a solid sphere of 683 atoms embedded in each of the samples. At T=0.557ε/k_B, both samples crystallize. Figure 3.14 shows the result. Clearly, the large system has a longer lag time τ_2 ($\approx$1 ns) than τ_1 ($\approx$0.4 ns) in the smaller system. This phenomenon can be attributed to the size dependence of thermal fluctuations. For a system consisting of N atoms, the thermal fluctuations are proportional to $1/\sqrt{N}$. So the larger system has smaller thermal fluctuations than the smaller system. The smaller fluctuations (in the larger system) make the solid nuclei slower to pass through the nucleation barrier. Thus, the larger system always has a longer solid-liquid coexistence time. However, the relation of $r^* \sim \Delta T^*$ is not affected by the system size, as shown in Figure 3.12.

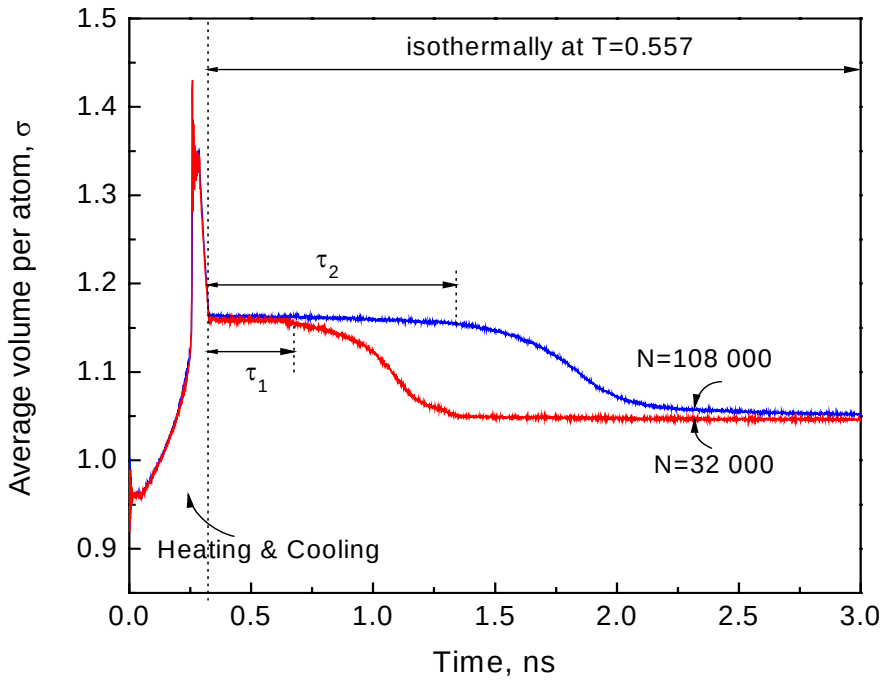

Figure 3.14. Size dependence of the lag time before massive crystallization. The larger sample has a much longer lag time than the smaller sample ($\tau_2 \approx 3\tau_1$).

3.2.8. Temperature Dependence of Interfacial Free Energy

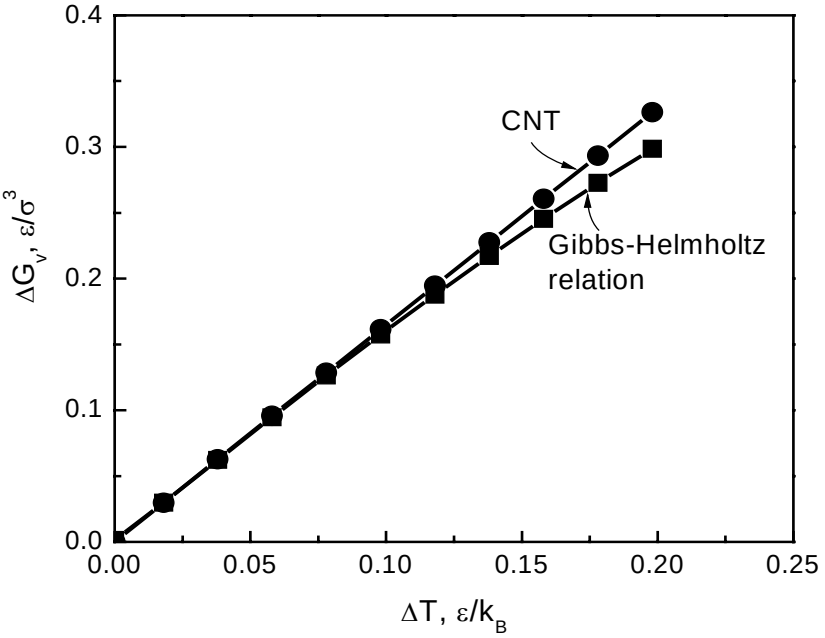

Figure 3.15**.** A comparison of the driving force used in CNT relation (solid circles) and calculated from Gibbs-Helmholtz relation (solid squares). The data of CNT relation are calculated from Eq. (3.3), and the data of Gibbs-Helmholtz relation are calculated from Eq. (3.13) and (3.14).

The temperature dependence of the interface energy is also investigated in our model simulations. In classical nucleation theory (CNT) the interfacial energy is assumed to be temperature-independent. However, this assumption, which is valid in shallow undercooling, may not be true at deeper undercoolings. One approximation of CNT is that the Gibbs free energy difference between solid and liquid is linear with undercooling temperature, i.e., $\Delta G_V \cong \Delta T / T_m \Delta L_V$, as shown in Figure 3.15. In order to calculate the

exact value of ΔG_V, we use Gibbs- Helmholtz relation [34] (valid for zero external pressure) to calculate the solid-liquid chemical potential difference per atom:

$$\Delta\mu_n = T\int_T^{T_m} \frac{[E_l(T) - E_s(T)]}{T^2} dT, \tag{3.13}$$

where $E_l(T)$, $E_s(T)$ are the enthalpy per liquid and solid atom respectively [Eq. (3.9) and (3.10)]. The Gibbs free energy difference per unit volume can be calculated with the relation

$$\Delta G_V = \Delta\mu_n \cdot \rho_s, \tag{3.14}$$

where ρ_s $(= n/V)$ is the temperature-dependent number density of the solid phase [Eq. (3.7)]. From Eqs. (3.7), (3.9), (3.10), (3.13), and (3.14), we can calculate ΔG_V, which is shown in Figure 3.15.

Using the relation $r^* = \frac{2\gamma_{SL}}{\Delta G_V}$ [Eq. (3.4)], we can calculate the temperature dependence of solid-liquid interfacial energy. Here the critical sizes r^* at different undercoolings were determined in the same way as described in section 3.2.3 and 3.2.6. Figure 3.16 shows the temperature dependence of interfacial free energy. We found the interfacial free energy increases slightly with increasing temperatures. The best fit to the data from our simulations yields $\gamma = 0.19083 + 0.19771 \times T$. We also draw Turnbull's empirical relation[1] of the interfacial free energy, $\gamma_{SL} = 0.32\Delta H_f \rho_s^{2/3} / N_a$ [Eq. (3.1)], for comparison, where $\Delta H_f / N_a$ $[= E_l(T) - E_s(T)]$ and ρ_s are temperature-dependent quantities. The best fit to Turnbull's relation yields $\gamma = 0.09578 + 0.39247 \times T$ shown in Figure 3.16. The tendency of the temperature dependence of interfacial free energy is in good agreement with Spaepen's analysis [33,88] of Turnbull's homogeneous nucleation

data for mercury [6], Miyazawa and Pound's data for gallium [116], and Wood and Walton's data for water [117]. Spaepen's analysis, based on the Gibbsian description of interfaces, showed that the positive temperature coefficient of the interfacial free energy could be attributed to the entropy loss in the liquid due to the ordering near the crystal-melt interface [33,88].

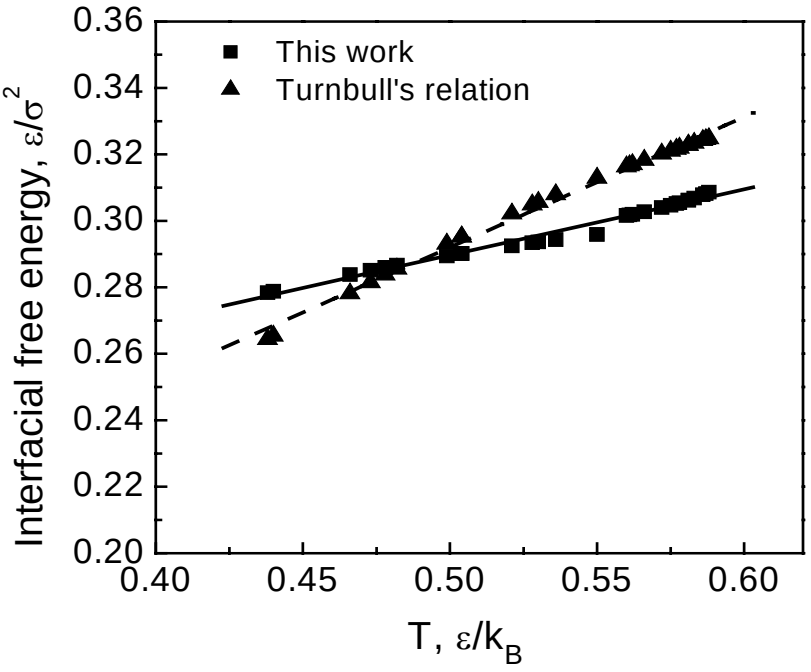

Figure 3.16**.** Temperature dependence of interfacial free energy. A positive temperature coefficient is found. Turnbull's empirical relation is shown for comparison.

3.2.9. Anisotropic Interfacial Free Energy

So far we have used the spherical nuclei to calculate the orientationally averaged interfacial free energy. However, the information of the anisotropy is lost in this method.

In order to calculate the face-dependent interfacial free energy, we inserted non-spherical nuclei into the undercooled liquids. Specifically, we prepared crystal nuclei with all surface areas covered by a desired crystallographic plane. Depending on the atomic plane, the nucleus has a specific geometric shape, as shown in Figure 3.17.

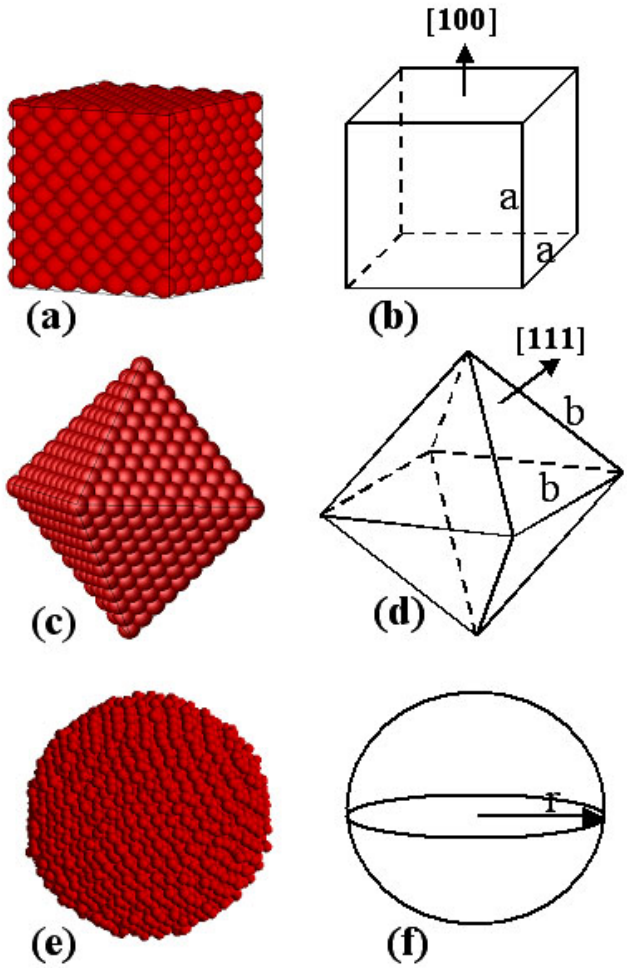

Figure 3.17. Nuclei of different geometric shapes. (a) and (b): A cubic nucleus with {100} planes on the surface. The edge length of the cubic nucleus is *a*. (c) and (d): A bipyramidal nucleus with {111} planes on the surface. The edge length is *b*. (e) and (f): A spherical nucleus of radius *r*.

If the surface of a crystal nucleus is covered by {100} planes, the geometric shape is cube, as shown in Figure 3.17 (a) and (b). If the edge length of the cubic nucleus is *a*, the surface area of the nucleus is $6a^2$ and the volume is a^3. If this crystal nucleus is formed in a supercooled liquid, the free energy change can be expressed as,

$$\Delta G(a) = a^3 \Delta G_V + 6a^2 \gamma_{100}, \tag{3.15}$$

where γ_{100} is the interfacial free energy of (100) face. The critical edge length a^* can be derived by taking the first-order derivative of Eq. (3.15), i.e., $\left.\frac{\partial \Delta G(a)}{\partial a}\right|_{a=a^*} = 3a^{*2}\Delta G_V + 12a^*\gamma_{100}$, from which we have

$$a^* = \frac{4\gamma_{100}}{\Delta G_V}. \tag{3.16}$$

If the number of atoms included in the cubic nucleus is *n* and the number density of the bulk solid is ρ_s, then $n/\rho_s = a^{*3}$ or $a^* = (n/\rho_s)^{1/3}$. Replace a^* and ΔG_V in Eq. (2), one can get

$$\left(\frac{n}{\rho_s}\right)^{1/3} = 4\gamma_{100}\frac{T_m}{L_V}\frac{1}{\Delta T}. \tag{3.17}$$

If the surface of a crystal nucleus is covered by (111) planes, the geometric shape is pyramid, as shown in Figure 3.17 (c) and (d). Suppose the edge length of the pyramid is *b*, then the surface area is $2\sqrt{3}b^2$ and the volume is $\frac{\sqrt{2}}{3}b^3$. Similarly, one can derive the critical edge length of the pyramid,

$$b^* = \frac{2\sqrt{6}\gamma_{111}}{\Delta G_V}, \tag{3.18}$$

where γ_{111} is the interfacial free energy of (111) face. Using the relation $n/\rho_s = \frac{\sqrt{2}}{3} b^{*3}$, one can get

$$\left(\frac{n}{\rho_s}\right)^{1/3} = 3.813\gamma_{111}\frac{T_m}{L_V}\frac{1}{\Delta T}. \tag{3.19}$$

For a spherical nucleus of radius *r* that we have discussed before, the surface area is $4\pi r^2$ and the volume is $\frac{4}{3}\pi r^3$. The critical radius is $r^* = \frac{2\gamma_{SL}}{\Delta G_V}$, where γ_{SL} is orientationally averaged interfacial free energy. Using the relation $n/\rho_s = \frac{4\pi r^{*3}}{3}$, one can get

$$\left(\frac{n}{\rho_s}\right)^{1/3} = 3.224\gamma_{SL}\frac{T_m}{L_V}\frac{1}{\Delta T}. \tag{3.20}$$

From Eqs. (3.17), (3.19), and (3.20), we know that the relation between *n* and ΔT is same except the geometric factor α. Therefore, similar to using the spherical nuclei, we insert the cubic and pyramidal nuclei in supercooled liquids to compute the interfacial free energies of (100) and (111) faces.

Similar to a spherical nucleus [61,62], a non-spherical nucleus is also in an unstable equilibrium with its surrounding supercooled liquid. At a given temperature, it could either shrink or grow. However, the shrinkage or growth of the non-spherical nucleus may prefer to occur in some specific orientations. For example, the shrinkage prefers to start from the corners of the cubic nucleus and bipyramidal nucleus, as shown in Figures 3.18 and 3.19. This is because the corner atoms lose more crystal neighbors relative to the flat interface atoms. Thus the crystal atoms at the corner are less stable.

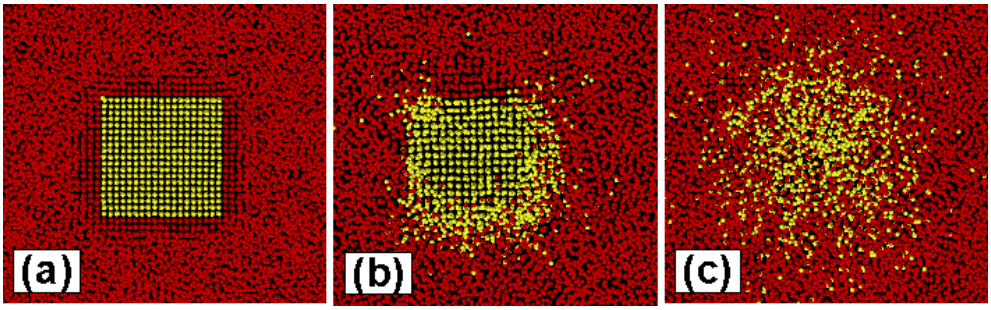

Figure 3.18. The shrinkage of a cubic nucleus in a supercooled liquid. (a) Initially, a cubic nucleus is embedded in a supercooled liquid. (b) After some time, the corners start to collapse. (c) Finally, the cubic nucleus dissolves into the liquid.

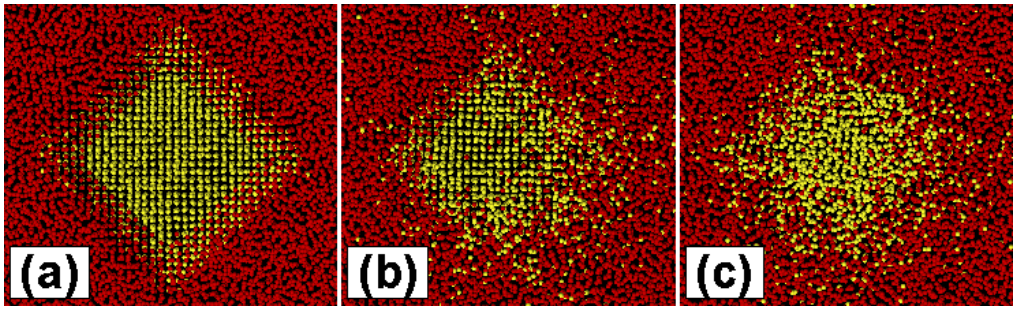

Figure 3.19. The shrinkage of a cubic nucleus in a supercooled liquid. (a) Initially, a cubic nucleus is embedded in a supercooled liquid. (b) After some time, the corners start to collapse. (c) Finally, the cubic nucleus dissolves into the liquid.

On the other hand, the growth of the non-spherical nuclei also prefers to occur in certain orientations. Usually, the crystal prefers to grow at the interface regions with small local curvature. For a cubic nucleus, it contains six locally flat interface regions. These flat interfaces make the crystal growth easier to start with. Similarly, a bipyramidal nucleus has eight locally flat interface regions. In our simulation, we find that the crystal

growth prefers to occur from these locally flat interface regions, as shown in Figure 3.20(a) and (b).

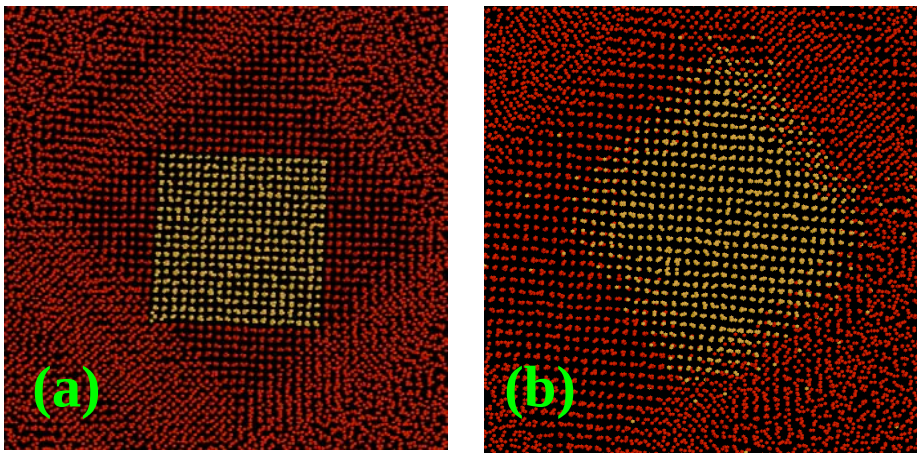

Figure 3.20. Crystal growth from non-spherical nuclei. The crystal growth prefers to occur at the locally flat interface regions. (a) The crystal growth from a cubic nucleus. (b) The crystal growth from a bipyramidal nucleus.

For each nucleus of a certain size and shape in a supercooled liquid, we can determine the corresponding critical temperature. By varying the nucleus size, we can determine the critical temperatures of various composite systems. After the critical temperatures are determined, we plotted $(n/\rho_s)^{1/3}$ as a function of $1/\Delta T$ for nuclei with different geometric shapes, as shown in Figure 3.21. Approximately, each set of data can be fitted with a linear line.

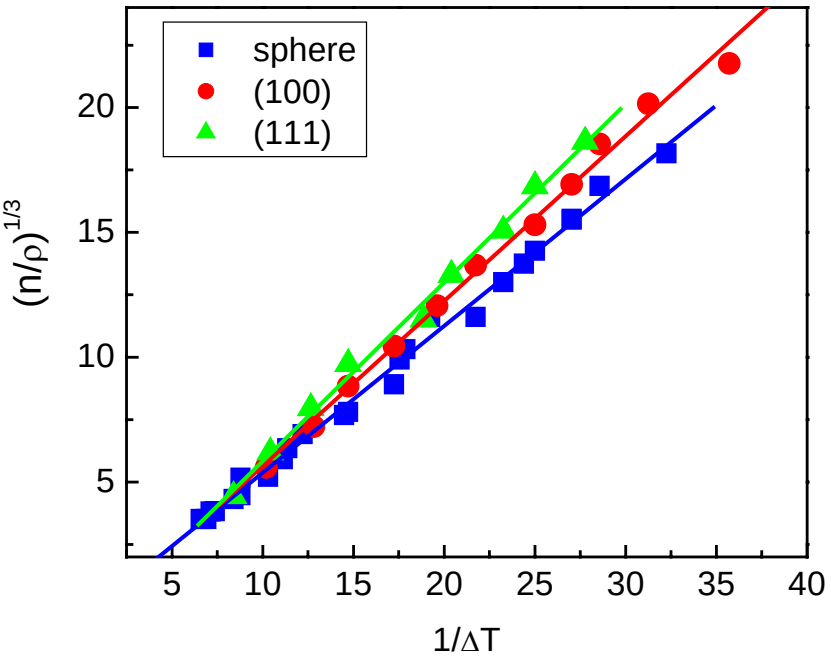

Figure 3.21. The linear relation between $(n/\rho_s)^{1/3}$ and $1/\Delta T$ for crystal nuclei with different crystal planes on their interfaces.

The linear fits in Figure 3.21 yields k_{100} = 0.66, k_{111} = 0.71, and k_{sphere} = 0.59. Using Eqs. (3.17), (3.19), and (3.20), we calculate the interfacial free energies of the (100) plane, (111) plane, and orientational average: γ_{100}=0.27ε/σ^2, γ_{111}=0.31ε/σ^2, and γ_{sphere}=0.30ε/σ^2.

Clearly, the interface free energies of different planes are still close to the orientationally averaged value: 0.30ε/σ^2. This is not surprising because the LJ system is very isotropic. The LJ potential does not contain any specification that is related to a specific atomic plane. Moreover, a solid atom at an ideally flat interface always loses half

of its surrounding crystal atoms, independent of the interface orientation. Since the interfacial free energy is primarily related to the loss of solid atoms, the interfacial free energy in such an isotropic system should be insensitive to the orientation. Thus, we should not expect a strong anisotropy in the interfacial free energy. The small anisotropy in the calculated interfacial free energy may be induced mainly by the simulation errors.

3.3. Conclusions and Discussion

To summarize, we used a classical nucleation theory based approach to calculate the solid-liquid interfacial free energy of a Lennard-Jones system. The model is constructed by "embedding" a series of pre-existing spherical solid nuclei in supercooled liquids to create ideal models of homogeneous nucleation. Using extensive molecular dynamics simulations, we accurately located the corresponding "coexistence" temperatures. The interfacial free energy is extracted by fitting the relation between the critical nucleus size and the reciprocal of the critical undercooling temperature, $r^* \cong (\frac{2\gamma_{SL}T_m}{L_V})\frac{1}{\Delta T^*}$. The orientationally averaged interfacial free energy was found to be $0.302\pm0.002\,\varepsilon/k_B$. Our calculated interfacial free energy is very close to Turnbull's empirical estimation, but much smaller than the calculated values from other approaches. Using the independent test of the spontaneous crystallization of a pure liquid as evidence, we found that our calculated value and Turnbull's estimation may be more accurate. The temperature dependence of interfacial free energy is also discussed. We found that it increases slightly with increasing temperature. The anisotropy in the interfacial free energy is calculated by inserting non-spherical nuclei into supercooled liquids. We have

found that the interfacial free energy in a LJ system is quite isotropic. The method for creating solid-liquid interfaces can be easily applied to other systems and used to create interfaces with different geometric shapes.

The thermodynamic and kinetic properties of crystal growth from embedded nuclei are also presented and discussed. The results provide a direct support for the validity of classical nucleation theory in a wide range of undercooling temperatures. We found that the polycrystalline structure, rather than the bcc structure as many people have assumed [98,99], should be the intermediate structure during the crystal growth. The newly formed crystal usually contains a lot of defects. However, most defects disappear if the simulation time is long enough. The finite size effects are also checked in this work. We found that the relation between the nucleus size and the undercooling temperature shows minor size effects. However, the lag time before the massive crystallization is strongly related to the simulation system size.

CHAPTER 4

TEST OF CLASSICAL NUCLEATION THEORY FOR SOLID SUPERHEATING VIA A SOLID- LIQUID COEXISTENCE MODEL

Melting and crystallization are two fundamental phenomena in nature and have been studied for centuries. For the crystallization process, i.e., transformation from liquid phase to crystal phase, some undercooling is always required [1]. For example, Turnbull and Cech [5] showed that if impurities or any other external nucleation catalysts were excluded, liquid metals could be supercooled tens to hundreds of degrees below their equilibrium melting temperatures without crystallization. Classical nucleation theory for homogeneous and heterogeneous nucleation had been proposed and successfully used for describing the crystallization phenomenon [1-6]. However, unlike crystallization that always requires some undercooling, melting usually occurs at the equilibrium melting temperature without superheating [1,7]. This is because the free surfaces of solids have small energy barriers for heterogeneous nucleation so that melting always starts from free surfaces [1,7]. In certain materials, several layers of surface atoms have been observed to become liquid-like atoms and form quasi-liquid layers at temperatures below the melting point [8,9]. Since most materials have free surfaces, superheating is generally difficult to achieve in experiment. However, Daeges and Gleiter [10] showed that superheating is achievable if the surface melting is properly suppressed. In their experiment, they coated a silver (Ag) sphere with a thin gold (Au) layer to “remove” the free surface of Ag. Since the melting point of Au is about 100 degree higher than that of Ag, the inner silver sphere could melt while the outer gold layer is still solid. Using this composite sample, they

observed that sliver could be superheated up to 25 K. This work told us that superheating is possible if the surface melting is suppressed. Superheating can also be achieved by ultra-short pulsed laser irradiation [11,12]. Due to the ability to focus light in a small area or even inside the solid, laser-irradiated materials can be heated internally, thus significant amount of superheating can be achieved. Although it is hard to prepare surface-free systems in experiment, it is very easy to create the surface-free system in computer simulations by applying the periodic boundary conditions [13]. Thus the superheating phenomenon caught a lot of researchers' attentions, and is one of the most popular topics in the research area of computer simulations [14-20]. Although numerous efforts [14-20] have been made to interpret the mechanism of melting at superheating in the past century, the nature and extent remain unveiled.

In most of the work described above, the researchers heated a perfect crystal sample with a very high heating rate (~ 10^{12} *K/s*) and investigated the melting and defect aggregation induced by the thermal fluctuations. Therefore, those theories primarily focused on the static instability limits of metastable superheating, i.e., the highest possible melting temperature. Little has been known for thermodynamics and kinetics of nucleation process at the *whole* range of superheating. In this range, some researchers simply assumed that the superheating is a reverse process of supercooling [22-25]. The classical nucleation theory, which is generally applied for solidification (supercooling) process, was directly applied to estimate the nucleation rates and the upper limits of superheating. However, the fundamental question is whether we can apply the classical nucleation theory directly for the superheating process. Unfortunately, it has not been

tested decisively. To date, there is no direct evidence from either experiments or simulations to support this assumption.

In this work, we use a solid-liquid coexistence model (i.e., a liquid nucleus embedded in a superheated crystal matrix) to test the classical nucleation theory for melting at superheating. Different from the usual way of continuously heating a homogeneous crystal sample, this method can be used to investigate the thermodynamics and kinetics of liquid nucleation at a *wide* range of superheating temperatures.

4.1. Theory, Model, and Method

4.1.1. Theory

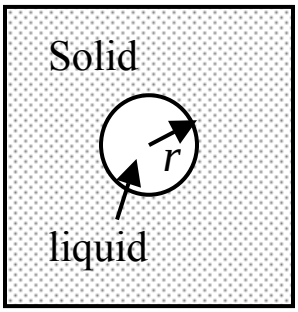

Figure 4.1. A spherical liquid droplet embedded in a superheated solid model.

In Chapter 3, we have shown that classical nucleation theory (CNT) is valid for describing the crystallization process. This model assumes that a solid sphere of radius *r* forms from an undercooling liquid. The relation between the radius *r* and the reciprocal of undercooling $\Delta T(=T_m - T)$ is linear, as shown by,

$$r \cong \left(\frac{2\gamma_{SL} T_m}{L_V} \right) \frac{1}{\Delta T}. \tag{4.1}$$

where γ_{SL} is solid-liquid interfacial free energy, and L_V is the latent heat of fusion per unit volume at T_m. The coexistence of the solid sphere and the surrounding liquid is unstable: the solid sphere either shrinks or grows, as shown in Chapter 3.

Similarly, we can embed the liquid droplet in a superheated solid matrix [Figure 4.1], which is an "inverse" model of supercooling, to simulate the solid superheating process. If the classical nucleation theory can be directly applied for solid superheating process as many researchers [22-25] had assumed, the radius of the liquid droplet should be proportional to the reciprocal of the superheating, as illustrated in Figure 4.2. In other words, Eq. (4.1) also can be applied for solid superheating. However, so far there is no such decisive test. Note that the ΔT in Eq. (4.1) is defined as $\Delta T = T - T_m$ for the superheating process.

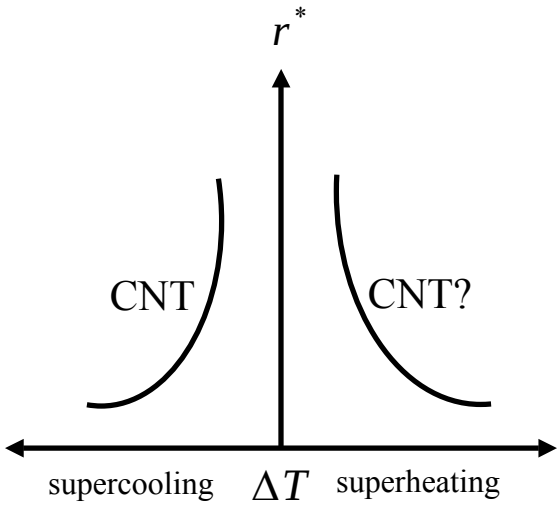

Figure 4.2. Unproven CNT relation between the critical nuclei size and the superheating temperature.

4.1.2. Simulation Method

In this work, we performed Molecular Dynamics (MD) simulations in an *NPT* ensemble. The Parrinello–Rahman method [68] was employed to control the external pressure (in this work, the external pressure was set to zero), and Nose thermostat [69] was used for controlling the system temperature. The atomic interaction potential used in this work is a standard Lennard-Jones (LJ) potential, $\phi(r) = 4\varepsilon[(\frac{\sigma}{r})^{12} - (\frac{\sigma}{r})^{6}]$, where parameter $\sigma = 3.405$Å, and $\varepsilon / k_B = 119.8K$. The initial lattice structure was face-center-cubic (fcc). To get rid of the surface melting and achieve superheating, period boundary conditions were employed in all directions [13]. In order to check the finite size effect, we have used three different size systems of 32 000, 128 000, and 256 000 atoms respectively. Standard reduced LJ units [13] were used in this work. The MD step is 5fs.

4.1.3. Creating the Coexistence Model for Solid Superheating

If one continuously heats a bulk crystal (i.e., without the free surfaces) from a low temperature to a high temperature, it starts to melt at a temperature much higher than the equilibrium melting point. This temperature is called the upper superheating limit. Usually, the maximum superheating, ΔT_s, is about 20% higher than T_m [14]. Similarly, if the impurities are effectively excluded from the system, the liquid can be supercooled to a temperature about 20% lower than the equilibrium melting temperature without crystallization, as shown in Turnbull's experiments of cooling mercury droplets [4-6].

In the previous work, especially in the simulation work [17,18,23,25], the upper limit of superheating was determined by continuously heating the sample until it melted.

In this method, the transition time is very short, which is usually of the order of 10^{-12} s. Therefore, only the information at the superheating limit can be obtained. However, we also want to know thermodynamic nature in a wide superheating regime, which includes shallow, moderate, and high superheating. Apparently, such information cannot be obtained from this method.

Similar to the supercooling process, it is almost impossible to form large nuclei spontaneously at shallow or moderate superheating. In computer simulations, the spontaneous nucleation is extremely difficult at shallow or moderate superheating due to the limitation in computing time [27]. This time barrier has been known to prevent detailed nucleation process from being seen in atomistic simulations.

In order to study the thermodynamics and kinetics of melting at the *whole* range of superheating, which is from the equilibrium melting point to the upper limit of superheating, we can artificially insert a "pre-formed" spherical liquid nucleus in a superheated crystal and create a coexistence system. At shallow or moderate superheating, we can insert nuclei with large sizes. At high superheating, we can insert nuclei with relatively small sizes. In experiment, this model is also achievable. For example, a small liquid nucleus can form within the bulk crystal by the laser irradiation, or a liquid nucleus can form around a local defect. Using this method, we can create a crystal-melt coexistence (but unstable) system at any temperature of the superheating regime. Therefore, the time-barrier limitation described above in MD simulations can be effectively circumvented. Using such a highly ideal model, we can test the inverse relation between the critical size and critical superheating [Eq. (4.1)], which is a key

feature of the classical nucleation theory. However, since the liquid nucleus is created artificially, we have to sacrifice the detailed information on the pre-critical nucleation.

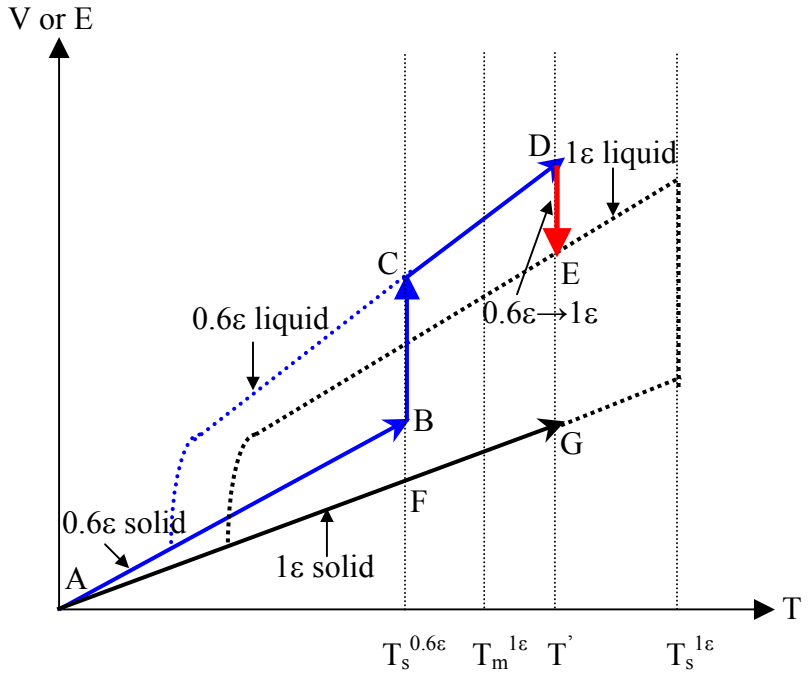

Figure 4.3. Schematic illustration of creating a liquid droplet in a superheated solid. The inner sphere goes along the path A→B→C→D→E, and the outer matrix goes along the path A→F→G. See text for details.

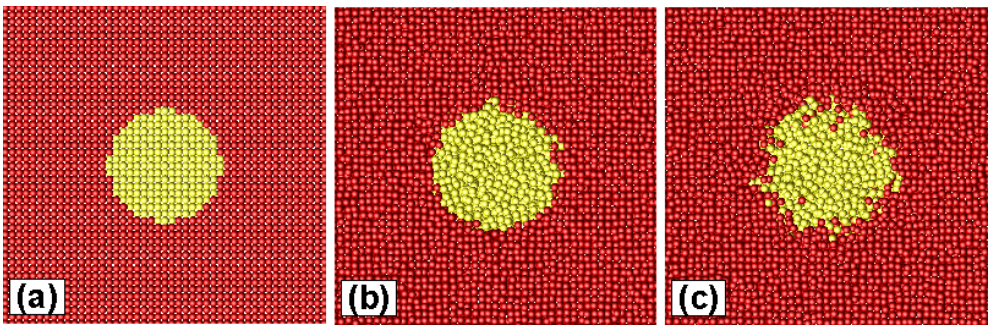

Figure 4.4. Cross-section snapshots of the atomic configurations. (a) Initial configuration (at point A in Figure 4.3). (b) At the superheating limit $T_s^{0.6\varepsilon}$, the inner sphere becomes a liquid. (c) At T' in Figure 4.3, the coexistence sample is created after the potential depth of the inner liquid sphere is changed from 0.6ε to 1ε.

In order to create this "composite" model, we use a similar method as that in Chapter 3. Different from creating the supercooling model, the melting point of the inner sphere is lower than that of the outer matrix. Therefore, the inner sphere can become a liquid while the outer matrix is still a solid. The detailed procedure of this method is shown in Figures 4.3 and 4.4. The simulation system has two parts: one is the outer cubic matrix, and the other one is a sphere embedded in this matrix. The two parts are indicated with different colors in figure 4.4(a). Initially all atoms are arranged in an fcc lattice, and have the same atom diameters as in the standard LJ potential, i.e., $\sigma_1 = \sigma_2 = \sigma$. However, the parameters of the LJ potential depth for the atoms in the two parts are different. In the outer matrix, atoms have the standard LJ potential depth ($\varepsilon_1 = \varepsilon$), while in the inner sphere, atoms have a smaller potential depth ($\varepsilon_2 = 0.6\varepsilon$). At the interface region, the potential depth for different species of atoms is taken the value of $\sqrt{\varepsilon_1 \varepsilon_2}$. At the beginning, both the sphere and matrix are fcc crystals as indicated by point A in Figure 4.3. Due to different thermal expansions of the sphere and the matrix, when the system is heated up, the average enthalpy or volume (per atom) of the sphere goes up along the path A→B while the matrix follows the path A→F, as shown in Figure 4.3. When the temperature is slightly higher than the upper superheating limit of the sphere ($T_s^{0.6\varepsilon}$), the sphere becomes a liquid (B→C), whereas the matrix still remains in crystalline state (point F). The corresponding snapshot at this temperature is shown in Figure 4.4(b). The system is continuously heated up to a temperature (T') in the superheating regime, i.e., between the equilibrium melting point of the matrix ($T_m^{1\varepsilon}$) and the upper superheating limit of the matrix ($T_s^{1\varepsilon}$). As the temperature increases, the average enthalpy or volume

(per atom) of the matrix goes up along the path F→G, and that of the solid sphere follows the line C→D. At temperature T', the matrix becomes a superheated crystal (with potential depth ε) while the central sphere is a liquid (still with potential depth of 0.6ε). At the temperature T', we gradually change the potential depth of atoms in the solid sphere to that of the matrix (i.e., $0.6\varepsilon \to \varepsilon$). So the average enthalpy or volume (per atom) of the solid sphere decreases gradually from D→E while that of liquid matrix remains at position G. The final outcome is that we create a liquid sphere (point E) in coexistence with the superheated crystal (point G), and most importantly, they have the *same* interaction potential ($\varepsilon_1 = \varepsilon_2 = \varepsilon$, $\sigma_1 = \sigma_2 = \sigma$). The corresponding snapshot of the atomic configuration is given in Figure 4.4(c). Therefore, we use only one single computer run and effectively bypass the difficulties of dealing with atom overlapping problems [30] at the interface.

Upon the "composite" system is created, one can bring the system to different temperatures in the superheating regime. Depending on the temperatures, the liquid droplet either grows or shrinks. Thus we can find a critical "coexistence" superheating, ΔT^*: if $\Delta T < \Delta T^*$, the liquid droplet disappears and becomes a crystal; if $\Delta T \geq \Delta T^*$, the liquid sphere grows. We can create a series of liquid nuclei of different radii r^*, and determine their corresponding ΔT^*'s. More details are given in the next several sections.

This method has several advantages. First, only one computer run is needed to create the composite system. Second, there is no atom-overlapping problem at the interface. Third, the superheating can be studied in a wide range of superheating regime. The problem of the time barrier in MD simulation is circumvented. Moreover, the morphologic complexities of pre-critical nuclei are excluded in this model. Thus, using

such an ideal model, one can focus on the thermodynamic and kinetic behaviors at a wide range of superheating temperatures.

4.2. Results

4.2.1. Surface Melting

If the periodic boundary conditions are applied in MD simulations, the surface melting is suppressed, and thus, the sample is superheated. Therefore, the melting point obtained from such a surface-free sample is the upper limit of superheating (about 20% higher than the equilibrium melting point). In order to determine the correct equilibrium melting point, two methods are used in this work. One is to determine the critical temperature at which solid and liquid phases can coexist with a flat interface, the other one is to determine the melting point of a system with a free surface. The first method is discussed in Chapter 3. In this section we focus on the second method.

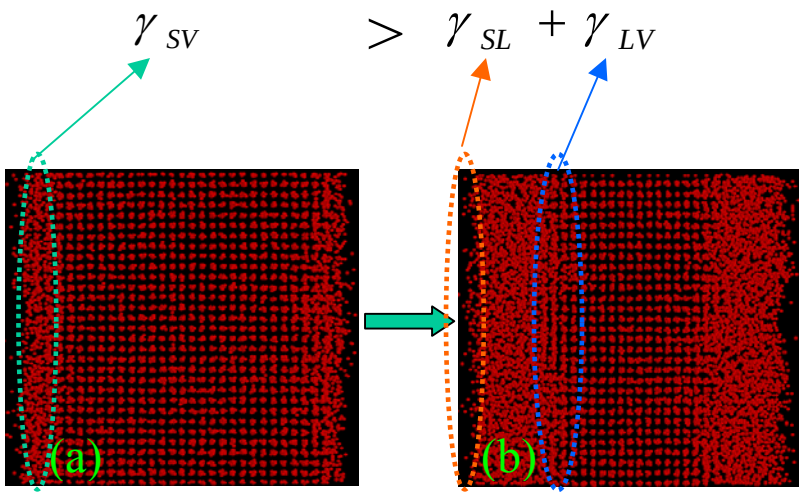

Figure 4.5. Melting starts from the free surface. (a) At $T < T_m^E$. (b) At $T \geq T_m^E$.

In the surface melting method, we construct a system with two free surfaces [Figure 4.5(a)] by disabling the periodic boundary condition in the horizontal direction. In the other two directions, the periodic boundary conditions are still applied. The external pressure, *P*, is set to zero. A few layers of atoms are disordered at or near the surfaces, which can be clearly seen in Figure 4.5(a). Typically the thickness of the surface is of about 3~4 atomic layers (1~1.3nm). We bring this system to different temperatures and hold the temperature isothermally for 200 000 MD steps (1 ns). If the surfaces are stable [Figure 4.5(a)], the temperature is below the melting point. On the other hand, if the surfaces are unstable and move towards the bulk material [Figure 4.5(b)], the temperature is higher than the melting point. In the next run, we increase or decrease the temperature depending on the last trial temperature being lower or higher than the melting point. After a series of trial-and-error tests, we find that the minimum temperature at which the surfaces become unstable is at $0.618\,\varepsilon / k_B$ (about 74.2 K). Therefore, the temperature of $0.618\,\varepsilon / k_B$ is the equilibrium melting point for a LJ system at *P*=0. Note that this method is also the way of determining the melting point in experiment. The physical explanation of the surface melting is that the free solid surface (solid-vapor interface) has very small energy barrier for heterogeneous nucleation of liquid [1]. The relation among the interfacial energies of solid/vapor, solid/liquid, and liquid/vapor interfaces has the form of $\sigma_{sv} \geq \sigma_{sl} + \sigma_{lv}$ [1]. At $T < T_m$, the interface is a solid/vapor interface with the interface energy σ_{sv}, as indicated in Figure 4.5(a). At $T \geq T_m$, the surface melting yields the liquid/vapor and solid/liquid interfaces with a lower combination of interface energies $(\sigma_{sl} + \sigma_{lv})$, as shown in Figure 4.5(b). In some materials, layers of surface atoms may become liquid-like atoms and form quasi-liquid

layers at temperatures slightly below the melting point [8,9]. Thus, the melting from free surface is always energetically favorable.

In Chapter 3, we have determined the thermodynamic melting temperature ($0.618\,\varepsilon / k_B$ at P=0) by locating the temperature at which the liquid-solid interface stays stationary. It is not surprising that the two methods yield the same result. In the surface melting method, once a liquid layer forms, the system is equivalent to a solid-liquid coexistence system with a flat interface. Thus, the surface can move towards bulk only when the temperature is above the melting point.

4.2.2. Calculation of the Solid Shear Modulus and Liquid Bulk Modulus

In Chapter 2, we have used Eq. (2.21) to calculate the elastic constants at different temperatures in an NVE ensemble. The temperature-dependent $C_{11}(T)$, $C_{12}(T)$, and $C_{44}(T)$ are fitted to the simulation data, as shown in Eq. (2.23). The shear modulus of the solid can be calculated by using the relation $\mu = C' = (C_{11} - C_{12})/2$. Although the shear modulus of a liquid is zero, its bulk modulus is not zero. However, the bulk modulus of a liquid, K_l, cannot be calculated with Eq. (2.21).

The definition of the bulk modulus is $K = -V\left(dP/dV\right)_T$, where P is the applied compressive hydrostatic pressure, and V is the volume of the system. Thus, the bulk modulus can be calculated by compressing the bulk liquid. At a temperature T, we can apply a hydrostatic pressure to the liquid and calculate the corresponding volume change, from which we can use the relation $K_l = -V\left(dP/dV\right)_T$ to obtain the liquid bulk modulus K_l. If this calculation is repeated at different temperatures, one can obtain the

temperature-dependent K_l. The results are shown in Figure 4.6. Clearly, the liquid bulk modulus (K_l) is larger than the solid shear modulus (μ). The linear fits to the data yield:

$$K_l = 39.19 - 38.96T \ , \qquad (4.2a)$$

and

$$\mu = C' = 23.27 - 24.51T \ . \qquad (4.2b)$$

Figure 4.6 also shows the bulk modulus of the solid (K_S) and another shear modulus of the solid (C_{44}) for comparison purpose. The bulk modulus of the solid (K_S) is always larger than the bulk modulus of the liquid (K_l). Moreover, the shear modulus of the cubic crystal system (C_{44}) is also larger than K_l.

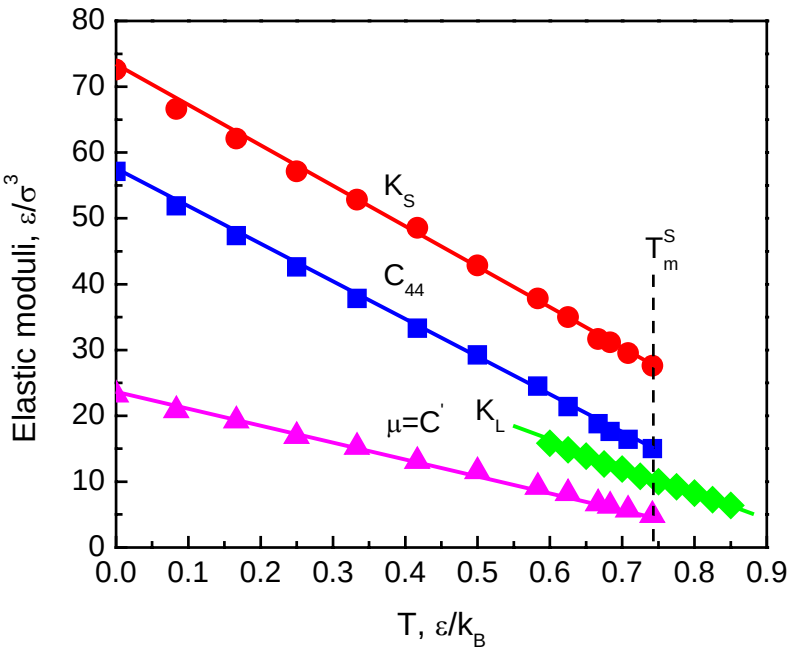

Figure 4.6. The shear modulus of the solid (μ) and the bulk modulus of the liquid (K_l). The bulk modulus (K_S) and another shear modulus (C_{44}) of the solid are also shown.

4.2.3. Determining the Critical Temperature of the Composite System

In section 4.1.3, we have described how to create a composite system of a liquid sphere embedded in a superheated crystal matrix. The liquid droplet is unstable in the composite system: it either grows or shrinks. There exists a critical temperature above which the liquid droplet grows and below which the liquid droplet shrinks. Here we give an example to explain how we determine the critical temperature.

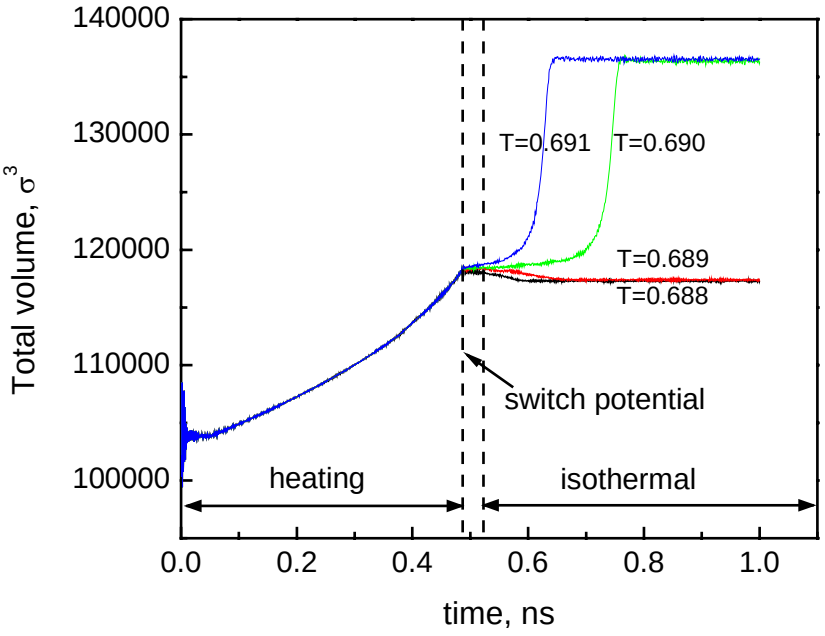

Figure 4.7. The total volume change as a function of time at different temperatures.

In a system of 108 000 atoms arranging in an fcc lattice, we divided it into two parts: an inner sphere of 2 491 atoms and a outer matrix of 105 509 atoms. The initial potential depth of the sphere is 0.6ε, and that of the matrix is 1ε (the regular LJ potential). The system is heated from a low temperature to a desired temperature T' at a

heating rate of 3.3×10^{11} K/sec. At T=0.56ε/k_B, the inner sphere starts to melt. However, the matrix is still a solid. At the desired temperature T', the potential depth of atoms inside the liquid sphere is changed gradually from 0.6ε to 1ε. The volume and other changes during this process can be effectively accommodated because the molecular dynamics simulation is performed in an *NPT* ensemble (*NPT* MD).

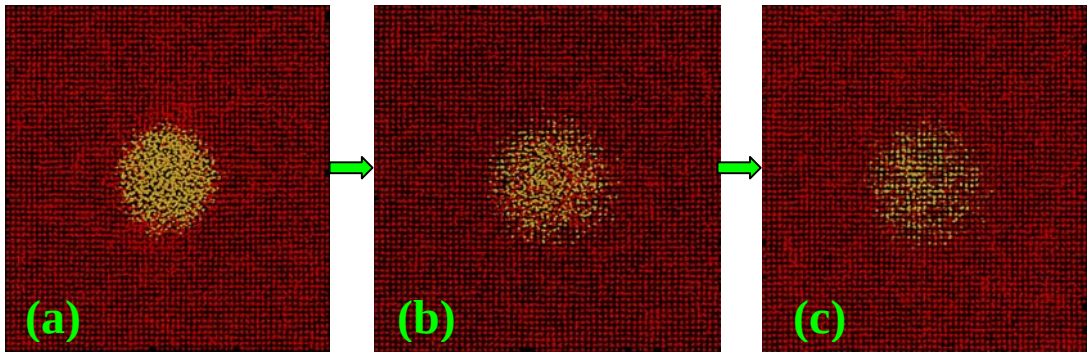

Figure 4.8. The cross-sectional snapshots at T=0.688ε/k_B after the potential is switched. (a) Initially, the liquid droplet is embedded in the crystal matrix. (b) After 0.1 ns, the liquid starts to crystallize. (c) After 0.15 ns, the liquid droplet becomes one part of the crystal.

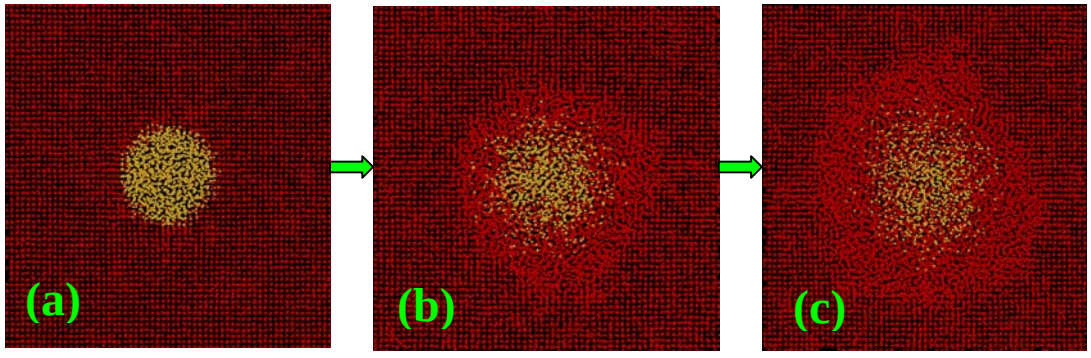

Figure 4.9. The cross-sectional snapshots at T=0.691ε/k_B after the potential is switched. (a) Initially, the liquid droplet is embedded in the crystal matrix. (b) After 0.1 ns, the liquid grows. (c) After 0.175 ns, the liquid droplet grows further.

After the potential is changed, we hold the temperature isothermally at T' for additional 100 000 ─ 200 000 time steps (0.5ns ─ 1ns). Depending on the value of T', the liquid sphere either grows if $T' > T^*$, or shrinks if $T' < T^*$. In the next run, we bring the system to a new temperature with an increment of $0.001\,\varepsilon / k_B$ if the liquid sphere shrinks in the previous run, or a decrement of $0.001\,\varepsilon / k_B$ otherwise. This procedure is repeated for several times until we determine the critical temperature. It is worth noting that although in principle the liquid sphere could coexist (i.e., does not grow or shrink) with the crystal matrix if $T' = T^*$, such coexistence generally cannot be observed. This is due to the unstable nature of the liquid sphere and the superheated crystal matrix. Since a small thermal fluctuation can break this unstable equilibrium, the liquid sphere either shrinks or grows in the simulation. Therefore, it is very difficult to determine the exact value of the critical coexistence temperature. Practically, we define the critical temperature T^* as the *minimum* temperature at or above which the liquid sphere grows. Fox example, as shown in Figure 4.7, in a run we brought the above example system to T =0.688 ε / k_B and held the temperature isothermally for 100 000 time steps (0.5ns). The total volume of the system decreases slightly at the first 0.15ns, and reaches a constant value thereafter. This is due to the shrinkage of the liquid sphere at this temperature. The atomic snapshots [Figure 4.8(a)-(c)] show that the liquid sphere disappears and becomes one part of the crystal. In the next run we brought the system to a slightly higher temperature T =0.691 ε / k_B and held the temperature isothermally for 100 000 time steps (0.5ns). At this temperature, the total volume increases significantly, indicating that the liquid sphere grows and turns the crystal matrix into liquid. The corresponding snapshots [Figure 4.9(a)-(c)] show that the liquid sphere grows and the crystal matrix melts from

the liquid sphere. Thus we can determine that the coexistence temperature is somewhere between 0.688 and 0.691. In the next several runs we brought the system to a series of temperatures with an increment or decrement of 0.001. As shown in Figure 4.7, if $T \le 0.689$, the liquid sphere disappears and becomes one part of crystal; if $T \ge 0.690$, the liquid sphere grows and the crystal matrix melts. Thus, we determined the coexistence temperature is at $T^* = 0.690\,\varepsilon / k_B$ or $\Delta T^* = T_m^{1\varepsilon} - T^* = 0.072\,\varepsilon / k_B$. The errors of this estimation are within $0.001\,\varepsilon / k_B$. We can improve the precision of our results further if needed. But it is not necessary to do so because it does not change our results qualitatively.

4.2.4. Statistical Nature at the Critical Temperature

The determined "coexistence temperature" is defined as the minimum temperature at or above which the liquid sphere grows. It is not the "real" coexistence temperature. The exact value of the critical temperature in the above example system is between 0.689 and 0.690. However, it is impossible to locate its exact value due to the statistical nature of the unstable equilibrium between the liquid sphere and crystal matrix. If the temperature is slightly lower than the critical temperature, i.e., $T_-^* < T^*$, the liquid sphere should shrink according to the classical nucleation theory. However, the thermal fluctuations give it a probability to grow. On the other hand, if the temperature is slightly higher than the critical temperature, i.e., $T_+^* > T^*$, it also has a probability to shrink although it "should" grow. Thus, this statistical nature at the top of the nucleation barrier brings the uncertainty of locating the exact coexistence temperature. In order to test the

statistical nature, we can keep the nucleus size constant but vary the temperature. We brought the above sample system to several temperatures within the narrow range between 0.68940 and 0.68950, and recorded the evolutions (growth or shrinkage) of the liquid sphere. The results are shown in Figure 4.10 and Table 4.1. The statistical nature is correctly reflected in this temperature range. For example, the liquid nucleus can grow at lower temperatures (such as 0.68942) and shrink at higher temperatures (such as 0.68949). The probability for growing or shrinking of the liquid sphere is close to 50%. At temperatures out of this narrow range, the evolution of the nucleus is more predictable: at low temperatures, liquid nucleus disappears with much higher probability; while at high temperatures, liquid nucleus grows more likely.

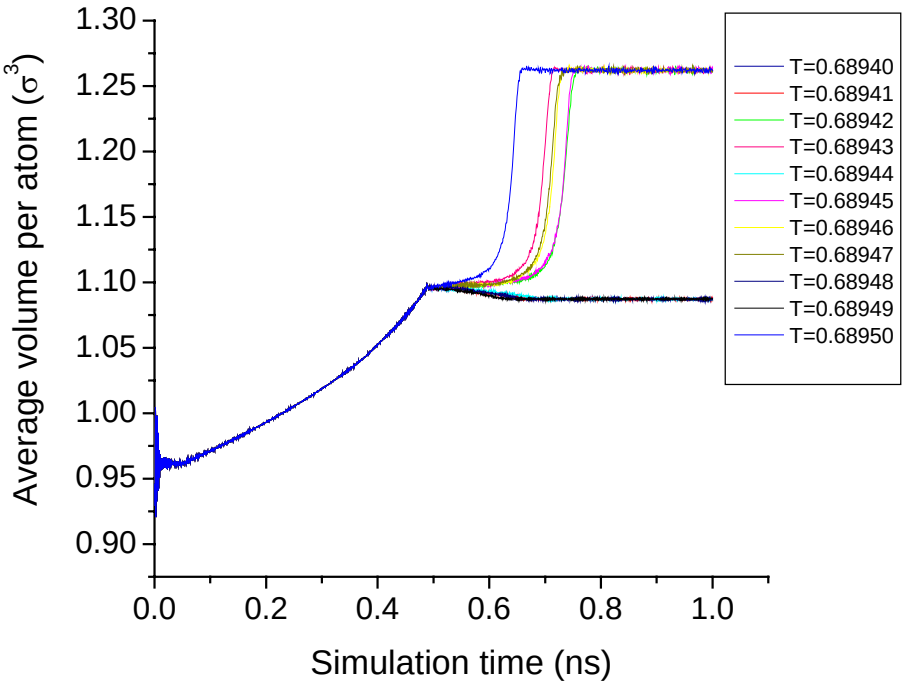

Figure 4.10. The statistical nature at the critical temperature. The evolution of the liquid sphere is listed in Table 4.1.

Table 4.1: The evolution (either shrinking or growing) of the liquid sphere. The probability of the growth or shrinkage is about 50%.

T (ε / k_B)	0.68940	0.68941	0.68942	0.68943	0.68944
Status of the liquid droplet (growth or shrinking)	shrinking	shrinking	growing	growing	shrinking
T (ε / k_B)	0.68945	0.68946	0.68947	0.68948	0.68949
Status of the liquid droplet (growth or shrinking)	growing	growing	growing	shrinking	shrinking

4.2.5. Relation between the Liquid Droplet Radius and the Critical Temperature

In last section, we give an example to explain how we determine the critical temperature for a given nucleus size. Following the same procedure, we changed the size of the liquid sphere (i.e., the number of atoms in the liquid sphere), and determined the corresponding critical temperatures. Thus, the relation between the liquid nucleus size and the critical superheating can be obtained to verify the validity of the classical nucleation theory for the solid superheating. In order to check whether the system size plays a role in affecting the results, we used three different size systems containing 32 000, 128 000, and 256 000 atoms respectively in this work. The number of atoms enclosed in the liquid sphere ranges from 19 to 16 764. The radius of the liquid sphere can be calculated with the equation of $r^* = \left[3n / 4\pi\rho_l(T)\right]^{1/3}$, where $\rho_l(T)$ is the number density of pure liquid and the formula is given in Chapter 3. The results are shown in Figure 4.11. In order to make comparison between the solid superheating and liquid

supercooling, we also show the results of liquid supercooling at the left-hand side of Figure 4.11.

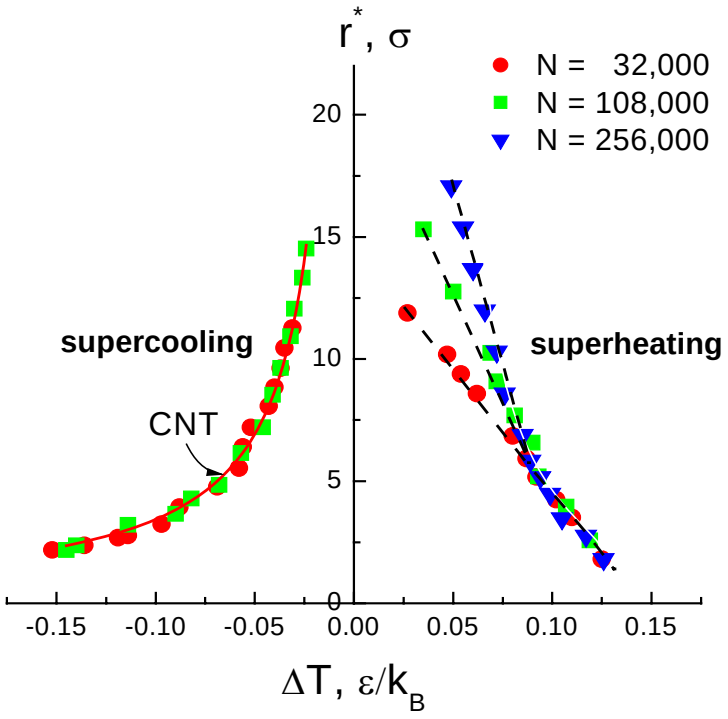

Figure 4.11. The r^* vs. ΔT relation in supercooling and superheating processes. CNT (the solid line at the left-hand side) represents the classical nucleation theory.

Clearly the relation of r^* vs. ΔT is asymmetric for the solid superheating and liquid supercooling. For the liquid supercooling, the data can be well fitted with the classical nucleation theory (CNT) relation of $r^* = \left(\frac{2\gamma_{SL}T_m}{L_V}\right)\frac{1}{\Delta T}$, which implies that the classical nucleation theory is valid for the liquid supercooling in a wide range of supercooling temperatures. As shown in Chapter 3, the solid-liquid interfacial free energy

is extracted from the fitting, $\gamma_{SL} = 0.301\varepsilon/\sigma^2$. Since two different size systems (N=32 000 and 108 000) yield almost the same set of data, the finite size effects are not significant in the supercooling simulations. Contrastively, in the solid superheating, the finite size effects are very significant. And most importantly, none of the three simulation systems yields data that can be well fitted with classical nucleation theory. This result is somewhat surprising, because most researchers think solid superheating simply an inverse process of supercooling [22-25]. Our simulation is the first decisive test to show that classical nucleation theory cannot be directly applied for the solid superheating even though we use the same assumptions as in the classical nucleation theory.

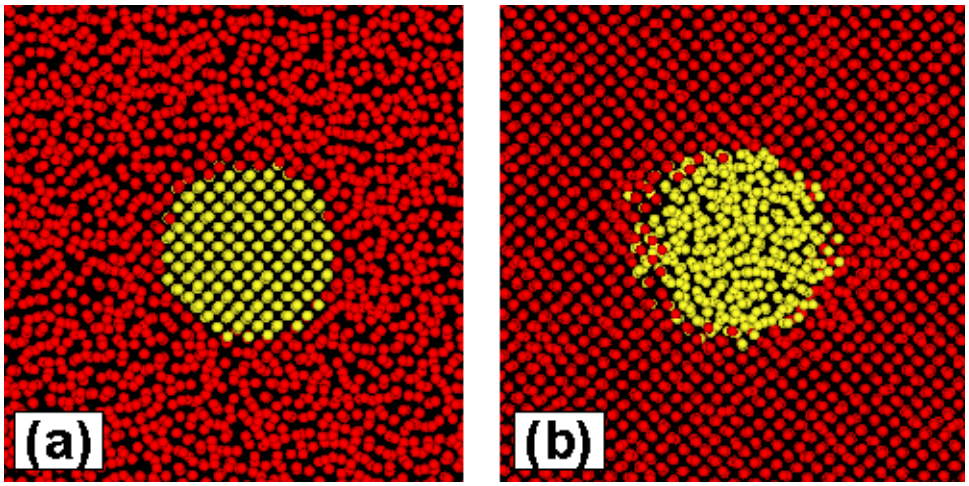

Figure 4.12. Cross-sectional snapshots of the supercooling and superheating models. (a) Supercooling model: a solid sphere is embedded in a supercooled liquid. (b) Superheating model: a liquid droplet is embedded in a superheated crystal.

The discrepancy between the classical nucleation theory and the simulation data in the solid superheating implies that some inherent physical properties of solid

superheating are not included in the classical nucleation theory. In the supercooling model [Figure 4.12(a)], when a crystal nucleus forms in a supercooled liquid, the volume of the crystallized region decreases. The structural difference between the crystal nucleus and the liquid matrix generates a slight tensile stress on the crystal nucleus. Since the liquid atoms are short-range correlated, the outer liquid can easily adjust and accommodate the volume shrinkage during the transformation. However, the situation is different for the solid superheating [Figure 4.12(b)]. We assume that a portion of crystal melts in the bulk and becomes a liquid nucleus. For most materials, including the LJ system in this work, the liquid phase has a smaller density (or larger molar volume) than the solid state has. Thus, the volume of the melted region increases after the phase transformation. The volume expansion pushes the surrounding crystal matrix outwards. Due to the long-range correlation nature of the crystal, the expansion must overcome the rigidity of the crystal matrix. Therefore, the liquid nucleus is under a high compressive pressure. In order to compare the magnitudes of the stresses applied on the liquid or solid nucleus, we calculate the internal stresses on the nuclei from the trace of the atomic stress tensor, as shown by

$$\Pi = \frac{1}{V_{nucleus}} \sum_{i=1}^{M} m_i \vec{v}_i \vec{v}_i^{\,T} - \frac{1}{2V_{nucleus}} \sum_{i=1}^{M} \sum_{j \neq i} \frac{\phi'(r_{ij})}{r_{ij}} \vec{r}_{ij} \cdot \vec{r}_{ij}^{\,T} , \tag{4.3}$$

where M is the number of atoms enclosed in the solid or liquid nucleus, $V_{nucleus}$ is the volume of the spherical nucleus, and $\phi'(r_{ij})$ is the first-order derivative of the interaction potential between the ith and jth atoms of a distance r_{ij}. Figure 4.13 shows the pressures on the solid nucleus in the liquid supercooling and on the liquid nucleus in the solid superheating. We have found that the pressure in the superheating is about $5 \sim 10$ times

larger than that in the supercooling. In supercooling the pressure roughly satisfies the Gibbs-Thomson effect, which can be approximated as $P \approx 2\gamma_{sl}/r^*$ [1]. However, in superheating the pressure does not satisfy this relation. This difference implies that the pressure in supercooling is induced by the structural difference between the solid and liquid phases, while in the superheating it is caused by the elastic deformation during expansion.

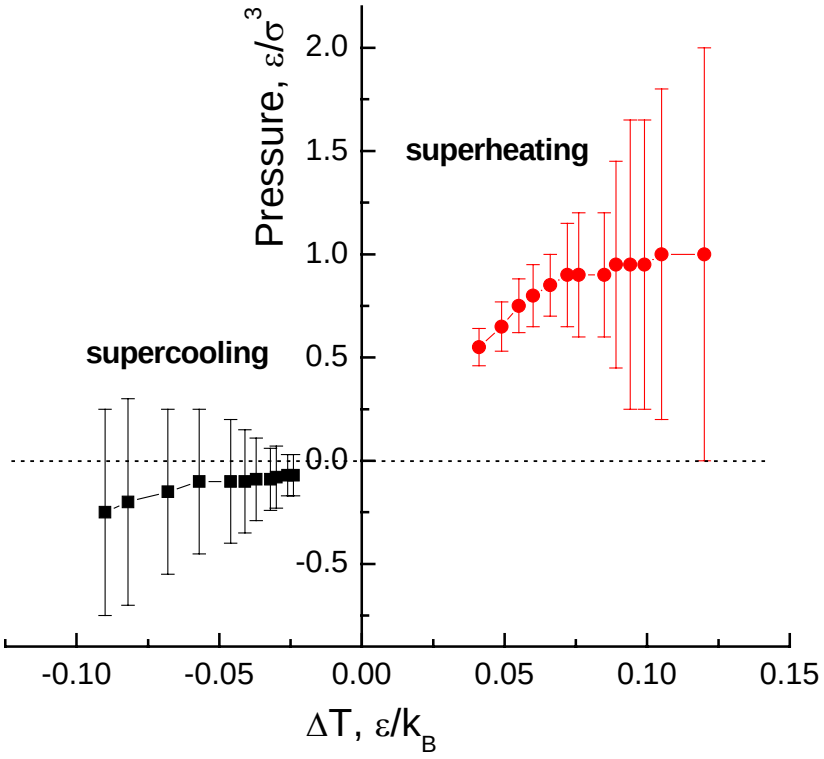

Figure 4.13. The interface pressures in the liquid supercooling and solid superheating models. The sign of the compressive pressure is positive and the sign of the tensile pressure is negative.

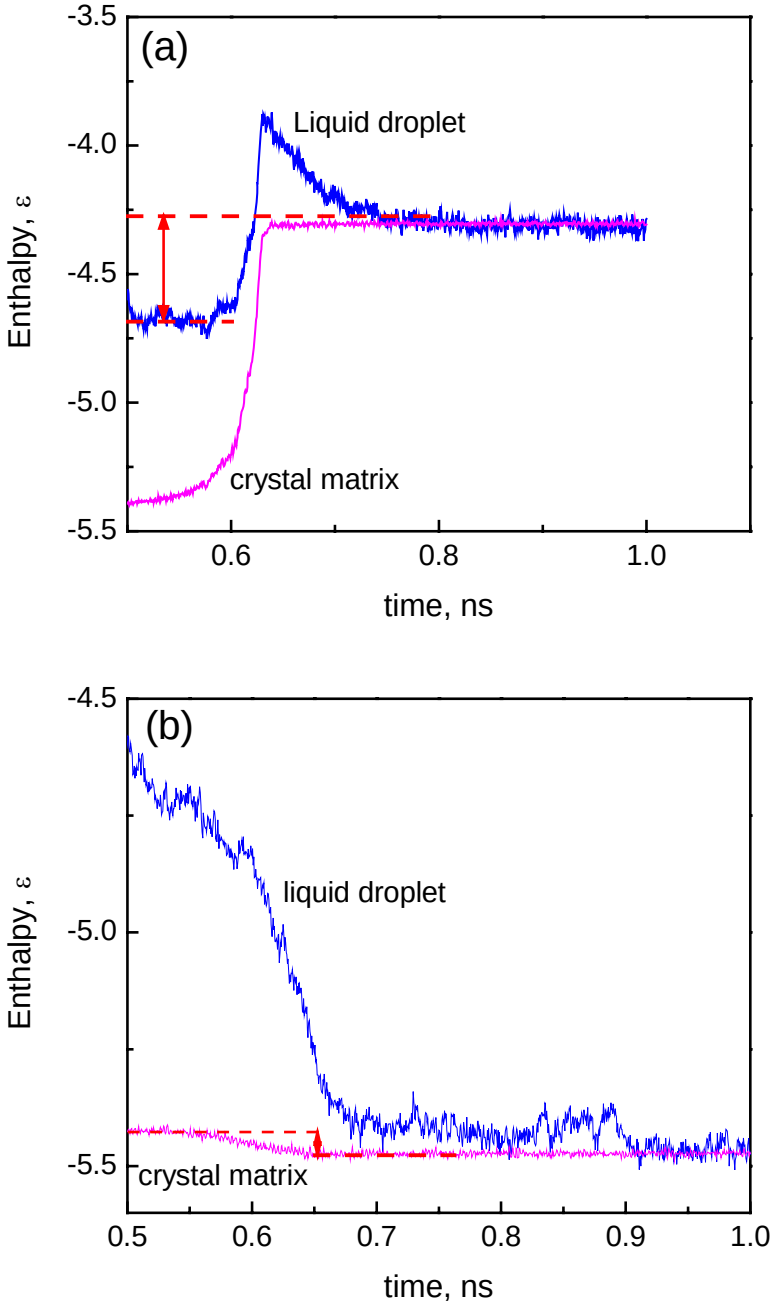

Figure 4.14. The enthalpy changes of the liquid droplet (blue line) and the crystal matrix (pink line). (a) At T=0.690 ε / k_B, the melting occurs. The enthalpy of the crystal matrix increases to the liquid value. (b) At T=0.689 ε / k_B, the liquid sphere disappears. The enthalpy of the liquid droplet decreases to the crystal value.

From the enthalpy changes of the liquid nucleus and the outer crystal matrix in the superheating model, we also observe the pressure effect on the liquid nucleus. Figure 4.14 shows the respective enthalpy changes of a 2491-atom liquid cluster and a 105 509-atom crystal matrix at different temperatures. When the liquid nucleus grows at $T=0.690\,\varepsilon/k_B$ [Figure 4.14(a)], the average enthalpy (per atom) of the crystal matrix increases from $-5.4\,\varepsilon$ to $-4.3\,\varepsilon$, indicating that the crystal matrix melts and becomes a pure liquid. At the same time, the average enthalpy (per atom) of the liquid cluster increases from the pressurized value of $-4.7\,\varepsilon$ to the unpressurized value of $-4.3\,\varepsilon$. Due to the pressure release associated with the melting of the crystal matrix, the enthalpy of the liquid cluster fluctuates to a peak value of $-3.9\,\varepsilon$ and thereafter dampens to the unpressurized value of $-4.3\,\varepsilon$. Clearly the compressive pressure on the liquid cluster lowers the enthalpy of the liquid cluster and makes it more stable. On the other hand, when the liquid nucleus shrinks at $T=0.689\,\varepsilon/k_B$ [Figure 4.14(b)], the enthalpy of the liquid cluster decreases from the pressurized value of $-4.7\,\varepsilon$ to the value of $-5.5\,\varepsilon$, which means the liquid cluster becomes one part of the solid matrix. Actually the crystal matrix also experiences a pressure from the liquid nucleus according to Newton's third law. Thus the enthalpy of the solid matrix is slightly elevated when it is under the pressure from the liquid droplet. After the liquid cluster crystallizes, the pressure on the crystal matrix is released. Consequently, the average enthalpy (per atom) of the crystal matrix decreases from a value of $-5.42\,\varepsilon$ to a value of $-5.48\,\varepsilon$. Clearly, the pressure effect on the liquid droplet is more obvious than on the crystal matrix. This is understandable because the liquid droplet contains less number of atoms.

4.2.6. Our Proposed Theory for Solid Superheating

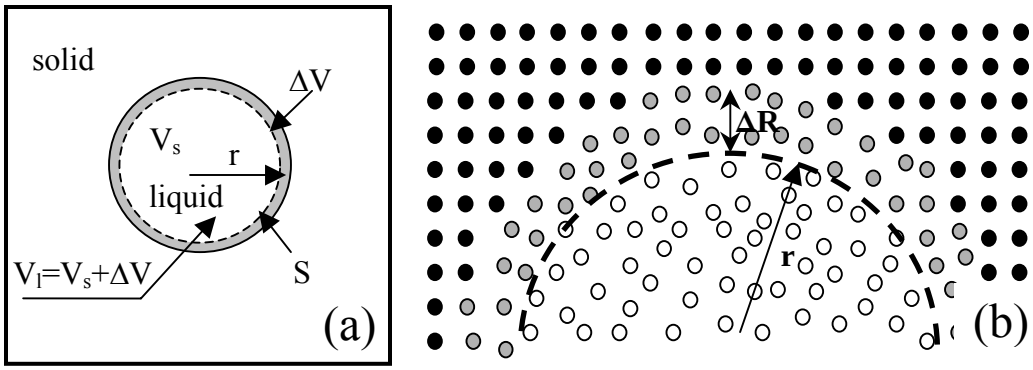

Figure 4.15. Schematic drawing of (a) a liquid droplet nucleating in a superheated solid, and (b) a curved solid-liquid interface. The disorder in the solid close to the interface is shown.

To formulate the theory for homogeneous nucleation of liquid phase, let's consider a solid is superheated above its normal melting point T_m. The shear modulus of the solid is μ. Without losing generality, we assume that the solid is isotropic. As shown in Figure 4.15(a), suppose a small amount of the solid phase occupying a sphere with radius r and volume V_s transforms into a liquid whose bulk modulus is K and volume is $V_l = V_s + \Delta V$, where ΔV is the relative volume change due to the solid/liquid density difference at melting. The free energy change of the system is

$$\Delta G(T) = (G_l V_l + E_l V_l + E_s V_s) - G_s V_s + G_{\text{int}} S , \qquad (4.4)$$

where G_l and G_s are the free energy densities of the bulk liquid and solid, G_{int} is the solid-liquid interface energy, E_l and E_s are the elastic energy densities of liquid and solid phases arising from the "mechanical" work done by the excess volume ΔV at

melting, and S is the interface area. Since the atomic volume of the liquid is larger than that of the solid, once the transformation occurs, the liquid and solid phases will experience additional forces: hydrostatic compression on the liquid and tension or pushing on the solid. The internal equilibrium is reached when each phase re-adjusts its volume so the total internal pressure in the system is zero. The volume changes in the liquid phase ΔV_l and in the solid phase ΔV_s at the equilibrium can be calculated [118]:

$$\Delta V_s = \frac{3K}{(3K+4\mu)}\Delta V, \tag{4.5a}$$

and

$$\Delta V_l = \frac{4\mu}{(3K+4\mu)}\Delta V. \tag{4.5b}$$

The associated elastic energy density for the liquid phase is $E_l = \frac{1}{2}K\left(\frac{\Delta V_l}{V_l}\right)^2$, and $E_s = \frac{2}{3}\mu\left(\frac{\Delta V_s}{V_s}\right)^2$ for the solid. Therefore, the total elastic energy of the system can be written as

$$\Delta E^{s-l} = (E_l + E_s) = \frac{2\mu K}{(3K+4\mu)}\left(\frac{\Delta V}{V}\right)^2, \tag{4.6}$$

where $V_l \approx V_s = V = \frac{4\pi}{3}r^3$ is assumed [118], and $\left(\frac{\Delta V}{V}\right)$ is the relative volume change at melting. The thermodynamic explanation of the elastic effects is shown in Figure 4.16.

Next let's consider the interface energy at melting. The liquid nucleus has a curved solid-liquid interface. The volume expansion at melting causes the disorder in the solid phase on and adjacent to the interface by expanding the interatomic distances between the solid atoms. On the other hand, the interatomic distances in the liquid

become smaller relative to the unpressurized liquid due to the compression. Since atoms in the outer solid matrix are less mobile, some of the disorder such as dislocations created would stay and become a part of the interface. The disorder on the liquid side is affected less due to the high mobility of atoms. As the nucleus radius becomes smaller, the increasing curvature of the interface would make the disorder more significant. These changes will lower the interface energy as a whole from that of the flat interface [Figure 4.15(b)]. The change of the interface energy can be obtained from Gibbs-Duhem equation that relates the change of the curved interface energy to the tangential stress difference between the liquid and solid phases across the interface, or an equivalent Laplace's law [119,120]. The result given below is from a simpler calculation: When a flat solid-liquid interface of a finite thickness ΔR is curved with a curvature $1/r$, the interface area change is $\Delta S \approx 2d^2 \Delta R / r$, where d is the interatomic distance between two neighboring interface atoms. The change of interface energy can be expressed as $\Delta\gamma = -\frac{\gamma_0 \Delta S}{d^2} = -\gamma_0 \frac{2\Delta R}{r}$, where γ_0 is the original flat solid-liquid interface energy. The interface energy becomes $\gamma = \gamma_0 + \Delta\gamma = \gamma_0(1 - 2\alpha / r)$, where $\alpha = \Delta R$. This expression has the same form as Tolman equation where α is the Tolman length [119,120]. Since α is of the order of an atomic diameter [90], the correction to the interface energy γ_0 would become significant as the nucleus size r approaches several atomic diameters. Note that this correction is not from the capillary effect as that in a liquid-vapor interface; it originates from the disordering at and near the solid-liquid interface.

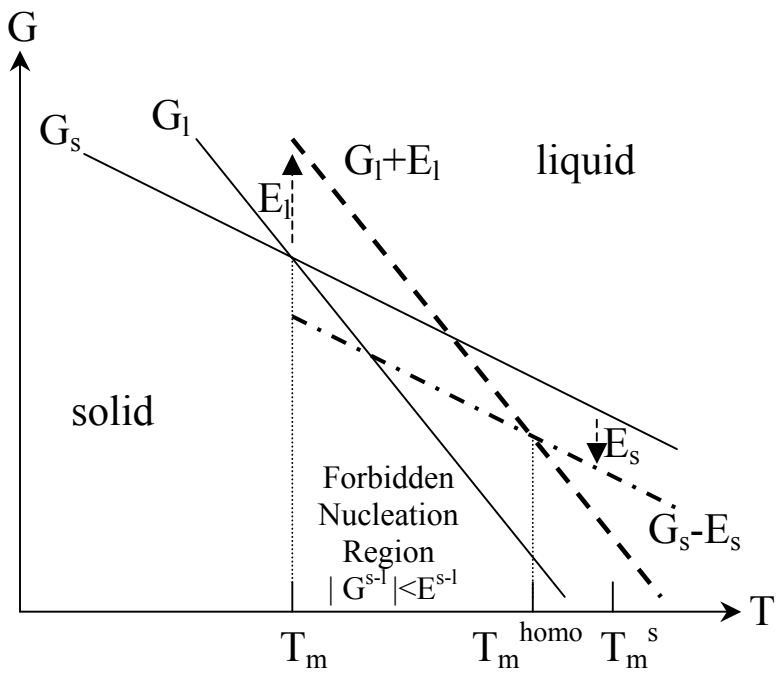

Figure 4.16. Schematic diagram of the free energies of solid and liquid phases as functions of the temperature. The solid lines marked by G_l and G_s are the free energies of the solid and liquid phases without the elastic energy. Their intersection gives the equilibrium melting temperature T_m. The dashed and dash-dotted lines marked by $(G_l + E_l)$ and $(G_s - E_s)$ are the free energies of the solid and liquid after including the elastic energies. Their intersection gives the homogeneous melting temperature T_m^{homo}. T_m^s is the ultimate superheating temperature. The forbidden nucleation region is $\Delta T_{gap} = T_m^{homo} - T_m$.

Putting all terms derived above in $\Delta G(T)$, we write the change of the free energy of the entire system as,

$$\Delta G(T,r) = \frac{4\pi}{3} r^3 \left(\Delta G^{s-l} + \Delta E^{s-l}\right) + 4\pi r^2 \gamma_0 (1 - \frac{2\alpha}{r}) - E_C, \qquad (4.7)$$

where $\Delta G^{s-l} = (G_l - G_S)$, $\Delta E^{s-l} = (E_l + E_S)$, and $E_C = \frac{4\pi}{3}(2\alpha)^3 \left(\Delta G^{s-l} + \Delta E^{s-l}\right)$. Note that E_C is a correction term to the body free energies due to the limitation imposed on

$r(\geq 2\alpha)$ by the interface energy γ. This restriction simply says that the size of the critical nucleus cannot be smaller than the interface thickness 2α.

The theory predicts a number of outcomes. First, the critical nucleus size can be obtained. Using the approximation $\Delta G^{s-l} = -\left|\Delta G^{s-l}\right| \approx -(\Delta T / T_m)\Delta L_V$, we have

$$r^* = \frac{2\gamma_0(1-\alpha/r^*)}{\left|\Delta G^{s-l}\right| - \Delta E^{s-l}} = \frac{2\gamma_0(1-\alpha/r^*)T_m/\Delta L_V}{\Delta T - T_m \Delta E^{s-l}/\Delta L_V}, \tag{4.8}$$

where L_V (>0) is the latent heat of fusion per unit volume at the normal melting temperature T_m, and ΔT is the superheating temperature $\Delta T = T - T_m$. Second, the critical activation energy is

$$\Delta G^* = \frac{16\pi\gamma_0{}^3 f}{(\left|\Delta G^{s-l}\right| - \Delta E^{s-l})^2} - E_c, \tag{4.9}$$

where $f = \frac{1}{3}(1-\frac{4\alpha}{r^*})(1-\frac{\alpha}{r^*})^2$. Note we do not express Equations (4.8) and (4.9) in close form in order to compare r^* and ΔG^* with those from conventional CNT. But they can be obtained straightforwardly.

Putting our modified classical nucleation theory [Eq. (4.8)] into Figure 4.11, we plot a new graph in Figure 4.17. When the liquid droplet size is small, the simulation data can be fitted with our theory very well in three size systems. When the liquid droplet size is large, the simulation data deviates from the theory due to the finite size effects. However, the trend is that the simulation data becomes closer to the theory when the total system size increases. Since our theory is developed for an infinite system, it can be predicted that the simulation data can be even closer to the theory if the simulation system size increases.

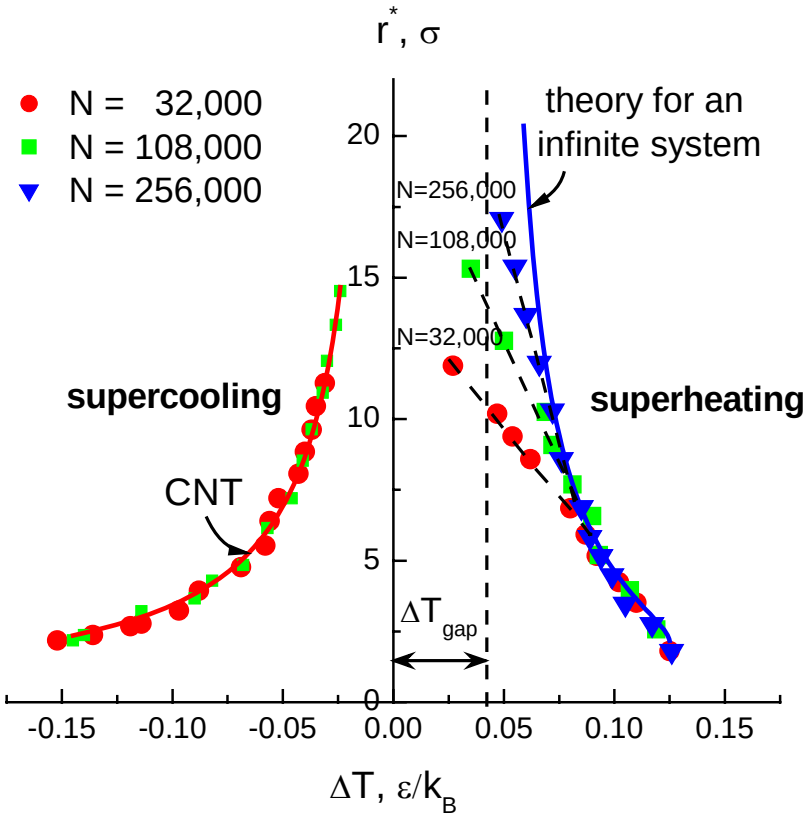

Figure 4.17. The relation between critical solid (liquid) nucleus radius r^* and supercooling (superheating) temperature ΔT^*. Samples of different sizes were used. The solid line in supercooling region is fitted to the relation, $r^* \cong (2\gamma_{sl}T_m / \Delta L_v)/\Delta T$. For superheating, finite-size effect is shown. The theoretical prediction [Eq. (4.8)] is plotted as the blue solid line. The results from the largest system tested (N=256 000) are in excellent agreement with the theory. The nucleation forbidden gap $\Delta T_{gap} = 0.044$ is indicated by the dotted line. At the superheating limit, the size of the liquid droplet is about 19 atoms.

The elastic energy ΔE^{s-l} in Eq. (4.8), which is caused by the solid/liquid density difference, effectively reduces the driving force. The activation energy becomes larger due to the increase in the free energiy of the liquid phase under compression and the

decrease in the free energy of the outer solid matrix under tension. Therefore, the equilibrium melting temperature for homogeneous nucleation of liquid phase at superheating regime, $T_m^{\mathrm{hom}o}$, is higher. $T_m^{\mathrm{hom}o}$ can be estimated when $\Delta T - T_m \Delta E^{s-l} / \Delta L_V = 0$. Thus $T_m^{\mathrm{hom}o} = T_m (1 + \Delta E^{s-l} / \Delta L_V)$. Therefore, ΔE^{s-l} functions effectively like another "barrier" for the liquid nucleation. Its effects on melting can be significant so that a forbidden gap for nucleating a liquid phase in the superheating region may be possible if $\left|\Delta G^{s-l}\right| < \Delta E^{s-l}$. The nucleation forbidden gap can be expressed as

$$\Delta T_{gap} = T_m^{\mathrm{hom}o} - T_m = T_m \Delta E^{s-l} / \Delta L_V . \qquad (4.10)$$

The presence of the nucleation forbidden gap makes it impossible for melting to start from the inside of a perfect crystal if the temperature is slightly above the equilibrium melting temperature. The form of the elastic energy ΔE^{s-l} is given in Eq. (4.6). The parameters for ΔE^{s-l} can be calculated from a homogeneous LJ system. The temperature-dependent bulk modulus of liquid $K(= 39.19 - 38.96T)$ and the shear modulus of solid $\mu(= 23.27 - 24.51T)$ are given in Eq. (4.2a) and Eq. (4.2b). The other parameters are calculated in Chapter 3: $\Delta L_V = 1.005\varepsilon / \sigma^3$, $T_m = 0.618\varepsilon / k_B$, $\alpha = 1.05\sigma$, and $\Delta V / V = 0.16$. For the LJ system, $\Delta T_{gap} = 0.044$ [Figure 4.17], which is about 7% above T_m or 30% of the entire superheating range. Within this gap melting can only start at free surfaces or grain boundaries where the compressive pressure is less or absent [Figure 4.5]. This finding provides a new perspective for surface melting, which is explained traditionally based on the relations among the solid-vapor, solid-liquid, and liquid-vapor interfacial free energies, i.e., $\gamma_{sv} \geq \gamma_{sl} + \gamma_{lv}$ [1]. This finding also helps us to

understand why melting easily occurs at internal interfaces and grain boundaries where the above relation does not even hold.

The modified classical nucleation theory also predicts an upper limit for superheating where the interface energy could become extremely small if $r^* \to 2\alpha$. It predicts that the critical liquid nucleus at this limit should be about the size of a cluster made of the first and second nearest neighbor shells. Under such conditions, melting at superheating could become spontaneous, where homogeneous nucleation of liquid becomes barrier-less. This marks the instability, or a catastrophe. As shown in Figure 4.17, the theory shows excellent agreement with our simulations. We observed not only the nucleation forbidden gap, but also the extremely small nucleus size at the superheating limit. Experimental results from superheating quartz, along with the theoretical consideration of ΔE^{s-l} [121], provide the direct support for our work. Melting at superheating is determined, therefore, by the interplay of the two energies, the rise of the elastic energy, and the reduction of the interface energy. In all cases, however, melting in superheating regime should remain as a first-order transition.

Figure 4.17 shows that the finite size effects are very significant in the superheating model, whereas they are not obvious in the supercooling model. This is due to the long-range nature of the elastic interaction between the liquid nucleus and the simulation box in the superheating model. In the supercooling model, the elastic energy is very weak so that the finite-size effects are only induced by the usual thermal fluctuations. In the superheating model, the finite distance between the liquid droplet and one of its periodic images is directly related to the elastic interaction in superheating. If the radius of the liquid droplet is small, then the distance is large. Therefore, the liquid

droplet can be viewed as being immersed in an infinite solid matrix. For small liquid clusters (i.e., at large superheating), the finite-size effects in three size systems are not significant. But if the liquid droplet radius is big, the distance between the liquid droplet and its periodic images is short. So the liquid droplet cannot be viewed as being immersed in an infinite solid matrix. Then the finite-size effects show up. If the size or radius of liquid cluster is same, the larger the system size, the more accurate the results. In Figure 4.17, the convergence to the theoretical prediction (which is for an infinite solid matrix) can be clearly seen in the trend of the three systems of increasing size.

4.2.7. Liquid growth from Disk Nuclei

So far we have discussed the model of a spherical nucleus embedded in a superheated crystal. In this model, the liquid growth is from a spherical liquid droplet. The growth morphology is roughly spherical, as shown in Figure 4.9. However, the spherical nucleus is a highly ideal case. In reality, the geometric shape is very irregular. Thus, the growth morphology from such non-spherical nuclei is of the general interests. For example, what kind of morphology is most likely to grow into if the liquid grows from a disk nucleus? Brener *et al.* [122] investigated this problem from the theoretical aspect. They assumed that the disk nucleus is very similar to a crack in the solid. Applying the same concept of the Griffith's theory for the crack problem, they proposed that the liquid growth prefers in the horizontal direction of the disk nucleus as shown in Figure 4.18. Thus, the disk nucleus will become more and more oblate. However, this theoretical analysis has never been verified in experiments or in computer simulations.

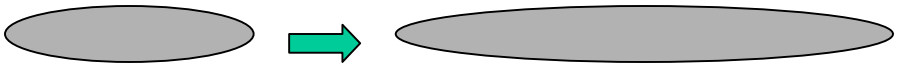

Figure 4.18. Brener *et al.*'s model [122] of the liquid growth morphology from a disk nucleus in a superheated crystal. Their model predicts that the disk nucleus prefers to grow in the horizontal direction.

In this section, we use MD simulations to study the liquid growth from disk nuclei. The simulation model is slightly different from the superheating model. Instead of using a spherical nucleus, we embed a disk nucleus in a superheated crystal, as shown in Figure 4.19. The height of the nucleus is of about two lattice constants (a_0) and is fixed for different configurations. The radius of the disk ranges from $2a_0$ to $14a_0$. The composite model is created by using the same method in section 4.1.3.

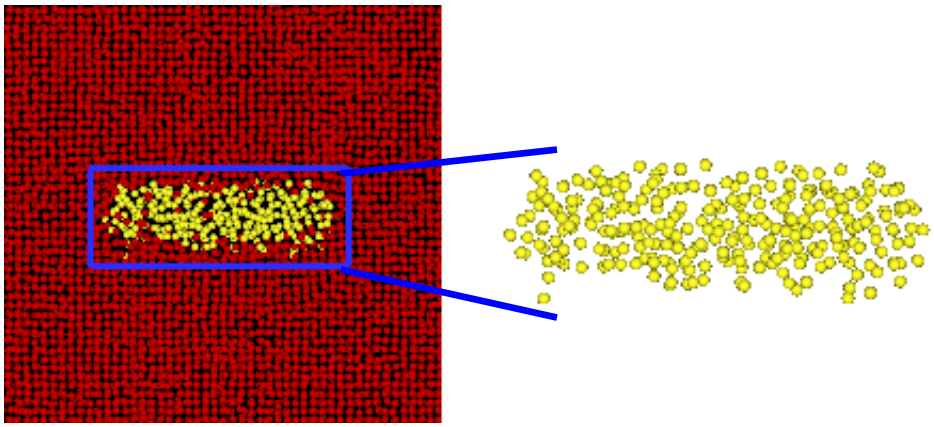

Figure 4.19. The cross-sectional snapshot of a liquid nucleus of a disk shape and the outer crystal matrix. The enlarged view of the liquid nucleus is shown at the right-hand side.

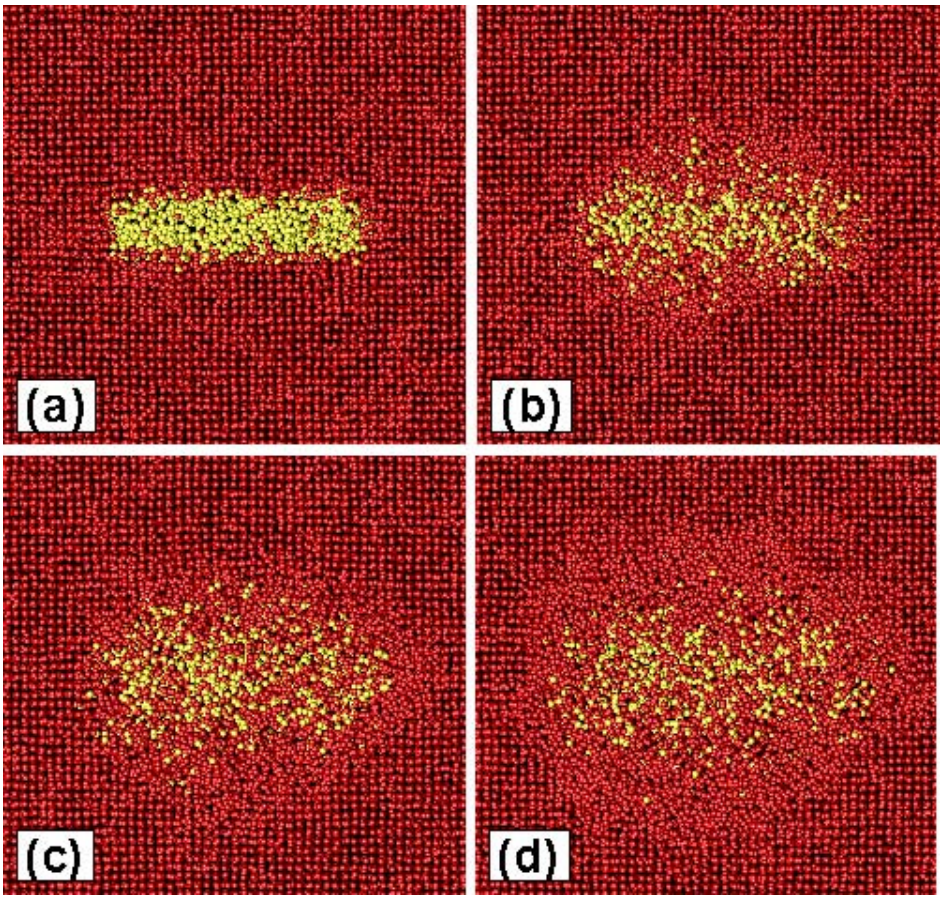

Figure 4.20. The cross-sectional snapshots of the liquid growth from a disk nucleus. (a) Initial configuration. (b) After 0.25 ns. (c) After 0.4ns. (d) After 0.65ns.

After the disk nucleus is created, the liquid nucleus can either grow or shrink, which is very similar to the spherical nucleus. In this work, we are only interested in the case of the liquid growth. Figure 4.20 shows the evolution of the liquid growth from a disk nucleus. Initially, a disk liquid nucleus is embedded in a superheated crystal matrix [Figure 4.20(a)]. The disk nucleus is very flat, which is similar to Brener *et al.*'s model [122]. After 0.25ns, the snapshot [[Figure 4.20(b)]] shows that the liquid grows from the liquid nucleus. However, it seems that the growth is in the vertical direction, which is

different from Brener *et al.*'s prediction. Since the atoms in the liquid nucleus are very diffusive, the atoms in the liquid nucleus mix with the new liquid atoms. After 0.4ns, the liquid grows further, as shown in Figure 4.20(c). It seems that the liquid growth is still along the vertical direction at this time. Contrastively, the liquid length increases only slightly in the horizontal direction [one can easily see it by comparing Figure 4.20(a) and (c)]. After 0.65ns, the disk nucleus almost grows into a spherical droplet [Figure 4.20(d)].

Clearly, the direct simulation shows that the disk nucleus prefers to grow into a sphere rather than a more oblate disk. Our simulation result contradicts Brener *et al.*'s prediction. Thus, it is questionable that the Griffith's theory for the crack problem can be applied for the liquid growth from a disk nucleus. One obvious difference between the two problems is that the stress applied on a crack is a tensile stress, whereas the stress applied on a disk nucleus is a compressive stress originated from the surrounding crystal matrix. To best of our knowledge, this difference is not considered in their model. The liquid growth morphology from a disk nucleus can be understood from Figure 4.21. The initial disk nucleus has two major curvatures at the solid-liquid interface: k_1 and k_2. The curvature k_1 is close to zero (flat interface) and k_2 is close to the reciprocal of the disk radius, i.e., $k_2 > k_1$. Generally, it requires small superheating for the liquid growth from the interface region of a small curvature. For example, a liquid can grow from the flat solid-liquid interface as long as $T > T_m$. Thus, the liquid growth can start earlier at the interface region of a small curvature than at that of a large curvature. For example, in Figure 4.21, the liquid prefers to grow at the interface region of the curvature k_1. The directional growth will eventually turn the new liquid into a spherical droplet.

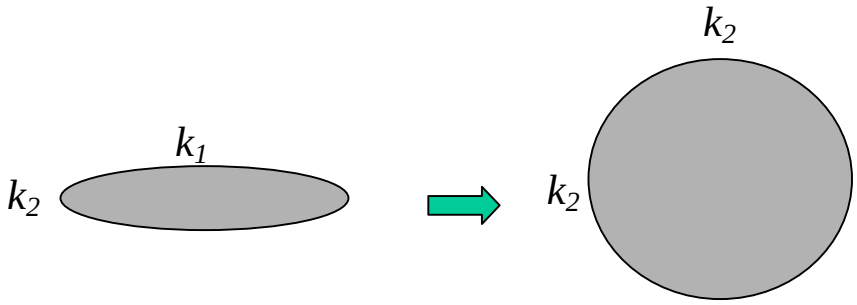

Figure 4.21. Illustration of the liquid growth morphology from a disk nucleus. The liquid prefers to grow from the interface of small curvature such as k_1.

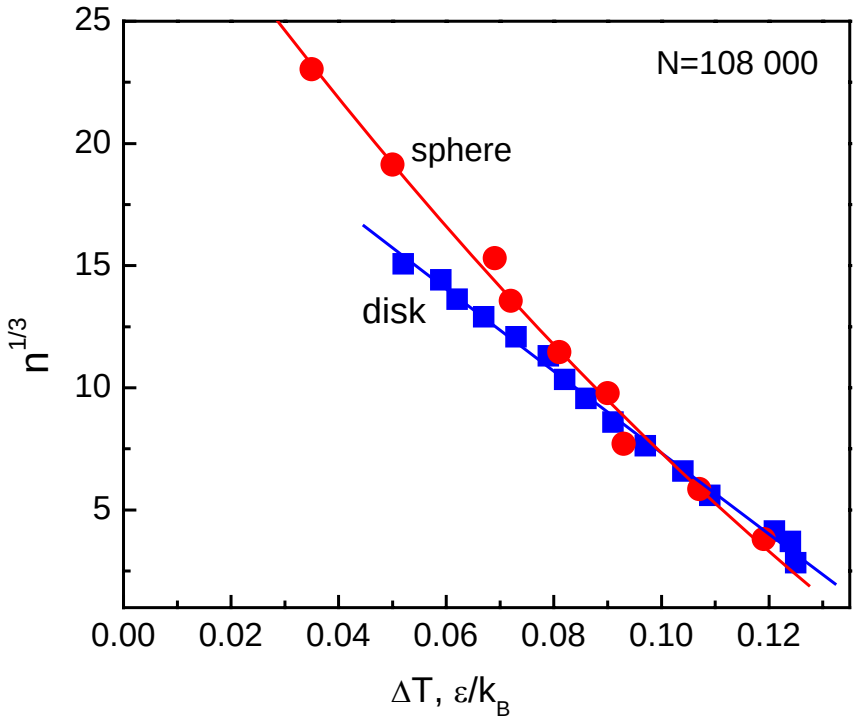

Figure 4.22. Comparison between the disk nucleus and spherical nucleus. The total number of atoms in the system is 108 000 in both systems.

It is interesting to make a comparison between the disk nucleus and spherical nucleus in the liquid growth. We use the same method as in section 4.2.3 to determine the critical temperature of a disk nucleus and its surrounding crystal matrix. The relation between the number of atoms in the disk nucleus and the critical temperature is shown in Figure 4.22. The relation for the spherical nucleus is also shown in this graph. When the disk radius is small, its height is close to its radius. Thus, it is equivalent to a spherical nucleus. Figure 4.22 also shows that the two systems yield same results when the nucleus size is small (or at high superheating). When the nucleus size is large, the discrepancy appears. It is found that if the numbers of atoms enclosed in the disk nucleus and in the spherical nucleus are same, the disk nucleus requires smaller superheating for growth. In other words, the growth from a disk nucleus is easier than from a spherical nucleus. This is a little bit surprising, because the spherical nucleus has the minimum area-to-volume ratio. However, in this work we know that the local curvature of the interface is also very important for the growth morphology.

Similar to the tests of the spherical nuclei [Figure 4.17], we also test the finite size effects for the disk nuclei. Two size systems are used: N=108 000 and 256 000. The results are shown in Figure 4.23. One can find that Figure 4.23 is very similar to Figure 4.17. The relation of $n^{1/3}$ vs. ΔT shifts upwards when the system size increases due to the finite size effects. Note the nucleation forbidden gap shown in Figure 4.23 is for the spherical nuclei. After a disk nucleus grows into a spherical droplet [Figure 4.20(d)], the further growth should be spherical. Thus, the presence of the nucleation forbidden gap is expected in the liquid growth from the disk nuclei.

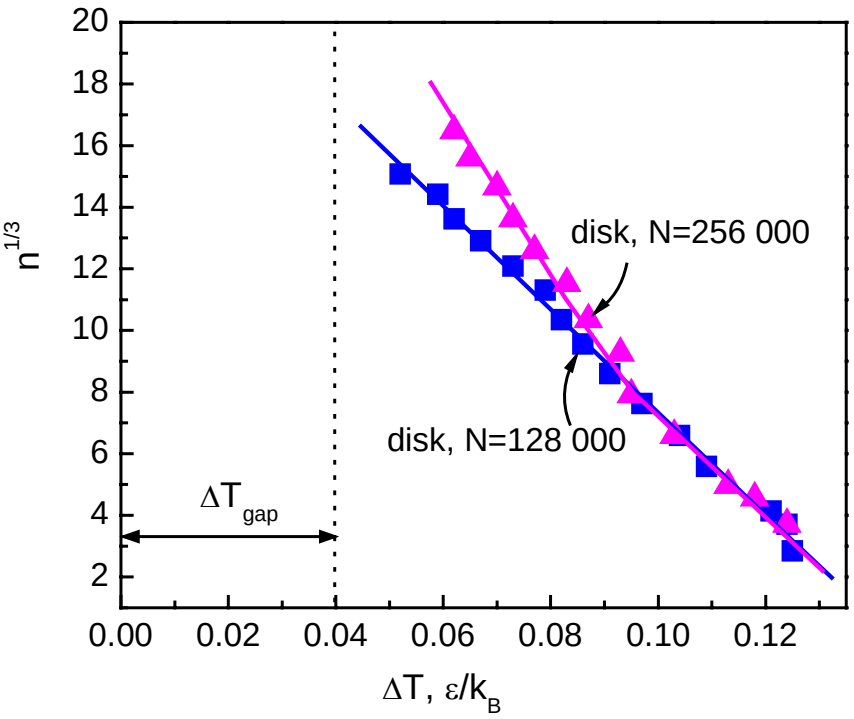

Figure 4.23. Finite size effects in the liquid growth from disk nuclei. The curve shifts upwards when the system size increases.

4.2.8. Kinetic Differences between Solid Superheating and Liquid Supercooling

Next we test the differences in *kinetic* behaviors between solid superheating and liquid supercooling. To do so, we use the flat interface model [Figure 4.24] to calculate the interface moving velocities, or the growth rates of the new phases at different temperatures. The detailed method is described in Chapter 5. Here we only report the results. The (100), (110), and (111) planes of a bulk fcc LJ crystal are in contact with a bulk liquid to form the crystal-melt interfaces with different orientations. The systems

with crystal-melt interfaces are brought to different temperatures. Depending on the brought temperature, the interface can move to either the crystal side or the liquid side, as shown in Figure 4.24.

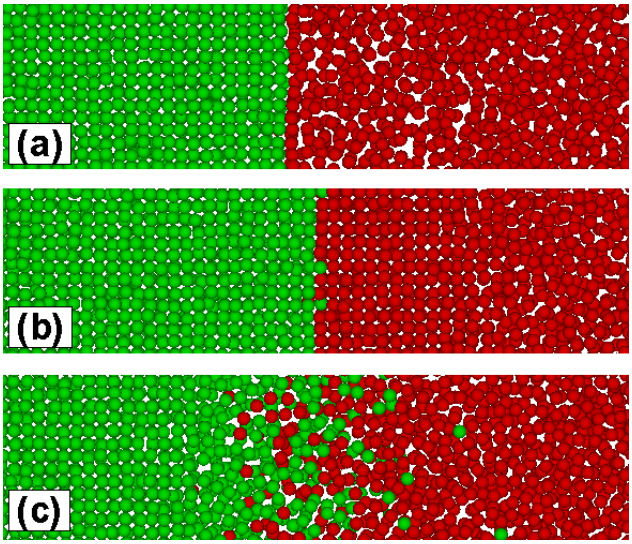

Figure 4.24. The flat interface model for calculating the interface moving velocities at the superheating and superheating regimes. The horizontal direction is [100] in this example system. (a) At $T = T_m$, the interface is stable. (b) At $T < T_m$, crystallization occurs. The interface is moving from the crystal side to the liquid side. (c) At $T > T_m$, melting occurs. The interface is moving from the liquid side to the crystal side.

The interface moving velocities are calculated at different superheating and supercooling temperatures, as shown in Figure 4.25. We find that the growth rate is anisotropic in supercooling, but isotropic in superheating. In the supercooling regime, the (100) plane has the fastest growth rate, whereas the (111) plane has the slowest. During crystallization, liquid atoms need to migrate to the interface and finally settle at the suitable lattice sites. The denser the atomic plane is, the longer this rearranging time, and

the slower the growth rate. As temperature decreases, the driving force for crystallization increases. On the other hand, the mobility of liquid atoms decreases with the decreasing temperature. Thus, the growth rate is a result of balancing the increasing thermodynamic driving force and decreasing atom mobility (diffusivity and viscosity) at supercooling. The maximum growth rate is reached at $\Delta T \approx 0.2$, which coincides with the favorable supercooling temperature of spontaneous nucleation.

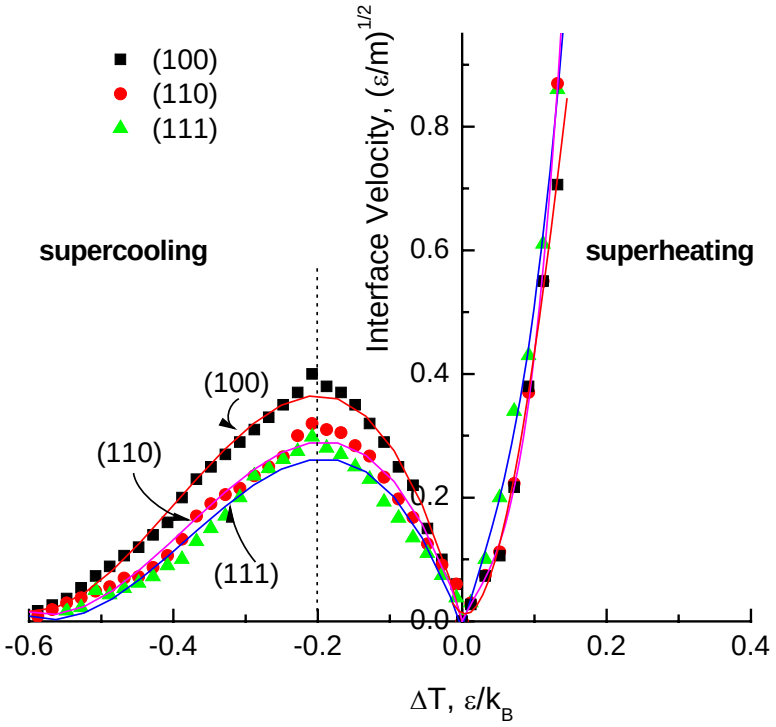

Figure 4.25. Interface moving velocities at different supercooling and superheating.

In contrast, for melting the kinetic process at the interface is dominated by breaking the atomic bonds. The bond-breaking process may be less related to the specific plane. Thus the growth rate of liquid phase shows the isotropic behavior. In addition,

since both driving force and atomic mobility increase with the increasing temperature, the growth rate increases monotonously with the increasing temperature. Note that the interface velocities within the nucleation forbidden gap are obtained from the flat liquid-solid interface where the compressive energy caused by the volumetric difference between the liquid and solid phases is absent. Therefore, nucleation forbidden gap is zero for a flat interface model. The kinetic behaviors of growth, as well as in nucleation, are originated from the difference in diffusion and viscosity change. The differences are the reason why crystallization can be easily bypassed during glass formation while superheating is hard to achieve, as demonstrated by Turnbull fifty years ago [6].

4.3. Discussion and Conclusions

In this Chapter, we have used a coexistence model of an inner liquid sphere and an outer crystal matrix to test the classical nucleation theory for melting at superheating. Contrast to many researchers' assumption that the solid superheating is an inverse process of liquid supercooling, we have found that the melting at superheating is fundamentally different from the solidification at supercooling in both thermodynamics and kinetics. When melting occurs internally, the volume expansion of the molten materials induces a strong stress on the liquid. As a result, the liquid growth experiences another energy barrier. If the driving force cannot overcome the elastic stress, it becomes impossible for liquid growing from the inside of the crystal. As a result, a nucleation forbidden gap appears. If the temperature is within this gap, the melting must start from the free surface or other stress-free regions. This may be one of the reasons for the asymmetry between the melting and freezing process: a solid (with a free surface) cannot

be superheated, while liquid can be supercooled. It is worth noting that some materials such as ice (below 2 kilobars), antimony, bismuth, and silicon show decrease in volume during melting. For these materials, the compressive stress is absent for homogeneous melting. However, the elastic energy may still present in the solid due to the "cavity" effect.

The liquid growth from disk nuclei is also investigated in this chapter. Although some theoretical models predict that the disk nucleus becomes more oblate during the liquid growth, our direct simulation shows that the disk nucleus prefers to grow into a sphere. This is due to the curvature induced melting: the melting prefers to starts from the local interface region with small curvature such as a flat interface. Moreover, we find that the disk nucleus is easier for the liquid growth than is a spherical nucleus if they have the same number of liquid atoms, although the spherical nucleus has a smaller surface to volume ratio. A nucleation forbidden gap also presents in the liquid growth from disk nuclei.

The crystallization rate at different supercooling temperatures and the melting at different superheating temperatures are also investigated. It is found that the crystallization rate is anistropic in the liquid supercooling, while the melting rate is isotropic in the solid superheating. The interface moving velocity of (100) face is fastest and that of (111) face is slowest. The crystallization is related to the face-dependent atom rearrangement at the interface. The melting is related to the atomic bond breaking which appears to be face-independent. Since the driving force increases and the atomic mobility decreases with the decreasing temperature in the liquid supercooling, the interface moving velocity has a maximum value. For the solid superheating, both the driving force

and the atomic mobility increases with the increasing temperature. Thus, the interface moving velocity always increases with the increasing temperature.

Although the models used in this work are simplified, the results gave us a detailed comparison between the solid superheating and liquid supercooling processes in thermodynamics and kinetics that otherwise are very difficult to obtain in experiment alone. The mechanisms uncovered in this work for superheating provides a new perspective for understanding melting and also a valuable guide for many applications involving melting at superheating such as laser processing of materials [123,124], geomaterials [124], explosive materials [124,125], and materials engineering [126].

CHAPTER 5

TEMPERATURE, FACE, AND SIZE DEPENDENCES OF STEADY-STATE CRYSTALLIZATION RATES

The crystal growth from its undercooled melt has gained great interests in the past several decades [1-6,34-42,127]. At deep undercoolings, usually the homogeneous nucleation takes place if the impurities are effectively excluded [4-6]. However, in many cases, the crystal growth starts from a crystal-melt interface and is a heterogeneous process. The moving velocity of the nonequilibrium solid-liquid interface, or the crystal growth rate, is an important physical quantity for understanding the kinetics and morphologies of the crystal growth [34-42]. Given the fact that many materials exhibit nearly isotropic interfacial properties such as interfacial free energy [30,84,85,89], interface density profile [128], interface thickness [41,128,129], etc., the anisotropy in the growth rates of different crystallographic faces, rather than in the interfacial free energy, may be more important in determining the macroscopic morphology of the crystal growth [127]. At macroscopic scale, the crystal growth rate is generally slow because the generated latent heat during the crystal growth must be dissipated away from the interface to the outside of the system. This thermal-diffusion limiting process can be well described by the conventional transition-state theory [130]. However, if the system size is small, for example, of a few ten to hundred nanometers, the heat flow can be very rapid so that the thermal diffusion may not be a primary limiting factor in affecting the crystal growth rate [127]. Recent experiments of the pulsed laser annealing have showed that the melting and crystallization rates are substantially fast in small systems [43-50]. In those

experiments, researchers used the picosecond pulse lasers to melt a small spot (~ 0.5 μm in depth) on a clean silicon or germanium surface and afterward solidify the liquid spot. The melting rate was found to be about 10 m/s while the subsequent recrystallization rate is about 5 m/s [44-50]. Clearly, the melting and crystallization rates in such experiments are not restrained by the thermal diffusivity, and therefore, the conventional transition-state theory may not be suitable for describing the transformation kinetics in such small size systems.

Recently, many technical advances in investigating the crystal-melt interface at the molecular scale have been achieved. For example, the *in situ* transmission electron microscopy [51], the synchrotron x-ray scattering techniques [52], and the high-resolution transmission electron microscopy [131,132] have been successfully used to investigate the ordering of the solid-liquid interfaces. Although valuable results have been obtained from those experiments, the knowledge of the crystal-melt interface is still limited. This situation can be partially attributed to the difficulties of accessing the solid-liquid interface in experiment [131]. Unlike the solid-vapor and liquid-vapor interfaces, the experimental measurements of the microscopic structure and properties of the solid-liquid interface are inherently difficult, because the solid-liquid interface is very thin (~ 2 nm wide) and is "buried" between two condensed phases [131]. Fortunately, the computer simulation provides an alternative way for investigating the detailed microscopic information of the solid-liquid interface. In the past several decades, theoretically, computer simulations have been used to investigate the heterogeneous crystal growth from a flat crystal-melt interface [34,38-42,129]. Broughton and co-workers [34,38] have used molecular dynamics simulation to calculate the interface

moving velocities of (100) and (111) faces over a wide range of undercooling temperatures. Their results showed [34,38] a strong anisotropy in the orientational crystallization rates: the interface moving velocity of (100) face is substantially fast over a wide range of temperatures, whereas that of (111) face is extremely slow at low temperatures. They concluded that, for a monatomic Lennard-Jones fluid, the crystal growth from (100) is free of activation energy barriers, while the crystal growth from the (111) face needs to overcome the energy barriers associated with competing for the appropriate fcc and hcp sites. The growth rate of (111) face is thus slow down by this site competing process. Using coupled Landau-Ginzberg theory based on a mean field approximation, Williams *et al.* [133] concluded that the large difference in structural fluctuations between (100) and (111) faces is the origin for the anisotropic interface moving velocities. Richards [130] argued that the change in density during the crystal growth plays an important role in affecting the anisotropic growth rates. This argument is supported by the work of Huitema *et al.* [41] and Gulam Razul *et al.* [129], who have used molecular dynamics simulations to investigate the crystal-melt interface structures. They concluded that the atoms have to hop from further-away liquid layers to the interface for (111) face, because the density of (111) face is much higher than the liquid density. On the other hand, atom hopping is not necessary for (100) face because its density is at the same level as the liquid density. As a result, the large density transport associated with (111) face causes its growth rate slower. However, the study by Oxtoby and Harrowell [134] gives an opposite conclusion in which the effects of the density change on the crystallization rates are less significant in most cases.

Apparently, there are many disputations on the mechanisms of the crystal growth. To date, the detailed understanding of the microscopic interface structures, the mechanisms of ordering during the crystallization, and the kinetics associated with the interface moving are still limited. Moreover, there is a large discrepancy in the crystallization rate between experiments and simulations. For example, the crystallization rates of silicon and germanium measured from pulsed laser annealing experiments are about 5 m/s, while the maximum moving velocity of (100) face of a Lennard-Jones system was found to be as large as 80m/s in Broughton *et al.*'s simulations [34,38]. The similarly high growth rates were found in other simulations [39-42] even at small undercoolings. It appears to be a general result that the velocities in simulation studies are much larger than those observed in experiments. Unfortunately, this large discrepancy between the experimental results and the theoretical predictions has not been resolved. The underlying physical origins for this discrepancy, therefore, still remain veiled to date.

In this chapter, I present our investigations on the face, temperature, and size dependences of the crystal growth rate via molecular dynamics simulations. Although the face and temperature dependences have been studied to some extent by many researchers, the finite size effects on the crystallization rate are seldom investigated. Therefore, it is unclear whether the system size plays a major role in affecting the crystallization rates. The detailed microscopic interface structures, the growth morphologies, the growth mechanisms, the kinetic theory, and the finite size effects are also investigated in this work.

5.1. Theory of Crystal Growth

The steady-state crystal growth of many materials can be described as a "diffusion-controlled", or "Wilson-Frenkel" process [35,36], in which the growth rate is determined by the long-range diffusion coefficient of liquid atoms and the free energy difference (or driving force) between two phases. Generally the steady-state motion of the crystal-melt interface as a function of the temperature T in the diffusion-controlled model can be expressed as [34]

$$v = (Da/\Lambda^2)(1 - e^{-\Delta\mu/k_BT})f\,, \tag{5.1}$$

where D is the diffusion coefficient of the liquid, a is the interatomic spacing, Λ is the mean free path, f is the atomic site acceptance ratio for crystallization which is usually treated as a constant ($0 < f < 1$), $\Delta\mu$ is chemical potential difference between a liquid and a crystal so that $(1 - e^{-\Delta\mu/k_BT})$ can be viewed as the driving force for crystallization, and k_B is the Boltzmann constant.

Similar to many metallic systems, the diffusion in a Lennard-Jones liquid is also a thermally activated process. The diffusion coefficient D can usually be described by the Arrhenius equation [1],

$$D = D_0 \exp(-Q/k_BT)\,, \tag{5.2}$$

where D_0 is a constant, and Q is the activation energy. For a standard LJ system, independent calculation [34] shows D_0 = 0.86, and Q = 2.1 (both are in reduced LJ units). As shown in Figure 5.1, the diffusion coefficient decays exponentially with the decreasing temperature. At low temperatures or deep undercoolings, the diffusion coefficient is very small. For example, at $T = T_m/2 \approx 0.31\,\varepsilon/k_B$, $D \approx 9.83\times10^{-4}$

$\left(\sigma^2\varepsilon/m\right)^{1/2} \approx 5.28\times10^{-7}$ cm^2/s. For most fcc metals at room temperature, $D \sim 10^{-8}$ cm^2/s [1]. Therefore, near half the melting point, the LJ system is as rigid as a solid and the diffusion coefficient is essentially zero on the simulation scale. If the crystal growth is a diffusion-controlled process, the crystallization rate is expected to be very slow or even zero at low temperatures. The diffusion-controlled model can be well fitted to the growth rates of covalently bounded materials such as GeO_2 [37,127] and multi-component solutions [135] in which the growth rate is mainly determined by the diffusivity. However, Walker [43] found that the crystallization rates of supercooled nickel and cobalt melts are very fast (~ 50 m/s) even at low temperatures, indicating that the crystal growth of pure metals may not be entirely thermally activated. In addition, as we have mentioned above, the crystallization rates of small-size silicon and germanium are about 5 m/s at deep undercoolings. Clearly, the diffusion-controlled model fails to predict the crystallization rates of those monatomic systems, particularly at low temperatures.

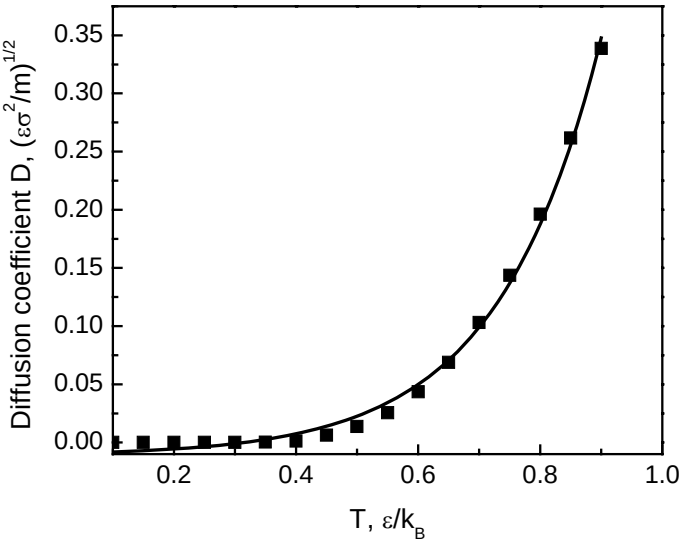

Figure 5.1. The temperature-dependent diffusion coefficient of a Lennard-Jones system.

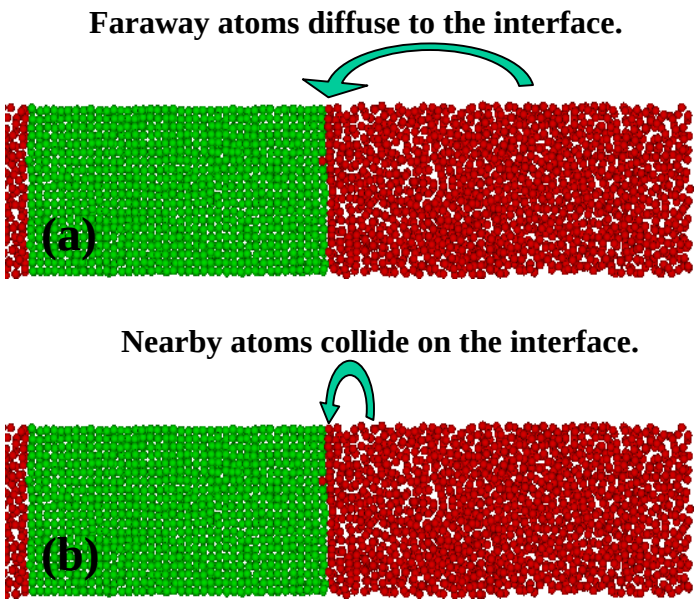

Figure 5.2. Two typical models of crystal growth from the undercooled melt. Crystals are at the left-hand side and liquids are at the right-hand side. (a) The diffusion-controlled model: atoms travel from the faraway liquid to the crystalline sites at the interface. (b) The collision-controlled model: the vicinity atoms "collide" on the interface and become a part of the crystal.

Turnbull and Bagley [37] argued that the crystallization of pure metals should not be a complete diffusion-controlled process, because it is hard to quench them into glassy state [34,37]. Since all atoms are *identical* in a monatomic system, it is not necessary to bring the faraway liquid atoms to the interface to form the new crystal. Actually, the nearby liquid atoms at the interface may already occupy the crystalline sites before the faraway atoms diffuse to the interface. Therefore, they [37] proposed a "collision-controlled" model for monatomic systems, in which the crystal growth rate is mainly controlled by the collision rate of the near-interface liquid atoms impinging on the interface, rather than the long-range transport rates of the liquid atoms traveling to the interface. Similar to an ideal gas model, the collision rate is proportional to the thermal

velocity $(3k_BT/m)^{1/2}$, where *m* is the atomic mass. The interfacial moving velocity in the "collision-controlled" model can be expressed as [34]

$$v = (a/\lambda)(3k_BT/m)^{1/2}\{1 - e^{-\Delta\mu/k_bT}\}f, \tag{5.3}$$

where λ is the average distance traveled by an atom. Normally, λ takes the value of $0.4a$ [34]. Equation (5.3) is similar to Eq. (5.1), but the diffusion coefficient *D* is replaced by the thermal velocity $(3k_BT/m)^{1/2}$. Figure 5.2 illustrates the physical pictures of the diffusion-controlled and collision-controlled models. The long-range diffusion in the diffusion-controlled model and the short-range diffusion in the collision-controlled model are the key differences between two models.

In order to compare the differences between the two models, we draw a graph as shown in Figure 5.3 to illustrate the temperature-dependent crystallization rates calculated from Eqs. (5.1) and (5.3). The parameters in the two equations are given as follows: $a = \sqrt{3}/3 \times a_0 = \sqrt{3}/3 \times 1.58 = 0.912\sigma$, where $a_0 = 1.58\sigma$ are the fcc lattice constant of the LJ system; $\lambda = 0.4a$; $\Lambda = 0.0829 - 0.0258T + 0.18588T^2$; $D = 0.86 \times \exp(-2.1/T)$; (note the coefficient 0.0258 was incorrectly reported as 0.258 in Ref. 34); $\Delta\mu = L_n \times \Delta T/T_m$, where $L_n = 1.024\varepsilon$ is the latent heat of fusion per atom, $T_m = 0.618\ \varepsilon/k_B$ is the equilibrium melting temperature, and $\Delta T = T_m - T$ is the undercooling; and $f = 0.27$. Clearly, there is a large discrepancy between two models in Figure 5.3. The crystal growth rate predicted by the collision-controlled model is much faster than by the diffusion-controlled model. The crystallization rate of the collision-controlled model is substantially fast over a wide range of temperatures and reaches the

maximum at $T = 0.27\varepsilon / k_B$. However, in the diffusion-controlled model, the crystallization rate is much slower and approaches zero at near half the melting point ($0.30\varepsilon / k_B$). At $T = 0.47\varepsilon / k_B$, the growth rate of the diffusion-controlled model reaches its maximum.

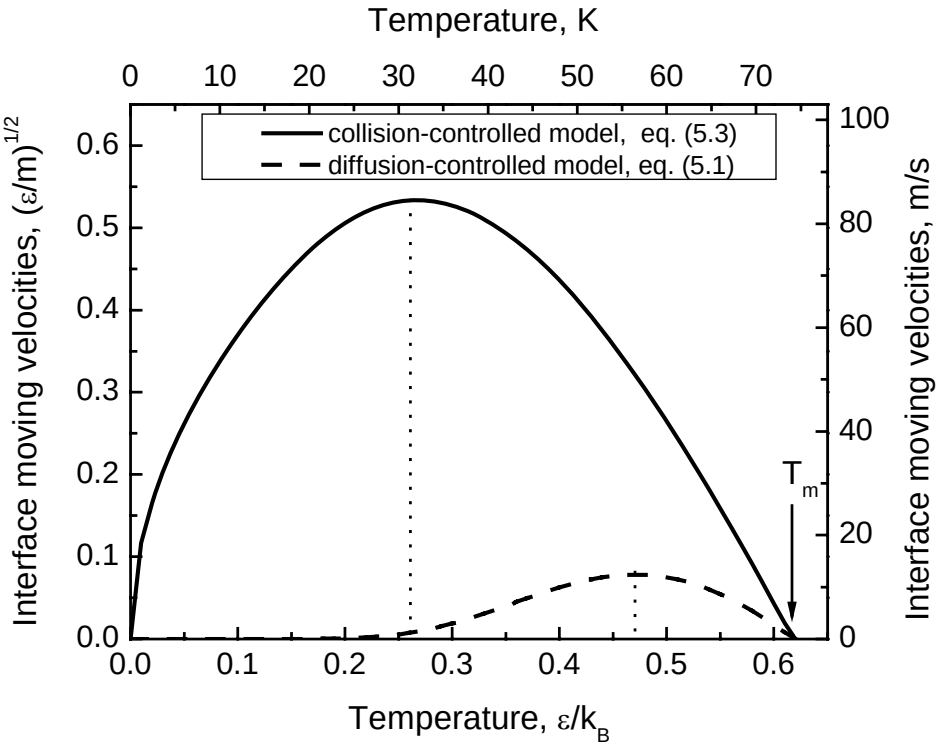

Figure 5.3. Comparison of the different crystallization rates between the diffusion-controlled [Eq. (5.1)] and collision-controlled [Eq. (5.3)] models. The units of the left and bottom axes are reduced LJ units, and those of the right and top axes are real units.

Broughton and co-workers [34,38] have calculated the interface moving velocities of (100) and (111) faces over a wide range of temperatures via molecular dynamics simulations. Their main conclusion is that the crystal growth of (100) face is a "collision-controlled" process [Eq. (5.3)], in which the energy barrier is absent; while that of (111) interface is a "diffusion-controlled" one [Eq. (5.1)], in which more time is needed for atoms to compete for the appropriate fcc and hcp sites [38]. However, some important issues were not addressed in their work. First, as shown Figure 5.3, the obtained maximum moving velocity of (100) interface is about 80 m/sec, while that of (111) interface is about 15-25 m/sec. Generally, such large orientation-related difference is not expected for the same materials. Moreover, the calculated maximum velocities of both faces are much larger than the experimental values (about 5 m/sec for Si and Ge [44-50]). Second, although their results show that the growth rate of (111) interface is size-dependent, the underlying mechanism was not adequately discussed. The "diffusion-controlled" model can only fit well to the data of the larger system. No further tests were performed to investigate whether the grow rate of (100) interface is also size-dependent. Third, the system size was of 1,200 atoms in their simulation, which may be too small to get a good statistical average. Fourth, as shown Figure 5.3, the temperature at which the growth rate reaches the maximum is $0.25\,\varepsilon / k_B$ (or $\Delta T / T_m = 0.6$) for (100) face. Since a liquid is already in the glass state at a temperature 60% below the melting point, it is thus questionable that the moving velocity can still be as high as 80 m/sec at such low temperature.

5.2. Models and Method

5.2.1. Model Configurations

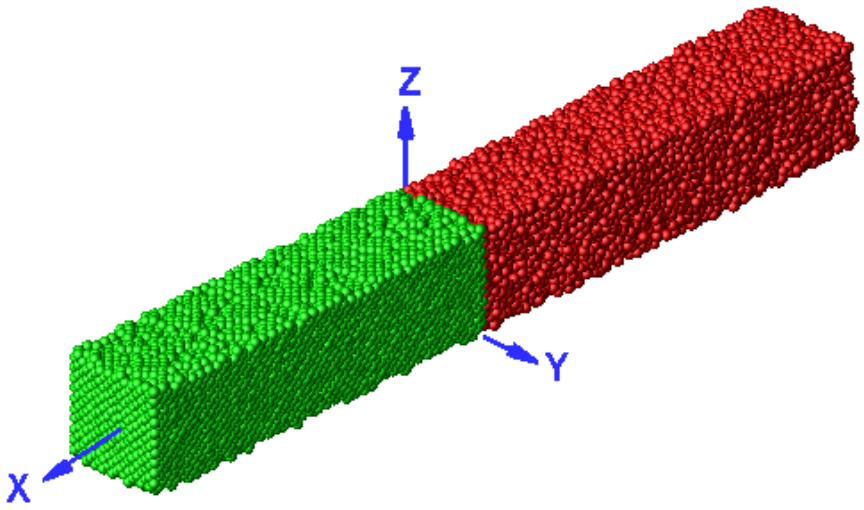

Figure 5.4. The 3D view of the rectangular flat-interface model. The green and red spheres represent crystal and liquid atoms respectively. The edge length in x direction is longest, while the lengths in y and z directions are same. The interface is at the middle of the x direction.

In this work, we have used a flat crystal-melt interface model to calculate the steady-state interface moving velocities of various crystallographic planes over a wide range of temperatures. The geometric shape of the simulation model is a rectangular box, as shown in Figure 5.4. The periodic boundary conditions (PBCs) were employed in all directions. The [100] and [111] orientations are set as the x direction for the (100) and (111) interfaces respectively. The interface is at the middle of the simulation box and perpendicular to the x direction. The crystal and liquid slabs are at each side of the interface. Since the periodic boundary conditions are used, actually there is another

interface at the bottom of the box in x direction. In order to avoid confusion, the interface induced by the periodic boundary conditions is not shown in Figure 5.4. The box length in the x direction, L_X, is longest and the crystal growth is along this direction. The lengths in the y and z directions are roughly same: $L_Y \approx L_Z$, i.e., $L_X > L_Y \approx L_Z$. For a system with a (100) interface, the x direction is [100], the y direction is [010], and the z direction is [001]. For a system with a (111) interface, the x direction is [111], the y direction is $[\bar{1}10]$, and the z direction is $[\bar{1}\,\bar{1}2]$.

Table 5.1: The total 16 different configurations of the simulation systems. The simulation box is rectangular. The x direction is [100] for (100) interface, and [111] for (111) interface. Note a_0 is the lattice constant of the fcc crystal.

(100) interface		(111) interface	
N	$L_X \times L_Y \times L_Z\,(a_0^3)$	N	$L_X \times L_Y \times L_Z\,(a_0^3)$
16,000	$40\times10\times10$	16,800	$25\sqrt{3}\times7\sqrt{2}\times4\sqrt{6}$
24,000	$60\times10\times10$	24,192	$36\sqrt{3}\times7\sqrt{2}\times4\sqrt{6}$
32,000	$80\times10\times10$	33,600	$50\sqrt{3}\times7\sqrt{2}\times4\sqrt{6}$
48,000	$120\times10\times10$	50,400	$75\sqrt{3}\times7\sqrt{2}\times4\sqrt{6}$
64,000	$160\times10\times10$	67,200	$100\sqrt{3}\times7\sqrt{2}\times4\sqrt{6}$
90,000	$100\times15\times15$	90,720	$60\sqrt{3}\times10.5\sqrt{2}\times6\sqrt{6}$
128,000	$80\times20\times20$	134,400	$50\sqrt{3}\times14\sqrt{2}\times8\sqrt{6}$
256,000	$160\times20\times20$	268,800	$100\sqrt{3}\times14\sqrt{2}\times8\sqrt{6}$

In order to check the finite size effects, eight configurations of different sizes were used for both (100) interface and (111) interface. Table 5.1 shows the total sixteen different configurations in this work. Here L_X, L_Y, and L_Z are in unit of the lattice constant a_0. Therefore there are total $L_X \times L_Y \times L_Z$ unit cells in each configuration. Since there are 4 atoms in an fcc unit cell, the total number of atoms in each configuration is $N = 4 \times L_X \times L_Y \times L_Z$. In this work, the number of atoms in the simulation box ranges from 16 000 to 256 000 for (100) interface and from 16 800 to 268 800 for (111) interface with half liquid and half solid.

5.2.2. Molecular Dynamics Simulations

Since the crystal growth is a non-equilibrium process and the system density and energy change continuously with time, we performed molecular dynamics simulations in a constant-number of atoms, constant-pressure, and constant-temperature (*NPT*) ensemble. The *NPT* MD can effectively adjust and control the system temperature, volume, and pressure at the desired conditions. For example, the latent heat can be dissipated and the volume shrinkage can be adjusted during crystallization. Note some researchers have performed their simulations with fixed volumes. This may cause some artifacts because the density change of the Lennard-Jones system is nontrivial during the crystallization. In order to compare our results with the other researchers' [34,38-42,129], we used a standard Lennard-Jones model system, $\phi(r) = 4\varepsilon[(\frac{\sigma}{r})^{12} - (\frac{\sigma}{r})^{6}]$, where parameter σ = 3.405Å, and ε / k_B = 119.8*K*. The cutoff distance is 2.5σ. The pressure was kept at zero throughout the simulation. The MD time step was set to 5 *fs*.

We used a similar technique as described in Chapter 3 to create the flat solid-liquid interface. Here I only introduce it briefly. Initially, all atoms were arranged in an fcc lattice. The potential depth of the atoms at the left-hand side of Figure 5.4 (green spheres) was 2ε, while that of the right-hand side atoms (red spheres) was 1ε. Therefore the melting temperature of the left-hand side slab is higher than that of the right-hand side slab. The system was heated from a low temperature to a high temperature until the slab at the right-hand side became a liquid. At the same time, the slab at the left-hand side was still a crystal. Then the system temperature was cooled down to a desired temperature T ($< T_m$). At this temperature, the potential depth of atoms at the left-hand side was changed gradually from 2ε to 1ε. Finally, the interface was created and the potential depth of all atoms in the two-phase system was 1ε. After the interface is created, the subsequent crystallization drives the interface to move from the solid side to the liquid side at T ($< T_m$). As a result, the three box lengths change with the simulation time. Figure 5.5 shows the changes of box lengths with simulation time in three directions during crystallization. Note the starting point of the time is after the interface is created. The box length in x direction, which is the interface moving direction, decreases almost linearly with the time. This linear decrease indicates the crystal growth is in steady state. On the other hand, the box lengths in y and z directions do not change much with the time. Therefore, the crystallization is a one-dimensional growth and the interface moving velocity in x direction represents the crystal growth rate.

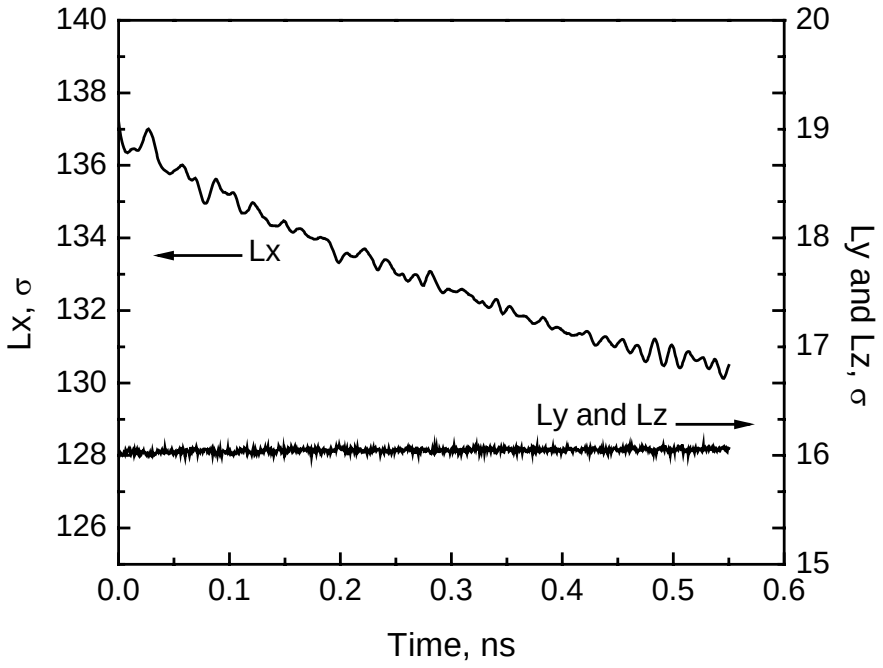

Figure 5.5. The evolution of three box lengths with simulation time in a system of 32 000 atoms and with a (100) interface. The left y-axis is for L_X and the right y-axis is for L_Y and L_Z.

5.2.3. Measuring Interface Moving Velocities via Energy Profiles

At the equilibrium (or thermodynamic) melting temperature $T_m = 0.618\,\varepsilon / k_B$, the interface stays stationary at zero external pressure. If $T<T_m$, the system is in a non-equilibrium state and the driving force makes the interface move in its normal direction. The interface moving velocities were calculated by using the following steps.

Step 1: The simulation sample is divided into N thin slices along the x (either [100] or [111]) direction. An example of the sliced sample is shown in Figure 5.6.

Typically, the thickness of each slice, d (= N/L_X), is of 2~3 atomic layers. Depending the system size, each slice contains a few hundred to a few thousand atoms.

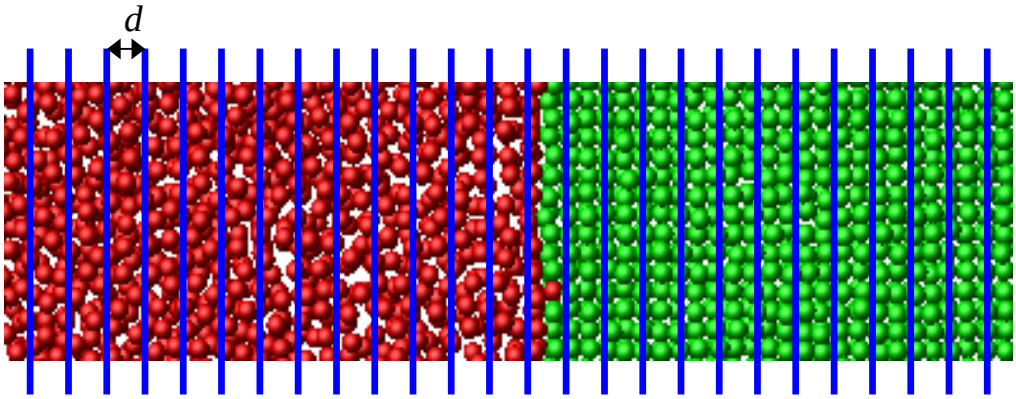

Figure 5.6. A sample is sliced evenly into N thin slices along the crystal growth (horizontal) direction. The thickness of each slice is d.

Step 2: After the sample is sliced, we calculate the average enthalpy per atom of each slice. The enthalpy is the sum of the potential energy and the kinetic energy at zero external pressure. Since the enthalpy difference between a bulk liquid and a bulk solid is quite distinct [61], we can use it as a criterion to discriminate the slice as either solidlike or liquidlike. Some researchers have used some order parameters such as the number of the first nearest neighbors as the criterion. However, as shown later in this chapter, the newly formed crystal contains a lot of defects that are different from a perfect crystal. Therefore, the accuracy of using the order parameters might be questionable. In our method, the enthalpy of each slice is averaged over several hundred to several thousand atoms within the slice. Therefore the statistical errors for specifying the state of each slice should be small. After the enthalpy of each slice is calculated, we can get an enthalpy

profile along the x direction. Figure 5.7 shows three snapshots and the corresponding enthalpy profiles in a system of 32 000 atoms and with a flat (100) interface. The system temperature is at $T = 0.51\ \varepsilon / k_B$. The snapshot in Figure 5.7(a) shows the initial interface positions when the two interfaces are created. Note the interface at the boundary of the box is created by the periodic boundary conditions. The arrow line indicates the length of the liquid. After 20 000 MD steps (0.1 ns), the length of the liquid decreases, as shown in Figure 5.7(b). After another 20 000 MD steps, the length of the liquid decreases further, as shown in Figure 5.7(c). The corresponding enthalpy profiles are shown in Figure 5.7(d). From the enthalpy profiles, one also can find that the liquid length decreases with the increasing time. One may find that the enthalpy profiles are not flat at the solid and liquid regions. Moreover, the enthalpy profiles are raised about 5% at the interface regions, as indicated by the circle in Figure 5.7(d). This is due to the released latent heat during the crystallization process. Since the crystal growth takes place at the interface, the generated latent heat increases the enthalpy of the interface region. Note Broughton *et al.* [34] found a similar effect in their simulations.

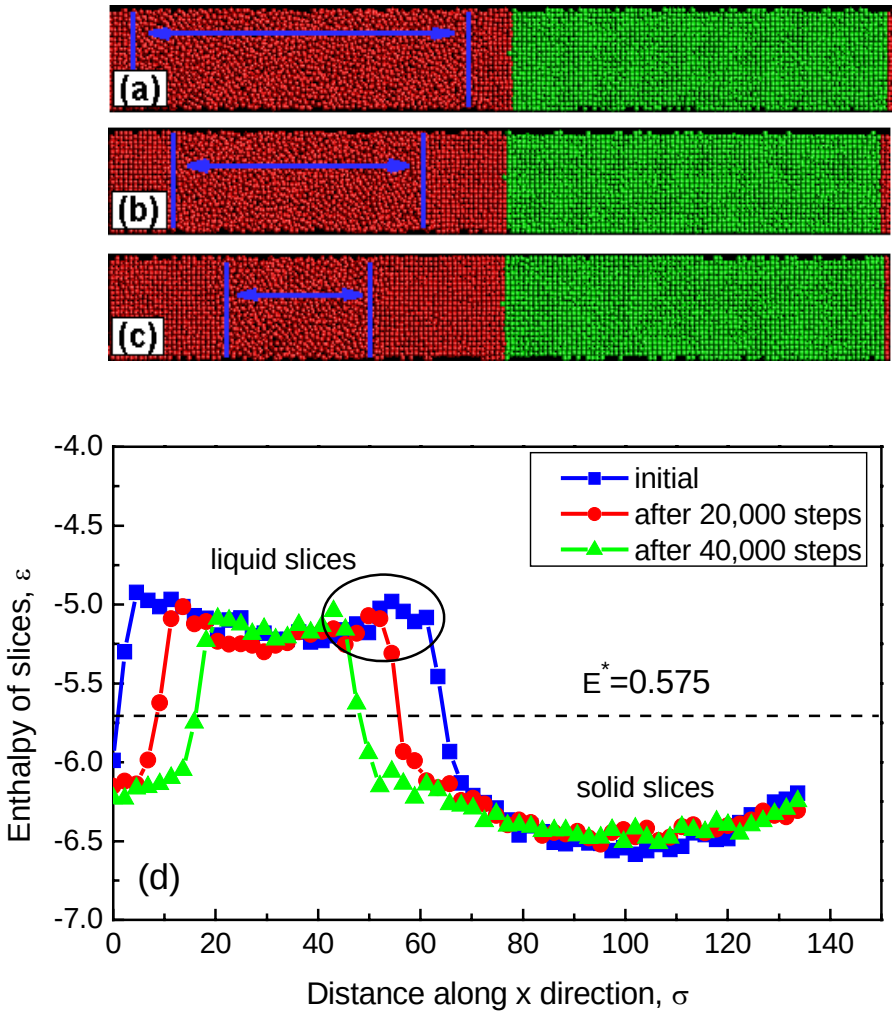

Figure 5.7. Three snapshots at different time and the corresponding enthalpy profiles at $T = 0.51\,\varepsilon/k_B$. The system has 32 000 atoms and two (100) interfaces. (a) The snapshot of the initial configuration. (b) After 20 000 MD steps. (c) After 40 000 MD steps. (d) The corresponding enthalpy profiles for (a), (b), and (c). The constant E^* is the critical enthalpy for discriminating the solid and liquid slices.

Step 3: From the enthalpy profile, one can count the number of liquidlike slices, N_L. In order to discriminate the solid and liquid slices, one should define a critical enthalpy E^*. A reasonable choice is the middle between the bulk solid and liquid enthalpies. For example, in Figure 5.7(d), the enthalpy of the bulk solid is $-6.5\,\varepsilon$ and that

of the bulk liquid is -5.2ε at $T = 0.51\,\varepsilon / k_B$. The middle value is -5.85ε. However, the newly formed crystal at the interface has a lot of defects that increase the enthalpy. In addition, the generate latent heat at the interface also increases the enthalpy. Therefore, a practical choice of the critical enthalpy is slightly higher than the middle value. For example, the critical enthalpy is -5.75ε at $T = 0.51\,\varepsilon / k_B$, as indicated in Figure 5.7(d). Note the critical enthalpy is temperature dependent. Different critical enthalpies should be carefully chosen at different temperatures. After the number of liquidlike slices is obtained, the total length of the liquidlike slices, which is the number of the liquidlike slices times the slice thickness (= $N_L \times$ d), can be calculated. Starting from initial time at which the interface is created, we calculated the total length of liquid-like slices after each 10 000 MD steps (0.05 ns). Note the sample should be re-sliced after each interval because the number of atoms in each slice changes with time. Figure 5.8 shows the linear correlation between the total length of the liquid and the simulation time during the crystallization process. In order to compare the interface moving velocities at different temperatures, Figure 5.8 shows the results of three temperatures, T = 0.27, 0.41, and $0.57\,\varepsilon / k_B$. Each linear decrease of the total liquid length with the simulation time implies that the crystallization is in steady state at the respective temperatures. Therefore, the slope of each linear fit gives the interface moving velocity at the corresponding temperature. Since there are two equivalent interfaces in the system due to the periodic boundary conditions, essentially the interface moving velocity is one half of the slope. The fittings yield [in reduced LJ unit $(\varepsilon / m)^{1/2}$]: $v_{0.27}$=0.125, $v_{0.41}$=0.20, and $v_{0.57}$=0.075. Clearly, the interface moving velocities at three temperatures have the relation

$v_{0.57} < v_{0.27} < v_{0.41}$, indicating that at both high (T = 0.57) and low (T = 0.27) temperatures, the crystallization rate is slow.

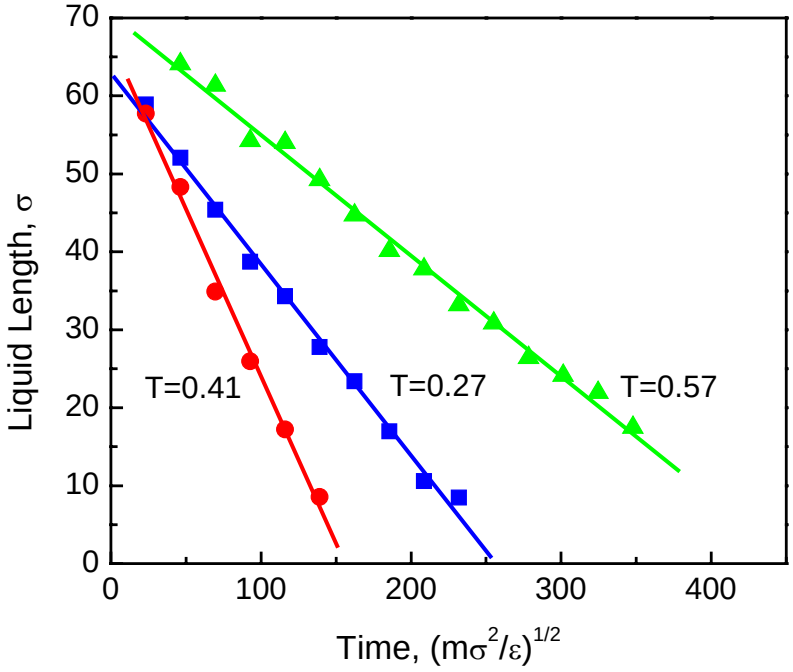

Figure 5.8. The linear decrease of the liquid length with the time at different temperatures. The system consists of 32 000 atoms and two crystal-melt interfaces normal to the [100] direction. The slope of each linear fit (divided by 2) is the steady-state interface moving velocity at the corresponding temperature.

5.3. Results

5.3.1. Crystal-melt Interface Structures of (100) and (111)

In many theoretical models, the crystal-melt interface is assumed to be atomically smooth. In this case the interface has infinitesimal thickness. Such a flat or sharp interface is called Gibbs dividing interface at which the total excess free energy is

located. However, in reality, the interface is usually atomic rough and the transition from liquid to solid usually takes place over a few atomic layers. This type of interface is called diffuse interface. Figure 5.9 illustrates the differences between the two types of interface.

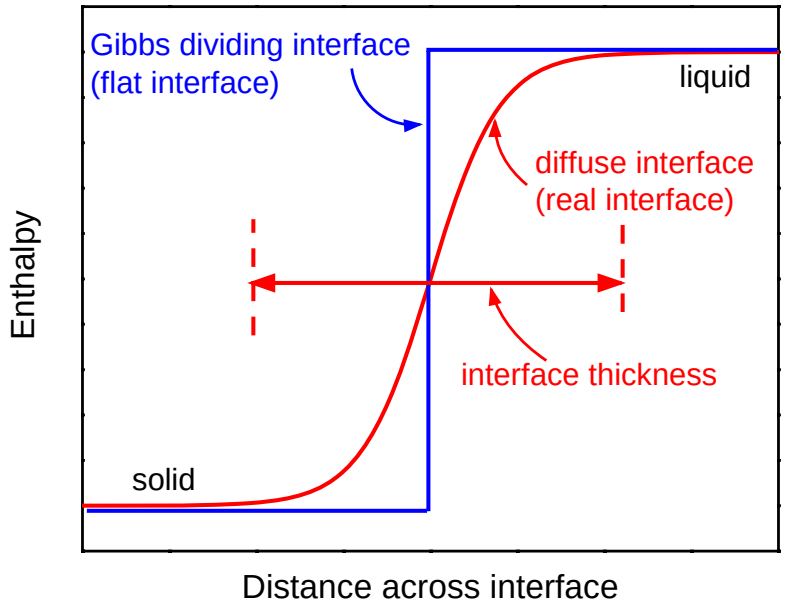

Figure 5.9. Illustration of Gibbs dividing (sharp) interface and diffuse (real) interface.

The diffuse interface is a transitional region at which the translational (long-range) symmetry of the crystal gradually vanishes. It is important to understand the details of the complex interface structure, because the interface plays an important role in providing the nucleation sites for crystallization. First, we use the density profile to investigate the interface thickness. Figure 5.10 shows a density profile of a system with two (100) interfaces at $T = 0.41\ \varepsilon / k_B$.

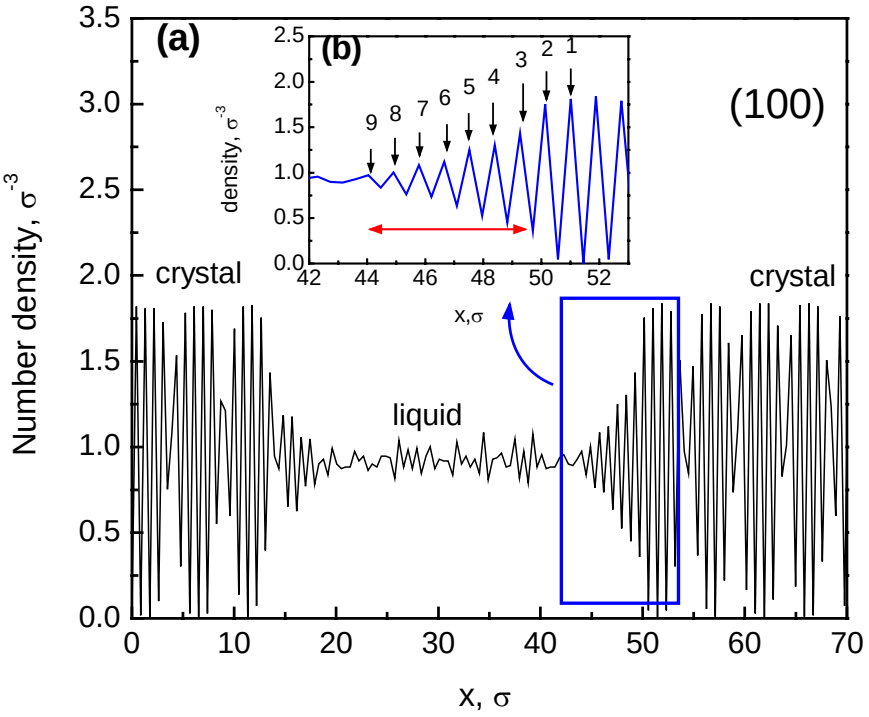

Figure 5.10. The density profile along the [100] direction. (a) The overall density profile of the sample with two crystal-melt interfaces. (b) The detailed density profile of the region surrounded by the rectangle in (a). The numbers indicate the atomic layers. The transition (interface) region is from layer 3 to layer 9.

In Figure 5.10(a), an overall density profile along the crystal growth direction is shown. The liquid is at the middle and is bounded by two crystal slabs. Therefore, there are two crystal-melt interfaces. Since the crystal atoms are ordered into many discrete atomic layers, the crystal density has large oscillations. On the other hand, the liquid atoms are disordered and the density has small variations. In order to investigate the detailed structure of the interface, we enlarge the density profile across the interface [the region bounded by the rectangle in Figure 5.10(a)] and show it in Figure 5.10(b). The oscillation peaks represent the locations of the corresponding atomic layers. The layer1

and layer 2 are crystal layers because their oscillation heights are at the same level as those of the crystal layers at the right-hand side. However, the oscillation height continuously decreases from layer 3 and finally approaches the liquid density at layer 9. The decrease of the oscillation height indicates that the crystallinity gradually disappears at the interface region. Clearly, the interface region is from layer 3 to layer 9. The interface thickness measured from Figure 5.10(b) is about $5.0\sigma \approx 1.7$ nm, which includes about 6-7 atomic layers at the (100) interface.

Since the transition from the crystal to the liquid takes place over a few atomic layers, we expect that the atomic structure of each interface layer should be partially ordered and partially disordered. In order to directly visualize how the interface structure changes, we draw the snapshots of the nine interface layers, as shown in Figure 5.11. Each snapshot [except (a)] is a two-dimensional (2-D) projection of the corresponding interface layer(s) parallel to the (100) interface. Figure 5.11 (a) shows the side view of the nine atomic layers across the (100) interface. The side view can give us a rough estimation of the interface ordering. For example, it seems that layer 1, 2, and 3 are well ordered; layer 4, 5, and 6 are partially ordered and contain some defects; layer 7, 8, and 9 are disordered. The detailed structures of the nine layers are shown as 2-D projections in Figure 5.11(b)-(i). Here we describe the structure in each atomic layer as follows:

Layer 1 and 2 [Figure 5.11(b)]: They are shown in the same 2D projection. Clearly, the two layers are well ordered. For (100) face, every other layer is directly on the top of the present layer. For example, the projection of layer 3 should be as same as layer 1, and the projection of layer 4 should be as same as layer 2. Therefore, we can use layer 1 or 2, which are well ordered, as a reference layer for the subsequent layers. In the

subsequent projections, the circles represent the atoms in the present layer and the blue crosses represent the atoms in the reference layer.

Layer 3 [Figure 3.11(c)]: The layer 1 (blue crosses) is shown as the reference layer for layer 3 (red circles). One can find that most atoms in layer 3 are directly on the top of the atoms in layer 1, indicating that layer 3 is also well ordered. However, layer 3 has some defects such as vacancies.

Layer 4 [Figure 3.11(d)]: Most atoms are well ordered, but a few atoms deviate from the positions at which they should be. Moreover, layer 4 also contains some vacancies.

Layer 5 [Figure 3.11(e)]: Most of the atoms are ordered, but some atoms are disordered at the right-hand side.

Layer 6 [Figure 3.11(f)]: About fifty percent of atoms deviate from the correct sites. In addition, the atoms are loosely packed and a lot of vacancies are shown. However, in the diagonal (<110> or close-packed) directions, the atoms are still well ordered.

Layer 7 [Figure 3.11(g)]: The atoms are disordered. But some ordering along the close-packed (diagonal) directions still can be founded, indicating that the ordering in the close-packed directions may be the precursor for the crystal growth.

Layer 8 [Figure 3.11(g)]: The atoms are almost completely disordered. But small amount of ordering still can be founded.

Layer 9 [Figure 3.11(i)]: The atoms are completely disordered.

From the projections of the nine layers, one can find that the interface region starts from layer 3 to layer 9, which is consistent with the density profile of the (100) interface [Figure 5.10].

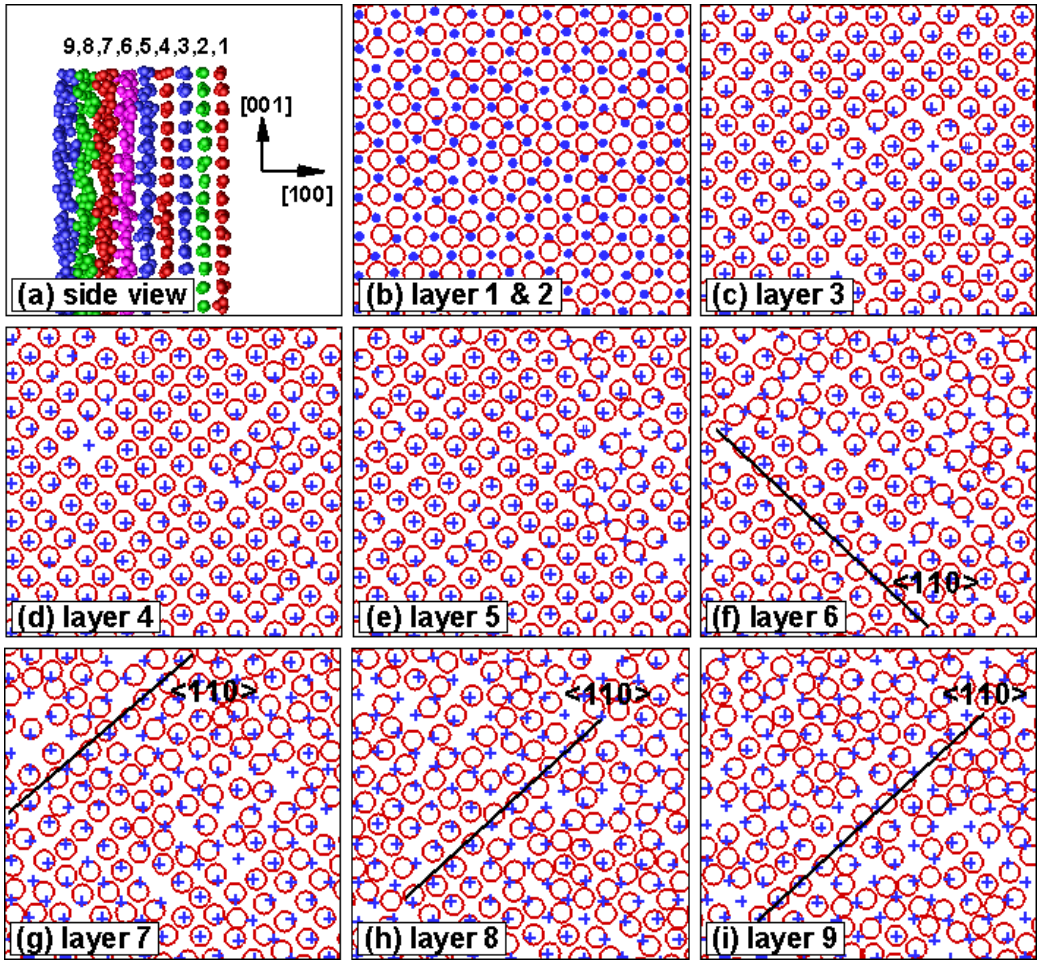

Figure 5.11. The 2-D projections of nine atomic layers at the (100) interface. (a) The side view of nine layers. (b) The projection of layer 1 (red circles) and layer 2 (blue dots). Layer 1 and layer 2 are alternatively shown in (c)-(i) as reference layers. (c)-(i): The projections of layer 3 to layer 9. Red circles represent the atoms of the present layer. The blue crosses represent the atoms of layer 1 in (c), (e), (g), and (i), and of layer 2 in (d), (f), and (h).

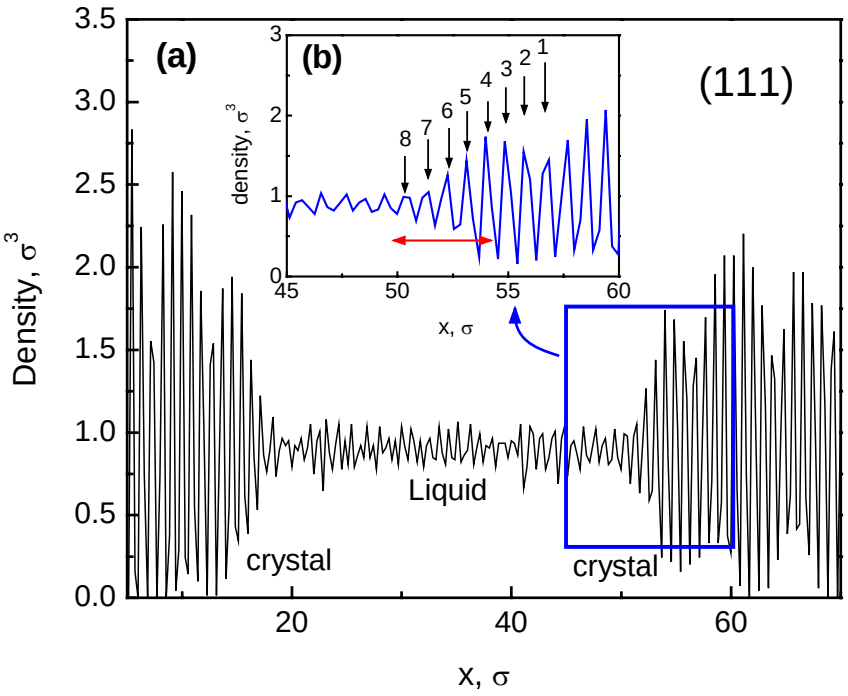

Figure 5.12. The density profile along the [111] direction. (a) The overall density profile of the sample with two crystal-melt interfaces. (b) The enlarged density profile of the interface region. The numbers in (b) indicate the corresponding atomic layers. The interface region is from layer 4 to layer 8.

Similarly, we can plot the density profile and the projections of the interface layers of the (111) interface. Figure 5.12(a) shows the overall interface profile along the direction normal to the (111) interface. The system consists of 33 600 atoms and two (111) interfaces. The system temperature is at $T = 0.41\,\varepsilon / k_B$. Similar to the (100) interface, the oscillation amplitudes of the density profile are large in the crystal region and small in the liquid region. The enlarged density profile at the interface region is shown in Figure 5.12(b). The density profile is a little bit rougher than that of the (100) interface. This is because the newly formed crystal from the (111) interface has a lot of

defects (we will show this later in this chapter). However, one still can find that the oscillation dampens gradually from layer 4 to layer 8, indicating that the (111) interface is across about 4~5 atomic layers. The direct measurement of the thickness gives 4.3 σ ($\approx$1.5 nm) for the (111) interface, which is a little bit thinner than the (100) interface ($\approx 5.0\sigma \approx$1.7 nm). Note the density profile in the liquid region still has some periodic or long-range oscillations and the frequency is close to that in the crystal region. However, this phenomenon is not found in the profile of the (100) interface [Figure 5.10]. This might indicate that perpendicular to the interface, atoms prefer to gather in the close-packed layers first; and parallel to the interface, atoms prefer to be ordered along the close-packed directions - <110> directions, which have been shown in Figure 5.11.

The snapshots or the 2D projections of the (111) interface layers are shown in Figure 5.13. Totally eight atomic layers across the (111) interface are shown. From the side view of those layers [Figure 5.13(a)], one can roughly estimate that layer 1 and 2 are well ordered; layer 3 and 4 are ordered but with slight disordering; layer 5 and 6 are disordered but some ordering is still present; layer 7 and 8 are totally disordered. The layer-by-layer descriptions of the detailed structures are given as follows:

Layer 1 [Figure 5.13(b)]: Atoms are ordered within this layer. However, not all atoms are closely packed. In addition, some vacancies are present. The atoms bounded by the pink rectangle are closely packed. The atoms indicated by the short vertical lines are not close-packed. It seems that they form a simple square lattice.

Layer 2 [Figure 3.13(c)]: The structure of layer 2 is similar to that of layer 1 except more disordering and vacancies are present.

Layer 3 [Figure 3.13(d)]: The close-packed region is smaller. The simple square lattice is not well ordered either. More open spaces are shown. Overall, layer 3 is still somewhat ordered, but the ordered structure is very complex.

Layer 4 [Figure 3.13(e)]: The structure of layer 4 is similar to layer 3 but is more disordered.

Layer 5 [Figure 3.13(f)]: The atoms are nearly disordered. Long-range ordering is barely seen. However, some short-range ordering can be founded. For example, some local close-packed structures can be found, and some atoms tend to line up to form some close-packed lines. These kinds of ordering in the close-packed directions [<110> directions] may be the precursor of the crystallization within the layer.

Layer 6 [Figure 3.13(g)]: The structure is similar to that of layer 5 but with less ordered lines.

Layer 7 and layer 8 [Figure 3.13(g)-(i)]: The atoms are almost completely disordered. But some locally close-packed structure still can be founded. The free spaces are large.

From the projections of the eight layers, one can find that the interface region starts from layer 4 to layer 8, which is consistent with the density profile of the (111) interface [Figure 5.12].

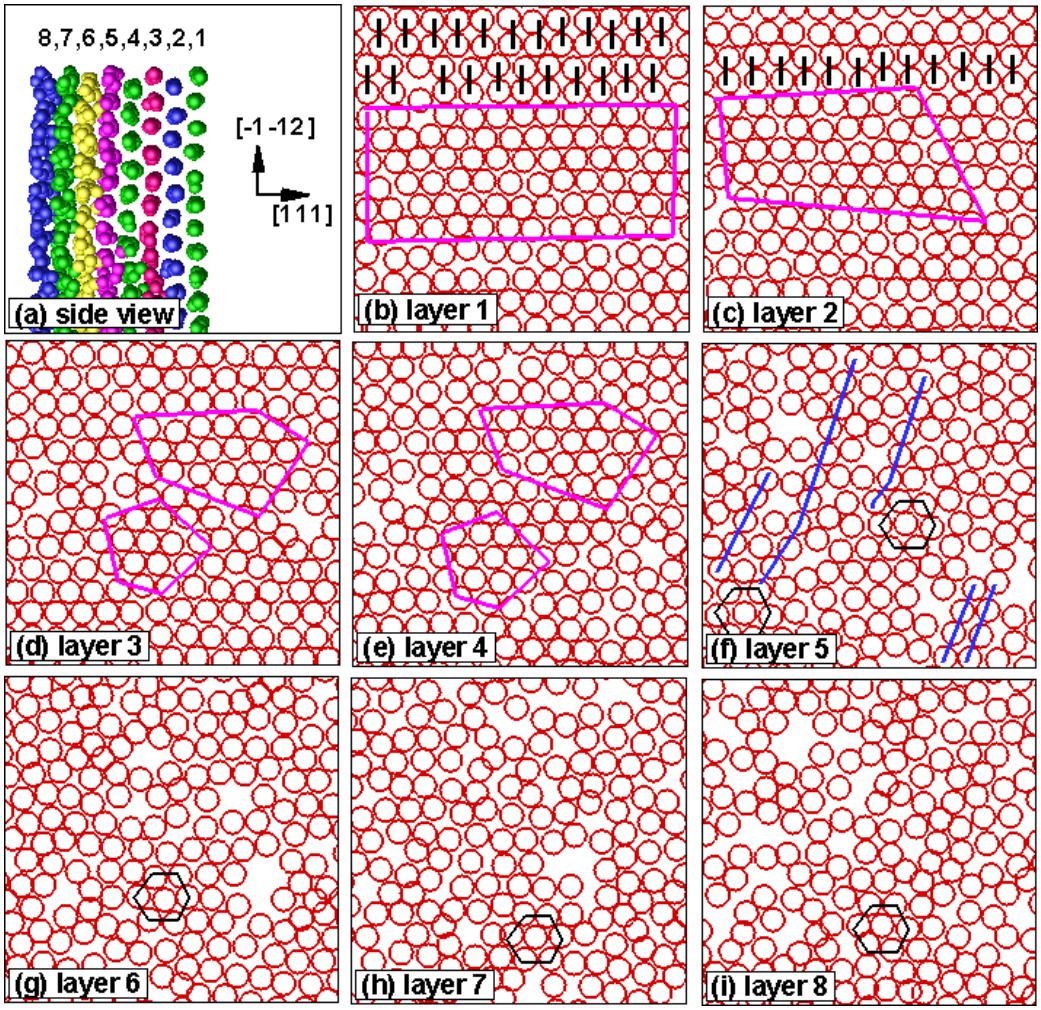

Figure 5.13. The 2-D snapshots of eight atomic layers at the (111) interface. (a) The side view of eight layers. (b)-(i) The projections of layer 1-8 (red circles). The close-packed regions are indicated by the pink polygons. Some other types of ordering are also indicated.

The above analysis of (100) and (111) interfaces shows that the crystal-melt interface is rough and spans about 1-2 nm across the interface. The thickness of the (111) interface is a little bit thinner than that of the (100) interface. The ordering is gradually vanishes from the solid side to the liquid side. A lot of defects present at the interface

layers, especially at the (111) interface. It seems that the partially ordered structures in the liquid present both perpendicular and parallel to the interface. The {111} planes and <110> directions may be energetically favorable as precursors for the ordering. Our results are consistent with many researchers' results, both in experiments and simulations. For example, Howe and Saka [51] have used *in situ* transmission electron microscopy (*in situ* TEM) to investigate the solid-liquid interface of a liquid Al-Si alloy on a Si{111}. They found that some partially ordered layers in the liquid and the interface is about 2 nm in thickness. From the TEM images of liquid xenon in small faceted cavities in aluminum, Donnelly *et al.* [132] have found that the structures of ordered liquid layers are different from the bulk xenon. van der Veen and Reichert [52] have used synchrotron x-ray scattering techniques to study the interface of a liquid Pb on a solid Si{001}. The found that the interface thickness is of about 1.5 nm. Gulam Razul *et al.* [129] have used MD simulations to investigate the interface structure of a LJ system. They found that the interface widths of 5.2 σ (1.77 nm), 5.0 σ (1.70 nm), 4.8 σ (1.63 nm) for (100), (110), and (111) interfaces, respectively, which are very close to our results. They also found that the (111) interface is sharper (narrower) than the (110) interface as we did. Huitema *et al.* [41] and Broughton *et al.* [128] have found that the distance between the density oscillations of (100) interface gradually changes from the (100) interplanar spacing to the (111) interplanar spacing in a LJ system via MD simulations. They concluded that the creating the planes with the interplanar spacing equal to d_{111} might be at the lowest energy cost, where d_{111} is the interplanar spacing of (111) planes. This conclusion may be cited as evidence to support our finding, in which

the close-packed directions, <110>, occur preferentially in the disordered liquid layers at the interface.

5.3.2. Crystal Growth Morphologies from (100) and (111) Interfaces

The morphology of a crystal growing from its undercooled melt is determined by many factors. For example, it is believed that the anisotropy in interfacial free energy is the key parameter for dendrite growth. The growth rate may also affect the growth morphology, because atoms or molecules have little time to relax if the growth rate is very fast. A good example is that the amorphous silicon is often founded during the pulsed laser annealing [44-50]. The crystal growth in different orientations may result in different morphologies. Here I present our investigations of the respective growth morphologies from (100) and (111) interfaces.

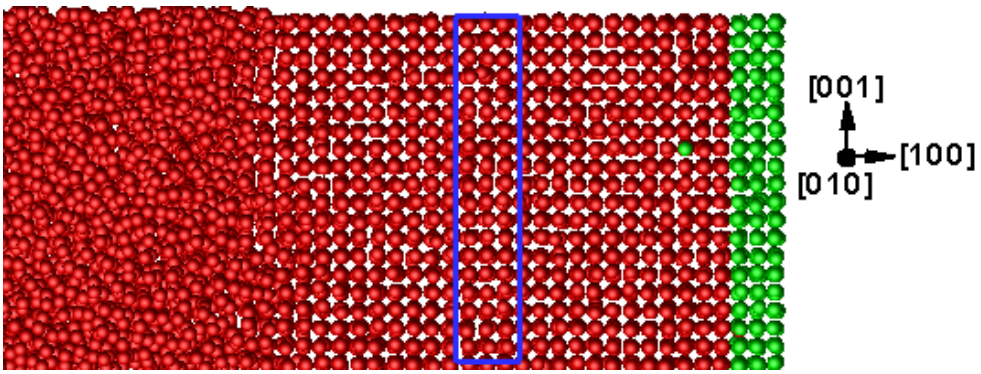

Figure 5.14. The side view of a crystal grown from a (100) interface. The red and green spheres represent the atoms originally in liquid state and solid state, respectively. A thin slice of 3-layer width [bounded by the blue rectangle] is picked from the newly formed crystal for detailed investigation in Figure 5.15.

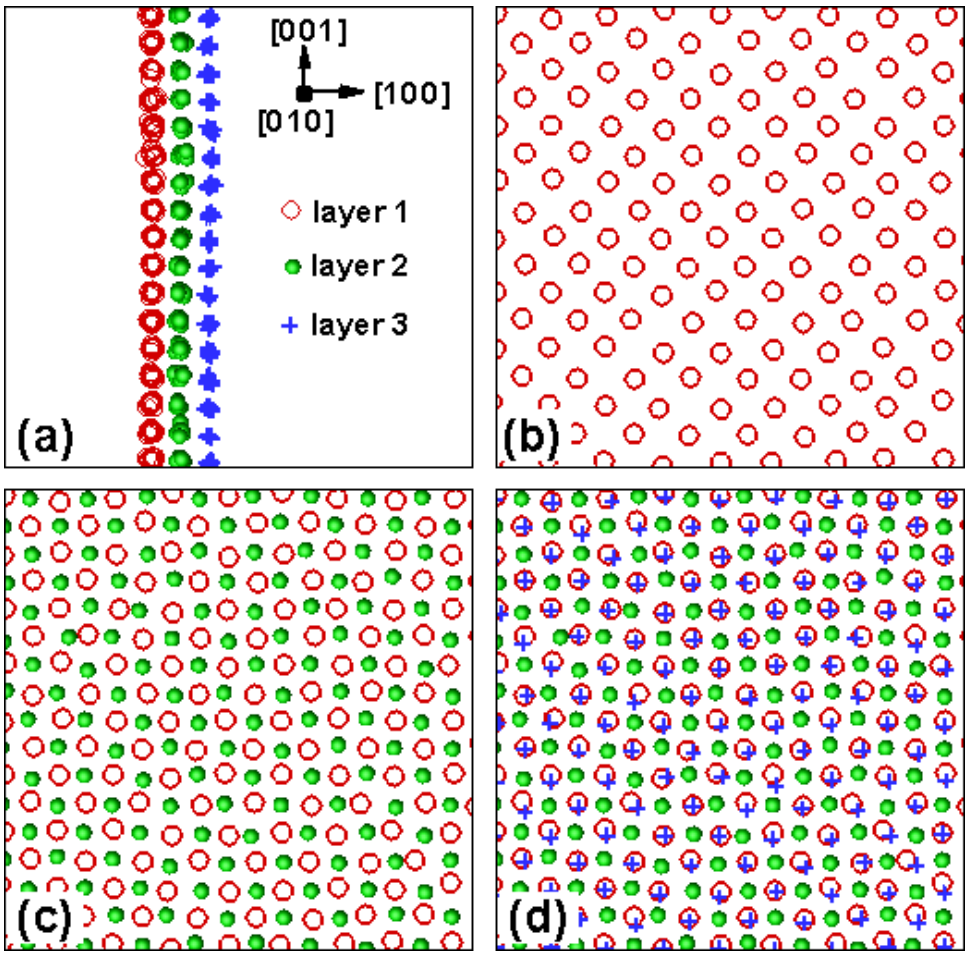

Figure 5.15. The detailed in-plane structure of the thin slice as indicated in Figure 5.14. (a) The side view of the 3-layer slice. (b) Projection of layer 1. (c) Projections of layer 1 and layer 2. (d) Projections of layer 1, layer 2, and layer 3. Red circles - Layer 1; Green spheres - layer 2; Blue crosses - layer 3.

Figure 5.14 shows a new crystal that grows from a (100) interface. The original interface is at the boundary between the green and red spheres. The current interface location is at the left hand-side. The crystallized region represented by red spheres is the

newly formed crystal. From the side view, one can see that the new crystal is well ordered and the atoms in the new crystal match well with the original crystal atoms (green spheres). In order to investigate the in-plane structures (parallel to the interface), a thin slice of 3-layer thickness [the rectangular region in Figure 5.14] is taken for investigation.

Figure 5.15 shows the detailed structure of this thin slice. The side view and the symbols of three layers are shown in Figure 5.15(a). The three layers are equally spaced along the [100] direction. The projection of layer 1 is shown in Figure 5.15(b). The [100] direction is normal to the projection. Clearly, the atoms in layer 1 [red circles] are well ordered although small variations can be seen. The atoms lie in a square array and the edge length of each square is $a_0/\sqrt{2}$, where a_0 is the lattice constant of the fcc crystal. The projection of layer 2 is shown in Figure 5.15(c). The atoms in layer 2 [green spheres] are also well ordered and they lie in the square interstices of the first layer. The interplanar distance between layer 1 and 2 is $a_0/2$. The projection of layer 3 is shown in Figure 5.15(d). Obviously, most atoms in layer 3 [blue crosses] are on the top of the atoms in layer 1 (but with a interplanar distance of a_0). Therefore, the new crystal grown from the (100) interface is well ordered and the defect concentration is low.

For (111) interface, we did a similar investigation. But this time we picked three thin slices from the newly formed crystal for detailed investigation. The locations of the three slices are shown in Figure 5.16. Similar to Figure 5.14, Figure 5.16 shows the side view of the new crystal (red spheres). The original crystal atoms (green spheres) are shown for the reference purpose. It seems that the new crystal is well ordered and evenly spaced. However, in the diagonal direction, the atoms in the original crystal (green

spheres) are linearly arranged, but those in the new crystal (red spheres) are not. Moreover, about 4-5 crystal layers at the left-hand side of the slice C are twisted and rotate to a new orientation. Therefore, the crystal growth from (111) interface is much rougher than from (100) interface.

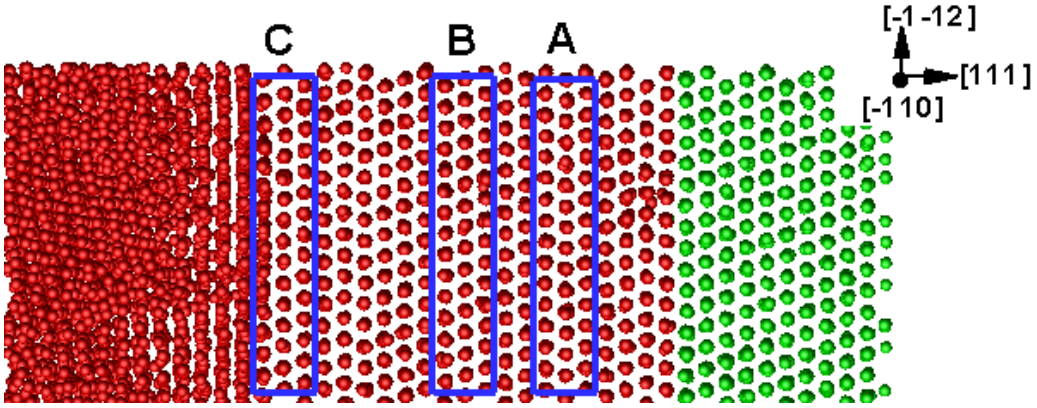

Figure 5.16. The side view of a crystal grown from a (111) interface. The red and green spheres represent the atoms originally in liquid state and solid state, respectively. Three crystal slices, A, B, and C, each of them is 3-layer wide, are picked from the newly formed crystal for detailed investigation in Figures 5.17-5.19.

The detailed in-plane structures of slices A, B, and C are shown in Figures 5.17-5.19. For ideal {111} planes in an fcc crystal, the stacking sequence is *abcabc*…. The atoms in the first layer (*a*-type) are close-packed, atoms in the second layer (*b*-type) lie in the alternate interstices of the first layer, and atoms in the third layer (*c*-type) go directly above the unoccupied interstices in the first layer. However, there is another possibility for the atoms in the third layer to go directly above the atom centers in the first layer. In such case, the third layer is identical to the first layer. Thus the stacking sequence

becomes *ababab*…, which forms an hcp structure. In Figures 5.17-5.19, the stacking sequence in each slice is investigated.

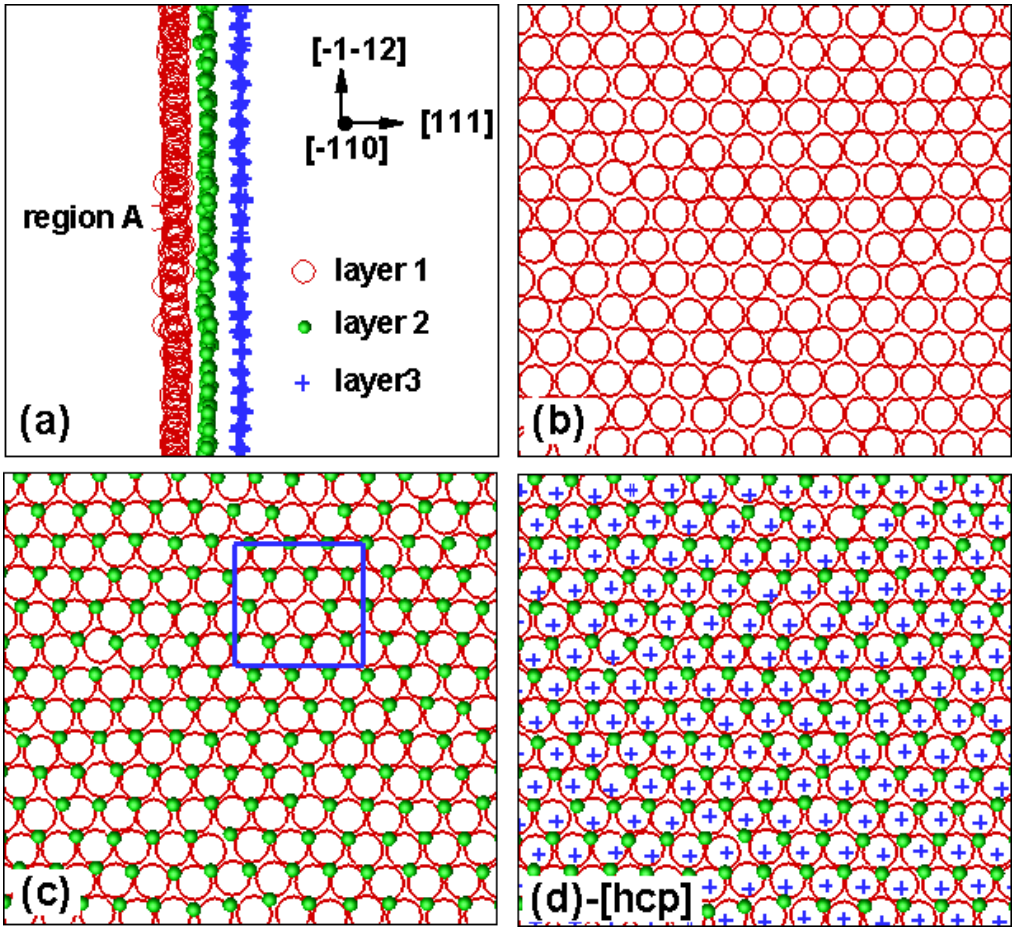

Figure 5.17. The detailed in-plane structure of slice A [in Figure 5.16]. (a) The side view of the 3-layer slice. (b) Projection of layer 1. (c) Projections of layer 1 and layer 2. A vacancy is indicated by the blue square. (d) Projections of layer 1, layer 2, and layer 3. The atoms in layer 3 are directly on the top of layer 1, indicating the structure of this slice is an **hcp** structure. Red circles - Layer 1; Green spheres - layer 2; Blue crosses - layer 3.

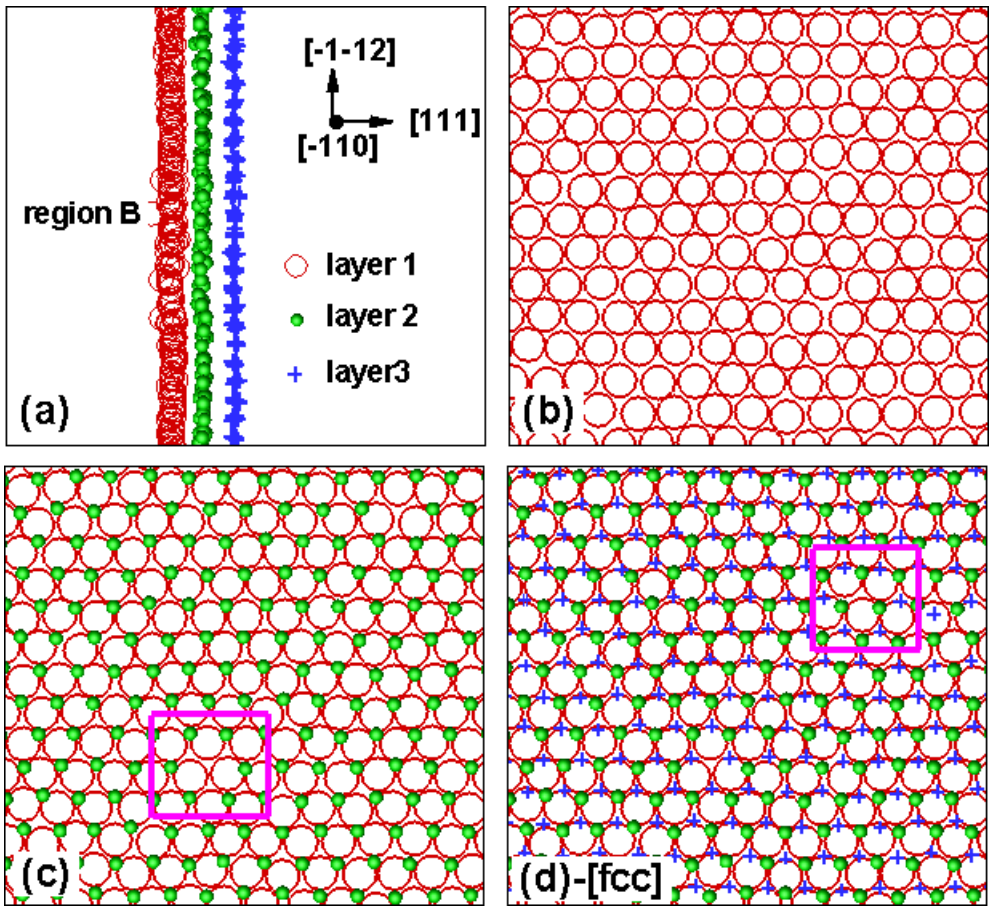

Figure 5.18. The detailed in-plane structure of slice B [in Figure 5.16]. (a) The side view of the slice. (b) Projection of layer 1. (c) Projections of layer 1 and layer 2. A vacancy is indicated by the pink square. (d) Projections of layer 1, layer 2, and layer 3. A vacancy is indicated by the pink square. The atoms in layers 2 and 3 lie alternatively in the interstices of layer 1, indicating the structure of this slice is an **fcc** structure. Red circles - Layer 1; Green spheres - layer 2; Blue crosses - layer 3.

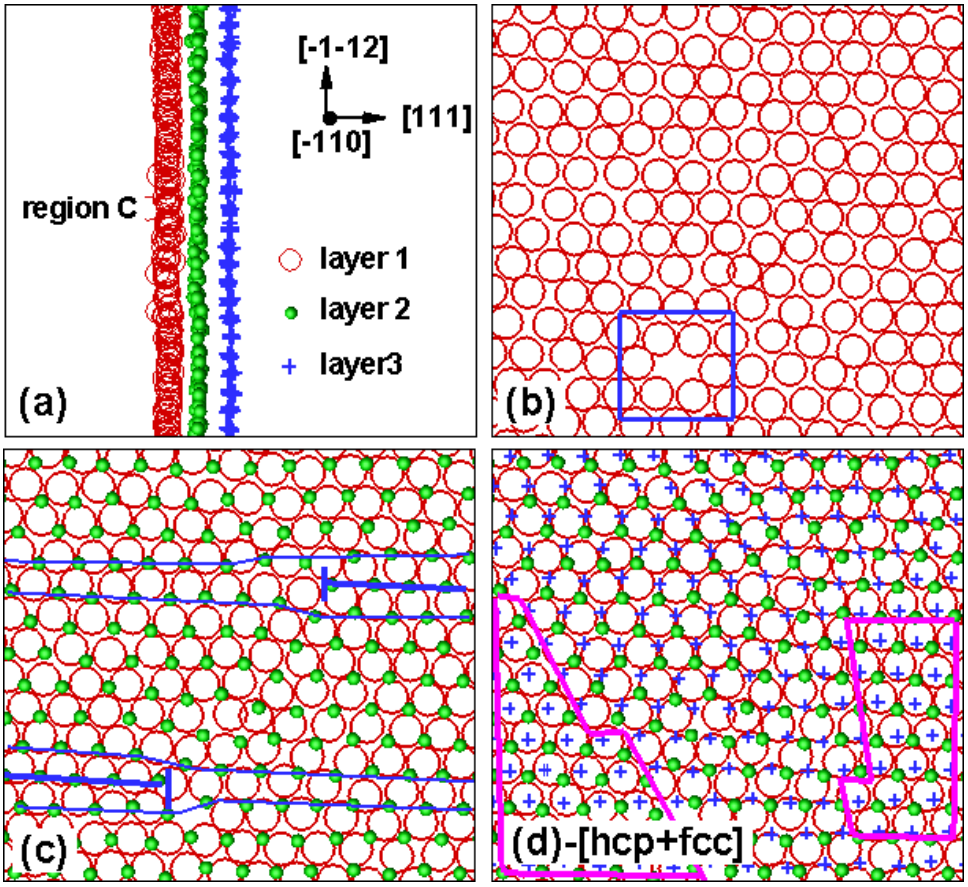

Figure 5.19. The detailed in-plane structure of slice C [in Figure 5.16]. (a) The side view of the 3-layer slice. (b) Projection of layer 1. A vacancy is indicated by the blue square. (c) Projections of layer 1 and layer 2. Two dislocations are indicated. (d) Projections of layer 1, layer 2, and layer 3. Some atoms in layer 3 lie in hcp sites (bounded by the pink polygons), and some atoms in layer 3 lie in fcc sites (unbounded region). The structure of this slice is a **hybrid (fcc+hcp)** structure. Red circles - Layer 1; Green spheres - layer 2; Blue crosses - layer 3.

Slice A: The detailed in-plane structure of slice A is shown in Figure 5.17. Figure 5.17(a) shows the side view and the symbols of the three layers. Figure 5.17(b) is the 2-D projection of layer 1 (red circles). The projection is parallel to the (111) interface. Clearly, the atoms in layer 1 are close-packed (in a hexagonal lattice) although small deviations can be seen. The projections of layer 1 and layer 2 (green spheres) is shown in Figure 5.17(c). Apparently, the atoms in layer 2 lie in the alternative interstices of the first layer. Most atoms in layer 2 are well close-packed. However, a vacancy can be seen as indicated by the blue square. The projection of layer 3 (blue crosses) is shown in Figure 5.17(d) together with the projections of layer 1 and layer 2. The most important feature is that layer 3 is directly on the top of layer 1 (blue crosses coincide with red circles). Thus, the stacking sequence of the three layers in slice A is *aba*, which is an **hcp** structure.

Slice B: The detailed in-plane structure of slice B is shown in Figure 5.18. The side view of the three-layer slice and their symbols are shown in Figure 5.18(a). The 2-D projection of layer 1 (red circles) is shown in Figure 5.18(b). The atoms in this layer are well ordered. However, slight distortions still can be seen. Figure 5.18(c) shows the projections of layer 1 and layer 2. The atoms in layer 2 (green spheres) lie in the alternate interstices of layer 1. A vacancy in this layer is indicated by the pink square. Figure 5.18(d) shows the projections of layer 1, layer 2, and layer 3. The atoms of layer 3 (blue crosses) lie in the unoccupied interstices of layer 1, which is different from Figure 5.17(d). Consequently, the stacking sequence of the three layers is *abc*, which is an **fcc** structure. Note a vacancy in this layer is indicated by the pink square.

Slice C: The detailed in-plane structure of slice C is shown in Figure 5.19. The side view of this slice and the layer symbols are shown in Figure 5.19(a). The projection of layer 1 (red circles) is shown in Figure 5.19(b). In this layer, atoms are ordered but with some defects. The alignments of atoms are not very straight. Some atoms have more free spaces. A vacancy appears as indicated by the blue square. The projections of layer 1 and layer 2 are shown in Figure 5.19(c). Although many atoms in layer 2 (green spheres) are on the alternate interstices of layer 1, some atoms are not on the interstitial sites of layer 1. The horizontal alignments of atoms are not straight. Some alignments shift to their neighboring alignments as indicated by the blue lines. As a result, some dislocations are formed. It seems that the structures of layer 2 and layer 1 are correlated. Most defects in layer 2 occur at the imperfect regions in layer 1. Figure 5.19(d) shows the combinded projections of layers 1, 2, and 3. Obviously, some atoms of layer 3 [blue crosses] lie in the unoccupied interstices of layer 1, and some atoms lie at the top of layer 1 (bounded by the pink polygons). The former stacking forms an fcc structure (unbounded region) and the later stacking forms an hcp structure [bounded region]. Therefore, the structure of this slice is a **hybrid (fcc+hcp)** structure.

The above analysis of the growth morphologies shows that the crystal growth from a {111} interface is much rougher than from a {100} face. In the later case, many defects such as stacking faults and vacancies manifest, whereas fewer defects are found in the former case. This is because the stacking sequence of {111} planes is not unique. The third layer can either lie in the unoccupied interstices of the first layer or on the top of the first layer. For a LJ system, the free energy difference between an atom in an hcp site and an atom in an fcc site is very small [38]. Thus, the atoms have no preference to

choose between the correct fcc sites and the incorrect hcp sites. In addition, atoms have no time to relax and anneal themselves when the growth rate is high. As a result, atoms would like to stay in the indiscriminating fcc/hcp sites once they find them. Therefore, the growth morphology from a (111) interface is very rough. In our work, the three slices from the same sample as shown in figure 5.16 show three different structures: hcp, fcc, and hybrid. Burke *et al.* [38] also found the growth morphology from a (111) interface is very rough. They claimed that the ratio of the correct sites to incorrect sites is about 50%. On the other hand, the crystal growth from a (100) interface is rather simple, because there is only one type of atomic sites. Therefore, the defect concentration is low.

The twist of the crystal is frequently founded in a crystal grown from a (111) interface. For example, the crystal layers at the left-hand side of the slice C in figure 5.16 grow in an orientation that is different from the orientation of the original crystal (green spheres). The hybrid structure (hcp+fcc) is found at this twisted region. Burke *et al.* [38] have argued that each (111) layer must completely anneal itself to either all fcc sites or all hcp sites in order to grow. However, our results show that some hybrid structures always appear in the crystal. The crystal can grow with the presence of defects. Thus, the validity of their argument is questionable. In addition, they have argued that this annealing process slows down the growth rate dramatically. As I will show later, the growth rate of the (111) interface is only slightly slower than that of the (100) interface.

5.3.3. Face-Dependent Crystal Growth Rates

The interface moving velocity is face-dependent. Many experiments and calculations show that the growth rate is anisotropic [38,45]. However, the microscopic

mechanisms for the discrepancy of the growth rate in different orientations are still under dispute. Using the method described in section 5.2, we have calculated the respective interface moving velocities of (100), (110), and (111) interfaces over a wide range of the undercooling temperatures, as shown in Figure 5.20.

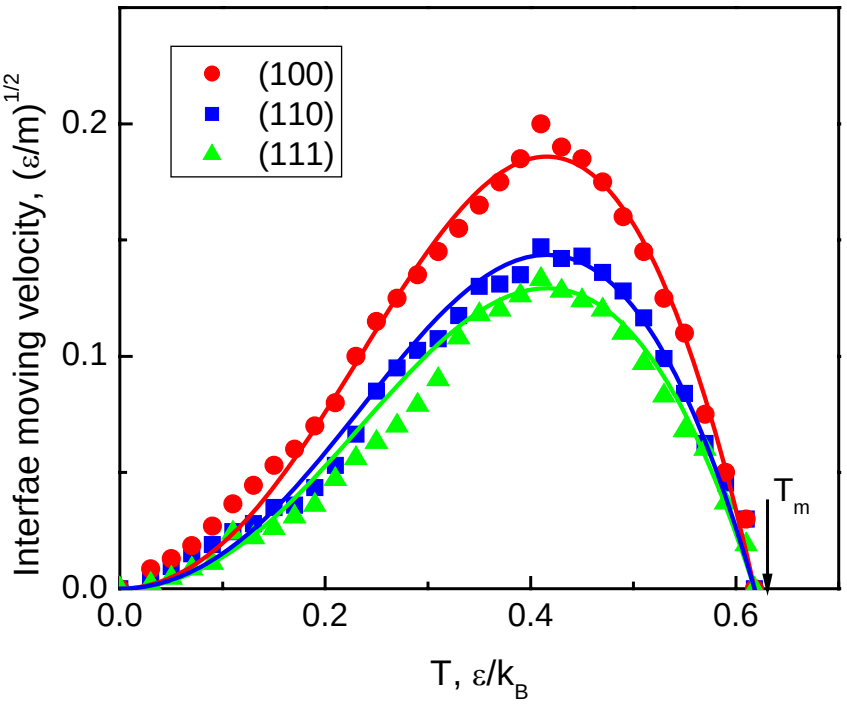

Figure 5.20. The temperature-dependent interface moving velocities of (100), (110), and (111) faces. The number of atoms is 32,000, 33,600, and 33,600 for the sample with a (100), (110), and (111) interface, respectively. Red filled circles – (100); Blue filled squares – (110); Green filled triangles – (111).

The number of atoms is 32,000, 33,600, and 33,600 in the sample with a (100), (110), and (111) interface respectively. Thus, they have roughly the same number of atoms. Clearly, the interface moving velocity is anisotropic: $v_{100} > v_{110} > v_{111}$. The

anisotropy in the crystallization rate has also been founded by Broughton *et al.* [38], Huitema *et al.* [41], and Gulam Razul *et al.* [42], although their calculations were mainly performed at shallow undercooling. Their results also show that the relation among the face-dependent crystallization rates is $v_{100} > v_{110} > v_{111}$.

Generally there are two prevailing theories for explaining the microscopic mechanism of the anisotropy. Broughton *et al.* [34,38] argued that atoms in the (111) interface need to compete for the nearly identical fcc and hcp sites. For the crystal growth from a (111) layer, the atoms must completely anneal themselves to lie in either all fcc sites or all hcp sties. The annealing process can be achieved through the cooperative motion of atoms. The energy barrier associated with the cooperative motion must be overcome during the annealing process. Therefore, they claimed that the annealing process slows the growth rate of the (111) interface. On the other hand, there is only one type of correct sites for atoms at the (100) interface. Thus the crystal growth of the (100) interface is a barrier-free process that does not involve the site-competing mechanism. In section 5.3.2, we have studied the growth morphologies of (100) and (111) interfaces. The hybrid (hcp+fcc) structure is found in the new crystal that grows from a (111) interface. In section 5.3.1, we have found that the interface structure of the (111) interface is very rough and the interface layers contain a lot of defects. Thus, the (111) interface can still move even if the stacking faults are not completely annealed. Moreover, if Broughton *et al.*'s argument [38] is true, the moving velocity of the (111) interface should be very slow at low temperatures and approach zero at $T_m/2$, while that of the (100) interface should be very fast over a wide range of temperatures. However, in Figure 5.20, one can find that the growth rates of both (100) and (111) interfaces behave

similarly. In addition, the growth rates are non-trivial at low temperatures. Therefore, Broughton *et al.*'s argument [38] is questionable.

Huitema *et al.* [41] and Gulam Razul *et al.* [42] argued that the atom hopping from a less dense layer further away from the interface to a denser one closer to the interface takes place for (110) and (111) interfaces, whereas atom hopping is rarely found for (100) interface; the number of atoms that have to change their layers is 3% for the (100) interface and 10% for the (110) and (111) interfaces. In other words, some atoms have to move via the long-range diffusion during the crystallization process for (110) and (111) interfaces, while such long-range diffusion is not required for the (100) interface. Thus, the hopping barrier reduces the growth rate significantly for (110) and (111) interfaces. In order to verify this argument, we have performed the following simulations.

In the liquid region, we selected a thin liquid slice. The thin liquid slice is parallel to the interface [either (100) or (111)]. The thickness of this slice is about 1 nm (about 3 atomic layers if it is in crystal state). The initial location of the thin layer is shown in Figure 5.21(a) for the sample with a (100) interface and in Figure 5.22(a) for the sample with a (111) interface, respectively. Then the two samples were brought to three different temperatures: a low temperature of $0.27\,\varepsilon / k_B$, a moderate temperature of $0.41\,\varepsilon / k_B$, and a high temperature of $0.55\,\varepsilon / k_B$. During the subsequent crystallization process, the atoms enclosed in the original thin liquid slice were traced. After the thin liquid slice is crystallized, we located the final positions of these atoms and investigated the travel distances from their original positions. Figure 5.21 and Figure 5.22 show the snapshots of these atoms at different temperatures. In order to get a good visualization, the atoms in the liquid slice are represented by big pink spheres.

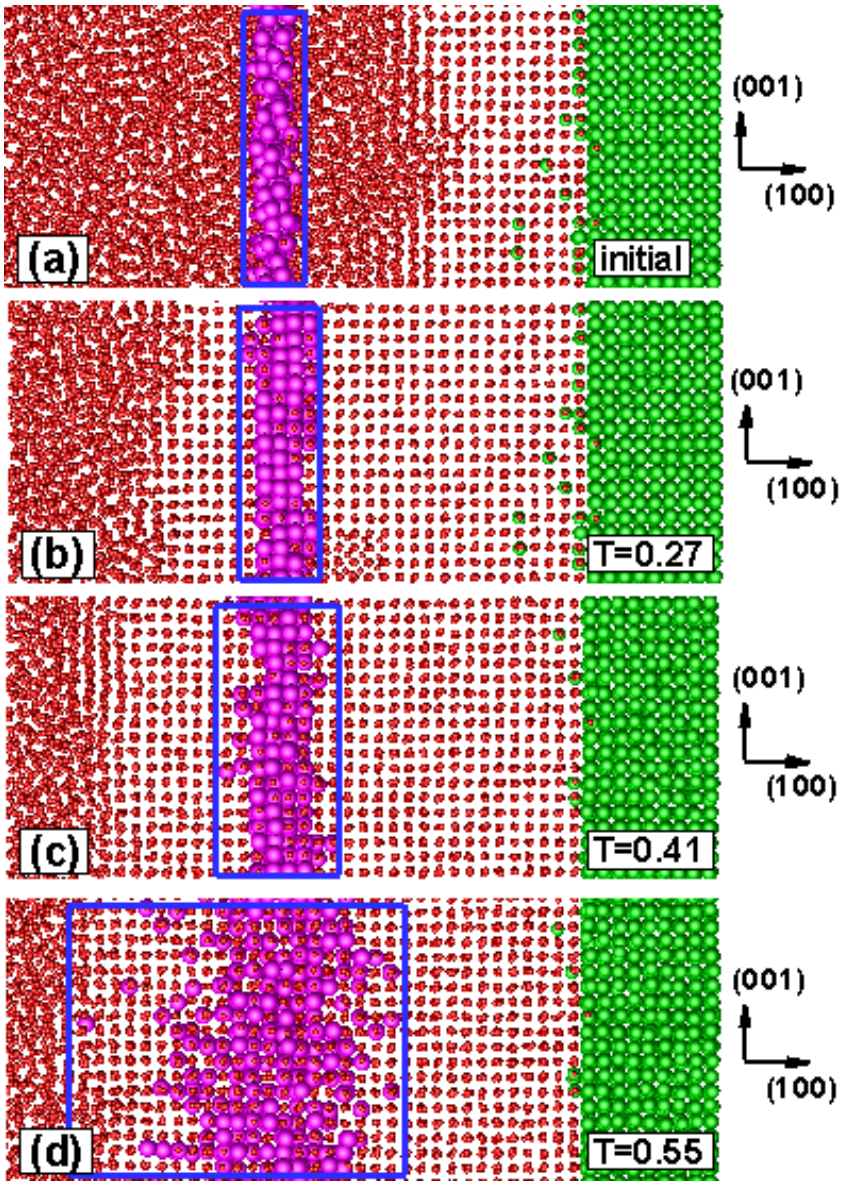

Figure 5.21. The snapshots of atoms in a thin liquid slice [bounded by a blue rectangle] at different temperatures during the crystallization. The sample contains a (100) interface. (a) The original liquid slice. (b) At T=0.27. (c) At T=0.41. (d) At T=0.55. Big pink spheres – atoms in the liquid slice; Small red spheres – original liquid atoms; Medium green spheres – original crystal atoms.

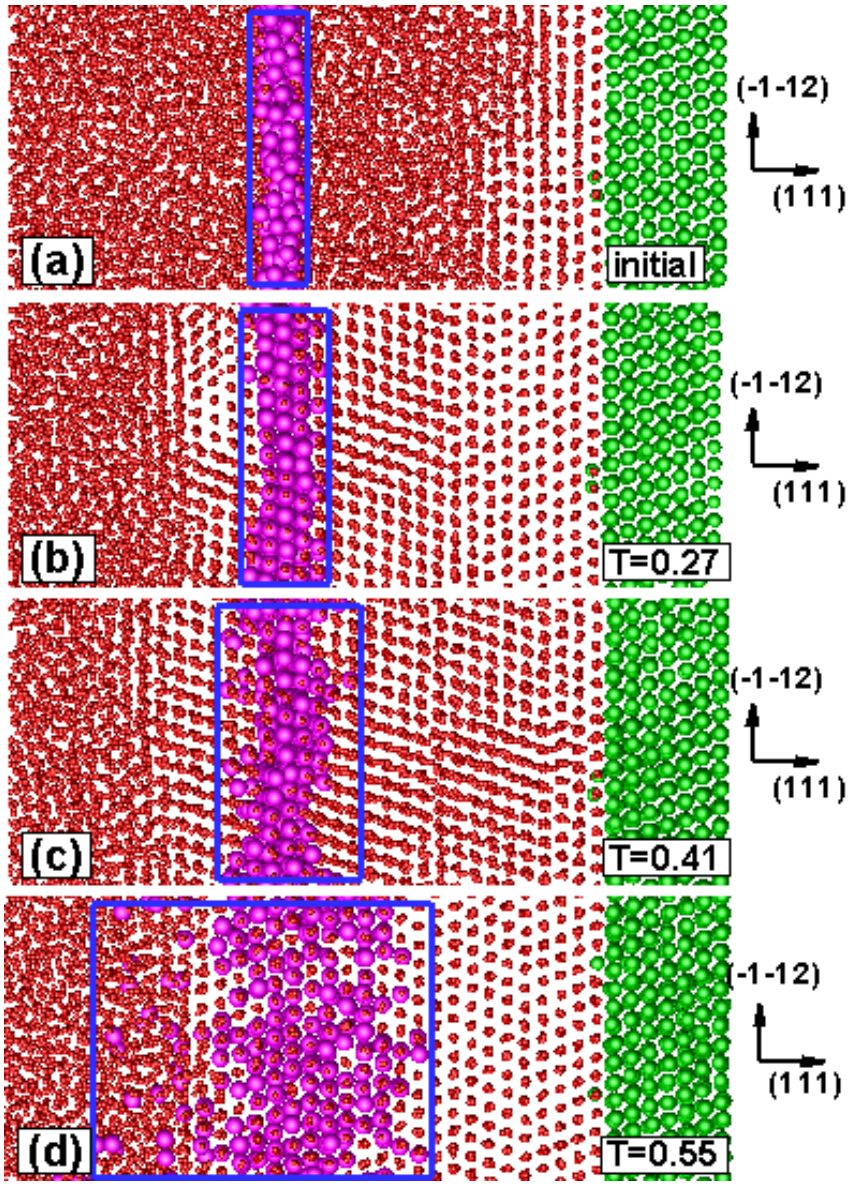

Figure 5.22. The snapshots of atoms in a thin liquid slice [bounded by a blue rectangle] at different temperatures during the crystallization. The sample contains a (111) interface. (a) The original liquid slice. (b) At T=0.27. (c) At T=0.41. (d) At T=0.55. Big pink spheres – atoms in the liquid slice; Small red spheres – original liquid atoms; Medium green spheres – original crystal atoms.

At the low temperature of $0.27\varepsilon/k_B$, the liquid is very viscous and the atomic mobility is very slow. The diffusion coefficient is essentially zero (in the simulation scale) at this temperature. Therefore, the crystal-melt system at this temperature can be viewed as a combination of a crystal and a glass. However, the supercooled liquid can still be crystallized when it contacts with a crystal, as shown in Figure 5.21(b) and Figure 5.22(b). Clearly, most atoms crystallize within the original liquid slice, except a few atoms move one atomic layer to the right and left sides of the liquid slice. Most importantly, for both (100) and (111) interfaces, the atoms in the liquid slice do not travel to further away sites to help the crystallization of those regions. Therefore, the long-rang diffusion (hopping) of atoms does not occur not only for the (100) interface, but also for the (111) interface. This result contradicts with the major conclusion by the Huitema *et al.* [41] and Gulam Razul *et al.* [42], for which the long-rang atom hopping is necessary for the crystal growth from a (111) interface.

At the moderate temperature of $0.41\varepsilon/k_B$, the diffusivity of the liquid is still relatively slow according to Eq. (5.2). After the crystallization, the atoms in the liquid slice diffuse at most 2 atomic layers for both (100) and (111) interfaces, as shown in Figure 5.21(c) and Figure 5.22(c). Again, the long-rang atom hopping is not found to help the crystallization of further away regions.

At the high temperature of $0.55\varepsilon/k_B$, the diffusivity of the liquid is high. Figures 5.21(d) and 5.22(d) show that the travel distances of some atoms in the original liquid slice are very long after the crystallization. However, there is still no clear difference between (100) and (111) interfaces, because they behave very similarly. In Huitema *et al.*'s work [41], they performed their simulations at a temperature of $60K$ ($\approx 0.5\varepsilon/k_B$), at

which the travel distances of liquid atoms can be as long as those shown in Figures 5.21(d) and 5.22(d). This could be the reason why they found the atom hopping during the crystallization. However, this atom hopping is just an inherent property of liquid at high temperatures and is not critical in affecting the crystallization rate. When the atom hopping is absent at the low temperatures, the crystallization rate still can be very fast for both (100) and (111) interfaces. Thus, the atom hopping may not cause the anisotropy in the crystallization rate.

For a monatomic system, all atoms are identical. The crystallization process does not have biases on the original positions of the liquid atoms. It just "picks up" the instantaneous liquid atoms that are close to the interface and turns them into the crystal atoms. At low temperatures, the liquid atoms vibrate around their original positions and can be crystallized only when the interface arrives. At high temperatures, the liquid atoms can diffuse away from their original positions. If they diffuse to positions close to the interface, they will be crystallized earlier. If they diffuse to positions further away from the interface, they will be crystallized later. Even though the (111) plane is denser and needs more atoms to fill the crystal sites, the crystallization process still chooses the liquid atoms near the interface to fill the "depletion zone". Therefore, for both (100) and (111) interfaces, the atom hopping should not affect the crystallization rate in a monatomic system.

Thus, it seems that the cooperative motion of atoms and atom hopping do not account for the anisotropy in the growth rate. Here I describe our understanding of the microscopic picture of the crystallization in a monatomic system. The crystallization only occurs at the interface region. The interface structure is complex with more ordering at

the crystal side and less ordering at the liquid side, as shown in Figure 5.11 and Figure 5.13. Only the instantaneous atoms near the interface can be crystallized. These near-interface atoms, no matter where they are originally located, are identical for crystallization. The ordering of atoms at a (100) interface is rather simple because there is only one type of atomic sites for crystallization. In Figure 5.21, one can find that all new crystals are well ordered at three different temperatures. In addition, the packing density of a (100) plane is lower than that of a (111) plane. On the other hand, the ordering of atoms at a (111) interface involves the competition of the near-identical fcc and hcp sites. As a result, more defects arise in the new crystal. These defects such as the stacking faults can be clearly seen in Figure 5.22, whereas such defects are rarely seen in Figure 5.21. It is worth noting that these defects are not necessary to be completely annealed away from a crystal. Moreover, the (111) plane is denser so that more atoms need to be ordered [note although the packing density of a (110) interface is lower than that of a (100) plane and a (111) plane, but more atomic layers need to be formed.]. Therefore, the high defect concentration and high packing density of the (111) interface slow the growth rate to some extent. But the grow rates of (110) and (111) interfaces are still non-trivial over a wide range of temperatures, as shown in Figure 5.20.

Figures 5.21(d) and 5.22(d) show that the diffusion length is long at high temperatures. Therefore, both the diffusion-controlled model [Eq. (5.1)] and the collision-controlled model [Eq. (5.3)] can fit well to the growth rate at high temperatures. In Figure 5.23, the two models are fitted to the growth rate of the (111) interface. At $T > 0.5\,\varepsilon / k_B$ ($\Delta T / T_m \approx 0.19$), the growth rate of the (111) interface can be well fitted with the two models. However, at $T < 0.5\,\varepsilon / k_B$, both models fail in the fitting. Similarly, the growth

rates of (100) and (110) interfaces also can be well fitted with two models at high temperatures (not shown in Figure 5.23). In other researchers' work, only the crystallization rates at high temperatures were calculated. Thus their data can be fitted by either the collision-controlled model or diffusion-controlled model. However, our results show that the two models are not appropriate in describing the growth rate over a wide range of temperatures.

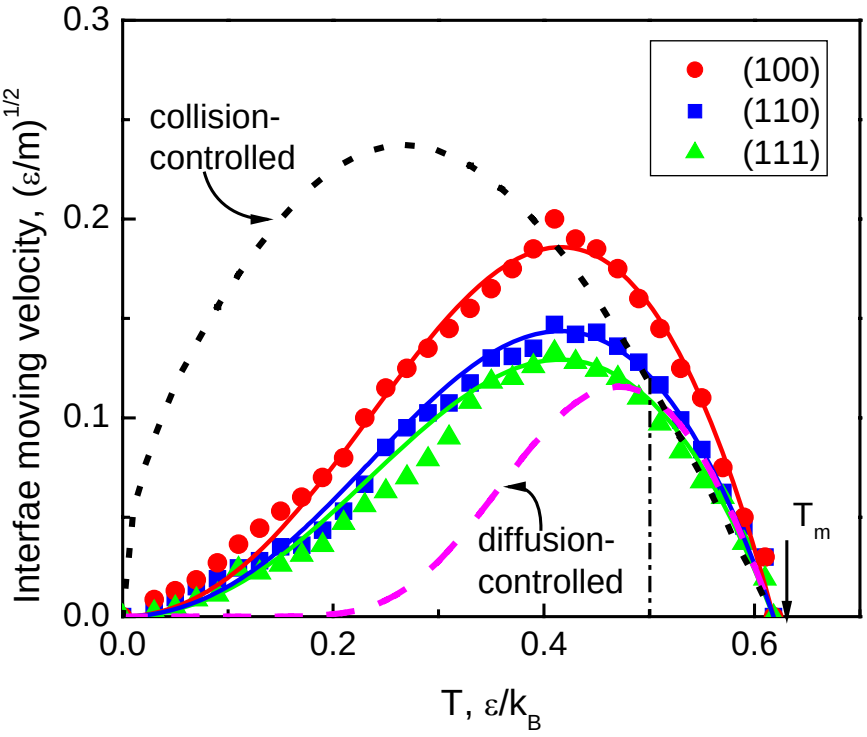

Figure 5.23. The fitting of the collision-controlled model [Eq. (5.3), dotted line] and diffusion-controlled model [Eq. (5.1), dashed line] to the growth rate of the (111) interface. The prefactor f_0 is 0.12 for the collision-controlled model and 0.40 for the diffusion-controlled model.

5.3.4. Relaxation Time of Crystal Growth

5.3.4.1. Definition of the Relation Time

In order to investigate the microscopic mechanisms of the face, temperature, and size dependences of the crystallization rates, we define a physical parameter - relaxation time to characterize the crystallization time. The relaxation time is the time needed when a thin slice of liquid transforms from the liquid state to the crystal state. First we picked up a thin liquid slice parallel to the interface for investigation. The thickness of this slice is about 1 nm and the number of atoms enclosed is *n*. An example snapshot of the thin liquid slice is shown in Figure 5.24. The system contains 32 000 atoms and a (100) interface. The liquid slice contains 366 atoms that are shown as yellow spheres. Initially, the distance between the crystal-melt interface and the thin liquid slice is same for all different configurations. During the crystallization process, we monitored the mean square displacements (MSD) of the atoms in the liquid slice.

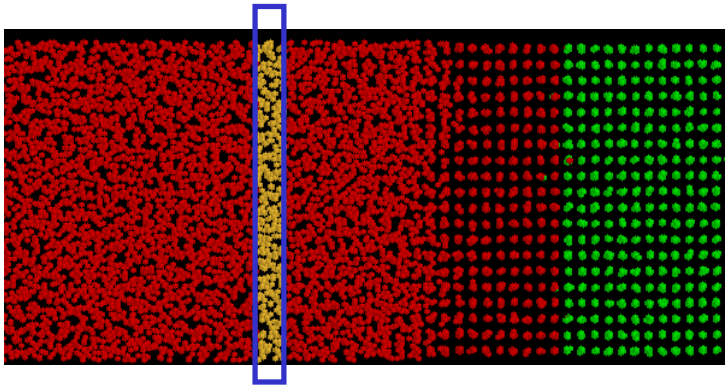

Figure 5.24. A snapshot of a sample with a thin liquid slice. The liquid slice is used for investigating the relaxation time. Green spheres – original crystal atoms; Red spheres – original liquid atoms; Yellow spheres – atoms in the liquid slice.

We define two types of MSD. The first one is defined as the mean square displacements of atoms from their original positions:

$$Z(t) = \sum_{i=1}^{n} (r_i^t - r_i^{t=0})^2 / n, \tag{5.4}$$

where n is the number of atoms enclosed in the liquid slice, r_i^t is the position of atom i at time t, and $r_i^{t=0}$ is the position of atom i at the initial time that we started to monitor the slice. Since the final positions of the atoms are the cumulative moves from the initial positions, we define this type of MSD as cumulative MSD (CMSD). Figure 5.25 shows the CMSD (black line) as a function of time. Before the crystal-melt interface arrives, the slice is in liquid state. Therefore, the diffusive nature of liquid atoms makes the CMSD increase almost linearly with the time. After the interface passes through the liquid slice, the crystallization makes the atoms in the thin liquid slice become crystal atoms. The crystal atoms are no longer diffusive so that they vibrate around their equilibrium sites. Thus the CMSD becomes leveled and does not increase with the time. The transition time between the linear increase region and the leveled region is defined as the relaxation time of CMSD, τ_{CMSD}, as shown in Figure 5.25.

The second MSD is defined as the mean square displacements (or travel distances) of atoms in the liquid slice in every interval of 100 time steps, as shown by

$$X(t) = \sum_{i=1}^{n} (r_i^t - r_i^{t-100})^2 / n, \tag{5.5}$$

where r_i^t and r_i^{t-100} represents the position of atom i at MD step t and t-100, respectively. Since the initial or referential atom positions for calculating atom displacements (or travel distances) are dynamically updated every 100 MD steps, we call it Dynamic MSD

(DMSD). Figure 5.25 shows the DMSD (blue line) as a function of time. Before the liquid slice crystallizes, $X(t)$ fluctuates around a large value, because the liquid atoms are diffusive. After the liquid slice crystallizes, $X(t)$ fluctuates around a small value because crystal atoms are localized. Therefore, the transition time for $X(t)$ dropping from the large value to the small value, τ_{DMSD}, is defined as the relaxation time measured from the DMSD.

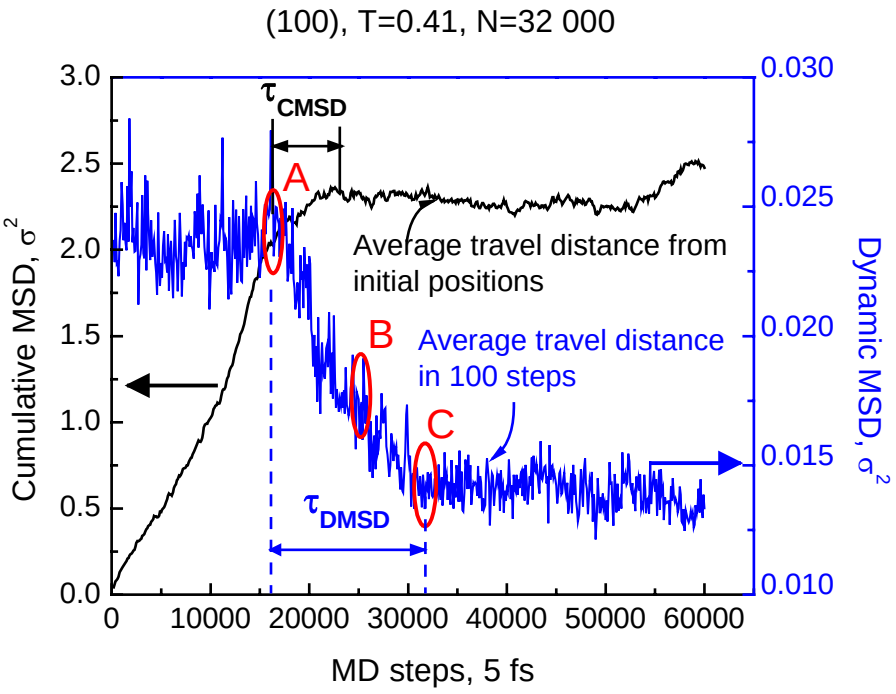

Figure 5.25. Two types of "mean-square-displacements" (MSD) of the atoms in the thin liquid slice. The left y-axis is for the cumulative MSD, and the right y-axis is for the dynamic MSD. The respective relaxation time measured from the two types of MSD, τ_{CMSD} and τ_{DMSD}, are indicated. The snapshots at time A, B, and C are shown in Figure 5.26.

Obviously, the transition period is more obvious in DMSD than in CMSD. The state (liquid, crystal, or transient) of the slice can be clearly identified from DMSD, while it is a little bit obscure in CMSD. Therefore, we have primarily used the DMSD to investigate the relaxation time in this work.

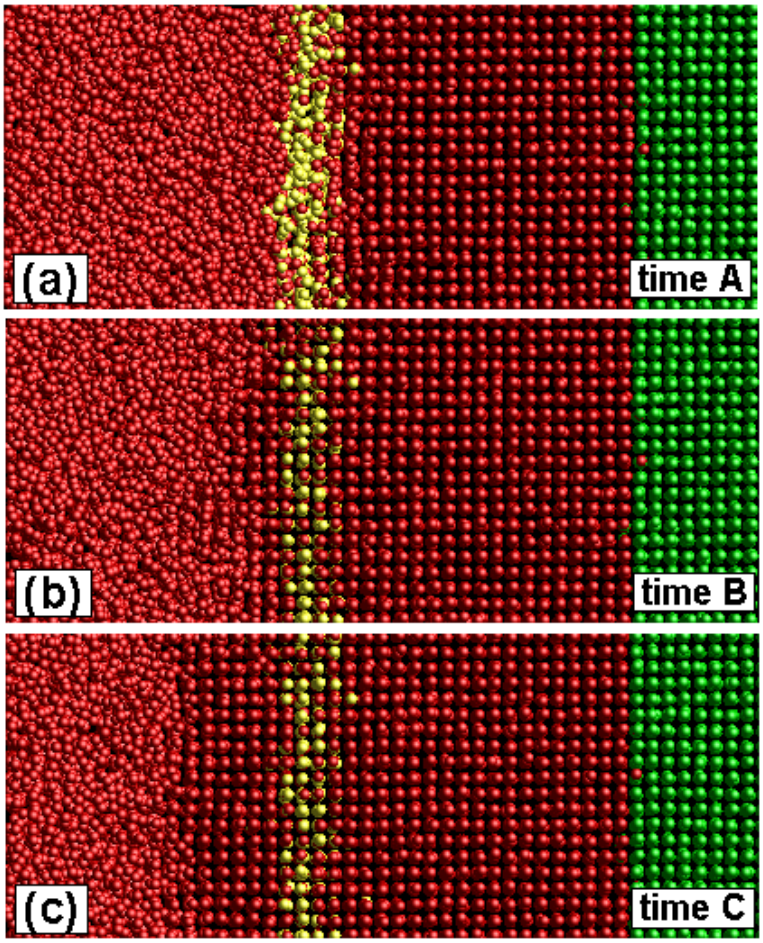

Figure 5.26. The snapshots of the sample at time A, B, and C as indicated in Figure 5.25. (a) At time A, the crystal-melt interface just arrives at the liquid slice. (b) At time B, the interface just passes through the thin slice. (c) At time C, the thin slice is completely crystallized. Green spheres – original crystal atoms; Red spheres – original liquid atoms; Yellow spheres – atoms in the original liquid slice.

Three moments A, B, and C are indicated in Figure 5.25. At time A, the DMSD starts decreasing, indicating that the crystal-melt interface has arrives at the thin liquid slice; At time C, the DMSD stops decreasing, which means that the liquid slice is completely crystallized; At time B, the DMSD decreases about half of its total decrease, indicating the liquid slice is partially crystallized. The corresponding snapshots at moments A, B, and C are shown in Figure 5.26. Figure 5.26(a) shows that the interface just arrives at the liquid slice at time A. In Figure 5.26(b), it seems that the liquid slice is crystallized because the interface has passed through the slice. But the DMSD shows that the movements of atoms are still large at time B, implying that the in-plane ordering takes place at this moment. Figure 5.26(c) shows that the interface already moves several atomic layers when the atoms in the thin slice are fully relaxed. Figure 5.26(c) indicates that the interface can move even if the new crystal is not fully crystallized. This result contradict Broughton *et al.*'s conclusion [38] in which the defects need to be completely annealed through the collective motions in order to grow further.

5.3.4.2. Face-Dependent Relaxation Time

In order to investigate the face dependence of the relaxation time, we have calculated the relation time of the (100) face and (111) face. Two samples were used. One sample consists of 32 000 atoms and a (100) interface, and the other sample consists 33 600 atoms and a (111) interface. Thus the two samples have roughly the same number of atoms. The number of atoms enclosed in the liquid slice is 366 for the (100) interface and 344 for the (111) interface. The distance between the liquid slice and the middle of the sample in x direction is 15σ for both samples. The calculations were performed at

the same temperature of $0.41\,\varepsilon/k_B$. Therefore, the comparison is purely focused on the face dependence. Since the DMSD clearly shows the transition period, we use it to investigate the relaxation time. The relaxation time of (100) and (111) faces is shown in Figure 5.27. The relaxation time of the (100) face, τ_{100}, is of about 14 000 MD steps (≈ 0.07 ns), while that of the (111) face, τ_{111}, is of about 19 000 MD steps (≈ 0.095 ns). Therefore, if the size of the system and the temperature are same, the relaxation time of the (111) face is longer than that of the (100) interface, i.e., $\tau_{111} > \tau_{100}$. In section 5.3.3, we have found that the interface moving velocity of a (100) face is faster than that of a (111) interface if the temperature and system size are same. In this section, we find that the (111) interface needs more time (about 30% in Figure 5.27) to change a thin liquid layer into a crystal layer. Therefore, the interface moving velocity of a (111) face is slower than that of a (100) face. In Figure 5.27, one also can find that the DMSDs of both interfaces behave similarly when the thin slices are in liquid state, indicating that the properties of the liquid are not dependent on the crystal orientation. After the liquid slices are in crystal state, the DMSD of the (111) face is slightly higher than that of the (100) face. This may be caused by the in-plane relaxation. Since the packing density of the (111) interface is higher, more defects appear during the crystallization, as we have shown in section 5.3.2. Therefore the (111) face needs more time to anneal out its defects. As a result, the average atom displacement in every interval is larger during the process of the defect annealing.

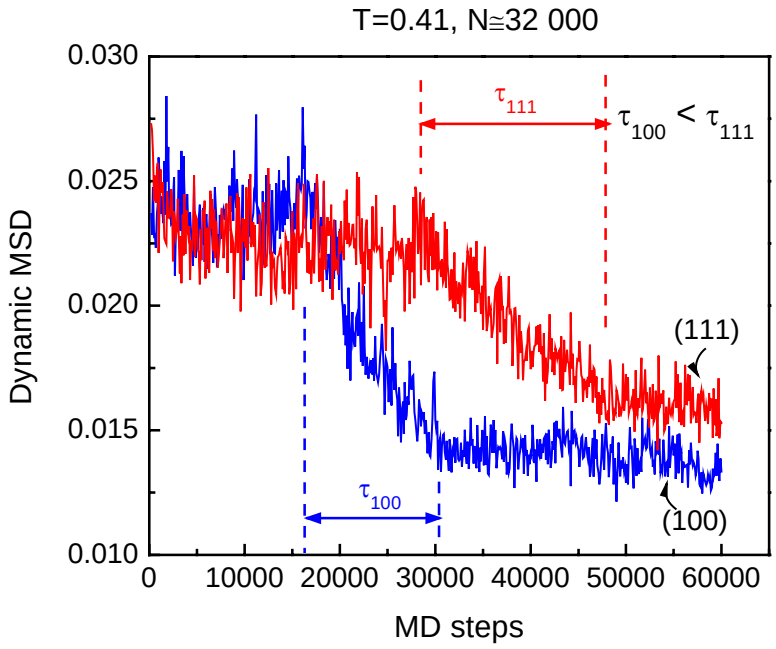

Figure 5.27. The comparison of the relaxation time between a (100) interface and a (111) interface at the same temperature and of roughly same system size.

5.3.4.3. Temperature-Dependent Relaxation Time

The temperature dependence of the relaxation time was investigated with the same sample at different temperatures. For example, we have investigated a sample with 32 000 atoms and a (100) interface at T = 0.41 and $0.27\,\varepsilon/k_B$ respectively. The result is shown in Figure 5.28. The relaxation time is of about 14 000 MD steps (0.07 ns) at T = $0.41\,\varepsilon/k_B$ and of about 20 000 MD steps (0.1 ns) at T = $0.27\,\varepsilon/k_B$. Therefore, we have $\tau_{0.27} > \tau_{0.41}$. If $T > 0.41\,\varepsilon/k_B$, the relaxation time should be larger than that at T = $0.41\,\varepsilon/k_B$. However, since the liquid atoms are very diffusive at high temperatures, the atoms in the original liquid slice diffuse far away from their original positions as shown

in Figure 5.21(d) and Figure 5.22(d). This brings difficulties for charactering the relaxation time at high temperatures. Thus the investigations of the relaxation time at high temperatures are not performed. But we can expect that it increases with the increasing temperature because the driving force decreases with the increasing temperature.

In Figure 5.28, one also can find that the DMSD at $T = 0.41\,\varepsilon / k_B$ is always larger than that at $T = 0.27\,\varepsilon / k_B$. This is because the atomic mobility decreases with the decreasing temperature. The average thermal velocity of atoms at a temperature T is $(3k_BT / m)^{1/2}$, where m is the atomic mass. Therefore, in the same time period, the average travel distance of atoms (or DMSD) at the higher temperature is longer than that at the lower temperature.

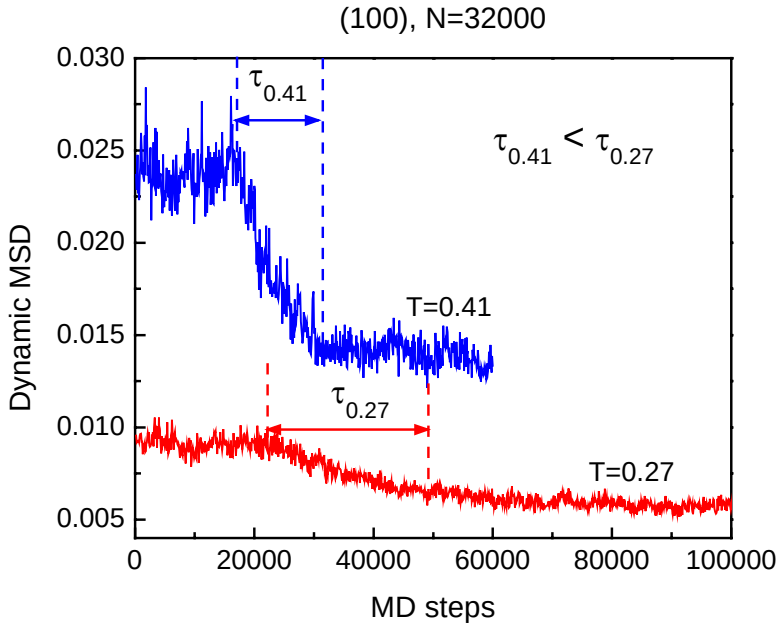

Figure 5.28. The comparison of the relaxation time at different temperatures for the same sample. The sample consists of 32 000 atoms and a (100) interface.

5.3.4.4. Size-Dependent Relaxation Time

In order to investigate the size dependence of the relaxation time, we have performed our calculations with three samples of different sizes: N = 32 000, 64 000, and 128 000, and each of them contains a (100) interface. All calculations were performed at the same temperature of $0.41\,\varepsilon/k_B$. Figure 5.29 shows the comparison of the DMSD among three samples. Clearly, the relaxation time increases with increasing system size: $\tau_{32000} < \tau_{64000} < \tau_{128000}$, where $\tau_{32000} \approx$ 14 000 MD steps (0.07 ns), $\tau_{64000} \approx$ 36 000 MD steps (0.18 ns), and $\tau_{128000} \approx$ 70 000 MD steps (0.28 ns).

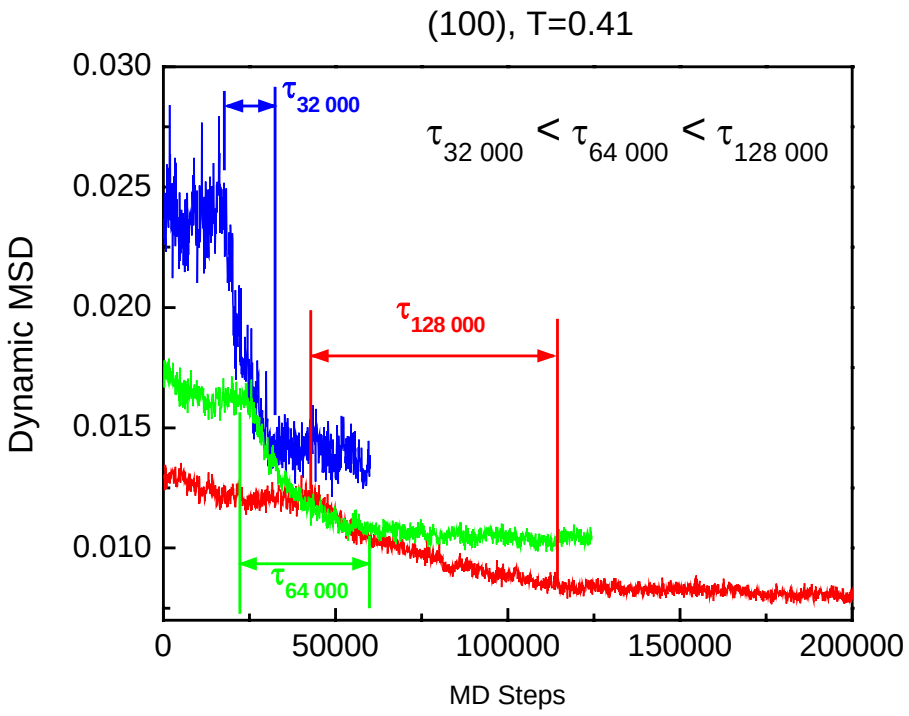

Figure 5.29. The size-dependent relaxation time. Three different size samples are used for comparison: N = 32 000, 64 000, and 128 000. Each sample has a (100) interface.

The longer relaxation time in the larger system implies that the crystallization rate decreases with the increasing sample size. Actually in section 5.3.5, we will show that the crystallization rate is size dependent. Moreover, one also can find that the DMSD decreases with the increasing size, indicating that the average atom travel distance over the same period is shorter in the larger system. Since all calculations were performed at the same temperature, the average atom thermal velocities in the three systems are same. However, Figure 5.29 shows that the atomic mobility decreases with the increasing sample size. This may be induced by the size-dependent fluctuations: the larger fluctuations in the smaller system increase the atomic mobility. The size-dependent fluctuations will be discussed in section 5.3.6.

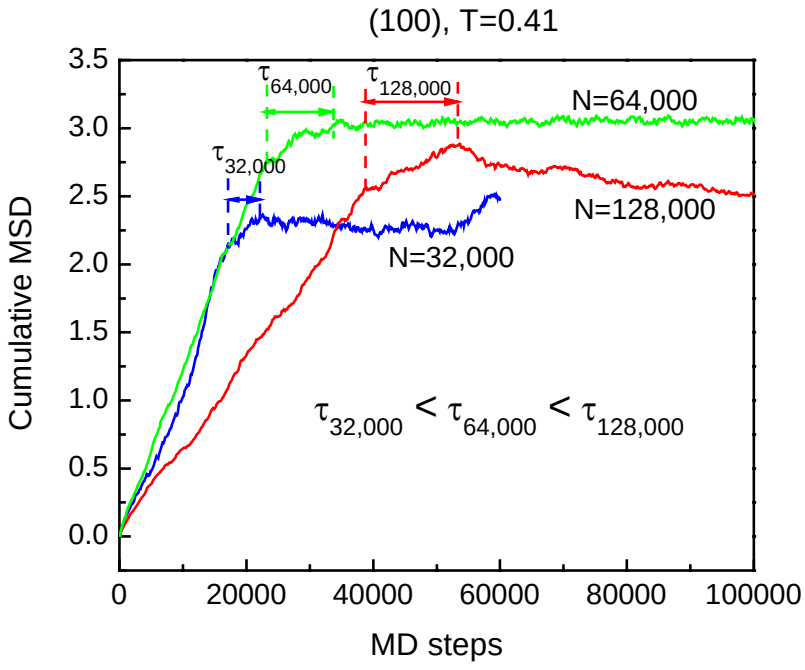

Figure 5.30. Comparison of the relaxation time in different size systems by using the cumulative MSD (CMSD).

The size dependence of the relaxation time also can be investigated by using the cumulative MSD (CMSD). Figure 5.30 shows the time evolution of the CMSD in three size samples. One also can find that $\tau_{32000} < \tau_{64000} < \tau_{128000}$. However, it seems that the CMSD is not a good physical parameter for characterizing the relaxation time, because the transition periods are not obvious in Figure 5.30.

5.3.5. Finite-Size Effects on Crystallization Rates

Using the method described in section 5.2.3, we have calculated the interface moving velocities over a wide range of temperatures for various configurations listed in Table 5.1. Totally eight configurations of different sizes are used for the (100) interface and another eight configurations are used for the (111) interface. In section 5.3.3, we have shown that the relation among the interface moving velocities of (100), (110), and (111) faces is, $v_{111}<v_{110}<v_{100}$. Therefore, we only calculated the interface moving velocities of (100) and (111) faces. Moreover, in order to save the computing time, we only calculated the growth rates around their maxima for some configurations. The interface moving velocities of the (100) face of different sample sizes are shown in Figure 5.31, and those of the (111) face are shown in Figure 5.32.

In Figures 5.31 and 5.32, it can be clearly seen that the interface moving velocity decreases with the increasing system size for both (100) and (111) interfaces. In addition, one also can find that the interface moving velocity of the (111) face is slower than that of the (100) face if they have roughly the same system size and at the same temperature. As we have discussed in section 5.3.3, this is because the atoms in the (111) face need to compete for the energetically equivalent fcc and hcp sites during the stacking process,

while atoms of the (100) face do not have this need [38]. In addition, the higher packing density and the higher concentration of defects make the interface moving velocity of the (111) face slower. Note that Honeycutt and Andersen [136] found that the nucleation rate in computer simulations is very fast in small systems (typically less than 500 atoms). They argued that the rapid nucleation is an artifact of the periodic boundary conditions, because the size of the critical nucleus exceeds the size of the simulation systems. However, the number of atoms in our simulations is sufficiently large. Therefore, the same concept cannot be used to interpret the size dependence of growth rate in our work.

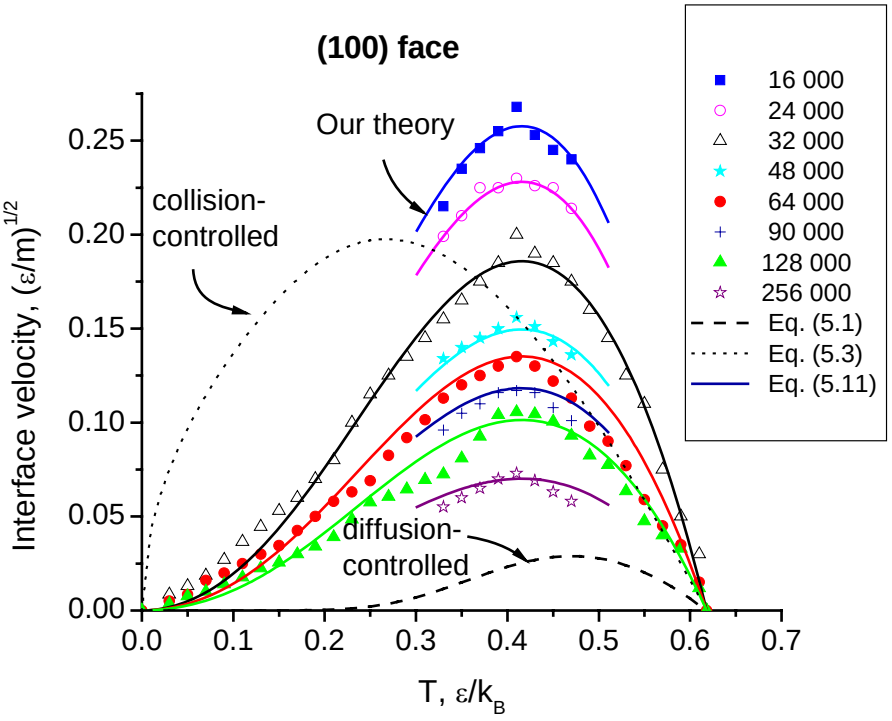

Figure 5.31. The (100) interface moving velocities of different size systems at different temperatures. The data points are calculated with our MD simulations. The diffusion-controlled model [Eq. (5.1)] and the collision-controlled model [Eq. (5.3)] are shown as dashed line and dotted line respectively. The solid lines are the fittings of our proposed theory in section 5.3.6 [Eq. (5.11)] to the simulation data. The reduced LJ unit of the velocity is $(\varepsilon / m)^{1/2} \approx 158$ m/s.

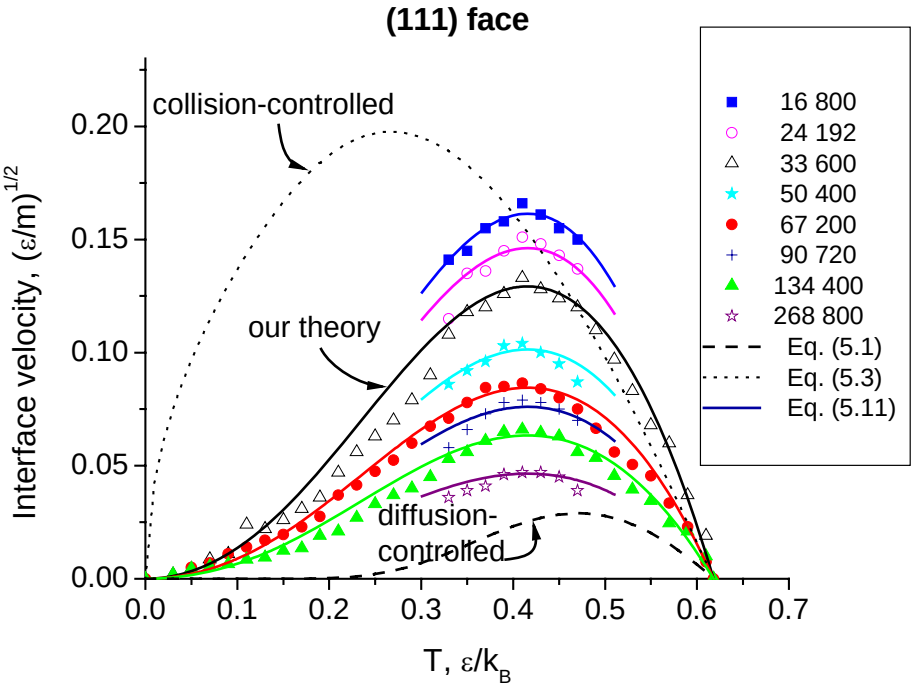

Figure 5.32. The (111) interface moving velocities of different size systems at different temperatures. The data points are calculated with our MD simulations. The diffusion-controlled model [Eq. (5.1)] and the collision-controlled model [Eq. (5.3)] are shown as dashed line and dotted line respectively. The solid lines are the fittings of our proposed theory in section 5.3.6 [Eq. (5.11)] to the simulation data. The reduced LJ unit of the velocity is $(\varepsilon/m)^{1/2} \approx 158$ m/sec.

At small undercoolings (or high temperatures), the growth rate of each size system increases approximately linearly with the increasing undercooling ΔT (or driving force), i.e., $v = k\Delta T$, indicating that the interface is atomically rough and the growth is continuous [1]. At T=0.41 ε/k_B, or $\Delta T/T_m \approx 0.33$, the growth rates of both (100) and (111) faces reach their maximum values. At T<0.41 ε/k_B, the growth rates decrease because of the decrease in the mobility of liquid atoms. However, even though the diffusivity of the liquid atoms is very slow at low temperatures, both (100) and (111)

interfaces still can move at significant velocities. For example, at $T = 0.20\,\varepsilon/k_B$ (or $\Delta T/T_m \approx 0.68$), the diffusion coefficient $D \approx 2.37\times10^{-5}\left(\sigma^2\varepsilon/m\right)^{1/2} \approx 1.27\times10^{-8}$ cm^2/s, which is essentially zero in the simulation scale. However, at this temperature, the interface moving velocity of the (100) face is about 0.08 $(\varepsilon/m)^{1/2} \approx 12.8$ m/s in a system of 32 000 atoms, while that of the (111) face is about 0.05 $(\varepsilon/m)^{1/2} \approx 8.0$ m/s in a system of 33 600 atoms. Therefore, it seems that the crystal growth is more like a "collision-controlled" process rather than a "diffusion-controlled" one for both (100) and (111) faces. The long-range diffusion does not play a major role in determining the crystallization rate, no matter what the orientation of the interface. Our results disagree with Broughton *et al.*'s conclusion [38] that the moving velocity of (100) interface is collision-controlled, while that of (111) interface is diffusion-controlled. Moreover, for all 16 configurations, both (100) and (111) interfaces reach the maximum velocities at the same temperature of $0.41\,\varepsilon/k_B$, or $\Delta T/T_m \approx 0.33$, which also differs from Broughton *et al.*'s $\Delta T/T_m \approx 0.60$ for (100) face [34] and $\Delta T/T_m \approx 0.23$ for (111) face [38].

To compare the two aforementioned models with our simulation data, we plot the diffusion-controlled model [Eq. (5.1)] with a dashed line and the collision-controlled model [Eq. (5.3)] with a dotted line in Figures 5.31 and 5.32. The parameters used for plotting the models are (in reduced LJ units): D = 0.86exp(-2.1/T) [34], $\Lambda = 0.0829 - 0.0258T + 0.18588T^2$ [Ref. 34, note 0.0258 was mistakenly written as 0.258 in this work], $\Delta\mu = 1.08\Delta T/T_m$ [61], $a = \sqrt{3}/3a_0 = 0.912$ [61], $\lambda = 0.4a$ [34], and f = 0.10 [note in Ref. 34 and 38, f = 0.27]. Clearly, the diffusion-controlled model fails completely in fitting the data. It underestimates the crystallization rate over a wide range

of temperatures. Particularly, this model predicts that the interface moving velocity is almost zero at $T = T_m/2 \approx 0.3\varepsilon/k_B$, whereas our simulation data shows that it is still substantially fast at this temperature. The collision-controlled model also fails in many aspects, although our results show the likelihood of the collision-controlled growth mechanism (because the calculated crystallization rates are still fast at low temperatures). First, it cannot predict the size dependence of the growth rate. It overestimates the growth rate at low temperatures and underestimates the growth rate at high temperatures. Second, the growth rates are observed to reach their maxima at T=0.41 ε/k_B for all configurations in our simulations, while the collision-controlled model predicts that this temperature is $0.25\varepsilon/k_B$ (or $\Delta T/T_m = 0.6$). At this temperature, the LJ liquid is almost in the glassy state because the diffusivity is very slow. Thus it is questionable that the maximum crystallization rate can be achieved at this temperature. Note in Figure 5.23, we have shown that the two models can fit the data well at high temperatures ($T > 0.5\varepsilon/k_B$) if the accommodation factor *f* is chosen appropriately. But over a wide range of temperatures, it seems that the two models are not appropriate.

It is interesting to note that the temperature for the maximum velocities coincides with the critical temperature of the spontaneous crystallization, which is $0.42\varepsilon/k_B$ in Figure 3.6 for a bulk LJ liquid. Moreover, according to the classical nucleation theory, the homogenous nucleation rate can be expressed as [1], $I \sim \exp(-\Delta G^*_{\text{hom}}/k_B T)$, where $\Delta G^*_{\text{hom}} = \left(\frac{16\pi\gamma_{SL}^3 T_m^2}{3L_V^2}\right)\frac{1}{(\Delta T)^2}$ is the critical nucleation barrier at an undercooling ΔT. Putting the crystal-melt interfacial free energy γ_{SL}= $0.301\varepsilon/\sigma^2$, the latent heat per

volume $L_V = 1.024\ \varepsilon/\sigma^3$, and $T_m = 0.618\,\varepsilon/k_B$ [61] into the nucleation barrier, we can calculate the temperature-dependent nucleation rate, which is shown in Figure 5.33. At $T = 0.418\,\varepsilon/k_B$ or $\Delta T = 0.2\ \varepsilon/k_B$, we find that the nucleation rate increases suddenly (hence the spontaneous crystallization occurs), at which the nucleation barrier is $\Delta G^*_{\text{hom}} \approx 9.64\,k_B T$. Therefore, both the direct freezing of a pure LJ liquid and the classical nucleation theory predicts the critical temperature is at about $0.42\,\varepsilon/k_B$, which is very close to the temperature of 0.41 ε/k_B for the maximum velocities in Figure 5.31 and Figure 5.32. However, the reason for this coincidence is not clear. Since both the crystal nucleation and growth are kinetic processes, they may have some similarities in the kinetic behaviors. The critical temperature may be one of those properties.

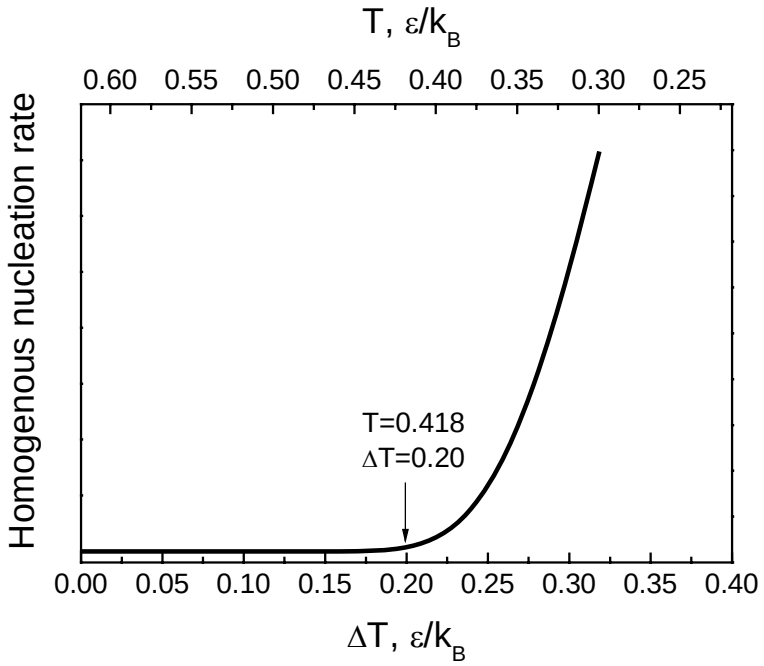

Figure 5.33. The temperature-dependent homogeneous nucleation rate of an undercooled LJ liquid. The bottom x-axis represents the undercooling ΔT, and the top x-axis represents the temperature *T*. The arrow indicates the critical undercooling/temperature for the spontaneous nucleation.

5.3.6. Our Proposed Theory for the Crystallization Rate

In Figures 5.31 and 5.32, we have shown that the two prevailing models of the crystallization rate, which are the diffusion-controlled model and collision-controlled model, are both failed in fitting our simulation data. The cause of the discrepancy may lay in the parameter f in Eqs. (5.1) and (5.3). The parameter f is the atomic site acceptance ratio or accommodation factor for crystallization, which was treated as a constant ($f = 0.27$) in previous works [34,38]. However, this assumption needs to be reconsidered for the following reasons: The collision-controlled model assumes that the liquid atoms act like the ideal gas atoms when they collide on the interface. In a solid-vapor system the acceptance ratio is primarily dependent on the solid surface structure, because the gas atoms are very dilute so that they do not affect their peers. However, for the solid-liquid system, the liquid is almost as dense as the solid. Therefore, the movement of the liquid atoms at the interface is influenced not only by the crystal structure on the solid side, but also by the *collective arrangement* of the neighboring liquid atoms. In other words, the liquid atoms cannot be simply treated as gas atoms. Moreover, at the interface region, the liquid atoms tend to stay at the positions of the local energy minima. However, since the liquid atoms are disordered and jammed, their instantaneous positions do not coincide with the correct crystalline sites. As a result, atoms need some additional relaxation time to find and move to the correct sites. Therefore, the atomic site acceptance ratio is primarily controlled by the relaxation time of these two events. In section 5.3.4,we have investigated the face, temperature, and size dependences of the relaxation time. We find that in the atomistic simulations the relaxation time increases with the increasing system size, and decreases with increasing

temperature. Moreover, the relaxation time of a (111) face is larger than that of a (100) face if other conditions are same. Thus, the acceptance ratio should be both temperature and size dependent. Here we propose a semi-empirical theory to describe these dependences.

Suppose that the acceptance ratio f is a function of temperature T and system size N, say, a simple product of two functions,

$$f = f(T, N) = f_1(T) f_2(N), \tag{5.6}$$

where $f_1(T)$ and $f_2(N)$ depends on T and N separately. As the system temperature increases, both the thermal velocity and the free volume of each atom increase. As a result, the atom mobility increases with the increasing temperature. Thus, $f_1(T)$ should be an increasing function of T, because the higher atom mobility at higher temperature results in higher probability for liquid atoms to find the correct crystalline sites. We propose a scaling relation to describe the temperature-dependent acceptance ratio, which can be expressed as

$$f_1(T) = \beta(T / T_m)^{\gamma}, \tag{5.7}$$

where β is a constant and γ is an exponent to be determined. Note this relation yields $f_1 \to \beta$ at $T = T_m$, and $f_1 = 0$ at $T = 0$.

The size-dependent acceptance ratio $f_2(N)$ may be related to the thermal fluctuations. The fluctuations are directly related to the finite sample size [137]. The smaller the system is, the larger fluctuations the system has. Thus the smaller system has the faster growth rate. When the system size is small, the fluctuations are large and become comparable with the system size. Consequently, the properties of the small system may differ from the bulk properties. For example, a nanomagnet may lose its

magnetism at a temperature much lower than the bulk transition temperature, because the large thermal fluctuations in the small system can disorder the orientation of magnetization [138]. In a Gibbs (*NPT*) ensemble, the fluctuation of the system volume is related to the sample size *N*, as shown by [137]

$$\Delta V / V_0 \sim 1/\sqrt{N}\,, \tag{5.8}$$

where ΔV and V_0 are the volume fluctuation and equilibrium volume respectively. For an isotropic liquid, this probability is proportional to $\Delta V / V_0$ [137].

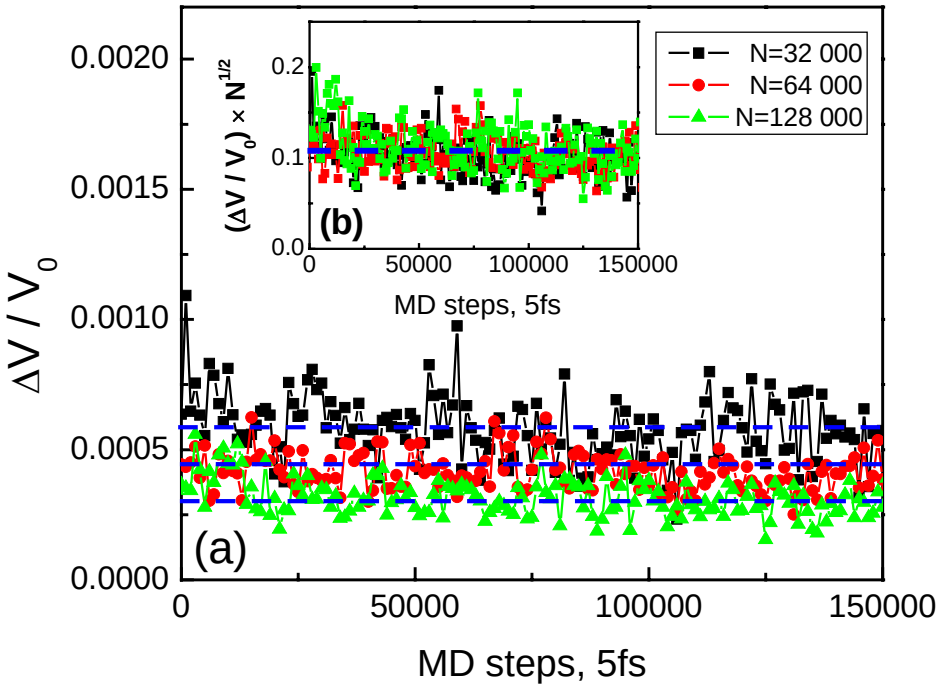

Figure 5.34. The volume fluctuations during the crystallization process in three size systems: N = 32 000, 64 000, and 128 000. Each blue dashed line indicates the corresponding average value of the fluctuations. (a) Size-dependent volume fluctuations. The smaller system has the larger fluctuations. (b) The normalized volume fluctuations by multiplying a factor of $\sqrt{N}$. The normalized volume fluctuations in the three size systems are almost identical.

In order to verify the relation between the volume fluctuations and the system size in our simulation systems, we have calculated the volume fluctuations in different size systems during the crystal growth. The volume fluctuations can be calculated by

$$\frac{\Delta V}{V_0} = \sqrt{\frac{< V^2 > - < V >^2}{< V >^2}}, \tag{5.9}$$

where V is the instantaneous sample volume and the angle bracket $< \cdots >$ represents the time average over 1 000 MD steps. Since the crystal growth is a non-equilibrium process, the average volume changes with the time. Thus, we averaged V^2 and V over every 1 000 time steps and calculated the volume fluctuations by using Eq. (5.9). Note we also have calculated the enthalpy fluctuations of the simulation systems, $\Delta E / E_0$. We find that $\Delta E / E_0$ behaves similarly as $\Delta V / V_0$. Thus we only show the volume fluctuations as an example. The calculated volume fluctuations in three size systems (N = 32 000, 64 000, and 128 000) are shown in Figure 5.34(a). Each system consists of a (100) interface and the calculation was performed at $T = 0.41\, \varepsilon / k_B$. The dashed lines indicate the averages of the fluctuations. Clearly, the smallest system (N = 32 000) has the largest fluctuations, while the largest system (N = 128 000) has the smallest fluctuations. In other words, the fluctuations decrease with the increasing sample size. In Figure 5.34(b), we show the normalized fluctuations of the three size systems. The normalized fluctuation is defined as the product of the fluctuation and the square root of the sample size, $\Delta V / V_0 \times \sqrt{N}$. Obviously, the normalized fluctuations become almost identical for the three size systems. The dashed line indicates that the mean value of the normalized fluctuations is about 0.1. Thus, Figure 5.34(b) testifies that the magnitude of $\Delta V / V_0$ is proportional to $1/\sqrt{N}$.

Further calculations have been performed for a wide range of sample sizes: N =16 000 ~ 256 000. For each sample, we calculated the volume fluctuations and estimated the mean value as we did in Figure 5.34(a). Figure 5.35 shows the mean volume fluctuation $< \Delta V / V_0 >$ as a function of $1/\sqrt{N}$. Clearly, the linear correlation between $< \Delta V / V_0 >$ and $1/\sqrt{N}$ indicates that Eq. (5.8) is valid for our simulation systems.

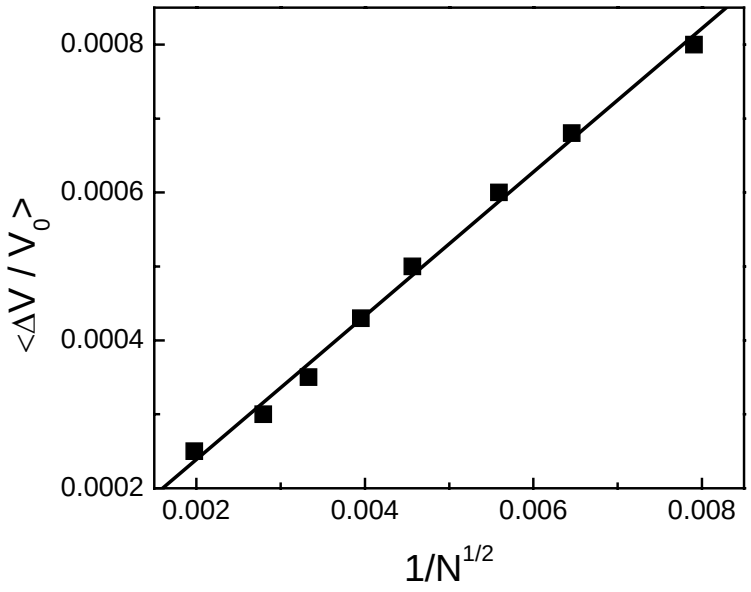

Figure 5.35. The linear relation between the volume fluctuation and the reciprocal of the square root of the system size. The data points are the average volume fluctuations in different size systems.

The volume fluctuation, or the dynamic volume change, resembling a mechanical "shaking" effect, provides an additional probability for the liquid atoms near the interface to move collectively in order to register with the crystal sites. Therefore, the size dependence of the crystallization rate in Figures 5.31 and 5.32 may directly relate to the

fluctuations. Similar to the volume fluctuations, we propose that the size-dependent acceptance ratio is also a function of $1/\sqrt{N}$:

$$f_2(N) = A_0 + B/\sqrt{N}, \tag{5.10}$$

where B is a constant and A_0 is the asymptotic value of $f_2(N)$ at $N \to \infty$. If those terms are introduced into Eq. (5.3), the best fits to the simulation data [solid curves in Figures 5.31 and 5.32] yields γ =3/2 and β =1. Thus the interfacial velocity in our model is

$$v = (a/\lambda)(3k_B T/m)^{1/2}(1 - e^{-\Delta\mu/k_b T})[(T/T_m)^{3/2} \times f_2(N)], \tag{5.11}$$

where the parameters are as same as in Eq. (5.3). Fitting Eq. (5.11) to the simulation data in Figures 5.31 and 5.32, we obtained f_2 for each configuration of N atoms. The fittings of Eq. (5.11) are shown as the solid lines in Figures 5.31 and 5.32. Apparently, our model can fit most of the data points very well over a wide range of temperatures.

After f_2 for each configuration is determined, we plot f_2 vs. $1/\sqrt{N}$ in Figure 5.36 for both (100) and (111) interfaces. We found that both f_2^{100} and f_2^{111} can be approximately fitted with a respective linear line, indicating the validity of our conjecture of the form of $f_2(N)$. The linear fits yield

$$f_2^{100} = 0.0103 + 38.07/\sqrt{N}, \tag{5.12a}$$

and

$$f_2^{111} = 0.0085 + 24.77/\sqrt{N}. \tag{5.12b}$$

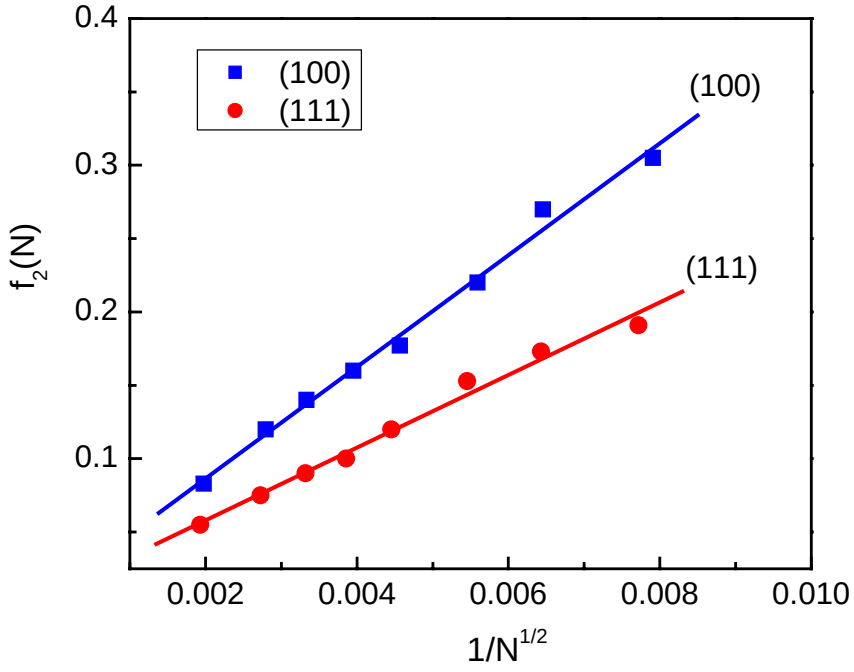

Figure 5.36. The linear fits of f_2 to $1/\sqrt{N}$ for (100) and (111) interfaces.

Since $f_2 \propto 1/\sqrt{N}$, we can rescale the interface velocities by multiplying the square root of the sample size, $\sqrt{N}$, to get the universal velocities for different size systems. Figure 5.37 shows the rescaled velocities for both (100) and (111) interfaces. Approximately, most data points follow their respective universal velocity line over a wide range of temperatures. Thus, the interface moving velocity decreases almost linearly with $1/\sqrt{N}$.

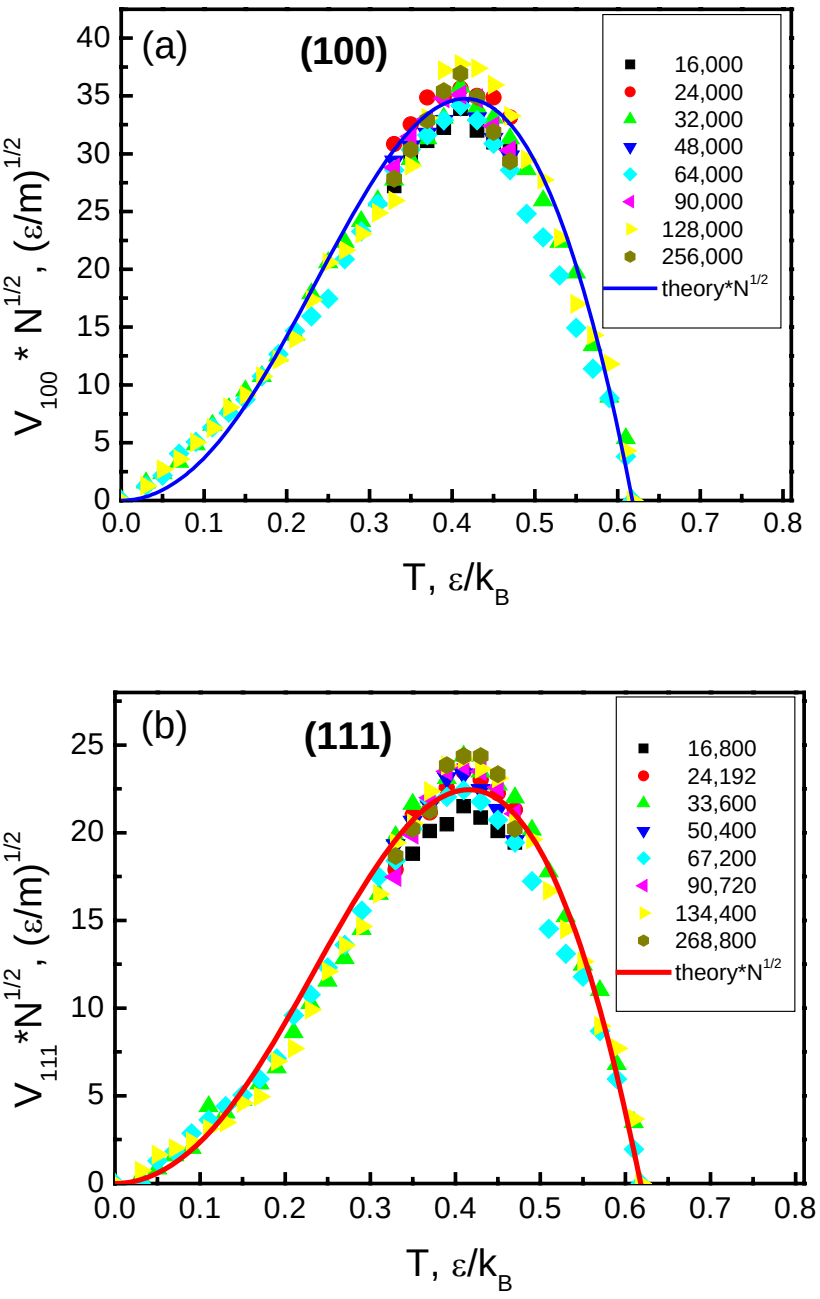

Figure 5.37. The rescaled interface moving velocities by multiplying a factor $\sqrt{N}$. The data points are calculated from simulations. The solid lines are plotted with the product of Eq. (5.11) and $\sqrt{N}$. (a) The (100) interface. (b) The (111) interface.

Similarly, the linear fit of the maximum velocity to $1/\sqrt{N}$ yields

$$v_{\max}^{100} = 0.0087 + 32.17/\sqrt{N}, \tag{5.13a}$$

and

$$v_{\max}^{111} = 0.0072 + 20.93/\sqrt{N}. \tag{5.13b}$$

Here the velocity is in the reduced LJ unit $(\varepsilon/m)^{1/2}$, which is about 158 m/s. Thus we can change the unit of Eqs. (5.13a) and (5.13b) to the real unit m/s: $v_{\max}^{100} = 1.36 + 5082.86/\sqrt{N}$ m/s, and $v_{\max}^{111} = 1.14 + 3306.94/\sqrt{N}$ m/s. For an fcc crystal, the system length can be approximated by $L = \left(N/4\right)^{1/3} a_0$, where a_0 is the lattice constant and has a value of 0.53 nm for a LJ system. Therefore, we can rewrite the maximum velocity as a function of the system length:

$$v_{\max}^{100} = 1.36 + 2541.43\left(a_0/L\right)^{3/2}, \tag{5.14a}$$

and

$$v_{\max}^{111} = 1.14 + 1653.47\left(a_0/L\right)^{3/2}. \tag{5.14b}$$

Here the velocity unit is m/s. If we know the depth of the liquid in the laser annealing experiments, *L*, we can use Eqs. (5.14a) and (5.14b) to estimate the corresponding crystallization rate. In Table 5.2, we use our model to predict the crystallization rates of the liquid silicon and germanium of various sizes.

Table 5.2: The comparisons between the experimental crystallization rates and the theoretical predictions. The theoretical predictions are calculated with our model, $v_{\max}^{100} = 1.36 + 2541.43\left(a_0 / L\right)^{3/2}$ [Eq. (5.14a)], where $a_0 = 0.53$ nm.

Materials	Liquid depth (nm)	Measured velocity (m/sec)	Our prediction (m/sec)
Si [7]	40	25	5.2
Ge [8]	98	3	2.4
Si [9]	160	5-15	1.8
Si [10]	450	2.8-3.3	1.5
Si [11]	600	2-3	1.4

Our model predicts that the crystallization rate is about 2 m/sec when the system length is about a few hundred nanometers [Table 5.2], which is in good agreement with many experimental crystallization rates of silicon and germanium. For metals, generally it is difficult to use the laser annealing technique to study the rapid solidification. Moreover, the crystallization rates of the metallic systems are very scattered, ranging from a few to one hundred meters per second [43,49,50]. For example, MacDonald *et al.* [50] found that the crystallization rate of a 30-nm-thick gold/copper multiplayer is about 7.5 m/s and 100 m/s under different conditions. Tsao *et. al.* [49] found that the

crystallization rate of a 60-nm-thick liquid aluminum is about 3 m/s. Walker *et al.* [43] found the crystallization rate of a liquid Ni is about 50 m/s. Thus it is difficult to make direct comparisons with our model.

If the system length is $1\,\mu m$, our model predicts that the maximum velocity is saturated at 1.39 m/sec for (100) interface and 1.16 m/sec for (111) interface. If the system size becomes even larger, the thermal conductivity becomes important. Under such circumstance, the crystallization rate is mainly determined by the rate of dissipating the latent heat from the interface front to the outside of the system [127]. The thermal diffusion coefficient (D_T) of silicon is $0.8 cm^2/sec$ [139]. The thermal diffusion length, D_T/v, is the range of the uniform temperature around the interface [127]. If the crystal growth rate is 5 m/sec, the thermal diffusion length of silicon is $16\,\mu m$, which is much larger than the depth of the melted spot (typically less than $0.5\,\mu m$ [43-50]). Therefore, the latent heat can be dissipated very quickly in those experiments. Under such circumstance, the crystal growth rate is not controlled by the heat flow.

5.4. Discussion and Conclusions

In this chapter, we have used extensive molecular dynamics simulations to calculate the steady state crystallization rates of a standard Lennard-Jones system. The temperature, face, and size dependences of the interface moving velocities are investigated. We have found that the crystal growth rates of both (100) and (111) interfaces decrease with the increasing system size, and the size dependence is related to the system fluctuations. We conclude that the abnormal fast growth rates in other researchers' work are primarily due to the small sample size. In this work, a new method

is developed for characterizing the relaxation time of the crystallization. It is found that the relaxation time increases with the increasing system size, and decreases with the increasing temperature. Moreover, the relaxation time of a (111) interface is longer than that of a (100) interface. Our results show that the two prevailing growth models, which are diffusion-controlled model and collision-controlled model, both fail in interpreting our simulation data. We have modified the collision-controlled model by introducing a temperature- and size- dependent atomic site acceptance ratio, $f(T,N) = f_1(T) \times f_2(N)$, to fit our simulation data. We have found that the simulation data can be fitted very well if $f_1(T) \propto (T/T_m)^{3/2}$, and $f_2(N) \propto 1/\sqrt{N}$. Using this model, we predict that the crystal growth rate is about 2 m/s if the thickness of a liquid is about 200 nm, which is in good agreement with many experimental crystallization rates of silicon and germanium in rapid solidification. The corrections from the finite sample size is not only a practical utility for obtaining macroscopic crystallization rates from small system calculations, but also an important application in crystal growth for the small systems such as nanoscale materials [140]. It is worth noting that the fitting of f_2 is still over a narrow range of system sizes. It is unclear whether the linear relation between f_2 and $1/\sqrt{N}$ still holds if the system size increases further. One possibility is that the crystal growth rate could decrease slowly when the sample size is large, or might approach the saturated velocity earlier. Nevertheless, it is still reasonable to expect that the growth rate approach a small value when the system size is large, because from Figures 5.31 and 5.32 we know that the interface moving velocity indeed decreases substantially with the system size.

The microscopic interface structures of (100) and (111) interfaces are carefully investigated. The crystal-melt interface is always a diffuse interface with more ordering

at the crystal side and less ordering at the liquid side. The partially ordered structures both perpendicular to the interface and parallel to the interface are found at the liquid side of the interface. It is found that the interface thickness of the (100) interface is about 1.7 nm, while that of the (111) interface is about 1.5 nm. The interface structure of the (111) interface is much rougher than that of the (100) interface. At the liquid side, it is found that the {111} interplanar spacing and the in-plane alignment in the <110> directions may be the precursors for the crystal growth.

The growth morphologies from (100) and (111) interfaces are very different. When crystal grows from a (100) interface, there is only one type of atomic sites for atoms to lie in. Thus, the structure of the new crystal is very well ordered and the defect concentration is low. On the other hand, the growth morphology of the (111) interface is very complex. This is because there are two nearly identical types of atomic sites for atoms in the (111) face to choose: fcc and hcp sites. Thus atoms can choose either fcc sites or hcp sites during the crystal growth. As a result, a lot of stacking faults, dislocations, and vacancies form during the crystal growth. The hcp, fcc, and hybrid structures are found at different regions of the new crystal grown from a (111) interface.

The growth rate of the (100) interface is the fastest and that of the (111) interface is slowest. The growth rate of the (110) interface is intermediate. There are two explanations for the slower growth rate of the (111) interfaces. Broughton *et al.* [38] claimed that the in-plane structure of a (111) plane should be annealed completely into either an hcp structure or an fcc structure in order to grow further. However, we find that the interface can move further before the new crystal is completely relaxed. Moreover, the in-plane structure can be hybrid. Huitema *et al.* [41] and Gulam Razul *et al.* [42]

argued that the higher density of the (111) face causes the atom hopping from furtheraway layers in order to fill the depletion zone at the interface. But our microscopic analysis shows that the atom hopping does not occur at low and moderate temperatures for both (100) and (111) interfaces. At high temperatures, the atom hopping is just an inherent property of the liquid and this atom hopping does not faciliate the crystallization process in a monatomic system. Only the instaneous atoms at the interface can be crystallized no matter where the atoms are originally from. Moreover, if the above two explanations are correct, the crystal growth of the (111) interface should be more like a diffusion-controlled behavior. However, our results show that the interface moving velocity of the (111) interface is still substantially fast at temperatures below the half melting point. Thus the crystal growth from the (111) interface is still like a collision-controlled process. Due to the higher pakcing density and defect concentration, the growth rate from the (111) interface is slower than that from the (100) interface.

CHAPTER 6

NUCLEATION AND MELTING FROM NANOVOIDS

Melting is one of the most commonly observed phase transformations in nature [1]. And yet the detailed microscopic and thermodynamic mechanisms are still not entirely known despite numerous experimental and theoretical studies made over the past hundred years [7-12,14-25]. Usually there are two types of melting: melting from intrinsic or extrinsic defects (such as free surfaces, grain boundaries, voids, etc.) [7-9], and melting from within by spontaneous nucleation [10-12,14-25]. The former is a heterogeneous process and the later is a homogenous one. Generally melting starts from the free surface of a material, because the disordered atomic layers at the surface provide barrier-free nucleation sites for melting. The melting temperature determined from the surface melting is as same as the thermodynamic melting temperature at which the solid and liquid coexist with a flat solid-liquid interface [61]. Therefore, no superheating is required for surface melting [1,7]. However, superheating can be achieved by suppressing the surface melting. For example, some researchers have used the pulsed laser irradiation [11,12,22,24] to initiate the melting from the bulk, or "removed" the surface by coating a thin layer of another material of higher melting point on the surface [10]. Using those techniques, significant amount of superheating (about 20-30% [14,23,25]) can be achieved in defect-free systems. In reality, most materials contain certain amount of internal defects such as impurities, grain boundaries, voids, etc [1]. These defects are characterized by the low packing densities and open spaces at the defect cores. In nanoporous materials, the volume fraction of voids and open spaces could be more than

50% [54]. These imperfect regions provide the nucleation sites with much lower nucleation barriers for melting. Thus the melting initiated from the internal defects is usually the dominant process other than the homogeneous nucleation. Understanding the mechanisms of melting at the defects is of great interests for studying the melting process in nature.

Although the melting at superheating (both homogenous and heterogeneous) has been successfully observed in experiment, the detailed investigations on the microscopic mechanisms are still lacking. First, the melting at superheating is an extremely fast event. Usually the transition time is at the nanosecond scale [11,12,22,24]. It is thus difficult to observe and record the detailed information in such short time period. Second, for both melting from internal defects and homogenous nucleation, the transition takes place in the bulk of the crystal. This will bring difficulties for using the transmission electron microscopy (TEM) to investigate the transition process. Third, it is not easy to suppress the melting at the free surface in experiment. Nevertheless, the melting at superheating can be easily modeled in computer simulations [13,63,64]. The free surface can be removed by using periodic boundary conditions. In the past several decades, the homogenous melting at the superheating has been studied extensively [14-25]. The primary research focus of this area is to find how the melting is triggered in a defect-free system. Unfortunately, the detailed microscopic mechanism is still unclear. On the other hand, the heterogeneous melting at the internal defects is less investigated until recently some researchers have used molecular dynamics (MD) simulations to investigate the melting from internal voids [55-59]. Most of them have reported an interesting phenomenon of the void melting: initially the melting temperature of the void-containing

system decreases rapidly with the increasing void size; and after the void radius is larger than a critical value, the melting temperature reaches a plateau. The asymptotic temperature in the plateau was empirically considered as the thermodynamic melting temperature at which a bulk liquid and a bulk solid coexist with a flat interface. Figure 6.1 illustrates the typical relation between the melting temperature of a void-containing system and the radius of the void in those simulations.

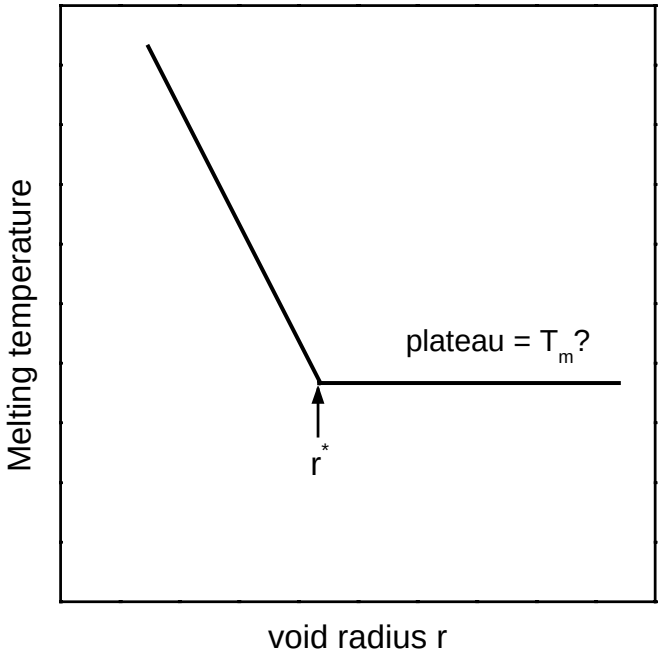

Figure 6.1. Illustration of the relation between the melting temperature of a void-containing system and the void radius. r^* is the critical radius beyond which the melting temperature reaches a plateau.

Although this unusual relation between the melting temperature and void size has been reported, the underlying origin for the presence of the plateau is still unclear. As pointed out by Agrawal *et al.* [55], by far the mechanism of void melting is still lacking and the theoretical basis for the unusual melting behavior is still unknown. Therefore, it is a rather superficial conclusion that the plateau temperature is as same as the thermodynamic melting temperature, because no detailed understanding of the microscopic mechanisms or in-depth thermodynamic considerations have been provided to support this argument.

In this Chapter, I will present our investigations on the heterogeneous nucleation and growth in melting from nanovoids via extensive molecular dynamics simulations. We have found that there are four distinct stages in the void melting. Melting in each of the stages is governed by a unique mechanism originated from the variations and the interplay of the following properties: the solid-vapor, liquid-solid, and liquid-vapor interface energies, the curvature of the void surfaces, and the elastic energy induced by the volume change at the solid-to-liquid transition. The strong void size dependence of these properties leads to three different local melting temperatures, the complex melting sequence, and the melting kinetics in the nanovoid-containing solids. The void melting cannot be viewed as a simple inverse process of its counter part- nanoparticle melting. In addition, both our proposed theory and simulation results predict that the melting temperature approaches a plateau when the volume fraction of the voids is about 5-6% in a uniformly distributed void-containing system.

6.1. Models and Method

6.1.1. Creating a Nanovoid at the Center of a Crystal

In this work, we investigate a system contain a single void at the center of a crystal. In some researcher's work, the system contains some randomly distributed voids. That will bring some complexities in rationalizing the melting mechanism of void melting. Therefore, we only investigate the nucleation and melting process from a single void. Initially, all atoms were arranged in an fcc lattice. The geometric shape of the simulation sample is a cubic box. The total number of atoms is *N*. Then we removed the atoms within a radius r_0 from the center of the crystal. The number of removed atoms is *n*. Thus the number of atoms in the simulation system is *N*-*n*. Figure 6.2 illustrates how we create a void at the center of the crystal.

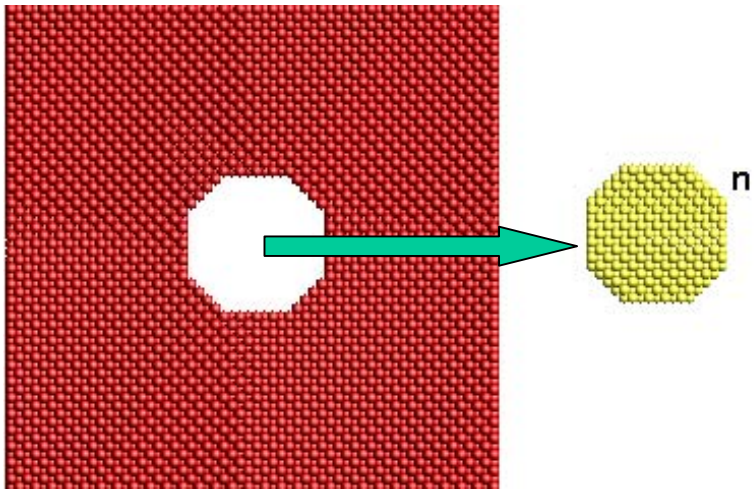

Figure 6.2. Cross-sectional projection of a crystal sample containing a void. In this figure the total number of atoms in this sample (before creating a void) is $N = 108\,000$ and the number of atoms removed for creating the void is $n = 1\,505$ (or $r_0 = 0.73$nm).

In previous work [55-59], the system sizes are very small in those simulations. Typically the total number of atoms in a simulation system is less than 2 000 and the number of atoms removed for creating the voids was less than 100. As I will show in this chapter, the melting temperature and other properties are strongly dependent on the system size. Thus the small system may lead to incorrect results. In order to check the finite size effects and find the trend of the size dependences, we have used three different size systems (before a void was introduced) with 32 000 ($20\times20\times20$ unit cells), 108 000($30\times30\times30$ unit cells), and 256 000 ($40\times40\times40$ unit cells) atoms respectively. The initial void radius r_0 ranges from 0.58 to 6.62 nm. The periodic boundary conditions were applied in all directions. Thus the outer free surface is erased but the free surface around the void still exists.

6.1.2. Molecular Dynamics Simulations

In this work, we have used molecular dynamics (MD) simulations to investigate the nucleation and melting process from the voids. Since melting is a non-equilibrium process, we performed our simulations in a constant-pressure and constant-temperature (*NPT*) ensemble. The *NPT* MD can effectively adjust the volume, pressure, and temperature changes and keep the system at the desired conditions during the phase transition. We have used the Parrinello–Rahman method [68] to control the system pressure and the Nose thermostat [69] to control the system temperature. The system pressure was kept at zero throughout the simulation. In order to be consistent with many literatures, a standard Lennard-Jones (LJ) potential $\phi(r)=4\varepsilon[(\sigma/r)^{12}-(\sigma/r)^{6}]$ was

used, where $\varepsilon = 119.8k_B$ and $\sigma = 3.405\overset{0}{A}$. The standard reduced units are still used in this work: the length unit is in σ, the energy unit is in ε, and the temperature unit is in $\varepsilon / k_B \approx 120K$. The cutoff distance was set to 2.5σ. The MD time step was set to 5×10^{-15} s. The initial void radius r_0 ranges from 0.58 to 6.62 nm. In each run, a spherical void was created at the beginning of the simulation. After the void was created, the system was relaxed at $T = 0.2\varepsilon / k_B$ ($\approx 24K$) for 10 000 MD steps (0.05ns). Thereafter, the system was heated from $0.2\varepsilon / k_B$ to a desired temperature T with a heating rate of 1.33×10^{12} K/s. At temperature T, the system was held isothermally for about 200 000 MD steps (1ns). During the isothermal runs, we investigated the phase transition (if any) at the void surface. Figure 6.3 illustrates the typical procedure of our simulations. Depending on the temperature, the system could be totally melted (at T=0.665), partially melted (T=0.650), or not melted (T=0.636).

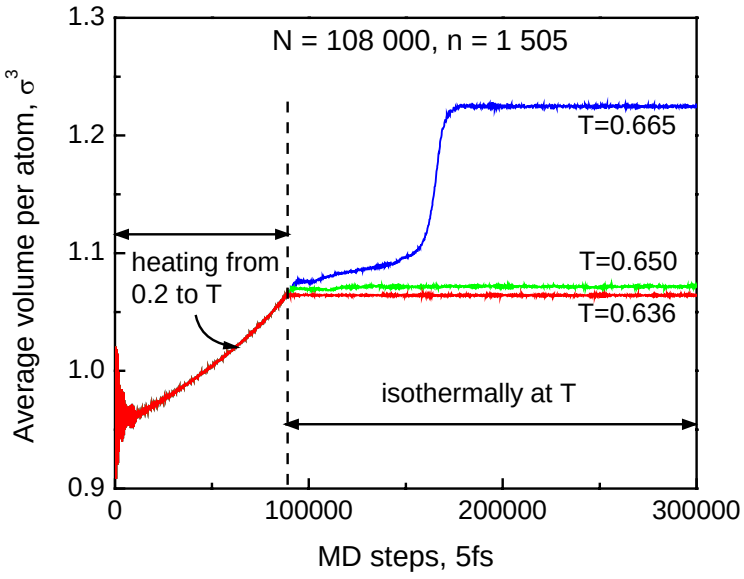

Figure 6.3. An example of the simulation procedure. See the text for details.

Note we have used isothermal heating (IH) rather than the gradual heating (GH) method to investigate the void melting. The gradual heating is that the system temperature is continuously increased until the system melts completely. The isothermal heating is to keep the system at a desired temperature isothermally. To the best of our knowledge, most researchers have used the gradual heating method to determine the melting temperature of the void melting. Since the inherent time barrier in computer simulations, the heating rate is very fast. Typically it is about 10^{11} K/s. Such a high heating rate may cause the hysteresis effect on the melting temperature. Most importantly, as it will be shown later in this chapter, some important transition process could be missed if one uses this method. Unfortunately, the differences between the isothermal heating and gradual heating have not been considered seriously.

In order to illustrate the hysteresis effect on the melting temperature caused by the gradual heating, we did the following tests. As shown in Figure 6.4, in a sample of 108 000 atoms with 1 505 atoms removed for creating a void, first we heated the sample gradually from $0.2\varepsilon/k_B$ to $0.9\varepsilon/k_B$ with a heating rate of 10^{11} K/s. We found that the system starts to melt at $0.722\varepsilon/k_B$. Thus the obtained melting temperature from the gradual heating is $T_m^{GH} = 0.722\varepsilon/k_B$. In the second run, we heated the same sample from $0.2\varepsilon/k_B$ to $0.663\varepsilon/k_B$. Then we held the system temperature isothermally at this temperature. After some time (note the time cannot be shown in Figure 6.4 because the x-axis represents the temperature), the system becomes a liquid. Thus the melting temperature obtained from the isothermal heating is $T_m^{IH} = 0.663\varepsilon/k_B$. Therefore, the gradual heating method overestimates the melting temperature about 9%. Apparently, the hysteresis effect caused by the gradual heating is non-trivial. Therefore, in this work, we

use the isothermal heating to determine the melting temperature in order to get more accurate results.

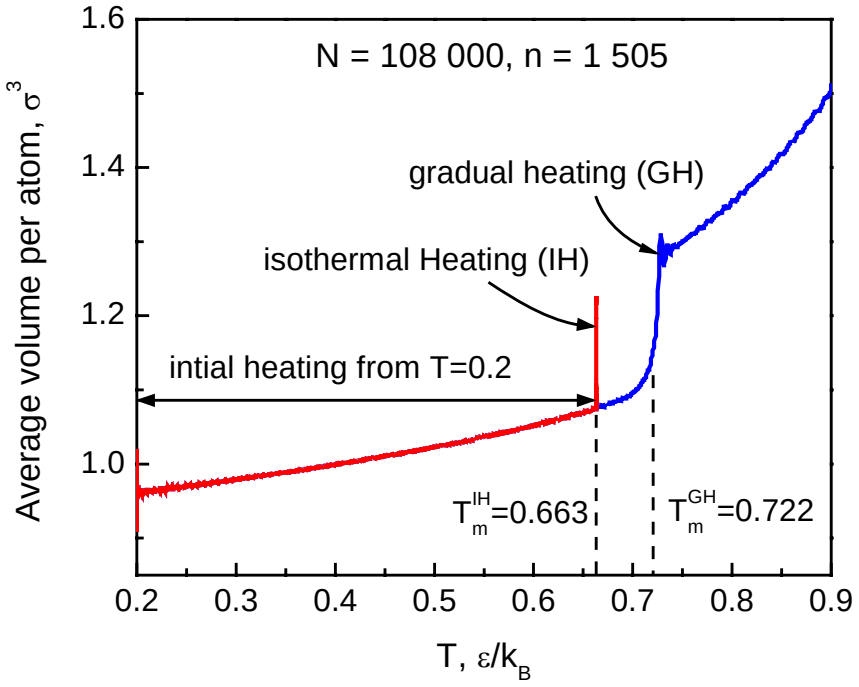

Figure 6.4. Comparison between the gradual heating (GH) and isothermal heating (IH) method. The gradual heating shows a strong hysteresis effect on the melting temperature.

The equilibrium or thermodynamic melting temperature T_m^E was determined by two methods. One is to find the temperature at which a flat crystal-melt interface stays stationary. The other is to locate the melting point of a crystal slab with two flat free surfaces. Both methods yield T_m^E=0.618 ε / k_B at zero pressure [61], which agrees well with Broughton *et al.*'s result (T_m^E=0.617 ε / k_B at $P = 0$) [128].

6.2. Results

6.2.1. Four Stages of Void Melting

As described in section 6.1.2, the void-containing sample was heated from $0.2\,\varepsilon / k_B$ to a desired high temperature T and the system was held isothermally at this temperature for 200 000 MD steps (1 ns). In the isothermal temperature range, we monitor the evolution of the system. Depending on the temperature T, the state of the system has several possibilities. Here we give an example. We removed 1 505 atoms from the center of a crystal containing 108 000 atoms to form a void of radius of 2.48 nm. The subsequent isothermal testing at different temperatures reveals that the void melting has four distinct stages. The time evolution of the volume is shown in Figure 6.5. The corresponding snapshots at different stages are shown in Figure 6.6.

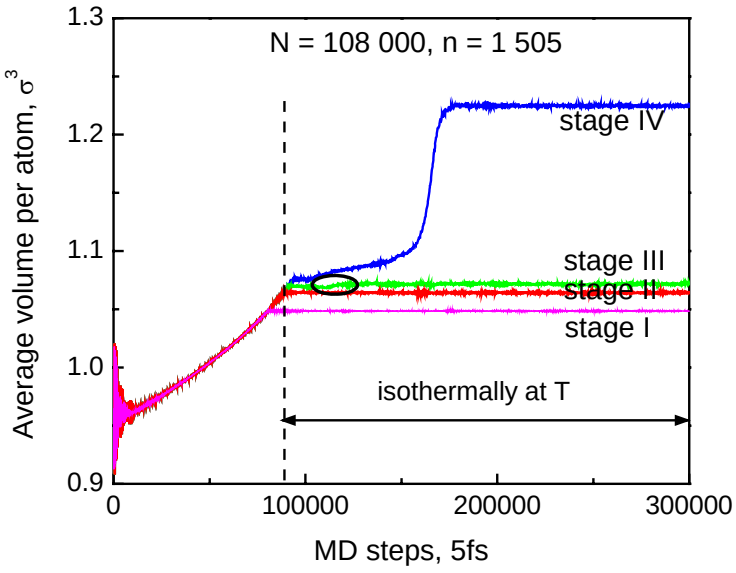

Figure 6.5. The time evolution of the average volume per atom at different temperatures. The snapshots at the four stages are given in Figure 6.6. The circle indicates a bump in stage III. Stage I: $T = 0.590$; Stage II: $T = 0.630$; Stage III: $T = 0.645$; Stage IV: $T = 0.670$.

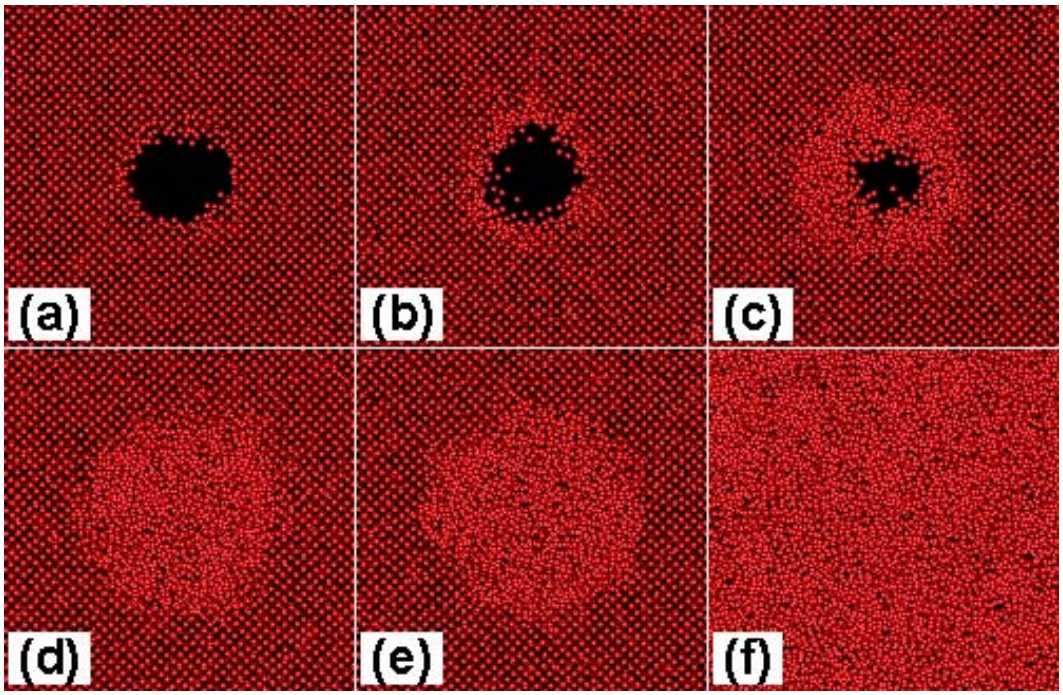

Figure 6.6. The cross-sectional snapshots of the four stages (shown in Figure 6.5) during void melting. (a) Stage I: at $T < T_m^E$, the solid-vapor void surface is stable. (b) Stage II: at $T_m^E \le T < T_m^A$, a thin liquid layer nucleates around void surface. (c)-(e) Stage III: at $T_m^A \le T < T_m^B$, the thin liquid layer grows [(c)]; after some MD runs the liquid atoms fills the void completely [(d)]; the liquid droplet stops growing and the radius does not change even after very long MD runs [(e)]. (f) Stage IV: at $T > T_m^B$, the sample melts completely. See the text for the definition of the notations T_m^E, T_m^A, and T_m^B.

Stage I ($T < T_m^E$): *The solid is stable and characterized by a stable solid-vapor interface*. As shown in Figure 6.6(a), the solid-vapor interface is stable at T = 0.590 ε / k_B. The corresponding volume evolution in Figure 6.5 (pink line) also shows that the whole sample is in solid state.

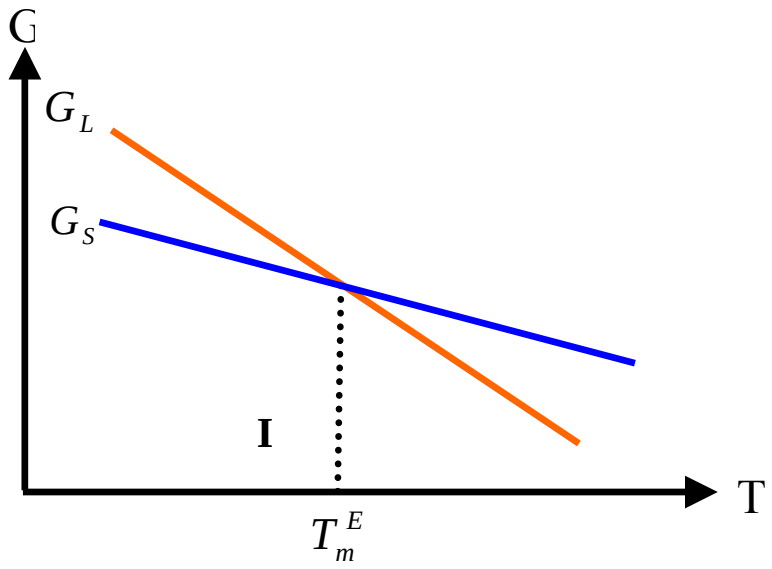

Figure 6.7. The free energy diagram of stage I ($T < T_m^E$) in the void melting. See the text for details.

In fact at any $T < T_m^E$ (=0.618 ε / k_B), the solid phase is more stable than the liquid phase, as shown in Figure 6.7. The top atomic layer on the surface is found disordered to some extent due to the loss of some neighboring atoms in forming the surface. In addition, the surface has a negative curvature and the vapor pressure is almost zero inside the void. Figure 6.8 shows that even after 200 000 MD steps (1 ns), the void surface does not change too much (the solid-vapor interface is stable.). Similar to a flat solid-vapor interface (i.e., of zero curvature), the disordered void surface provides barrier-free heterogeneous nucleation sites for void melting. Due to the inequality among the solid-vapor, solid-liquid, and liquid-vapor interfacial free energies expressed as $\gamma_{sv} \geq \gamma_{sl} + \gamma_{lv}$ [1], a liquid prefers to nucleate on the surface in order to lower the total free energy of the

system. As a result, a liquid layer is found to readily occur around the void surface at T_m^E despite its negative curvature.

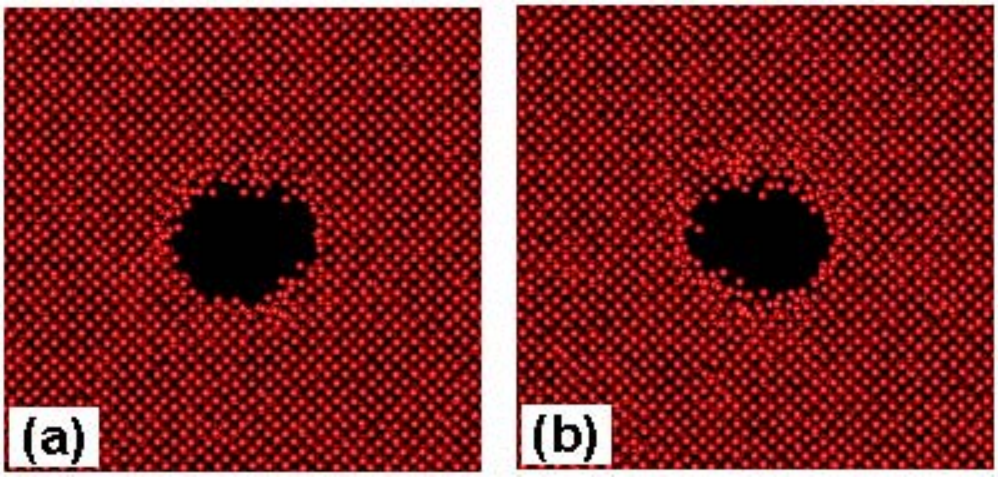

Figure 6.8. The cross-sectional snapshots of the sample at different simulation time in stage I. (a) Initial snapshot at T = 0.590. The surface atoms are slightly disordered. (b) After 200 000 isothermal runs, the void surface is still stable.

Stage II ($T_m^E \le T < T_m^A$): *Surface melts and the solid coexists with a stable thin layer of liquid nucleating around the void surface*. If T is above T_m^E, a liquid starts to nucleate at the surface [Figure 6.6(b)], because the liquid phase is more stable than the solid phase [Figure 6.7] at this temperature. As we have shown in Chapter 5, for a flat surface, once a liquid layer forms, the liquid can continuously grow as long as $T > T_m^E$ [63]. However, this does not happen in void melting. When a liquid layer forms around a void, the free energy of the solid changes from G_s to $G_s^{'} = G_s - \Delta G_{\text{interface}}$ due to the

presence of the negative curvature of the solid-liquid interface, where $\Delta G_{\text{interface}} = 2\gamma_{eff} / r$ is the excessive interface free energy induced by the curvature, γ_{eff} is the effective solid-liquid interfacial free energy, and r is the effective radius of the solid-liquid interface. The free energy diagram of this stage is shown in Figure 6.9. The free energy $G_s^{'}$ of the solid phase intersects the free energy G_l of the liquid phase at a temperature T_m^A ($>T_m^E$), which is the effective local melting temperature at the curved solid-liquid interface. Therefore, if $T_m^E \le T < T_m^A$, the liquid does not have enough driving force to grow continuously from the curved interface.

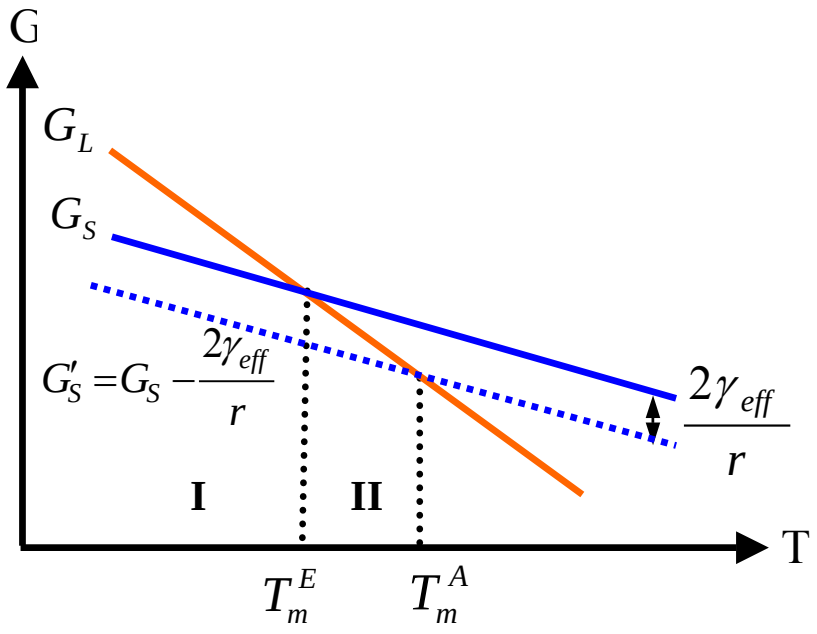

Figure 6.9. The free energy diagram of stage II ($T_m^E \le T < T_m^A$) in the void melting. See the text for details.

Figure 6.6(b) shows that a thin layer of liquid forms around the void surface at T = 0.630 ε / k_B, or with the superheating $\Delta T / T_m^E$ = 1.94% (Note T_m^A = 0.637 ε / k_B in this example system). Despite a thin layer of liquid nucleates around the void surface, the majority of the sample is still in crystal state. The time evolution of the total volume in Figure 6.5 also shows that the whole sample is still a solid. This thin liquid layer is stable at this temperature because the driving force is not enough for the liquid layer growing further. Indeed even after 200 000 isothermal MD runs (1 ns), we found that the thickness of the liquid layer does not change much, as shown in Figure 6.10.

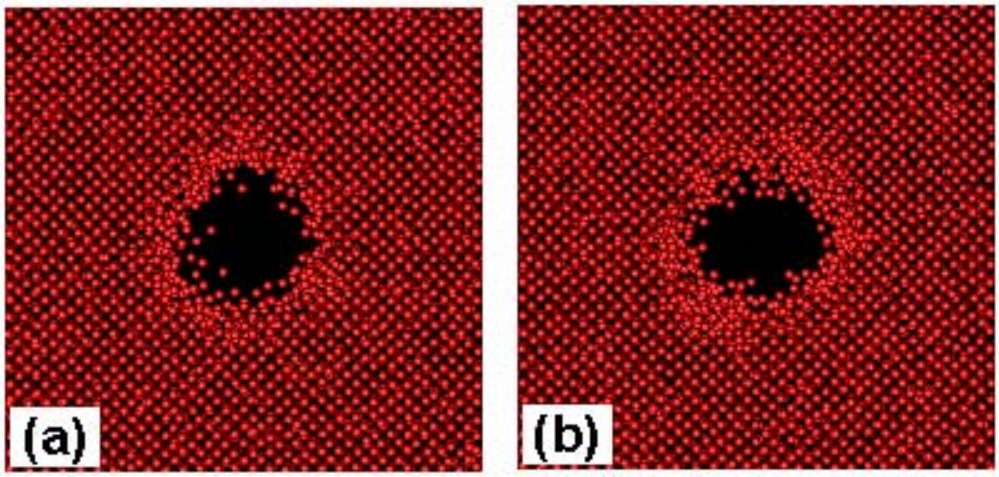

Figure 6.10. The cross-sectional snapshots of the sample at different simulation time in stage II. (a) Initial snapshot at T = 0.630. A thin liquid layer (represented by the disordered atoms) forms at this temperature. (b) After 200 000 isothermal runs, the thin liquid layer only changes slightly.

Stage III ($T_m^A \le T < T_m^B$): *The partially melted solid fills the void, the liquid and solid coexist, and the crystal host is stable*. If $T \ge T_m^A$, the liquid phase gains enough

driving force to overcome the energy barrier $2\gamma_{eff}/r$ induced by the curvature solid-liquid interface [Figure 6.9]. As a result, the thin liquid layer formed in Stage II grows. As shown in Figure 6.6(c) – (e), the liquid indeed grows at $T = 0.645\,\varepsilon/k_B$ or $\Delta T/T_m^E$ = 4.19% (Note $T_m^A = 0.637\,\varepsilon/k_B$ and $T_m^B = 0.663\,\varepsilon/k_B$ in this example system). Since the liquid has a larger molar volume than the solid, the liquid expands and gradually fills the void [Figure 6.6(c)]. After 80 000 steps (0.4 ns), the liquid fills the void completely and forms a homogeneous liquid droplet embedded in the superheated crystal [Figure 6.6(d)]. However, we find that the liquid droplet stops growing after it fills the void. Even after 200 000 (1 ns) MD steps at this temperature, its radius does not change much [Figure 6.6(e)]. Only when the system temperature increases, the liquid droplet can grow further.

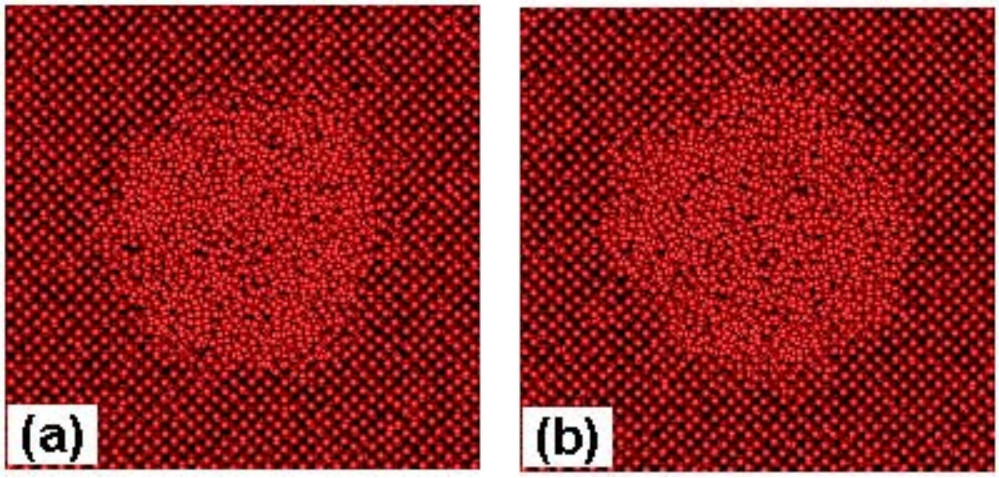

Figure 6.11. The stable coexistence between the liquid droplet (disordered region) and the crystal matrix. (a) Initial snapshot at T = 0.645. (b) After 130 000 isothermal runs, the thin liquid droplet only changes slightly.

As we have shown in Chapter 4, if the liquid droplet forms spontaneously from a superheated *perfect* crystal, it is in an *unstable* coexistence with its crystal host: it could either shrink or grow. However, if the liquid droplet forms from a void as shown in this chapter, shrinking is unlikely because the liquid has to decrease its entropy and recreate the void that was filled up before. On the other hand, if the liquid droplet grows further, the surrounding rigid crystal has to accommodate the expansion of the newly formed liquid [due to the larger molar volume of the liquid]. Consequently, a compressive pressure is generated that prevents the liquid from further growth. The elastic energy induced by the compressive pressure acts as an additional barrier. If the driving force is not enough to overcome the elastic energy, the growth of the liquid stops. The final outcome is that the liquid droplet can be in a *stable* coexistence (no shrinking or growing) with the surrounding crystal matrix. This stable coexistence is a unique characteristic of void melting, which cannot occur during the homogenous nucleation of a liquid in a perfect crystal [63,64]. Since the liquid droplet is embedded in the crystal matrix, the composite system is still like a crystal. As shown in Figure 6.5, the volume of the system at this stage is still close to the original crystal volume. However, there is a small bump in the system volume [indicated by a circle]. This bump indicates that the void is filled with the molten material. After the bump is formed, there is no clear change in the system volume, indicating that the liquid droplet does not grow further. Figure 6.11 shows the snapshots of the initial liquid droplet and the final liquid droplet after 130, 000 MD steps (0.65 ns). Clearly, the radius of the liquid droplet changes very slightly.

The free energy diagram of stage III is shown in Figure 6.12. Since the expansion of the liquid induces the elastic energy ΔE on the liquid droplet [63,64], the free energy

of the liquid phase increases from G_l to $G_l^{'} = G_l + \Delta E$. The intersection between $G_s^{'}$ and $G_l^{'}$ yields another local melting temperature T_m^B. If the temperature is higher than T_m^A (but less than T_m^B), the solid at the solid-liquid interface could melt and the liquid droplet grows. Consequently, the radius of the liquid droplet increases from r_A to r_B. The corresponding volume change of the liquid droplet is $\Delta V / V \sim \Delta r / r_A$, where $\Delta r = r_B - r_A$ and V is the volume of the liquid droplet at T_m^A. Therefore the elastic energy of the system is proportional to the volume change $(\Delta V / V)^2 \sim (\Delta r / r_A)^2$ [63,64]. As shown in Figure 6.12, in stage III the free energy of the solid ($G_s^{'}$) is always lower than that of the liquid ($G_l^{'}$). Thus, the liquid droplet would stay in equilibrium with the solid at each temperature between T_m^A and T_m^B. Different from the homogeneous melting where the volume change at melting is a step function, $\Delta V / V$ changes gradually in void melting as each layer of the solid atoms melts and shares the volume already occupied by the liquid. Therefore, the solid and the liquid could coexist at a series of temperatures above T_m^A due to the balance between the driving force and the elastic energy. The maximum melting temperature T_m^B is reached when the liquid growth can overcome the elastic energy ($G_s^{'} = G_l^{'}$). At this temperature, the system reaches a critical state where any further increase in liquid droplet volume at melting would be governed by the homogenous melting [63,64], or the solid becomes unstable and melts completely.

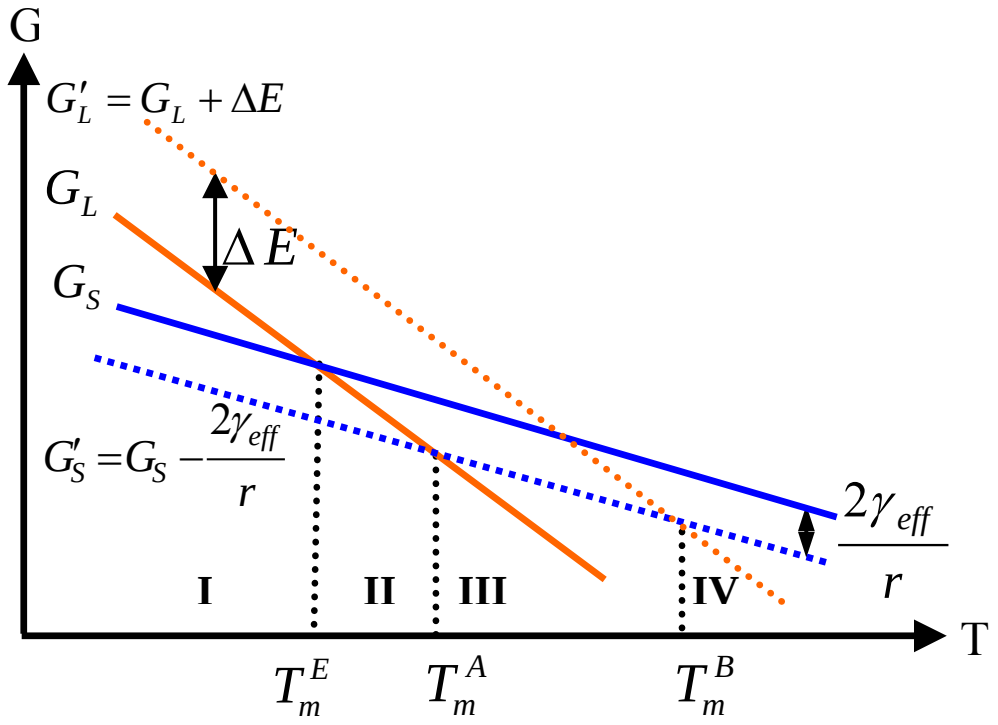

Figure 6.12. The free energy diagram of stage III ($T_m^A \le T < T_m^B$) and stage IV ($T \ge T_m^B$) in the void melting. See the text for details.

At T_m^A, The radius of the liquid droplet is minimum for the same void-containing sample. This is because if $T < T_m^A$, the liquid droplet cannot form; if $T > T_m^A$, the radius of the liquid droplet increases due to the larger driving force. When the void is just filled up at T_m^A, the internal pressure has not risen yet. Thus, we can assume that the elastic energy at T_m^A is very weak, because small amount of elastic energy could stops the liquid growth at this critical temperature. In order to estimate the radius of the liquid droplet at T_m^A, r_A, we propose the following relation.

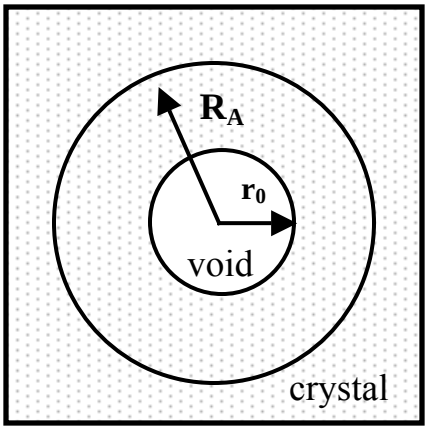

Figure 6.13. The model for estimating the final liquid droplet radius r_A at temperature T_m^A. All the crystal atoms in the shell between r_0 and r_A become liquid atoms that form a liquid droplet of radius r_A.

As shown in Figure 6.13, let the initial radius of the void be r_0 and the radius of the final liquid droplet be r_A when the void is completely filled at T_m^A. The number densities of a bulk solid and a bulk liquid are ρ_s and ρ_l respectively. If the number of atoms removed in creating the void is *n*, then we have $n = 4\pi r_0^3 \rho_s / 3$. Since the solid density is larger than the liquid density, the expansion of the liquid volume increases faster than the consummation of the solid volume. Thus the void is gradually filled by the liquid atoms. When the void is completely filled, the radius of the liquid droplet is r_A. Therefore, all solid atoms enclosed in the shell between r_A and r_0 become liquid atoms at T_m^A. Since the pressure is expected to be very small at T_m^A, the densities of the liquid and solid are very close to their bulk values. Given that the number of the atoms during the transition is conserved, we have the following relation,

$$4\pi(r_A^3 - r_0^{\,3})\rho_s / 3 = 4\pi r_A^3 \rho_l / 3, \tag{6.1}$$

where the left-hand side of Eq. (6.1) is the number of the crystal atoms in the shell between r_A and r_0, and the right-hand side is the number of liquid atoms in the liquid droplet of radius r_A. Using $n = 4\pi r_0^3 \rho_s / 3$ to replace either r_0 or *n* in Eq. (6.1), one can get

$$r_A = \left(\frac{3n}{4\pi(\rho_s - \rho_l)} \right)^{1/3} = \left(\frac{\rho_s}{\rho_s - \rho_l} \right)^{1/3} r_0 . \tag{6.2}$$

From Eq. (6.2), we know that r_A is determined only by the solid and liquid densities and the initial void size. The total system size (*N*) is irrelevant for determining r_A. For the sample shown in Figure 6.11(b), in which *n* = 1 505, $\rho_s = 0.935\,\sigma^{-3}$ and $\rho_l = 0.825\,\sigma^{-3}$ at $T_m^A = 0.637\,\varepsilon / k_B$ [61], we calculate $r_A = 14.8\,\sigma$ from Eq. (6.2). The direct measurement from our simulation yields $r_A = 14.3\,\sigma$. The two are in excellent agreement.

Stage IV ($T \geq T_m^B$): *Complete melting*. If *T* is higher than the maximum T_m^B, the liquid droplet has sufficient driving force to overcome the elastic energy ΔE. As shown in Figure 6.12, the solid becomes unstable if $T \geq T_m^B$. Thus, the liquid droplet can grow continuously until it consumes the entire sample. For example, at $T = 0.670\,\varepsilon / k_B$ or $\Delta T / T_m^E$ = 8.41% (note $T_m^B = 0.663\,\varepsilon / k_B$ in this example system), the whole system becomes a liquid [Figure 6.6(f)].

6.2.2. The Relation between T_m^A and r_0

By far we have shown that there are four stages in void melting and two local melting temperatures: T_m^A and T_m^B. At the local melting temperature T_m^A, the melting starts from the internal void surface and forms a liquid droplet. The elastic energy is not involved during this process. Thus the melting process is under the unpressurized condition and T_m^A is related to the void radius and the solid-liquid interfacial free energy. On the other hand, at the local melting temperature T_m^B, the melting starts from the pressurized liquid droplet and extends to the whole sample. Therefore T_m^B is the melting temperature of the whole system and is strongly related to the elastic energy. If we use the gradual heating method as many researchers did [55-59], only the melting temperature of the whole system can be obtained. The information of the stage III and the internal melting temperature T_m^A are completely missed. Moreover, as we have shown in Figure 6.4, the gradual heating yields strong hysteresis effects which overestimate T_m^B. Therefore, the isothermal heating method used in this work reveals the complete melting sequence of the void melting. Note there is another local melting temperature T_m^E at which a bulk solid and a bulk liquid can coexist with a flat surface. This thermodynamic melting temperature coincides with the melting point of the system with a flat solid-vapor surface (or $r_0 \to \infty$ in the void melting), at which $T_m^A = T_m^B = T_m^E$. In general, however, both T_m^A and T_m^B are functions of the initial void size r_0. By varying the void sizes, we can find the corresponding T_m^A and T_m^B.

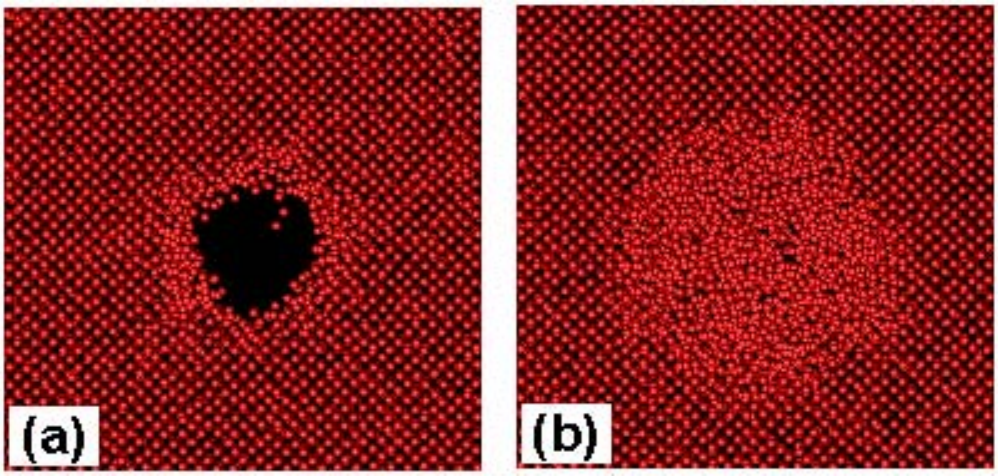

Figure 6.14. The procedure of using visualization to determine T_m^A. Here N = 108 000 and n = 1 505. (a) At T = 0.636, the thin liquid layer is stable after 200 0000 MD runs. (b) At T = 0.637, the void is filled up by the molten material.

Since T_m^A is the internal melting temperature at the void surface, it is difficult to determine it from the time evolution of the total volume (Figure 6.5). In order to determine T_m^A, we visualize the snapshots at different temperatures to determine whether the internal melting occurs. First we bring the system to a temperature T ($>T_m^E$) and hold the temperature isothermally for about 200 000 MD steps (1ns). If only a thin liquid layer forms around the void surface and the liquid layer is stable, the system is in stage II, or ($T<T_m^A$). Then in the next run the system temperature is increased slightly. If the liquid grows from the void surface and fills the void completely, the state of the system is in stage III, or ($T\geq T_m^A$). Accordingly, in the next run the system temperature is decreased slightly. After several runs, the critical temperature T_m^A can be located in a narrow

temperature range. For example, Figure 6.14(a) shows that a thin liquid layer nucleates around the void surface. This liquid layer is stable at $T = 0.636\ \varepsilon / k_B$ even after 200 000 MD steps. In Figure 6.14(b) the liquid grows into a spherical liquid droplet at $T = 0.637\ \varepsilon / k_B$. Thus we determine $T_m^A = 0.637\ \varepsilon / k_B$ for this sample. The estimation error is about $0.001\ \varepsilon / k_B$.

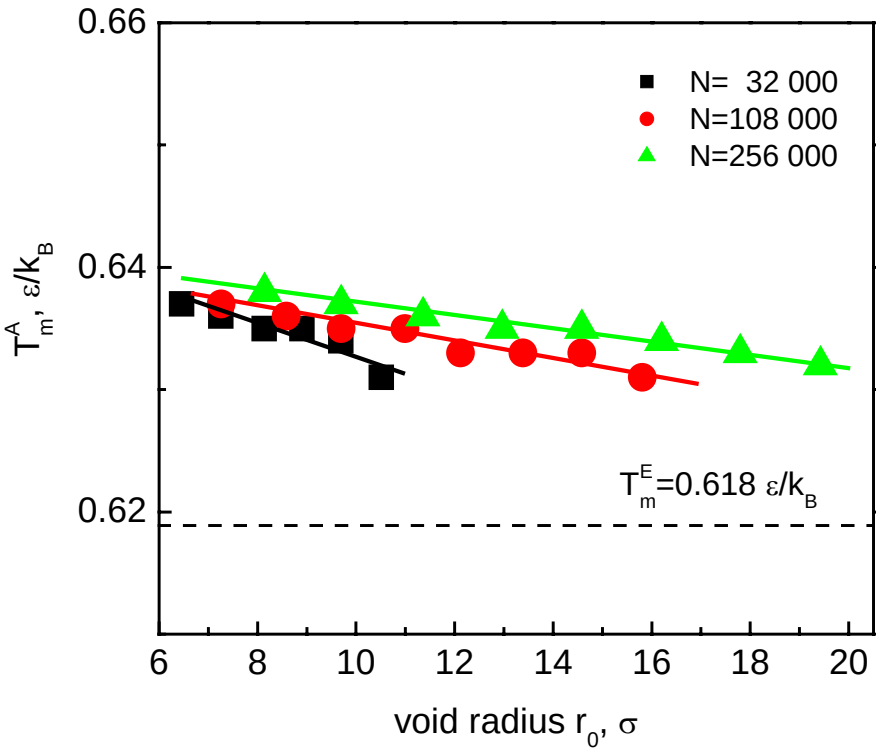

Figure 6.15. The internal melting temperature from the void surface (T_m^A) as a function of the void radius (r_0). Three sample sizes are used and the finite size effect is not strong. The equilibrium melting temperature T_m^E=0.618 ε / k_B is indicated by the dashed line.

Similarly, we can determine T_m^A for different size systems with various void radii. The relation between T_m^A and r_0 is shown in Figure 6.15. Three size systems are used: N = 32 000, 108 000, and 256 000. The result shows a weak finite size effect. For the same void size, T_m^A is slightly higher in the larger system. But the difference is very small among different size systems (only about 0.8% of T_m^A). Apart from the finite size effect, in all systems T_m^A decreases very slowly with the increasing void size. The values of T_m^A are within $0.63 \sim 0.64\,\varepsilon / k_B$, which are always higher than the thermodynamic melting temperature T_m^E=0.618 ε / k_B. This is because the void surface has a negative curvature [Figure 6.16(c)] compared to a flat solid-vapor surface [Figure 6.16(b)]. The liquid nucleation at the flat surface is a barrier-free process. Thus the melting of the system with a flat surface always occurs at the thermodynamic melting temperature T_m^E. In the void melting, the negative curvature of the void surface yields a nucleation barrier for void melting. Therefore, the melting temperature of a void-containing system (if the outer surface is removed) is always higher than the thermodynamic melting temperature. If the void radius goes to infinity, the void melting temperature T_m^A will approach T_m^E. On the other hand, a nanoparticle has a positive curvature [Figure 6.16(a)] compared to a flat surface. The positive curvature increases the free energy of the nanoparticle and the liquid can nucleate at the nanoparticle surface at a temperature lower than the thermodynamic melting temperature. As a result, the melting temperature of the nanoparticle is always lower than those of the other two.

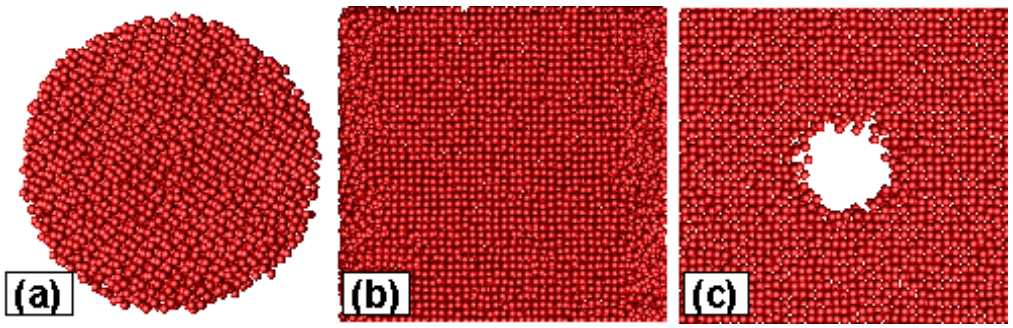

Figure 6.16. Three types of solid-vapor interfaces. (a) A nanoparticle of a positive surface curvature. (b) A flat surface of a zero surface curvature. (c) A void of a negative surface curvature.

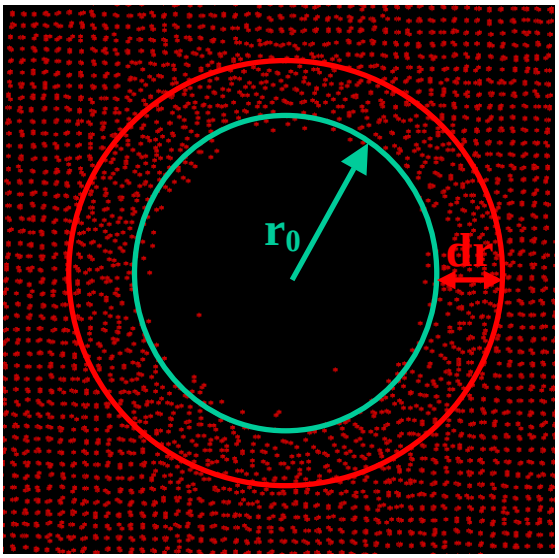

Figure 6.17. The effective radius of the solid-liquid interface in the void melting. r_0 is the initial void radius, and dr is the thickness of the solid-liquid interface (or the thin liquid layer). The effective radius is thus $r_0 + dr$.

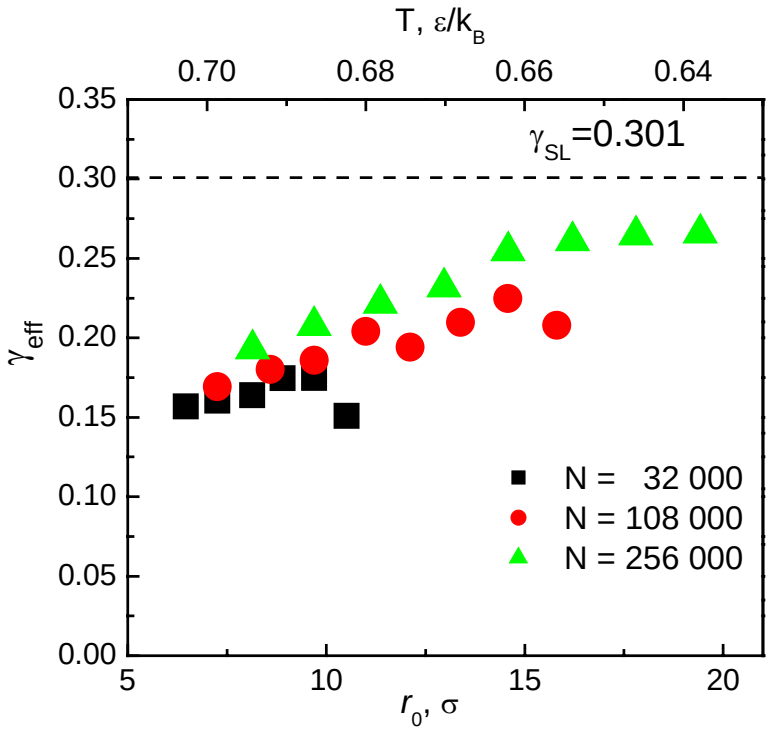

Figure 6.18. The effective interfacial free energy γ_{eff} as a function of the void radius. γ_{eff} increases with the increasing void radius (or with the decreasing temperature) and has a trend to approach the solid-liquid interfacial free energy.

As we have described in section 6.2.1, a thin liquid layer nucleates around the void surface if the temperature is lower than T_m^A [Figure 6.6(b)]. The thin liquid layer forms a solid-liquid interface, as shown in Figure 6.17. If the initial void radius is r_0 and the thickness of the liquid layer is *dr*, then the effective radius of the solid-liquid interface is $r = r_0 + dr$. This is similar to the melting of a nanoparticle, in which the effective radius is $r_0 - dr$ [141]. From our simulation, we find that *dr* is of about three atomic layers (~ $3.5\sigma \approx$ 1.2 nm). Since the elastic energy is absent before the void is completely filled, T_m^A is primarily determined by the curvature-induced interface free energy

$\Delta G_{\text{interface}} = 2\gamma_{eff} / r$ [Figure 6.12], where γ_{eff} is the effective interfacial free energy, and r is the effective radius of the solid-liquid interface. To grow, the liquid must overcome the excessive energy $2\gamma_{eff} /(r_0 + dr)$. At the superheating $\Delta T = T_m^A - T_m^E$, the driving force for the solid-liquid transition is $\Delta G_V = (\Delta T / T_m^E)\Delta L_V$, where $\Delta L_V = 1.024\,\varepsilon/\sigma^3$ is the latent heat of fusion per volume [61]. Therefore we have $(\Delta T / T_m^E)\Delta L_V = 2\gamma_{eff} /(r_0 + dr)$, or more explicitly,

$$\gamma_{eff} \approx \frac{(r_0 + dr)}{2}\frac{\Delta T}{T_m^E}\Delta L_V . \qquad (6.3)$$

Note that Eq. (6.3) has the same form as the classical nucleation theory (CNT). From Figure 6.15, the corresponding ΔT $(=T_m^A - T_m^E)$ for different initial void size r_0 in different size systems can be obtained. Using Eq. (6.3), we calculated the values of γ_{eff} for different void sizes, which are shown in Figure 6.18. The value of γ_{eff} is around $0.15\sim0.25\,\varepsilon/\sigma^2$. Independent calculation shows that the solid-liquid interfacial free energy is γ_{sl} =$0.30\,\varepsilon/\sigma^2$ [Chapter 3]. Figure 6.18 also shows that γ_{eff} has a tendency to increase slightly with the increasing r_0 (or with the decreasing temperature) and approaches γ_{sl} as $r_0 \to \infty$ (or $T \to T_m^E$). As a comparison, the value of the solid-vapor interfacial free energy is $\gamma_{sv} = 1.32\varepsilon/\sigma^2$ [142], and the value of the liquid-vapor interfacial free energy is $\gamma_{lv} = 0.82\varepsilon/\sigma^2$ [142]. Apparently, γ_{eff} is much closer to the solid-liquid interfacial free energy than the other two types of interfacial free energy. In other words, the melting temperature T_m^A is primarily determined by γ_{sl} rather than γ_{sv} and γ_{lv}. This result is a little bit surprising because many people may think the solid-

vapor interfacial free energy determines the melting temperature. However, from our four-stage analysis we can know that the solid-vapor interfacial free energy primarily determines the nucleation process, i.e., forming a thin layer of liquid around the void surface, while the solid-liquid interfacial free energy indeed controls the subsequent liquid growth from this thin liquid layer and determines the melting temperature T_m^A.

Since the smaller void radius corresponds to a higher T_m^A, we also can conclude that the interfacial free energy decreases with the increasing superheating. In Chapter 3 we have shown that the crystal-melt interface free energy decreases slightly with the increasing undercooling. Although the estimation errors may affect the accuracy of the interfacial free energy at the superheating regime [Figure 6.18], the general trend may be correct. It implies that the liquid nucleation barrier may further decrease at the upper limit of the superheating due to the decrease of the solid-liquid interfacial free energy. The method described in Chapter 3 is only can be used to estimate the interfacial free energy at the supercooling regime. In this chapter we show that the void melting could be a new method for estimating the crystal-melt interfacial free energy at the superheating regime.

6.2.3. The Relation between T_m^B and r_0

Since T_m^B is the temperature at which the system melts completely, we can determine it either by the visualization of the snapshots or from the time evolution of the total volume (Figure 6.5). In order to determine T_m^B, we bring a sample to different temperatures (higher than T_m^A) and monitor whether the complete melting occurs. If $T < T_m^B$, a liquid droplet forms and the liquid droplet is stable even after 200 000 MD steps

(1ns). Now the state of the system is in stage III. In the next run the system temperature is increased slightly. If the liquid droplet grows and expands to the whole system, the system melts completely and the state of the system is in stage IV, or ($T \geq T_m^B$). Accordingly, in the next run the system temperature is decreased slightly. After several trials and errors, the critical temperature T_m^B can be located in a narrow temperature range. For example, Figure 6.19(a) shows that the liquid droplet is stable at T = $0.662\,\varepsilon/k_B$ even after 200 000 MD runs. In Figure 6.19(b) the system melts completely at $T = 0.663\,\varepsilon/k_B$. Thus we determine $T_m^B = 0.663\,\varepsilon/k_B$ for this sample. The estimation error is about 0.001 ε/k_B. Note the liquid droplet in Figure 6.19(a) (at $0.663\,\varepsilon/k_B$) is bigger than that in Figure 6.14(b) (at $T_m^A = 0.637$).

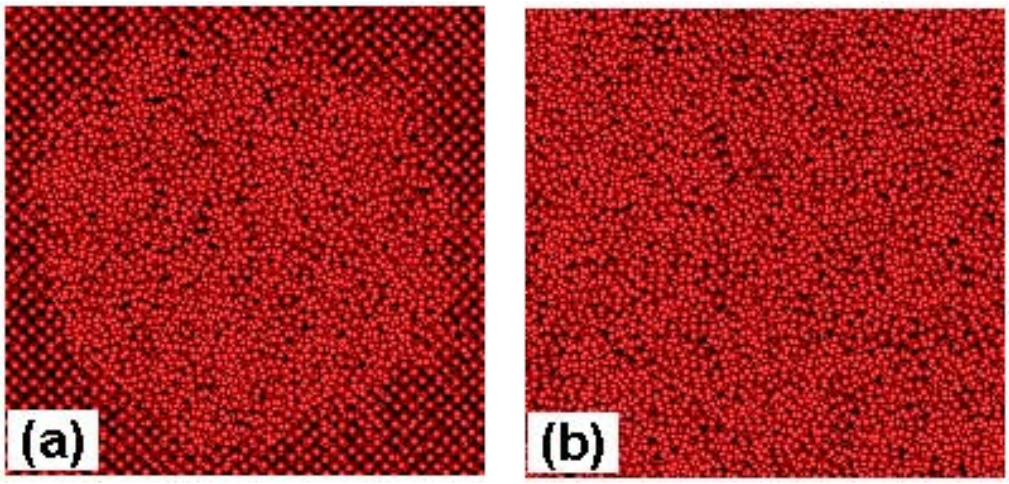

Figure 6.19. Determining T_m^B by using the visualization of the snapshots. Here N = 108 000 and n = 1 505. (a) At T = 0.662, the liquid droplet is stable after 200 0000 MD runs. (b) At T = 0.663, the system melts completely.

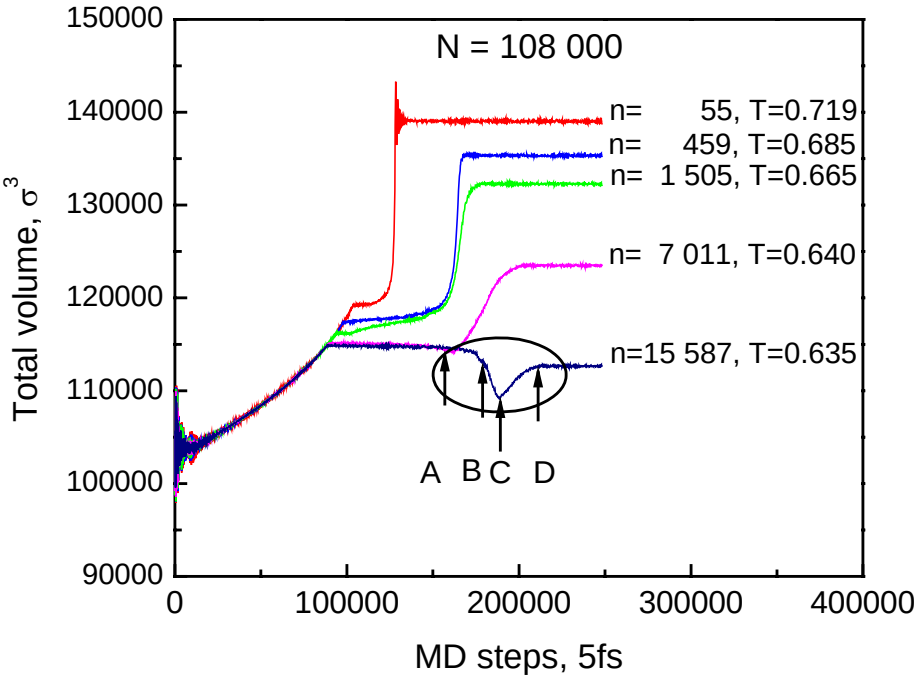

Figure 6.20. The total volume changes of systems with different void sizes during the melting. The circled region indicates the cavity effect when the void size is large. The snapshots at moments A-D are given in Figure 6.21.

The complete melting temperature T_m^B also can be determined by monitoring the change of the total volume, as shown in Figure 6.5. This is because the total volume increases substantially after the melting. However, this case is not always true. If the initial void size is large, the total volume may shrink after the melting in order to fill the empty void space. Figure 6.20 shows the total volume change during the melting for systems with different void sizes. If the void size is small, for example, if n = 55, 459, 1 505, and 7 011, the increase of the total volume is obvious. However, the liquid volume

decreases with the increasing void size, because more atoms are needed to fill the larger void space. If the void size is very large such as n = 15 587, the total volume decreases after the melting. Moreover, a dent (indicated by the circle) is shown in Figure 6.20. This dent is corresponding to the cavity effect, because the softened system cannot sustain the unfilled void space. The snapshots at A – D is shown in Figure 6.21.

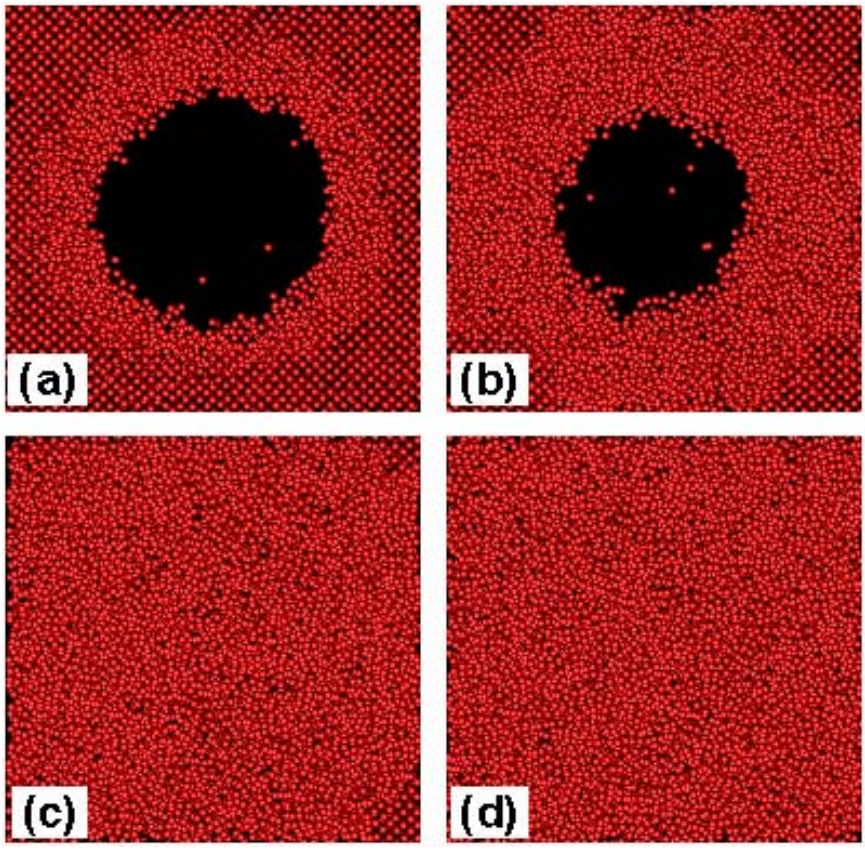

Figure 6.21. The snapshots at moments A-D indicated in Figure 6.20. (a) At moment A, the liquid grows from the void surface. (b) At moment B, the liquid front reaches the crystal boundaries but the void is still not completely filled. (c) At moment C, the void is filled, but the crystal can be seen at the corners. (d) At moment D, the system becomes a liquid.

Figure 6.21 shows the cavity effects induced by the large void size. At moment A in Figure 6.20, the liquid nucleates and grows at the void surface. Although the fraction of the crystal in the system decreases, it still can sustain the hollow space in the system. So the total volume does not change at this moment, as shown in Figure 6.20. At moment B, the liquid grows and reaches the boundaries of the simulation box. However, the empty space is not completely filled yet. The crystal is broken into several pieces at the corners of the simulation box by the liquid. Consequently, the crystal cannot sustain the hollow space. The system volume starts to shrink, which can be clearly seen in Figure 6.20. At moment C, the volume shrinkage "squeezes" the hollow space, and finally the empty space is completely filled at the expense of the decrease of the total volume. Only small amount of crystal can be found at the corners. The system volume is smallest at this moment [Figure 6.20]. At moment D, the system melts completely. The final volume of the liquid is smaller than the initial volume of the system (combination of the crystal and void), as shown in Figure 6.20. Since the void is not completely filled before the liquid reaches the boundaries, the elastic energy does not show up from moments A – D.

The relation between T_m^B and r_0 is shown in Figure 6.22. A strong finite size effect is shown. The larger system has the higher T_m^B. Apparently, T_m^B decreases very fast with the increasing void radius r_0 at the beginning. However, there exists a critical void radius beyond which T_m^B becomes leveled. We also found that for all three simulation systems of different sizes, the asymptotic temperature is about 0.635 ε / k_B or $\Delta T / T_m^E$ = 2.8%. This is the so-called "plateau" temperature observed by others in void melting.

Many considered it as the thermodynamic melting temperature T_m^E, despite the fact that it is about 2.8% higher than T_m^E.

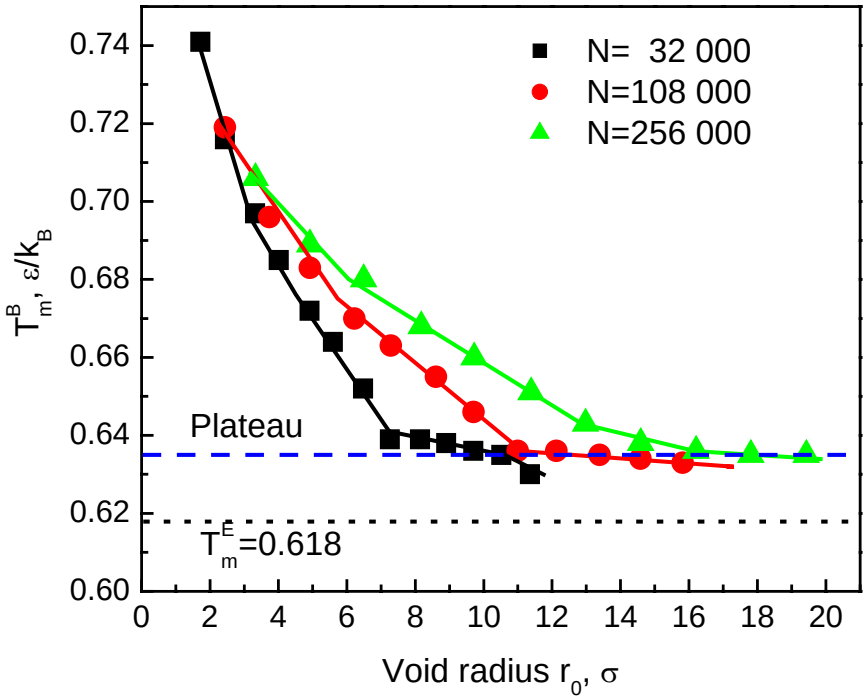

Figure 6.22. The complete melting temperature T_m^B as a function of the void radius r_0. A strong finite size effect is shown. In all size systems, $T_m^B > T_m^E$.

The underlying mechanisms for the fast decay and the plateau of T_m^B can be understood from the following two aspects: (1) The elastic energy scales with the void radius as $1/r^2$ [63,64], while we know from above that the interface free energy scales with $1/r^\delta$ with $\delta < 1$ due to the dependence of γ_{eff} on r. Clearly, the volume dependent ΔE, or T_m^B, changes faster than the surface curvature dependent T_m^A with r_0. At small r_0,

the ΔE dependence is dominant; and as r_0 becomes bigger, the surface energy and curvature begin to dominate. The crossover point marks the beginning of the plateau. (2) The distribution of voids also influences the rate of decay in T_m^B vs. r_0, which is manifested as a finite size effect as seen in Figure 6.22. In our simulation, the voids with the same size are present uniformly as the periodic images. After the void is completely filled by the liquid that grows from the void surface at $T = T_m^A$, the radius of the liquid droplet is r_A. Note that the compressive pressure has not shown up before the void is completely filled. If the radius is smaller than one half of the simulation box length *L*, i.e., $r_A < L/2$, the droplet is still embedded in the crystal host [Figure 6.19(b)]. Therefore, the system temperature needs to be increased above T_m^A in order to overcome the elastic energy. As a result, the melting temperature of the total system, T_m^B, is higher than the internal melting temperature, T_m^A. This case happens when the initial void size r_0 is small. If $r_A \geq L/2$, the liquid droplet begins to connect its "neighboring" liquid droplets (induced by the periodic boundary conditions) [Figure 6.23(a) and (b)]. The newly merged droplet has a bigger effective radius. Thus T_m^B decays faster and approaches the slow changing T_m^A [Figure 6.22]. Actually if the initial void size is big, the front of the solid-liquid interface can reach the boundaries of the simulation box *before* the void is completely filled at $T = T_m^A$ [Figure 6.23(c)]. In this case the shape of the liquid is a shell, not a spherical droplet. Thus, the liquid can continuously consume the whole sample because there is no compressive pressure to stop the liquid growth. As

a result, the melting temperature of the total system, T_m^B, is as same as the internal melting temperature, T_m^A, if the condition $r_A \geq L/2$ is satisfied.

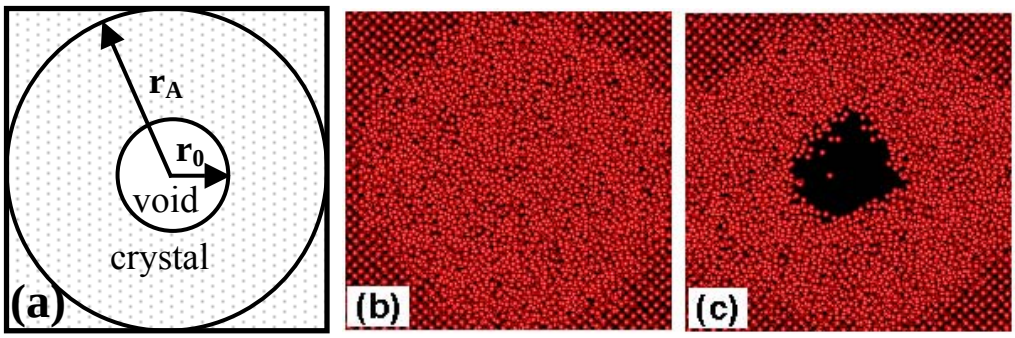

Figure 6.23. The critical condition under which the elastic energy will not show up. (a) Illustration of the critical condition. If the radius of liquid droplet at T_m^A, r_A, reaches the boundaries of the simulation box, the elastic energy will not show up. (b) A snapshot of a system with a critical liquid droplet at T_m^A. The radius of the critical liquid droplet is half the edge length of the simulation box. (c) A snapshot of a system with an unfilled space when the liquid reaches the boundaries at T_m^A.

For the same r_0, the smaller the sample size is, the smaller the distances between the droplet and its periodic images are. Since these distances are directly related to the elastic energy, we see the finite size effects on the decay region in Figure 6.22. This finite size effect can be removed if we plot T_m^B versus the volume fraction of the void, $f_{void} = n/N$ [Figure 6.24], where *N* is the total number of atoms in the sample before a void is created, and *n* is the number of atoms removed for creating this void. The melting

temperatures of all three systems indeed behave similarly. The data becomes identical in three size systems and can be well fitted with a universal line. This result implies that the volume fraction of the void is more important than the void size itself for determining the melting temperature.

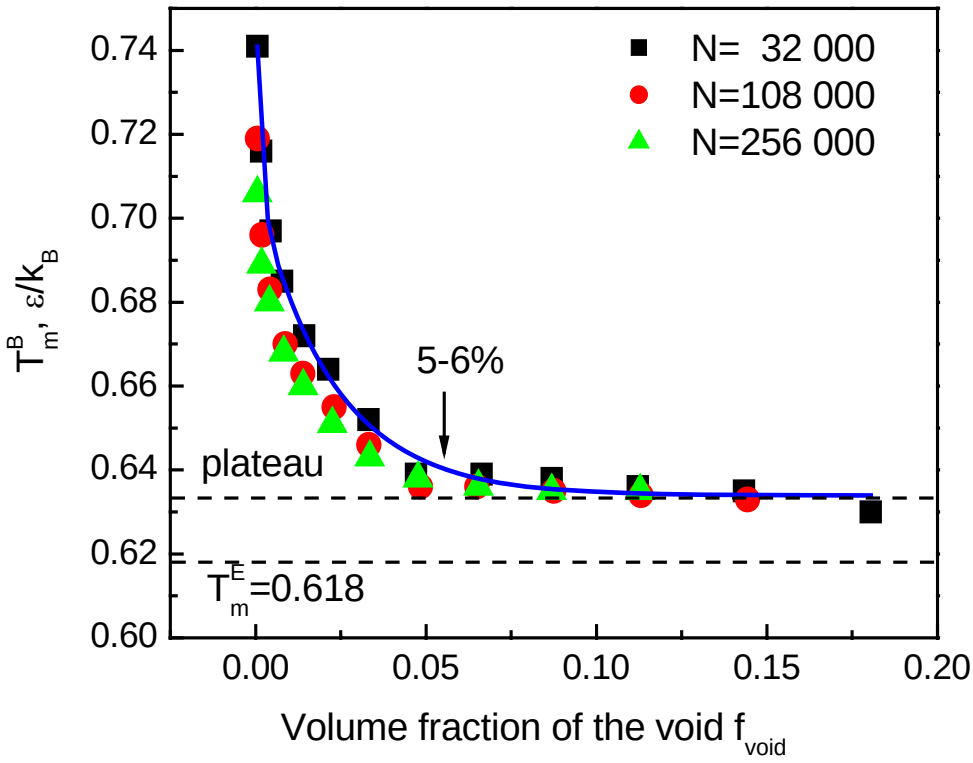

Figure 6.24. The complete melting temperature T_m^B as a function of the volume fraction of the void. The finite size effects are removed compared to Figure 6.22. The critical volume fraction for reaching the plateau is estimated to be 5-6%.

In addition, we found in Figure 6.24 that the plateau (i.e., $T_m^B \to T_m^A$) occurs at a universal f_{void}^*=5-6%. As shown in Figure 6.23, the critical condition for the presence of the plateau region is

$$r_A^* = \frac{L}{2} = \frac{(N/\rho_s)^{1/3}}{2}, \tag{6.4}$$

where the relation $N = \rho_s L^3$ is used to derive this equation. From Eq. (6.2), which is $r_A = \left(\frac{3n}{4\pi(\rho_s - \rho_l)} \right)^{1/3}$, and Eq. (6.4), we proposed a quantitative relation to predict the critical void size n^* or the critical volume fraction of the void f_{void}^*, as shown by

$$f_{void}^* = \frac{n^*}{N} = \frac{\pi}{6}\left(\frac{\rho_s - \rho_l}{\rho_s} \right). \tag{6.5}$$

Therefore, the critical volume fraction for the presence of the plateau in Eq. (6.5) is only related to the densities of the solid and liquid. Given that $\rho_s = 0.935\sigma^{-3}$ and $\rho_l = 0.825\sigma^{-3}$ at $T_m^A = 0.637\varepsilon/k_B$ [61], this theoretical prediction yields f_{void}^*=6.2% for the uniformly distributed void-containing systems, which is in excellent agreement with the simulation result which is about 5-6% in Figure 6.24.

6.3. Discussion and Conclusions

In this chapter, the melting in the solids containing nanovoids has been studied by using molecular dynamics simulations. The finite size effects are treated with different size systems. For the first time, we have found four typical stages and three melting temperatures in the void melting that are different from the melting of bulk materials and

nanoparticle. As a result, the local melting temperatures show a strong dependence on the void size, which is the root cause for the observed complex hierarchical melting sequence.

By far we have established that the melting from nanovoids are determined by three factors: interface curvature, solid-liquid interfacial free energy, and the elastic energy. The elastic effect is important for a liquid nucleating *within* a solid. For example, the migration of the liquid droplets to the grain boundaries [143] is clearly a stress-driven event. The strain energy in void melting also could be verified in experiment. For instance, one can embed the void-containing materials in a crystal matrix to suppress the melting from the surface. Melting is expected to initiate from the internal void surface. The results of this work may also help us understand the melting and freezing of the pore filling materials [144,145]. In reality, the above three factors would change depending on systems and testing conditions. For example, in nanoporous materials, the voids can be open or closed, or interconnected. The melting is expected to initiate from the pore surfaces with positive curvatures. Since the elastic energy can be relaxed quickly for the voids that are open or connected, melting may be dominated by the interface curvature and the sold-liquid interface energy. For the materials with closed or isolated voids, elastic energy will appear and dominate melting.

Since the void surface has a negative curvature, the melting temperature of a void-containing system is higher than the thermodynamic melting temperature. On the other hand, the positive curvature of a nanoparticle results in a melting temperature lower than the thermodynamic melting temperature except when they are surrounded by the matrix with different elastic moduli. The zero curvature of a flat surface makes the melting occur

right at the thermodynamic melting temperature. In void melting, the transition has four distinct stages: (a) a stable void surface; (b) a thin liquid layer nucleating around the void surface; (c) the internal melting in which the liquid grows to form a liquid droplet. The liquid droplet is in a stable equilibrium with the superheated crystal matrix; (d) the complete melting of the system. In nanoparticle melting [141], which is the counterpart of the void melting, the free surface is always open and thus the elastic energy is not involved during the melting. The relation between the melting temperature and the nanoparticle size is as same as Eq. (6.3) except that $r_0 + dr$ should be replaced by $r_0 - dr$ [141].

The internal melting temperature T_m^A is determined by the effective solid-liquid interfacial free energy and the effective curvature of the solid-liquid interface. Many people may think the surface (or solid-vapor interface) free energy determines the melting temperature in void or nanoparticle melting. Actually, the solid-vapor interfacial free energy contributes the liquid nucleation from the disordered void surface, while the solid-liquid interfacial free energy determines the subsequent liquid growth from this thin layer. We have found that the effective solid-liquid interfacial free energy increases with the increasing void radius and has a trend to approach the exact solid-liquid interfacial free energy. It also has a tendency to decrease with the increasing superheating. At T_m^A, the liquid starts to grow from the thin liquid layer nucleating around the void surface and finally fills the void completely to form a liquid droplet. The arising compressive pressure on the liquid droplet stops the further liquid growth. Thus, the liquid droplet can be in a stable coexistence with the surrounding superheated crystal matrix. The stable coexistence is a unique characteristic of the void melting, which is different from the

homogeneous nucleation of a liquid droplet in a perfect crystal matrix. In the latter case the liquid droplet either shrinks or grows. Since T_m^A is reached before the liquid droplet forms, it is not affected by the elastic energy. Thus T_m^A also can be viewed as the unpressurized melting temperature in the void melting.

On the other hand, the complete melting temperature T_m^B is strongly related to the elastic energy. The elastic energy results in an additional barrier for the liquid growth. Consequently, the liquid droplet must gain enough driving force at the higher temperatures to overcome the elastic energy. Therefore, T_m^B is elevated above T_m^A. When the initial void size increases, T_m^B decreases rapidly with the increasing void size. If the initial void radius is large enough, the liquid can reach the boundaries of the system *before* the void is completely filled. After the liquid reaches the boundaries, the crystal is broken into several pieces and the complete melting occurs. During such process, the elastic energy does not appear because the void is not completely filled. As a result, once the system temperature reaches the internal melting temperature T_m^A, the system can melt completely. In other words, the internal melting temperature T_m^A and the complete melting temperature T_m^B are same. In such case, the complete melting temperature reaches the so-called "plateau" region. The physical origin for the appearance of this plateau is that the elastic energy is absent when void size is large. Basing on this argument, we have proposed a relation to estimate the critical volume fraction of the void for the presence of the plateau. Our proposed relation predicts that the critical volume fraction is about 6%, which is in good agreement with the value of 5-6% estimated from the simulations. The relation between T_m^B and void radius also shows a finite-size effect.

However, this size dependence can be removed by plotting T_m^B as a function of the volume fraction of the void.

The above results are valid for the system with uniformly distributed nanovoids. Although there is only a single void in the system, the periodic boundary conditions make the system resemble a system with evenly distributed voids. In reality, there is always a non-uniform distribution of voids of various sizes. The growth of the liquids leads to coarsening, or joining of neighboring voids, which would change the effective void sizes and, therefore, the local melting temperatures T_m^A and T_m^B. This will undoubtedly lead to competing melting kinetics in void-containing solids: The bigger voids can melt easily and thus grow bigger, while the smaller ones will grow slower and may be "eaten" by the fast growing bigger ones, which resembles the Ostwald ripening [97] in grain growth. In addition, if the melting temperatures of the larger voids are shifted toward T_m^A as the voids grow bigger, their melting temperatures will not change much with further increase of the void sizes. This will lead eventually to the homogenization of the local melting temperatures over the entire sample.

The result in this work represents an extreme case of the melting with volume shrinkage. For example, the liquid densities of the silicon and water are higher than their solid densities. When melting occurs in such systems, the volume shrinks which is different from the volume expansion in the melting of a LJ system. From our results of the void melting, we expect that superheating still exists in such systems but the melting process may be primarily determined by the surface-curvature and the solid-liquid interfacial free energy.

CHAPTER 7

HOMOGENEOUS MELTING AND RING DIFFUSION AT THE UPPER LIMIT OF SUPERHEATING

In Chapter 4, the thermodynamics of melting in a wide range of superheating temperatures has been investigated by using a homogeneous nucleation model. It is found that the solid superheating cannot be simply viewed as an inverse process of the liquid supercooling. The classical nucleation theory well describes the thermodynamics of a supercooled liquid, but fails to describe that of a superheated solid. The key difference is that elastic energy caused by the liquid expansion during the melting plays an important role in affecting the liquid nucleation, while no such effect presents in the supercooling process. As a result, a nucleation forbidden gap appears to prevent the liquid nucleation and melting from the bulk. If the system consists heterogeneous nucleation sites such as free surfaces, the melting starts from these places at the thermodynamic melting temperature. This could be one of the reasons for which the crystallization always requires some undercooling but melting usually occurs at the equilibrium melting temperature [1]. In Chapter 6, the melting from nanovoids has been investigated (note the melting from a free flat surface is an extreme case of void melting when the void radius becomes infinite). This is a heterogeneous process because the disordered void surface provides the heterogeneous nucleation sites. The melting always initiates at the void surface and propagates to the whole sample. Since the void surface has a negative curvature relative to a flat surface, the melting temperature in void melting is higher than the thermodynamic melting temperature. The void melting is a complex process because

there are four melting stages and three types of melting temperatures. The interplay of the elastic energy, void size, system size, and interfacial free energies (solid-vapor, liquid-vapor, and solid-liquid) determines the complex hierarchical melting sequence.

The melting investigated in the above two chapters takes place from either the preformed liquid nuclei or the heterogeneous nucleation sites. Another interesting problem of general interests is how a liquid nucleates in a perfect (i.e., surface-free and defect-free) crystal to trigger the melting at the upper limit of superheating. Although this problem has been studied extensively over the past century [7-12,14-25], the microscopic mechanism is still unclear. Since all materials have surfaces, the superheating is difficult to achieve in experiments because the surface melting is always dominant. However, the superheating can be obtained if the surface melting is suppressed by using special techniques. For example, Daeges and Gleiter [10] coated a thin gold layer around a silver sphere. Since the lattice constants of the gold and silver are very close, it is equivalent that the free surface of the silver is "removed". Moreover, the melting temperature of the gold is higher than that of the silver. Therefore, the silver can melt earlier than the gold and the melting starts from the bulk. It was observed that the silver is superheated up to 25 K for a time period of about one minute. Superheating can also be achieved by the picosecond pulsed laser irradiation [11,12,22,24]. The laser irradiation heats the materials internally and initiates the melting from the bulk. Substantial superheating (about 20% above the normal melting point) has been observed from these experiments. Unfortunately, the melting is extremely fast in these experiments. Typically, the transition time is of a few nanoseconds. Thus, it is difficult to investigate the detailed microscopic mechanism of melting at the superheating from these experiments.

Recently, the computer simulation [17-20,23,25] becomes an important tool for studying the superheating problem. To achieve maximum superheating, the system needs to be surface-free and defect free. Such systems can be easily prepared in computer simulations. The free surface can be removed by using the periodic boundary conditions (PBCs) [13]. The defects can be excluded by arranging the atoms in a perfect crystal lattice. Due to such convenience, the melting at the upper limit of superheating has been investigated extensively in computer simulations. Several instability theories [15,16,19,20] have been developed to interpret the melting mechanism. Born [15] proposed that the melting occurs when the shear modulus falls to zero at high temperatures. This theory is based on the fact that a liquid does not have a shear modulus. Originally Born shear instability theory was proposed for the melting from the free surface, and later it was applied for the melting at the superheating. Lindemann [16] proposed a vibrational lattice instability theory in which the melting is triggered when the root-mean-square displacement (RMSD) of atoms reaches a critical fraction of the nearest neighbor distance. Some researchers [17,18,146] claimed that they have bridged the above two instability criteria for the melting at superheating. Fecht and Johnson [19] proposed an entropy catastrophe theory that is analogous to Kautzmann's paradox [20,21] for the glass transition. They argued that the entropy of a superheated solid increases continuously due to the presence of the defects such as voids at high temperatures. When the entropy of a solid equals to that of a liquid, a catastrophe or melting occurs instantly, because it is against the physical law if the entropy of a solid is larger than that of a liquid. The interstitial instability model [147-152] states that at high temperatures the thermal fluctuations create interstitial defects. These interstitial defects have higher

energy state and cause the instability of the system. If the interstitial defects aggregate to a critical number, the melting occurs. Forsblom and Grimvall [147,148] artificially inserted interstitial-vacancy pairs into a crystal aluminum lattice to create interstitial defects. Their results show that the critical number of point defects is about ten. Another instability model is the dislocation-line model [153-155]. At high temperatures, the thermal fluctuations and distortions create some defective atoms. Usually the atoms whose first nearest neighbors are not twelve are defined as the defective atoms. When these atoms become neighbors of each other, they can be connected by a line, which is usually called dislocation line. Many researchers claimed that the melting occurs when the length of the dislocation line is close to the system length [153-155].

Another interesting topic is whether the homogeneous melting is a first-order or second-order transition. According to Ehrenfest's classification, the first-order transitions are accompanied by a discontinuous change of state, while the second-order transitions are accompanied by a continuous change of state [156]. Due to the aforementioned instabilities and catastrophes, most researchers viewed the melting at superheating as a first-order transition [15,157,158]. However, in Fecht and Johnson's model [19], the entropy difference between liquid and solid phases goes to zero continuously, which is similar to a glass transition (a second-order transition). Moreover, Hansen and Verlet [159] argued that the melting is a second-order transition.

In this chapter, we will investigate the mechanism of the homogeneous melting at superheating. Various instability theories such as the Born shear instability theory, Lindemann vibrational instability theory, the interstitial instability model, and the evolution of the number of the first nearest neighbors will be discussed. Particularly, we

will use the isothermal heating method to investigate the nucleation process at temperatures slightly below the upper limit of superheating. We have found that the ring diffusion occurs in the superheated crystal and the self-diffusion of the crystal atoms is related the nucleation process. The order of the transition will also be discussed in this chapter.

7.1. Gradual Heating and Isothermal Heating

In Chapters 2-6, the simulation systems contain either different phases or defects. In this chapter, we use a perfect crystal to investigate the homogeneous melting. Initially all atoms of the same type are arranged in an fcc lattice. Periodic boundary conditions are applied in all directions. Therefore the system is both surface-free and defect-free. The atoms interact via a standard Lennard-Jones (LJ) potential $\phi(r) = 4\varepsilon[(\sigma/r)^{12} - (\sigma/r)^{6}]$, where $\varepsilon = 119.8k_B$ and $\sigma = 3.405\overset{0}{A}$. The parameters ε and σ are used as the reduced units of the energy and length respectively. The temperature unit is in $\varepsilon / k_B \approx 120\ K$. The cutoff distance is set to 2.5σ. Molecular dynamics simulations are performed in a constant number of atoms, constant-pressure, and constant-temperature (NPT) ensemble. The Parrinello–Rahman method [68] is used to control the system pressure and the Nose thermostat [69] is used to control the system temperature. The pressure of the system is kept at zero throughout the simulations. The MD time step was set to 5×10^{-15} sec.

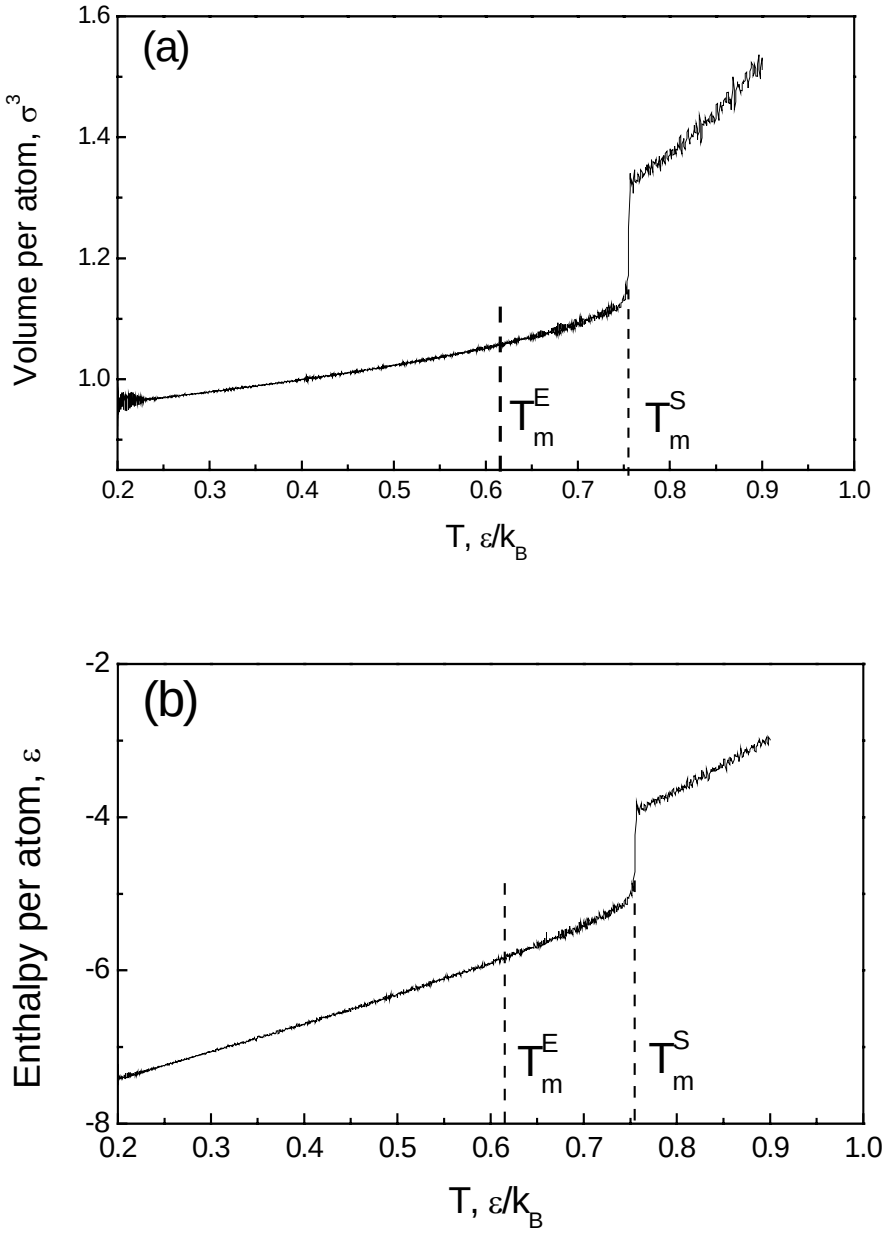

Figure 7.1. The melting in the gradual heating method. The number of atoms in the system is 4 000. The melting occurs at the upper superheating limit $T_m^S = 0.76\,\varepsilon / k_B$. (a) The change of the volume per atom with the increasing temperature. (b) The change of the enthalpy per atom with the increasing temperature.

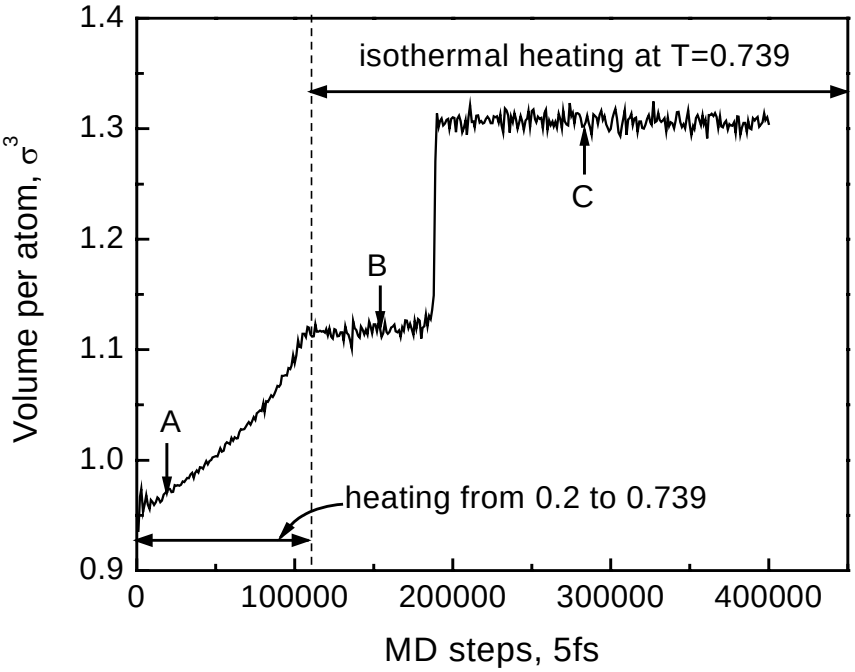

Figure 7.2. The evolution of the volume per atom with the simulation time in the isothermal heating method. The melting occurs at $0.739\,\varepsilon/k_B$. The number of atoms in the system is 4 000. The snapshots at A, B, and C are shown in Figure 7.3.

There are two methods to melt the sample: gradual heating and isothermal heating. The gradual heating method is to heat the sample continuously from a low temperature to a high temperature with a constant heating rate. This method has been used extensively by many researchers for investigating the homogeneous melting at the upper limit of superheating. The isothermal heating method is to hold the system isothermally at a desired temperature. Figure 7.1 shows the melting process in the gradual heating method. The sample is heated continuously from $0.2\,\varepsilon/k_B$ to $0.9\,\varepsilon/k_B$ with a heating rate of 1.33×10^{11} K/s. The number of atoms in this sample is 4 000. As the

temperature increases, the system volume and enthalpy increases. At $T = 0.76\,\varepsilon / k_B$, both the volume and enthalpy jump to a higher value (i.e., a catastrophe occurs) which corresponds the melting transition. Usually this temperature is called the upper limit of the superheating, T_m^S. The equilibrium melting temperature T_m^E is defined as the temperature at which a bulk solid and a bulk liquid coexist with a flat interface. For a LJ system, $T_m^E = 0.618\,\varepsilon / k_B$. Thus the maximum superheating is $(T_m^S - T_m^E)/T_m^E \approx 23\%$.

Figure 7.2 shows the melting process in the isothermal heating method. The system is heated from $0.2\,\varepsilon / k_B$ to $0.739\,\varepsilon / k_B$ with a heating rate of 1.33×10^{11} K/s. At $T = 0.739\,\varepsilon / k_B$, the heating is stopped and the temperature is held isothermally. Initially the system is in crystal state. The thermal fluctuations in the system aggregate the defective atoms in this stage. After about 180 000 MD steps, a catastrophe of the system volume occurs and the system transforms from crystal state to liquid state very quickly. Thus, using the isothermal heating method, we find the melting occurs at $0.739\,\varepsilon / k_B$, which is about 3% lower than T_m^S. This difference is caused by the hysteresis effect in the gradual heating method. In Chapter 6, we have found the hysteresis effect caused by the gradual heating method in the void melting. The gradual heating yields a melting temperature about 8-9% higher than that obtained from the isothermal heating. In the homogeneous melting, this effect is not very strong but still obvious. The snapshots at time A (T = 0.3), B (T = 0.739, before melting), and C (T = 0.739, after melting) are shown in Figure 7.3. At the low temperature of $0.3\,\varepsilon / k_B$ [Figure 7.3(a)], the atoms vibrate slightly around their equilibrium sties and the structure is close to a perfect fcc crystal. At the high temperature of $0.739\ \varepsilon / k_B$ [Figure 7.3(b)], some atoms are

disordered but the crystal structure still maintains before the melting occurs. After melting occurs at this temperature [Figure 7.3(c)], all atoms are away from their equilibrium sites and become liquid atoms. Thus in the isothermal heating, there is a long time that the crystal keeps the crystal symmetry. By logging the atom positions in this critical period, we can investigate the kinetic motion of atoms before the catastrophe occurs. In the gradual heating method, it is difficult to gain such detailed information because the transition is too fast.

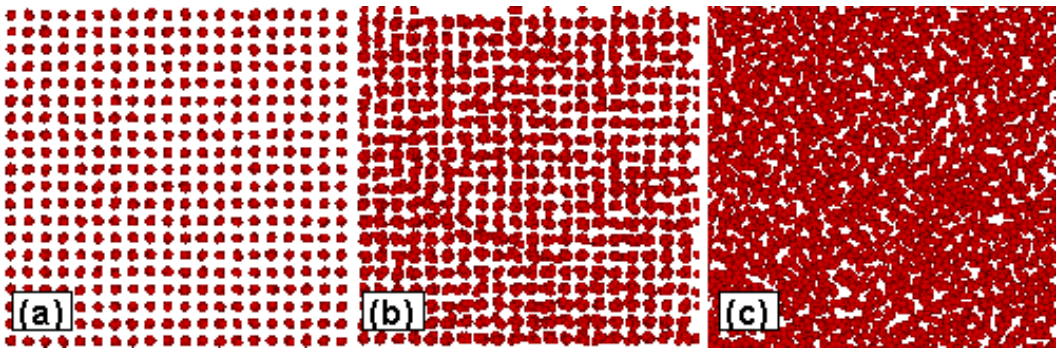

Figure 7.3. The snapshots at time A, B, and C [indicated in Figure 7.2]. (a) Time A, T = $0.3\,\varepsilon/k_B$. (b) Time B, T = $0.739\,\varepsilon/k_B$, before melting. (c) Time C, T = $0.739\,\varepsilon/k_B$, after melting.

Using the isothermal method, we also find a slight finite size effect on the melting temperature. Figure 7.4 shows the melting temperature as a function of the sample size. As the sample size increases from 500 to 32 000, the melting temperature increases slightly from $0.725\,\varepsilon/k_B$ to $0.740\,\varepsilon/k_B$. When the number of atoms is larger than 4 000, the melting temperature approaches the asymptotic value of $0.740\,\varepsilon/k_B$. The size

dependence may be related to the thermal fluctuations. The larger fluctuations in the smaller system could cause the premature melting. Thus the melting temperature shows a finite size effect. However, the finite size effects are not as significant as those in Chapters 3-6. This is because we use a pure system without any defect and interface. The systems used in the previous chapters contain either different phases or defects. Under such circumstances, the interaction between the sample and its periodic images is strong. Thus, the inhomogeneity usually causes strong finite size effects.

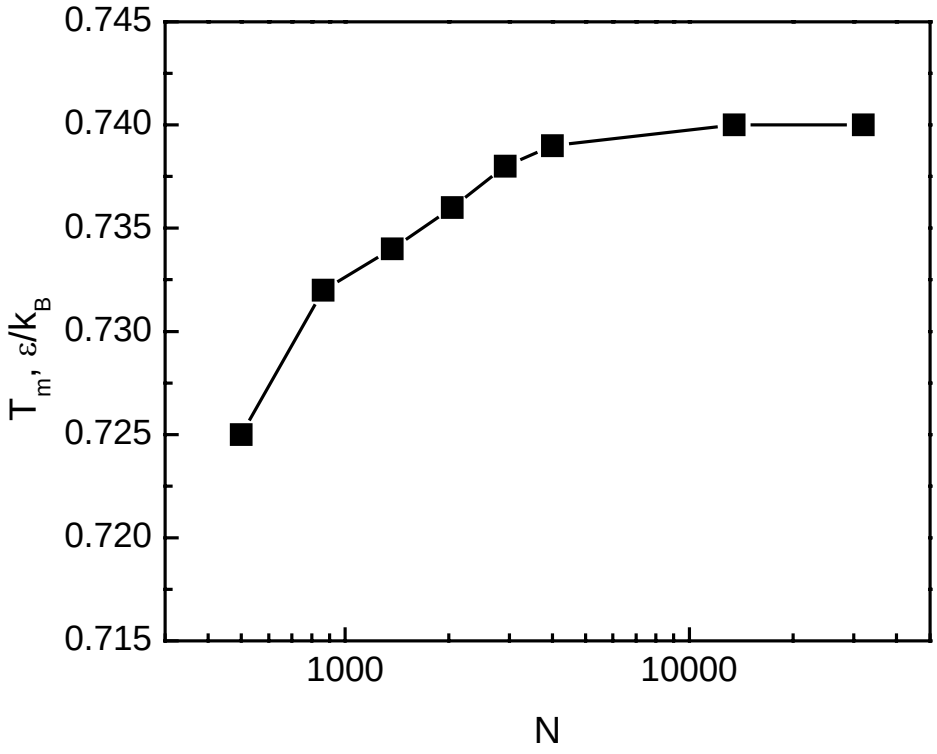

Figure 7.4. The size-dependent melting temperature obtained from the isothermal heating method. The melting temperature approaches $0.740\,\varepsilon / k_B$ at large sample sizes. The bottom axis is plotted with the logarithmic scale.

7.2. Instability Theories and Melting Criteria

7.2.1. Born Shear Instability Theory

Born [15] proposed that melting occurs when one of the crystal shear moduli falls to zero. The melting process is to break the translational symmetry of the crystal into the disordered structure of the liquid whose shear modulus is zero. In Born theory, the mechanical instability is responsible for this order-to-disorder transition. For an fcc crystal, there are two shear moduli: C_{44} and $C' = (C_{11} - C_{12})/2$. In Chapter 2 we have presented the method for calculating the elastic constants in the MD simulation. The temperature-dependent elastic moduli, C_{11}, C_{12}, C_{44}, and C', are shown in Figure 7.5. Before melting occurs, all elastic moduli decrease almost linearly with the increasing temperature. The relation among these elastic moduli is $C_{11} > C_{12} > C_{44} > C'$. At the melting temperature T_m^S =0.74 ε / k_B, the value of shear modulus C' is about $4.78\,\varepsilon/\sigma^3$ ($\approx$0.2 GPa). This value is very small relative to those at the low temperatures, but it is not zero. If the shear modulus C' is linearly extrapolated to high temperatures, it approaches zero at $T = 0.95\ \varepsilon / k_B$, which is about $1.54\,T_m^E$ (note $T_m^E = 0.618\,\varepsilon / k_B$ for the LJ system). Apparently, Born shear instability criterion overestimates the melting temperature at superheating. Similarly, Tallon [20] argued that Born melting criterion is incorrect or at least incomplete. Lu and Li [14] argued that the homogeneous nucleation as a kinetic instability occurs in advance of the shear instability, volume catastrophe, and entropy catastrophe. Therefore, the Born shear instability may not be observable. In Chapter 3, we also demonstrated that the critical nucleus size is only of about 10-20 atoms at the superheating limit. The large thermal fluctuations at high temperatures can

easily create such critical or postcritical nuclei. Therefore, it is possible that melting occurs with the non-trivial shear modulus. The validity of Born criterion is thus questionable.

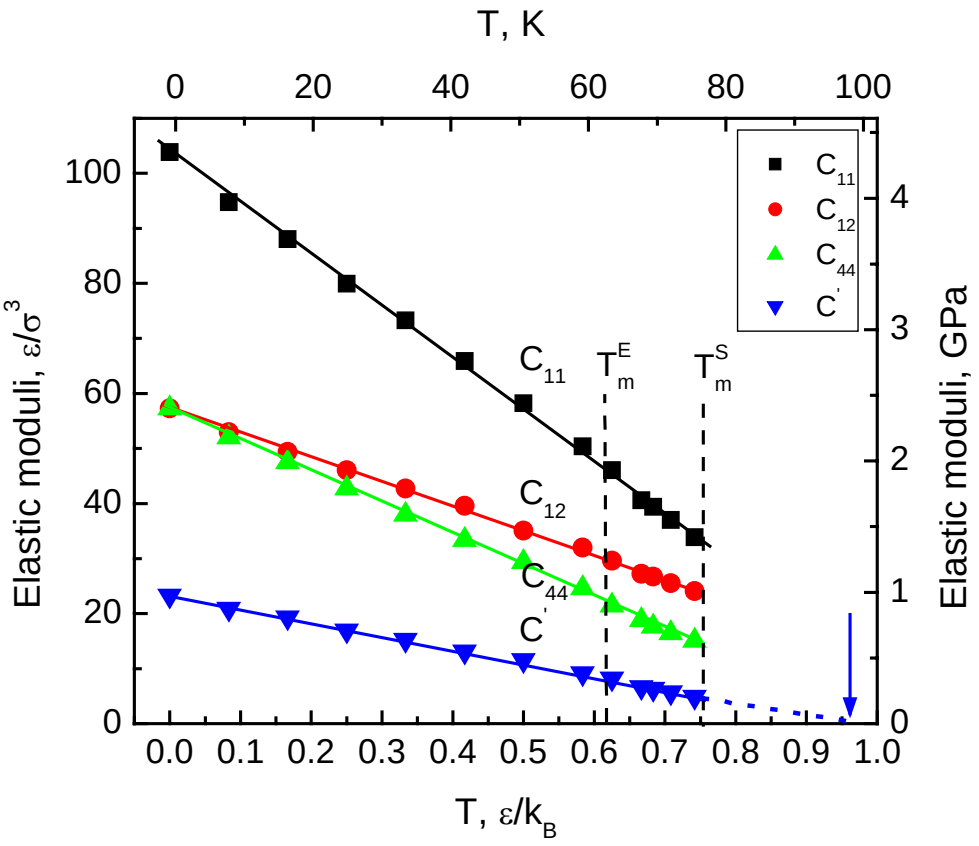

Figure 7.5. Temperature-dependent elastic moduli of a LJ crystal. The equilibrium melting temperature T_m^E and the superheating limit T_m^S are indicated by the dashed lines. The linear decrease of the elastic moduli indicates the crystal is softening with increasing temperature. The shear modulus C' still has finite value at the superheating limit T_m^S. The arrow indicates the temperature at which the extrapolation of C' approaches zero (Born shear instability). Bottom and left scales: in reduced LJ units; Right and top scales: in real units (GPa and K).

7.2.2. Lindemann Vibrational Instability Theory

At low temperatures, the crystal atoms vibrate slightly around their equilibrium sites. At high temperatures, the amplitude of the vibration becomes large. Lindemann [16] argued that the crystal loses its translational symmetry if the average vibration amplitude of the crystal atoms approaches a critical value (about 20-30% of the first nearest distance). Lindemann vibrational instability is often used as a criterion to define the upper limit of the superheating. Some researchers [7] even claimed that the Born shear instability and Lindemann vibrational instability occur simultaneously to trigger the melting at the superheating limit.

The vibrational amplitude of the atoms is usually expressed in term of the mean square displacement (MSD). The mean square displacement is a measure of atoms moving away from their initial positions. If the initial position of atom i at time $t = 0$ is $\vec{r}_i(0)$ and the new position at time t is $\vec{r}_i(t)$, the instantaneous square displacement of atom i is $\left|\vec{r}_i(t) - \vec{r}_i(0)\right|^2$. The mean square displacement is calculated by taking the average over all atoms in the system,

$$S^2(t) = \frac{1}{N}\sum_{i=1}^{N}\left|\vec{r}_i(t) - \vec{r}_i(0)\right|^2 . \qquad (7.1)$$

The Lindemann parameter x_L is defined as the ratio of the root-mean-square displacement $S(t)$ to the average distance between nearest neighbors $\bar{r}_{nn}$ [160], $x_L = \frac{S(t)}{\bar{r}_{nn}}$, which is a fractional quantity. The average distance between nearest neighbors can be calculated by the equation $\bar{r}_{nn} = \frac{\sqrt{2}}{2}a_0 = \frac{\sqrt{2}}{2}(4V_n)^{1/3}$, where a_0 is the

lattice constant and V_n is the average volume per atom. Figure 7.6 shows the change of the mean square displacement with the increasing temperature. At low temperatures, the MSD is small. As the temperature increases, the MSD increases as well. At the superheating limit, the MSD increases suddenly. The critical MSD measured from Figure 7.6 is about $0.12\sigma^2$. Using $V_n = 1.14\sigma^3$ [Figure 7.1(a)], we calculate the critical Lindemann parameter $x_L^* \approx 0.295$. This is in good agreement with Ziman's $x_L^* \approx 0.2$-0.25 [49], and Jin *et al.*'s $x_L^* \approx 0.22$ [17].

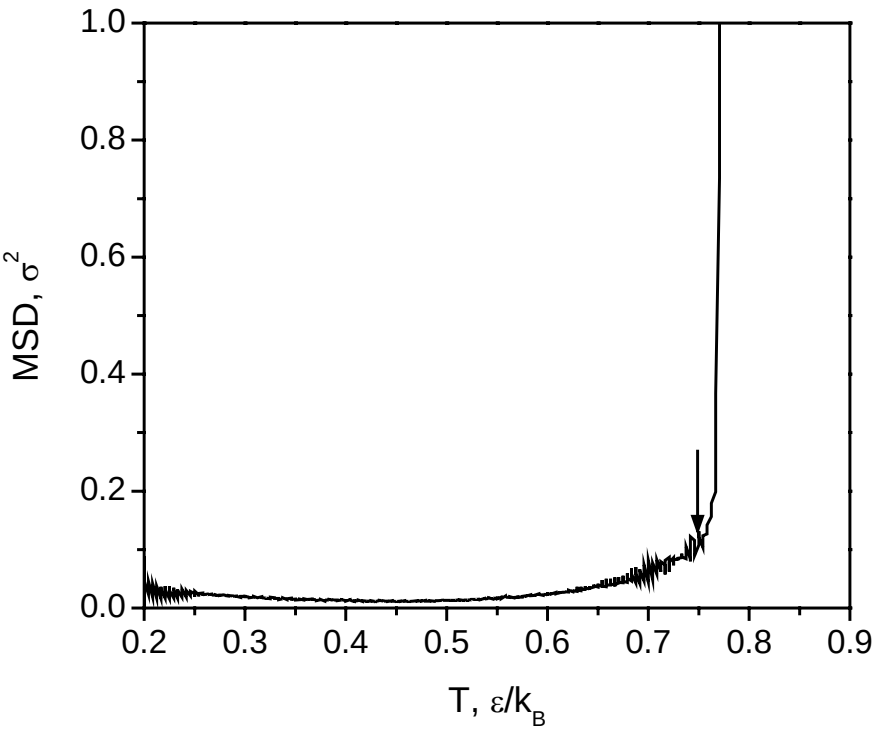

Figure 7.6. Mean square displacement (MSD) of atoms as a function of temperature. The arrow indicates the critical MSD at which melting occurs.

7.2.3. Interstitial Instability Theory

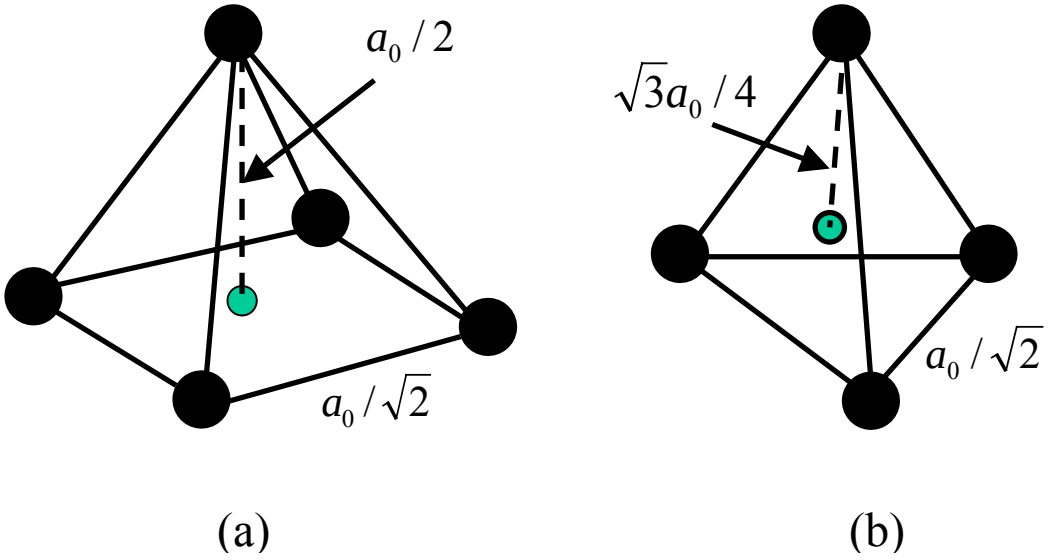

Figure 7.7. Two types of interstitial sites in an fcc crystal. The distance between an interstitial site (filled circle in green) and an atom (filled circle in black) is indicated by a dashed line in each figure. (a) Octahedral site. (b) Tetrahedral site.

The instability caused by the interstitial defects has been discussed recently [147-152]. If an atom jumps from a lattice site to an interstitial site, it creates an interstice-vacancy pair. The interstitial atom intends to push the surrounding atoms away from their equilibrium sites. Thus, the interstitial defect is in a high-energy state and could cause the instability to the system. For an fcc crystal, there are two types of interstitial sites: octahedral site [Figure 7.7(a)] and tetrahedral site [Figure 7.7(b)]. Forsblom and Grimvall [147,148] artificially inserted interstice-vacancy pairs into the crystal lattice to trigger the melting. They found that usually 6-7 interstitials and 3-4 vacancies could trigger the melting. However, a fundamental question is that whether the formation of such

interstice-vacancy pairs can occur naturally in a superheated crystal. As shown in Figure 7.7, the distance between an atom and an octahedral site is $r_{oct-atom} = a_0 / 2$ and the distance between an atom and a tetrahedral site is $r_{tet-atom} = \sqrt{3} a_0 / 4$, where a_0 is the lattice constant of an fcc crystal. At the temperature close to the superheating limit, $a_0 \approx 1.58\sigma$. Therefore, $r_{oct-atom} = 0.79\sigma$ and $r_{tet-atom} = 0.68\sigma$. Prior to melting, if the thermal fluctuations generate an interstitial defect, the distances between the defective atom and its surrounding atoms should be at least close to $r_{oct-atom}$. If the interatomic distance is even shorter, the tetrahedral interstice is likely to form. In order to check whether atoms can enter the interstitial sites, we did the following investigation. We heated a perfect crystal of 500 atoms from T = $0.2\varepsilon / k_B$ to its superheating limit $0.725\varepsilon / k_B$. At this temperature, the system is held isothermally for about 700 000 MD steps. Initially the system is in the crystal state and finally becomes a liquid. During this process, we calculated the distances between all atoms and found a shortest interatomic distance. The minimum interatomic distance is logged during this process as shown in Figure 7.8. During the heating period, the shortest interatomic distance decreases almost linearly with the increasing temperature, implying that atoms can displace longer and longer from their equilibrium sites. At T = $0.725\varepsilon / k_B$, the shortest distance is about 0.9σ, no matter what state of the system is. Most importantly, the shortest interatomic distance is much larger than $r_{oct-atom} = 0.79\sigma$ and $r_{tet-atom} = 0.68\sigma$. This result indicates that the atoms are unlikely to enter the interstitial sites for triggering the melting. Even if the system is in the liquid state, the shortest interatomic distance is still about 0.9σ. Therefore the validity of the interstitial instability is also questionable.

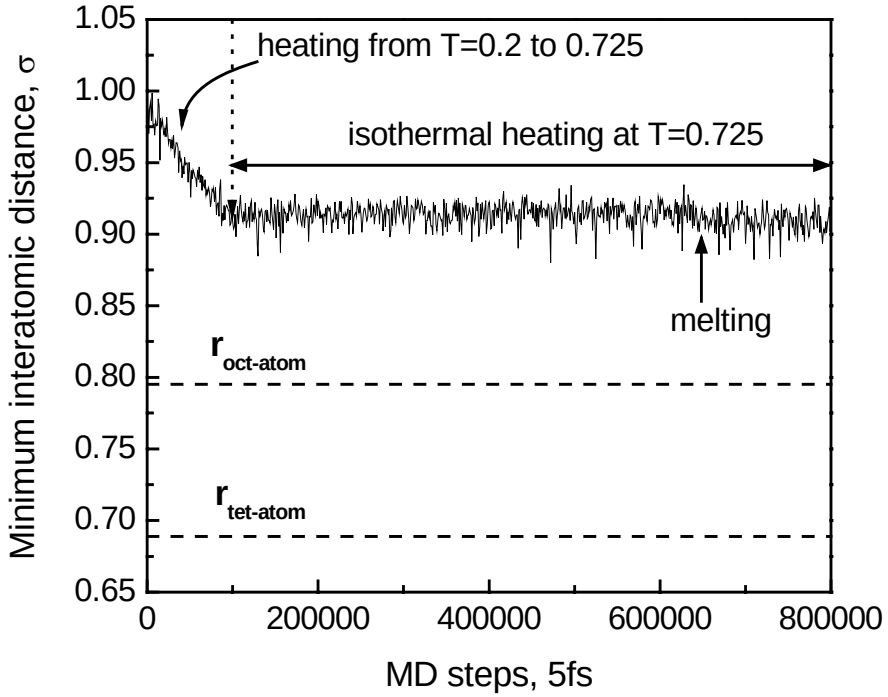

Figure 7.8. The evolution of the shortest interatomic distance with the simulation time. The system contains 500 atoms. The system temperature is increased from 0.2 to 0.725 ε / k_B and held at 0.725 ε / k_B isothermally. The gradual heating and isothermal heating periods are separated by the dotted line. The ideal distance between an octahedral interstitial site and a neighboring atom is indicated by $r_{oct-atom}$, and that between a tetrahedral interstitial site and a neighboring atom is indicated by $r_{tet-atom}$.

7.2.4. Relation between the Crystal Enthalpy at T_m^S and Liquid Enthalpy at T_m^E

At the same temperature, the enthalpy (note at $P = 0$ it is the internal energy) of a liquid is always higher than that of a crystal. However, the enthalpy of a superheated crystal can be higher than the enthalpy of a supercooled liquid. Similarly, the density of a superheated crystal also can be higher than the density of a supercooled liquid. Thus it is interesting to investigate if there is any connection between the crystal enthalpy and

liquid enthalpy at the critical temperatures T_m^E and T_m^S. Belonoshko *et al.* [161] used a constant-number of atoms, constant-volume, and constant-enthalpy (NVE) ensemble to investigate the melting at the superheating limit of a LJ system. Initially they provided the system with some kinetic energy and thereafter let the system relax. Upon melting at the superheating limit, they found that the system temperature drops from T_m^S to T_m^E at the corresponding pressure. The decrease of the temperature is due to the absorption of the latent heat for melting. Since the energy and volume in the NVE system is conserved, they concluded that the internal energy of a crystal at T_m^S is equal to that of a liquid at T_m^E at the same volume. More precisely, the "internal energy" should be replaced by "enthalpy", because the pressures are non-zero in their simulations. However, it is unclear whether this relation is related to the simulation ensemble. In our work, we did a test in a NPT ensemble to check the validity of this relation. We heated a single crystal from $0.2\,\varepsilon/k_B$ to $0.9\,\varepsilon/k_B$ and then cooled the system from $0.9\,\varepsilon/k_B$ back to $0.2\,\varepsilon/k_B$. During this heating-cooling process, the temperatures at the superheating limit (T_m^S=$0.76\,\varepsilon/k_B$) and of the spontaneous crystallization (T_c=$0.42\,\varepsilon/k_B$) can be obtained. The equilibrium melting temperature is determined in Chapter 3: T_m^E=$0.618\ \varepsilon/k_B$. The enthalpies per volume, which are $H_s\rho_s$ for the crystal and $H_l\rho_l$ for the liquid, are calculated at different temperatures, where H_s and H_l are the enthalpy per atom of the respective solid phase and liquid phase, ρ_s is the crystal density, and ρ_l is the liquid density. Figure 7.9 shows the crystal and liquid enthalpies per volume as a function of the temperature. It can be clearly seen that the crystal enthalpy per volume at T_m^S is lower

than the liquid enthalpy per volume at T_m^E. Thus, Belonoshko *et al.*'s argument [161] is not valid in the NPT ensemble.

The discrepancy may be caused by the incomplete melting in their NVE ensemble. Since an NVE ensemble is an isolated system, the energy is conserved. If a phase transition such as crystallization and melting occurs, the associated latent heat (either released or absorbed) comes from the system itself. The pressure and the system temperature change accordingly to accommodate the phase transition in the NVE ensemble. If the crystal is not fully melted, the liquid can coexist with the remaining crystal at the thermal dynamic melting temperature T_m^E at a corresponding pressure. Even if the remaining crystal is very small, the coexistence still exists because no external energy is induced to melt the crystal. As a result, the system temperature always drops to the equilibrium melting temperature at the corresponding pressure, as shown in Belonoshko *et al.*'s work [161]. In a NPT ensemble, the system can absorb sufficient energy from the external "thermostat" and the sample can become a pure liquid. Thus, the coincidence of the crystal enthalpy per volume at T_m^S and the liquid enthalpy per volume at T_m^E may be caused by the artifact of the NVE system. Actually, Morris and Song [162] have used this method to determine the thermodynamic melting temperature T_m^E in an NVE ensemble.

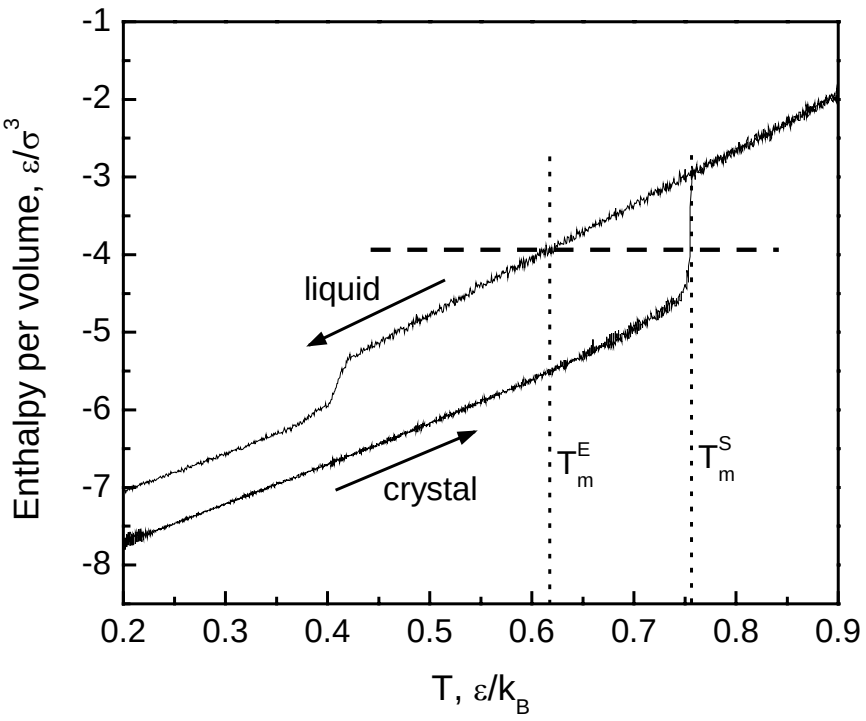

Figure 7.9. The enthalpy per volume as a function of the temperature during the heating-cooling process. The crystal enthalpy per volume at the superheating limit T_m^S is not equal to the liquid enthalpy per volume at the equilibrium melting temperature T_m^E (indicated by the dashed line).

7.2.5. Number of the First Nearest Neighbors

The number of the first nearest neighbors is an important characteristic of the crystal symmetry. For a perfect fcc crystal, this number is twelve. If the crystal structure changes, the number is different from twelve. Since the melting is an order-to-disorder transition, the number of the first nearest neighbor changes during the transition. In many researchers' work [153-155], an atom is defined as a defective atom if the number of its first nearest neighbors is not twelve. At high temperatures, the thermal fluctuations could aggregate the defective atoms to form clusters. Some researchers defined such clusters as

"dislocation lines". In order to investigate the evolution of the number of the first nearest neighbors, we calculated the average number of the first nearest neighbors. The critical cutoff distance for determining the first nearest neighbors is taken as the value at which the pair distribution function (PDF) of an fcc crystal reaches its first minimum [Figure 2.6]. Empirically, we chose this value as 1.35σ.

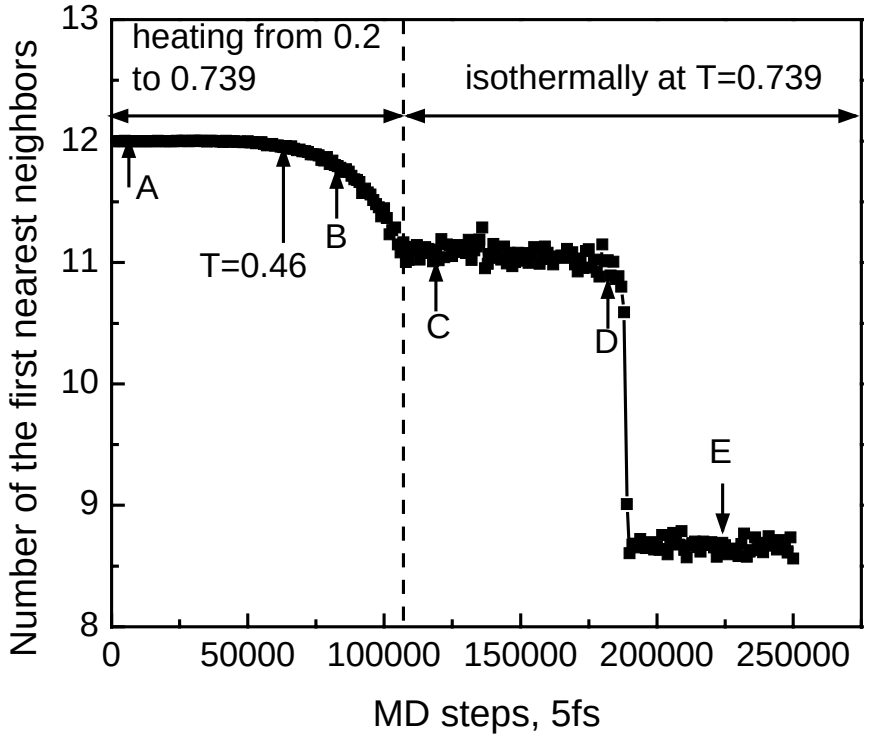

Figure 7.10. The evolution of the average number of the first nearest neighbors during the melting process. At T=0.46 ε / k_B, the number deviates from twelve. At T=0.739 ε / k_B, the number drops from 11 to 8.6 upon the melting. The distributions of the number of the first nearest neighbors at time A-E are shown in Figure 7.11.

Figure 7.10 shows the average number of the first nearest neighbors as a function of the simulation time. At low temperatures, the number is exactly twelve, indicating that

the crystal has a perfect fcc structure. As the temperature increases, the thermal fluctuations make atoms deviate from their equilibrium sites and some atoms may loose some nearest neighbors. As a result, the average number decreases with the increasing temperature. At T=0.46ε / k_B, the decrease of the average number becomes obvious. After the temperature reaches $0.739\varepsilon / k_B$, the system is held isothermally. Before melting occurs, the average number is about eleven. After melting occurs, the average number drops to 8.6.

In order to investigate the distribution of the number of the first nearest neighbors at different stages, we picked five typical stages A-E as shown in Figure 7.10 for investigation. The distribution is to show the fraction of atoms that have *n* nearest neighbors. The distributions are shown in Figure 7.11. At time A (T=0.205), one can find that 100% of atoms have 12 nearest neighbors, indicating that the crystal has a perfect fcc structure. At time B (T=0.588), one can find that about 80% of atoms have 12 nearest neighbors, about 19% of atoms have 11 nearest neighbors, and 1% of atoms have 10 nearest neighbors. This means that the crystal structure has some distortions, but the fcc structure is still maintained. At time C and D (T=0.739, but before melting occurs), the distributions are almost identical. Only 40% of atoms have 12 nearest neighbors. Some atoms even have only 8 nearest neighbors. The average number of the nearest neighbors is about 11. At time E (T=0.739, but after melting occurs), the distribution is very flat because the liquid is very disordered. The number of the nearest neighbors ranges from 4-12 and the average number is about 8.5 for the liquid.

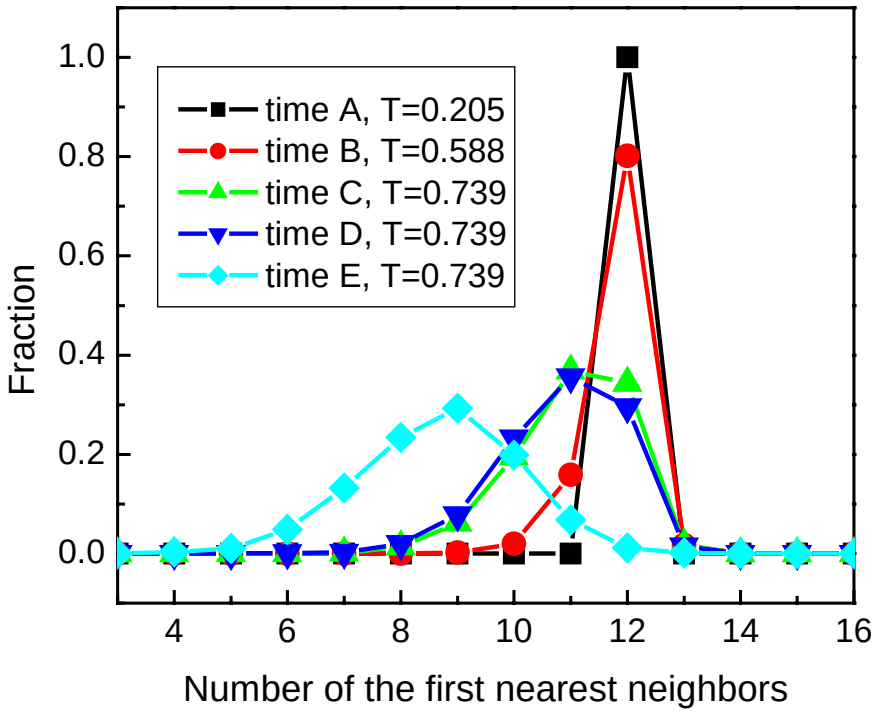

Figure 7.11. The distributions of the number of the first nearest neighbors at different stages. The stages A-E are indicated in Figure 7.10. See the text for details.

7.3. Ring Diffusion in a Superheated Crystal

7.3.1. Mean Square Displacement during the Isothermal Heating

Lindemann vibrational criterion states that a superheated crystal becomes a liquid when the mean square displacement (MSD) reaches a critical value. We have verified this criterion during the gradual heating as shown in Figure 7.6. In order to check the Lindemann criterion in the isothermal heating, we calculated the mean square displacement of 4 000 atoms at a temperature of $0.738\,\varepsilon / k_B$, which is slightly below the melting temperature of $0.739\,\varepsilon / k_B$. The temperature is held isothermally at this

temperature for about 700 000 MD steps and the sample does not melt. The MSD in this period is shown in Figure 7.12. At the end of the calculation, the MSD reaches about $0.8\sigma^2$ which is much larger than the critical value of Lindemann criterion (~$0.12\sigma^2$). It seems that the Lindemann criterion is not valid during the isothermal heating.

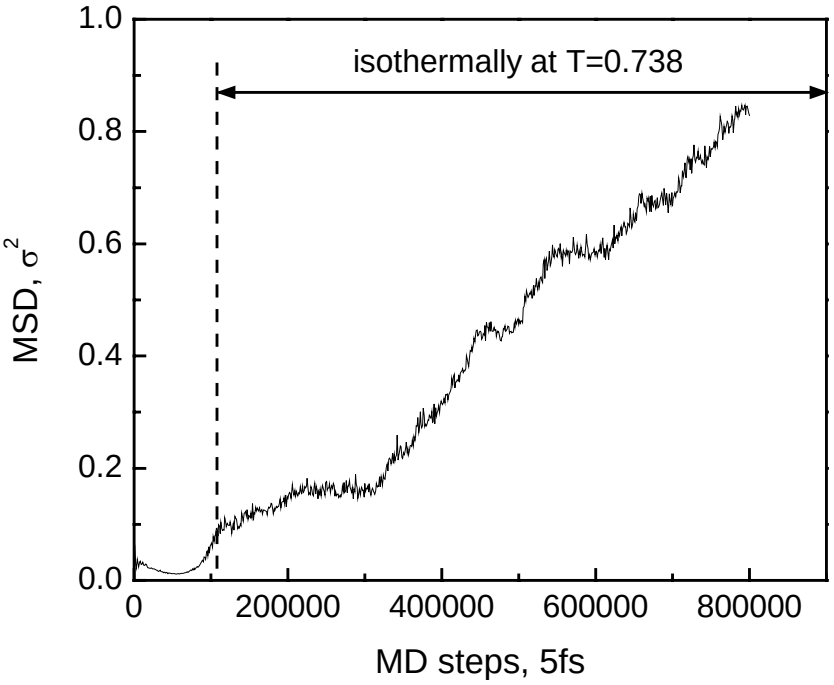

Figure 7.12. The time-dependent mean square displacement at the isothermal temperature T = 0.738. The MSD is larger than the critical value of 0.12 but the sample does not melt.

In order to check the travel distance of atoms, we plot the distributions of the atomic displacements at different time, as shown in Figure 7.13. The atomic displacement distribution measures the fraction of the atoms that travel a distance *r* from their original equilibrium sites. We calculated the distributions at three moments: at the initial time

when the temperature reaches 0.738, after 200 000 isothermal runs, and after 400 000 isothermal runs. The initial distribution shows that the first peak is at the displacement $r \approx 0.03\sigma$, indicating that all atoms vibrate around their original equilibrium sites. After 200 000 isothermal runs, most atoms still vibrate around their original sites, but some atoms travel about 1.2σ (the second peak in Figure 7.13), as indicated by the arrow. This displacement is very close to the first nearest neighbor distance ($\sqrt{2}/2a_0 \approx 1.16\sigma$), implying that atoms may jump to their neighboring lattice sites. After 400 000 isothermal runs, the height of the second peak increases, indicating that more atoms jump to their neighboring sites. Moreover, another peak can be seen at $r \approx 1.6\sigma$, which is very close to the second nearest neighbor distance $a_0 \approx 1.58\sigma$. This implies that some atoms may have the second-order jump.

Usually atoms are very difficult to jump or diffuse in a crystal without vacancies. Since the initial crystal is perfect in our simulations, the jump of atoms must be with the help of the thermally activated defects. At high temperatures, the atoms loose some of their nearest neighbors, as shown in Figures 7.10 and 7.11. Thus, the self-diffusion becomes possible in a superheated crystal. However, such kind of self-diffusion may not be observable during the gradual heating, because the heating rate in the gradual heating method is too fast so that atoms do not have enough relaxation time to jump. In other words, the fast heating rate suppresses the thermodynamic events. In the gradual heating method, the thermal fluctuations can aggregate the collective movement of atoms and make them to jump from their original lattice sites to the neighboring sites. After the jump, the atoms are in new lattice sites. Thus the system is still in the crystal state.

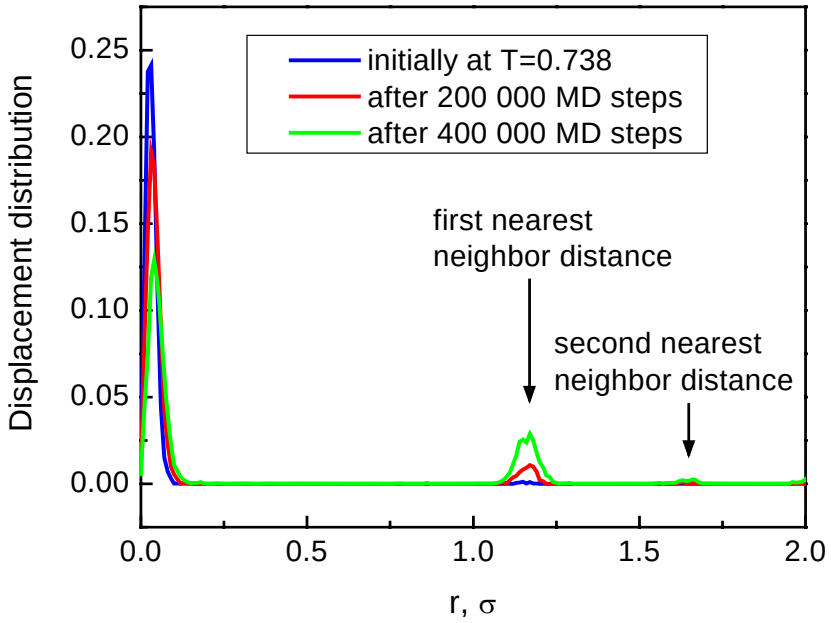

Figure 7.13. The distribution of the atomic displacements at T = 0.738 at different simulation time. The horizontal axis represents the atomic displacement. The two arrows indicate the first and second nearest neighbor distances respectively.

7.3.2. Ring Diffusion in a Superheated Crystal

Figures 7.12 and 7.13 show that the mean square displacement of atoms in a superheated crystal could be much larger than the critical Lindemann parameter but the sample still keeps the crystal structure. This is due to the atom hopping inside the superheated crystal. As shown in Figure 7.13, the average atom hopping distance is close to the first nearest neighbor distance, implying that the atoms are hopping among their nearest neighbors. The atom hopping may be destructive to the stability of the system and cause the melting. In order to clearly illustrate this process, we have used the following method to visualize the snapshots of the system.

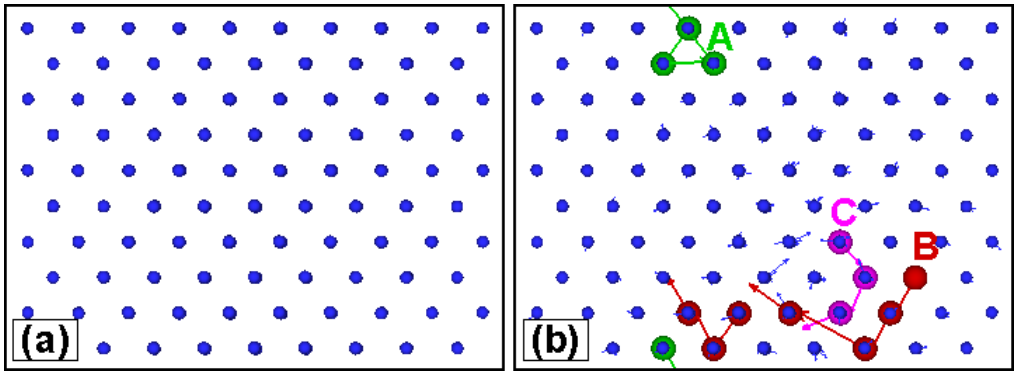

Figure 7.14. The atom hopping in a superheated crystal of 500 atoms at T=0.739 ε / k_B. The blue spheres represent the equilibrium sites of the atoms. (a) The equilibrium atom positions. (b) Clusters formed by the atom hopping. The hopping atoms are represented by large spheres. The arrow heads represent the new atom positions.

When the system is brought to the desired temperature and held isothermally, the atomic positions are averaged over the first 10 000 MD steps. Usually the atom hopping has not occurred yet during this period. Therefore the average positions represent the equilibrium positions of atoms. The averaged positions are used as the reference positions for the following visualization. Figure 7.14(a) shows the average or equilibrium atomic positions. Clearly the equilibrium atomic positions are well ordered and form a nearly perfect fcc lattice. Next, the atom positions are averaged over every 100 MD steps and a series of new atom positions are obtained. The distance between the new position of an atom and its equilibrium position is the displacement of that atom. We plot a vector pointing from the equilibrium position of each atom to its new position to indicate its displacement. At the isothermal temperature, the aggregation of the atom movements makes it possible for the atom hopping among their nearest neighbors. Figure 7.14(b) Shows the atom displacements after 530 000 MD steps. The atom displacements are

represented by the vectors pointing from their equilibrium positions to their new positions. Clearly, the lengths of the displacements of some atoms are close to the nearest neighbor distance, indicating that the atoms jump from their equilibrium sites to their neighboring sites. After these atoms jump to the new lattice sites, they are identical to the atoms originally in these sites. The large value of MSD shown in Figure 7.12 is mainly caused by this kind of atom hopping. It is worth noting that the atom hopping may not be observable in the gradual heating method because the extremely fast heating rate suppresses the collective movements of atoms.

Figure 7.14(b) also shows that the atom hopping occurs in a collective way. Namely, these hopping atoms form clusters that are similar to the diffusion rings. Since there are no preformed vacancies in the superheated crystal, a hopping atom must "kick" another atom away in order to occupy its lattice site. The atom been kicked must kick the third atom away, and so forth. As a result, these atoms form a diffusion ring or diffusion loop. There are two types of the diffusion loops: close loop and open loop, as illustrated in Figure 7.15. In the close loop, each atom displaces one first nearest neighbor distance. After the hopping completes, the original lattice site of the first hopping atom is occupied by the last hopping atom, and thus there is no vacancy left in the crystal. In the open loop, the first hopping atom leaves a vacancy and the last atom moves less than one nearest neighbor distance. The transient loop during the formation of a close loop can be viewed as an open loop. For example, loop A in Figure 7.14(b) is a close loop (note the bottom atom in green color is one part of the loop due to the periodic boundary conditions), while loops B and C are open loops.

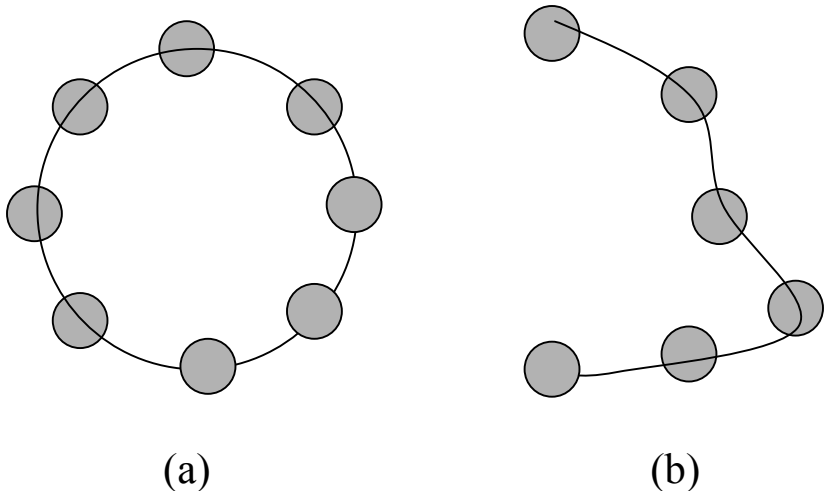

Figure 7.15. Illustration of two types of diffusion loops. (a) A close diffusion loop. (b) An open diffusion loop.

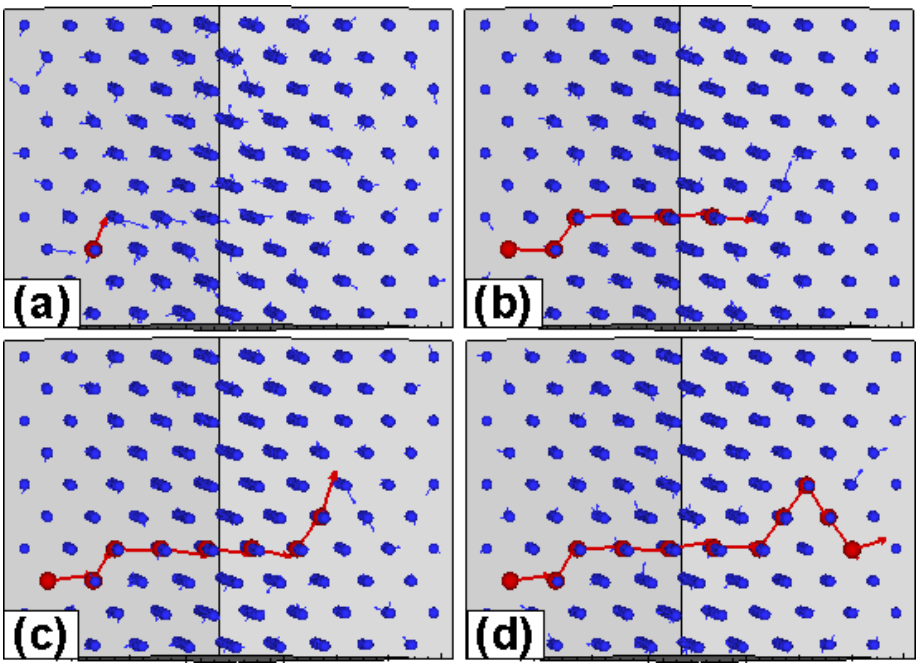

Figure 7.16. The snapshots of forming a close diffusion loop. The blue spheres represent original equilibrium sites. The red spheres represent the hopping atoms. The vectors represent the atom displacements. (a) Initial. (b) After 320 MD steps (1.6 ps). (c) After 880 MD steps (4.4 ps). (d) After 1 220 MD steps (6.1 ps).

In order to estimate how fast an atom jumps from one lattice site to another one, we picked up a loop for investigation, as shown in Figure 7.16. The blue spheres represent the original equilibrium atom positions. The red spheres represent the atoms that have already diffused to their nearest neighbors. The vectors represent the atom displacements from the original equilibrium sites to the new positions. Initially, as shown in Figure 7.16(a), an atom (indicated by red color) moves to one of its nearest neighboring sites. The original atom in that site is pushed away as indicated by the long blue vectors. In addition, another atom tends to fill the vacancy created by the hopping atom. After 320 MD runs (1.6 ps), six atoms have hopped from their initial positions. The six atoms form an open loop. The two atoms (in blue color) near the end of the loop have already moved away from their original positions but have not arrived at the new lattice sites yet. After 880 MD runs (4.4 ps), eight atoms have hopped from their initial positions, as shown in Figure 7.16(c). After 1 220 MD runs (6.1 ps), eleven atoms have hopped from their initial positions. Due to the periodic boundary conditions, the eleven atoms form a close loop. Thus, the average time for an atom traveling one nearest neighbor distance is about $6.1/11 \approx 0.55$ ps.

7.3.3. Melting Caused by the Ring Diffusion

In the superheated crystals studied in this chapter, there are no pre-existing vacancies. In order to diffuse in the crystal, the hopping atoms need to push the surrounding atoms away from their equilibrium sites in order to gain more space for moving. Therefore, the atom hopping can cause the local instability. As shown in Figure 7.16, the ring diffusion has a collective hopping feature. Depending on the sample size,

the size of a diffusion loop could be as small as of a few atoms and as large as of a few thousand atoms. Therefore, in the isothermal heating regime, the atom hopping in a superheated crystal could be related to the liquid nucleation and the subsequent melting.

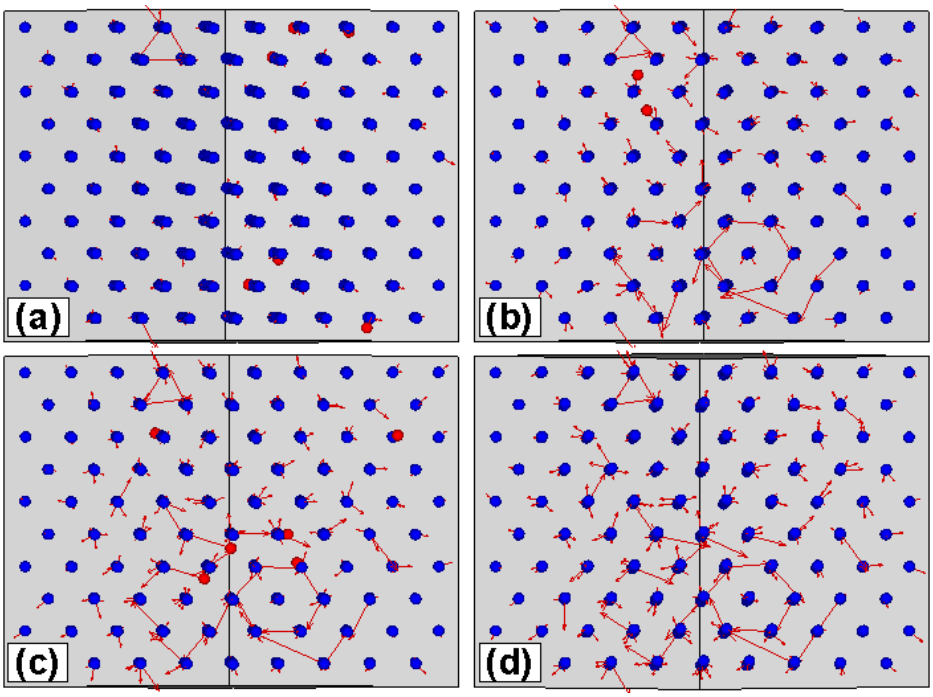

Figure 7.17. Snapshots of close-pair atoms and displaced atoms during the formation of the diffusion loops. The close-pair atoms are represented by red spheres. The blue spheres represent the original equilibrium sites of atoms. The vectors represent the atom displacements. (a) Initial stage when melting occurs. (b) After 1 400 MD steps. (c) After 1 800 MD steps. (d) After 1 840 MD steps.

When two atoms are very close, the strong repulsive force between two atoms could cause the local instability. At a temperature close to the upper superheating limit, the average nearest neighbor distance is about 1.16σ. Here we define the critical

distance between two atoms as 0.95σ. If the distance between two atoms is shorter than the critical distance, we define them as close-pair atoms. In order to check whether the atom hopping is induced by the close-pair atoms, we mark them with read spheres in the snapshots, as shown in Figure 7.17. Note in these snapshots, the close-pair atoms are shown with their new positions for better visualization. In Figure 7.17(a), it seems that the crystal is still stable even though several close-pair atoms appear. Some atoms displace slightly from their equilibrium sites but they are not at the vicinity of the close-pair atoms. In Figure 7.17(b), some diffusion loops are formed and some atoms displace from their equilibrium sites. Nevertheless, it seems that the close-pair atoms are far away from the diffusion loops and other displaced atoms. In Figure 7.17(c), some close-pair atoms are close to the diffusion loops and the largely displaced atoms. However, at the same time, the atoms near other close-pair atoms only displace slightly. In Figure 7.17(d), no close-pair atoms appear in the system. However, a lot of atoms still displace largely from their equilibrium sites. Therefore, from Figure 7.17(a)-(d) we can find that the displaced atoms do not always appear at the vicinity of the close-pair atoms. It seems that there is no direct connection between the close-pair atoms and the displaced atoms.

At high temperatures, the large thermal fluctuations can break the local symmetries of the atoms. Although the system is still in the crystal state, some atoms lose some of their crystal features. For example, as shown in Figures 7.10 and 7.11, the average number of the first nearest neighbors is eleven rather than twelve at high temperatures. Many researchers [153-155] defined the atoms with non-twelve nearest neighbors as defective atoms. It seems that this definition overestimates the number of the defective atoms at high temperatures, because the average number of the first nearest

neighbors is eleven. Here we define the critical number as eight. If an atom has less than eight nearest neighbors, it is classified as a defective atom. In Figure 7.18, we show the defective atoms in the snapshots during the melting process. The defective atoms are represented by red spheres. It seems that the defective atoms appear at the vicinity of the atoms with large displacement. This coincidence becomes more obvious in Figure 7.18(d) where more defective atoms appear at the disordered region.

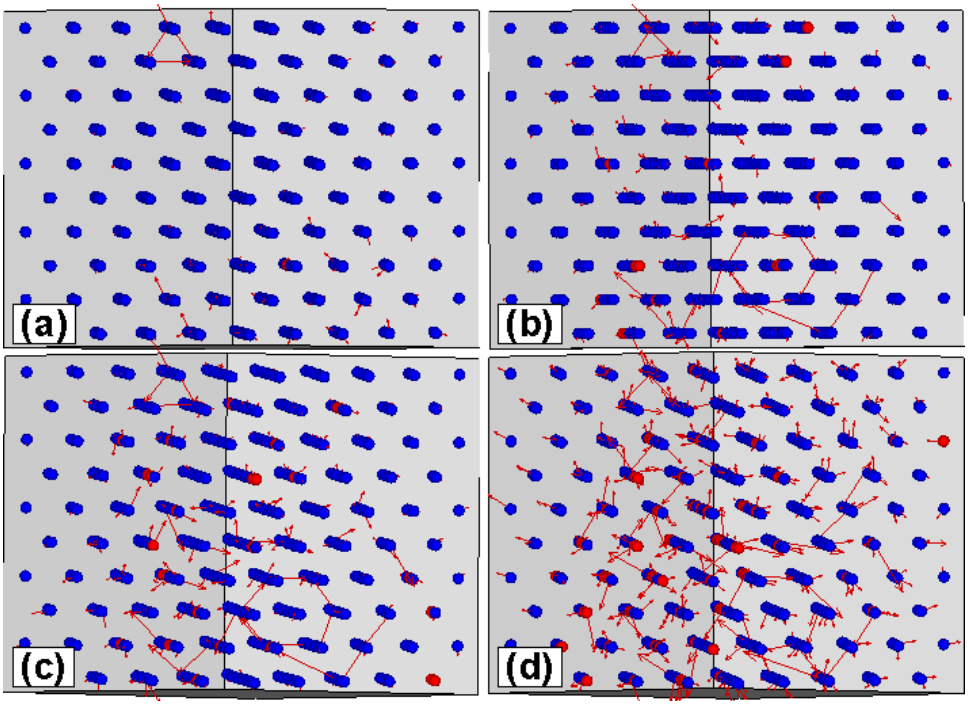

Figure 7.18. Snapshots of defective atoms and displaced atoms during the formation of the diffusion loops. An atom is defective if the number of its first nearest neighbors is less than eight. The defective atoms are represented by red spheres. The vectors represent the atom displacements. (a) Initial stage when melting occurs. (b) After 1 400 MD steps. (c) After 1 800 MD steps. (d) After 1 840 MD steps.

When melting occurs, the enthalpy of the system increases because the liquid has a higher enthalpy than the crystal. If an atom loses some nearest neighbors, the enthalpy of that atom should be higher. If two atoms are very close, the enthalpy is expected to increase as well. Therefore, any structural change can be reflected in the enthalpy change. In order to check the relation between a displaced atom and its enthalpy, we calculated the enthalpy of each atom. In the snapshots as shown in Figure 7.19, the atoms are colored differently according to their respective enthalpies. The color continuously changes from bright green (for solidlike atoms) to dark purple (for liquidlike atoms). In Figure 7.19(a), most atoms are solidlike atoms because they are vibrating around their equilibrium sites. Since the diffusion loop shown in this picture is a close loop, the atoms in this loop are still solidlike atoms. In Figure 7.19(b), some atoms displace away from their equilibrium sites. It can be clearly seen that most displaced atoms have dark green colors, indicating these atoms are in the intermediate state between solid and liquid. In Figure 7.19(c), more displaced atoms are shown and some of them become liquidlike atoms. In Figure 7.19(d), almost all atoms displace largely from their equilibrium sites. At the same time, the color of these atoms becomes dark purple, indicating that they are liquidlike atoms. Therefore, the displaced atoms coincide with the atoms of high enthalpies. Moreover, one can find that initially the liquidlike atoms prefer to appear at the vicinity of the open diffusion loop. Thereafter, the growth of the liquidlike atoms starts from this region and propagates to the whole system very quickly. Thus, it seems that the diffusion loop causes the local instability and provides the environment for the formation of the liquid embryos.

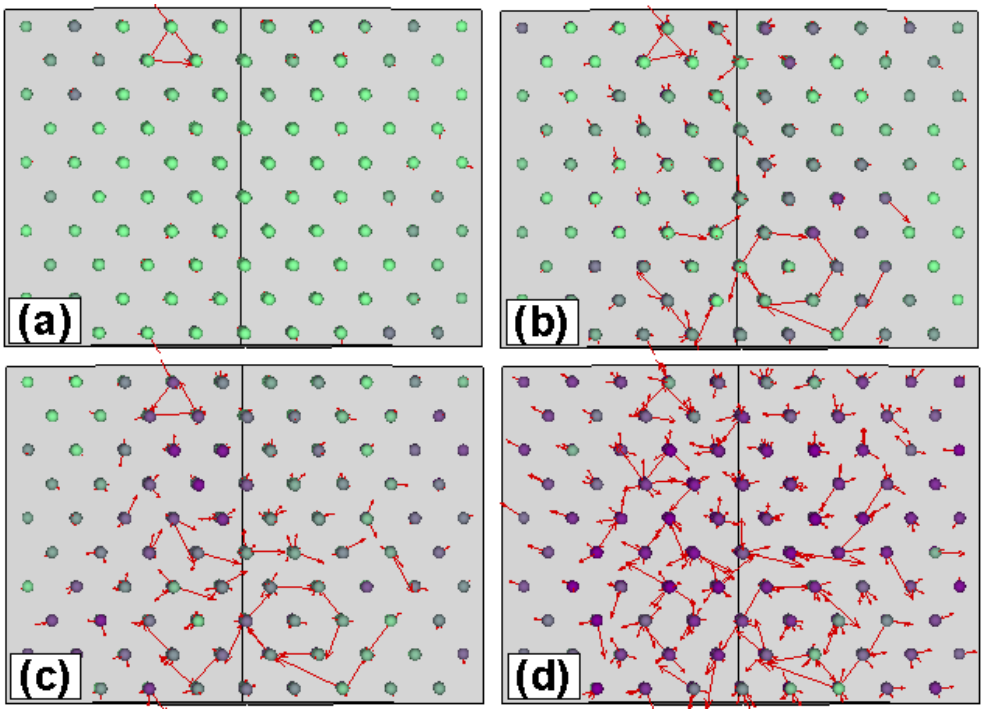

Figure 7.19. The enthalpy change of each atom during the formation of the diffusion loops. The enthalpy level is represented by the color of the spheres. The bright green is for solidlike atoms (lower enthalpy) and the dark purple is for liquidlike atoms (higher enthalpy). The vectors represent the atom displacements. (a) Initial stage when melting occurs. (b) After 1 400 MD steps. (c) After 1 800 MD steps. (d) After 1 840 MD steps.

The evolution of the diffusion loops is shown in Figure 7.20. In order to illustrate the diffusion loops more clearly, only the atoms in the diffusion loops are shown. Figure 7.20(a) shows a close diffusion loop in which each atom moves one nearest-neighbor distance. The vector pointing from each atom indicates the moving direction of that atom. After the diffusion loop forms, the atoms in the loop are vibrating around their new positions and become new crystal atoms. Thus, the close loop does not affect the stability of the crystal once the transition is complete. However, during the transition, the loop is an open loop that could cause the instability to the system. Figure 7.20(b) shows more

diffusion loops appearing after 1 400 MD steps. The close loop shown in Figure 7.20(a) is still there, indicating the atoms in this loop do not have a second-order diffusion. Three new open loops appear at this moment. The loop in green color and the loop in red color are very close to each other. After another 400 MD steps, the two open loops join together to form one loop, as shown in Figure 7.20(c). The combination of two loops involves more atoms than the growth of a single loop. Therefore, the combination process may cause more instability to the system. The 2D snapshot of the total system is shown in Figure 7.19(c). We find indeed some atoms around this loop displace largely from their equilibrium sites, and the enthalpies of these atoms are close to the liquid enthalpy. After additional 40 MD steps, more open loops appear in the system, as shown in Figure 7.20(d). The high concentration of the open loops causes the system unstable. As a result, the spontaneous melting occurs and most atoms become liquid atoms, which can be clearly seen in Figure 7.19(d). Thus, the dynamic evolution of the open loops could be the precursor of the diffusion loop mediated melting. It is worth noting that the diffusion loops are rarely seen if the system is heated with a fast heating rate. In the gradual heating method, the fast heating rate suppresses the aggregation of the atom displacements (or self-diffusion). As a result, the system can be superheated until the shear modulus cannot sustain the driving force for changing from the solid to the liquid. Thus, the upper superheating limit obtained in the gradual heating method is about 3% higher than that of the diffusion loop mediated melting. In other words, the diffusion loop mediated melting occurs earlier than that caused by Lindemann vibrational instability in the gradual heating method. The heating rate dependence of the melting temperature has been verified in experiment. For example, the superheating limit is outreached to $1.5T_m^E$ in the experiment

of using the femtosecond electron pulses to melt a thin aluminum film [60,163], while that obtained from the picosecond laser irradiation is about $1.2T_m^E$ [11,12,22,24].

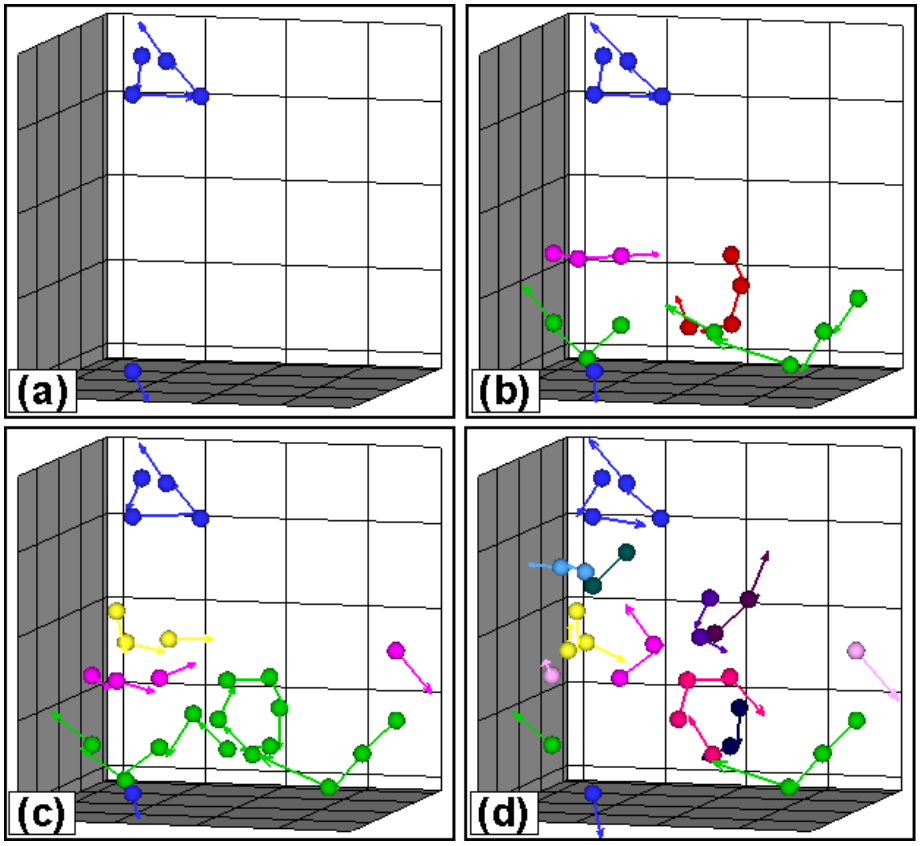

Figure 7.20. The 3D snapshots of the diffusion loops during the melting process. Different loops are distinguished by different colors. (a) Initial stage when melting occurs. (b) After 1 400 MD steps. (c) After 1 800 MD steps. (d) After 1 840 MD steps.

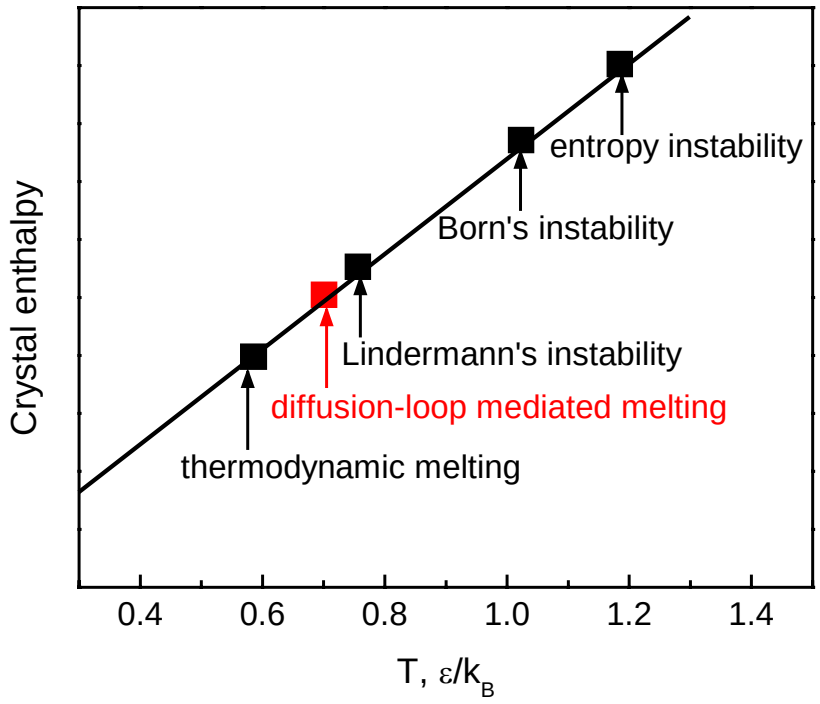

Figure 7.21. Illustration of the melting sequence. The temperature scale is for a LJ model system.

The melting sequence is illustrated in Figure 7.21. At the thermodynamic melting temperature, the melting occurs from the free surface. At this temperature, a bulk liquid and a bulk solid also can coexist with a flat solid-liquid interface. If the surface melting is suppressed, the melting temperature can be elevated. In the diffusion-loop mediated melting, atoms can diffuse collectively in the superheated crystal even though there are no preformed vacancies. The self-diffusion causes the instability to the system. When the accumulation of the open diffusion loops reaches a critical value, the melting is triggered. If the self-diffusion is suppressed such as in the gradual heating, the melting temperature can be further elevated. When the average vibrational amplitude of atoms exceeds the

critical fraction of the nearest neighbor distance, the melting is triggered by Lindemann instability. The Born instability occurs when the shear modulus vanishes. The entropy instability occurs when the solid entropy is equal to the liquid entropy. However, the melting triggered by the last two instabilities may not be observable in general, because they are preceded by the diffusion-loop mediated melting and Lindemann vibrational instability.

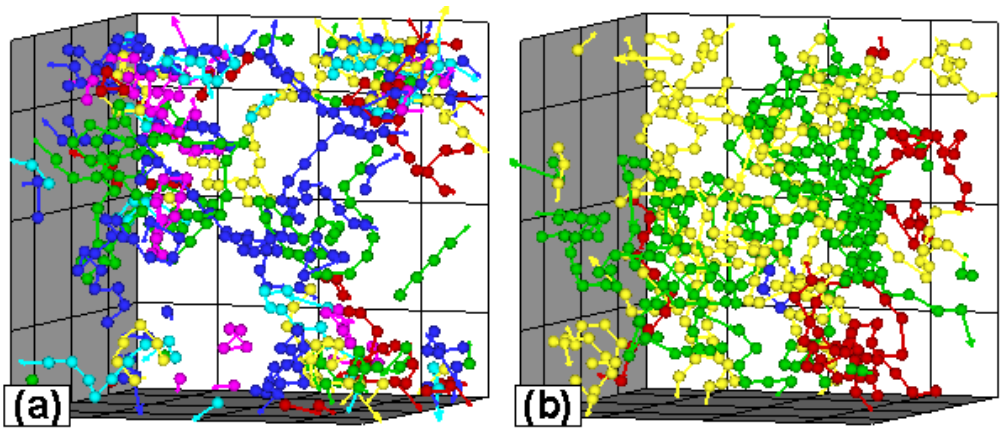

Figure 7.22. The open diffusion loops in a system of 4 000 atoms at two different temperatures. The loops are discriminated by different colors. (a) At T=0.739 ε / k_B. The melting occurs at this temperature. (b) At T=0.738 ε / k_B. The melting does not occur at this temperature.

As mentioned above, the ring diffusion manifests at high temperatures. However, the presence of the self-diffusion does not guarantee the occurrence of the melting. For example, extensive self-diffusion takes place in a crystal of 4 000 atoms at both T =

$0.739\,\varepsilon/k_B$ and T = $0.738\,\varepsilon/k_B$. The corresponding snapshots of the open diffusion loops are shown in Figure 7.22. At both temperatures, many atoms diffuse at least one nearest neighbor distance. However, eventually the crystal melts at T = $0.739\,\varepsilon/k_B$ but does not melt at T = $0.738\,\varepsilon/k_B$. Thus, there must be some critical parameters that determine the melting. In a close loop, all atoms vibrate around their new positions. Thus, the atoms in the close loop are still crystal atoms and do not cause the instability. In an open loop, the first jumping atom leaves a vacancy and forms the head of the loop. The last atom (tail atom) has not jumped to one of its nearest neighbors yet and could be viewed as a defective atom. The other atoms in the open loop have already jumped to their new positions. Thus, only the head and the tail in an open loop may cause the instability. The total number of the open loops, or the total number of the loop heads and loop tails, could be the critical parameter for determining the melting. Figure 7.23(a) shows the number of the open loops in the crystal as a function of time at two different temperatures. At T = $0.738\,\varepsilon/k_B$, the number of the open loops is usually less than 5. The maximum number is about 7. At this temperature, the system does not melt. At T = $0.739\,\varepsilon/k_B$, the number of the open loops increases rapidly when melting occurs. Figure 7.23(b) shows the enlarged graph of the transition period at T = $0.739\,\varepsilon/k_B$. The maximum number of the open loops is 21 when the system is in crystal state. However, if the number exceeds 36, the system melts very quickly. Thus the number of 36 could be the upper bound of the critical number of the open loops, and the number of 21 could be the lower bound of the critical number.

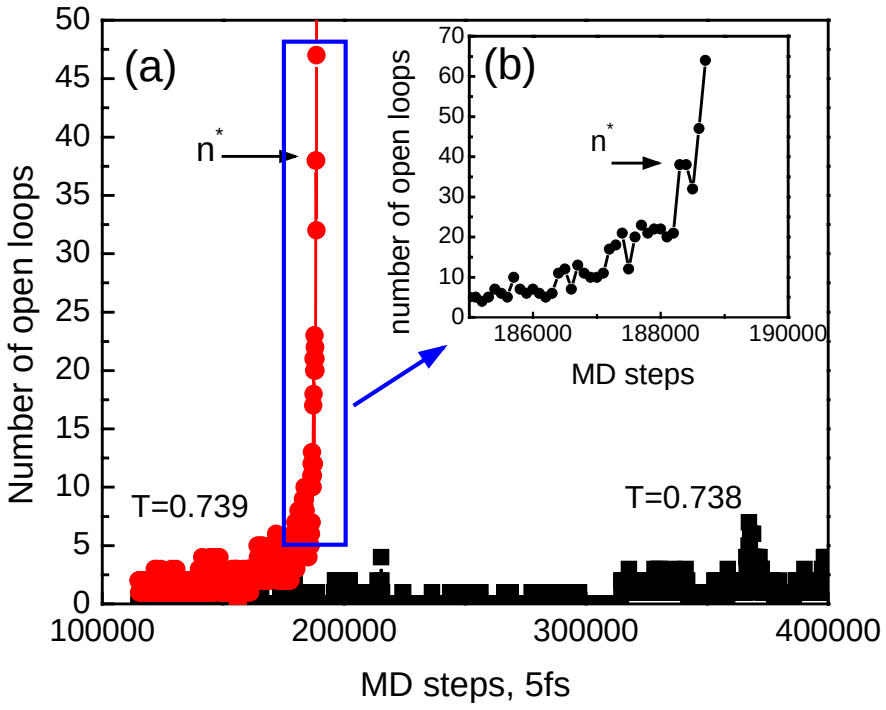

Figure 7.23. (a) The number of the open loops as a function of time at two different temperatures. The crystal contains 4 000 atoms. (b) The enlarged graph of the transition period enclosed in the blue rectangular.

However, different size systems have different critical numbers. For example, in a system containing 500 atoms, we find that the upper bound of the critical number of the open loops is about 5, and lower bound is about 3. Thus, it is more reasonable to use the critical density of the open loops to characterize the critical parameter. The critical density is defined as the ratio of the critical number to the total number of atoms in the system. In this work, we have investigated the critical density of the open loops in five different size systems: N = 500, 864, 1 372, 2 048, 2 916, and 4 000. The upper and lower bounds of the critical densities in each size system are shown in Figure 7.24. Clearly, the

upper bound of the critical density is around 0.85% in each size system, and the lower bound of the critical density is around 0.55%. Generally speaking, the rough range of the critical density is about 0.5% - 1%. If the density of the open loops aggregates to this range, melting can be triggered. If we consider the head and tail atoms in a loop as defective atoms, the fraction of the critical number of the defective atoms is about 1%-2%.

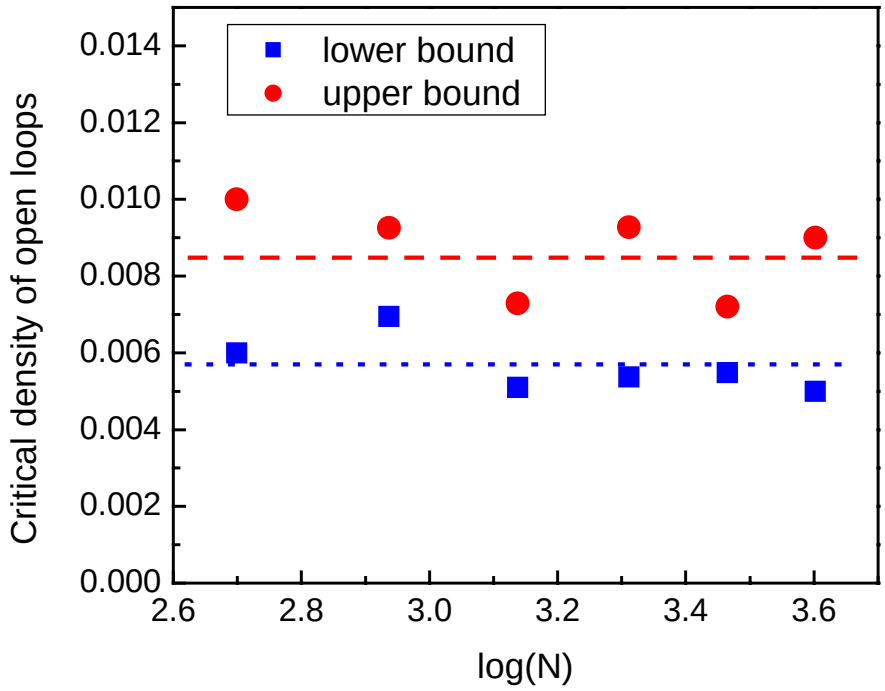

Figure 7.24. The upper and lower bounds of the critical densities in each size system. The bottom axis (total number of atoms in the system) is plotted with the logarithmic scale.

7.4. First-Order and Second-Order Transitions

7.4.1. Definition of the First-Order and Second-Order Transitions

At the critical point of a phase transition, the Gibbs free energy of each phase is usually equal to each other [156]. However, the derivative of the Gibbs free energy can be different. If the first-order derivative is discontinuous (different slope), then the transition is called "first-order". If the first-order derivative is continuous (same slope) but the higher order derivatives are discontinuous, then it is a "second or higher order" transition [156]. Since the first-order derivative of the Gibbs free energy is entropy, $S = -\left(\frac{\partial G}{\partial T}\right)_P$, one can use the entropy to represent the order of the transition, as shown in Figure 7.25. Generally, the entropy is discontinuous in the first-order transition but is continuous in the second-order transition.

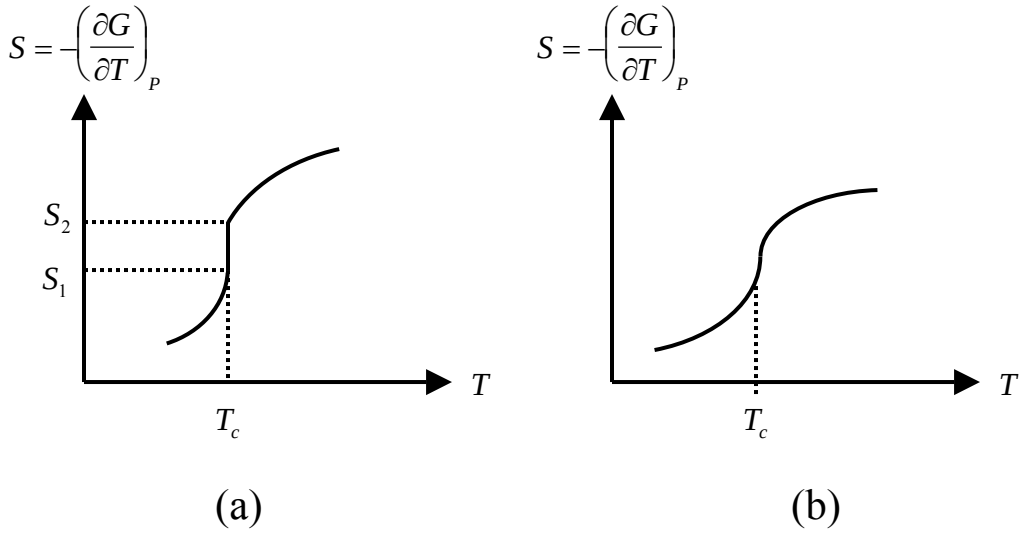

Figure 7.25. The difference in the entropy between (a) the first-order transition, and (b) the second-order transition [156].

The heat capacity, $C_P = \left(\partial H / \partial T\right)_P = T\left(\partial S / \partial T\right)_P$, is also different for the first-order and second-order transitions, as shown in Figure 7.26. The heat capacity in the first-order transition is discontinuous at the critical temperature, while that in the second-order transition is continuous and has a peak at the critical temperature.

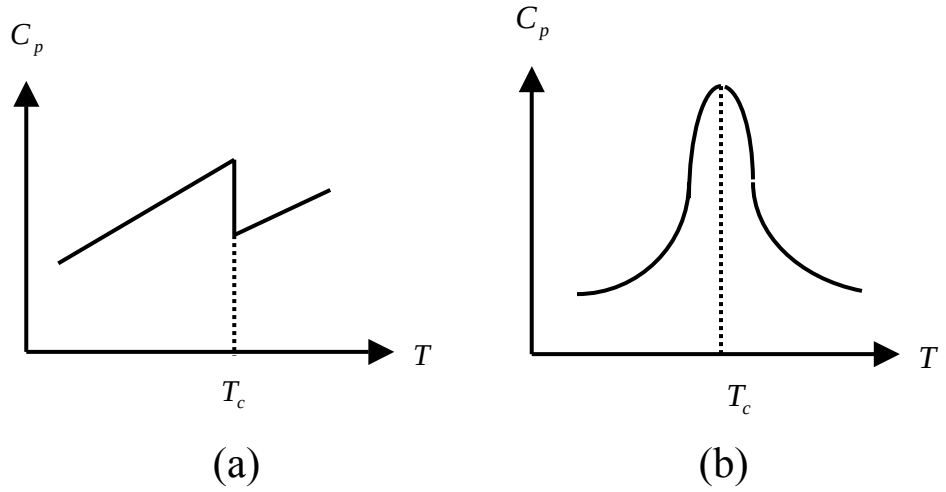

Figure 7.26. The difference in the heat capacity between (a) the first-order transition, and (b) the second-order transition [156].

7.4.2. Heat Capacity

During the melting at the superheating limit, many physical quantities such as volume and enthalpy change abruptly. It seems that the melting at the superheating is a first-order transition. However, Fecht and Johnson's model [19] implies that melting is a second-order transition. In this model, the solid entropy approaches the liquid entropy continuously at the upper limit of the superheating, which is like a reverse process of a

glass transition (a second-order transition). Moreover, Born criterion [15]] also implies that melting is a second-order transition, because the shear modulus decreases gradually to zero. In order to verify the order of the transition, first we calculated the heat capacity as a function of temperature, as shown in Figure 7.27. The heat capacity is calculated by taking the first derivative of the enthalpy, $C_P = \left(\partial H / \partial T\right)_P$. The heat capacity increases with the increasing temperature when the sample is in crystal state. At the critical temperature, the discontinuity of the heat capacity forms a peak. After the sample becomes a liquid, the heat capacity drops to a lower value and increases with the increasing temperature again. Clearly, Figure 7.27 is very similar to Figure 7.26(a), indicating that the melting at superheating is more like a first-order transition.

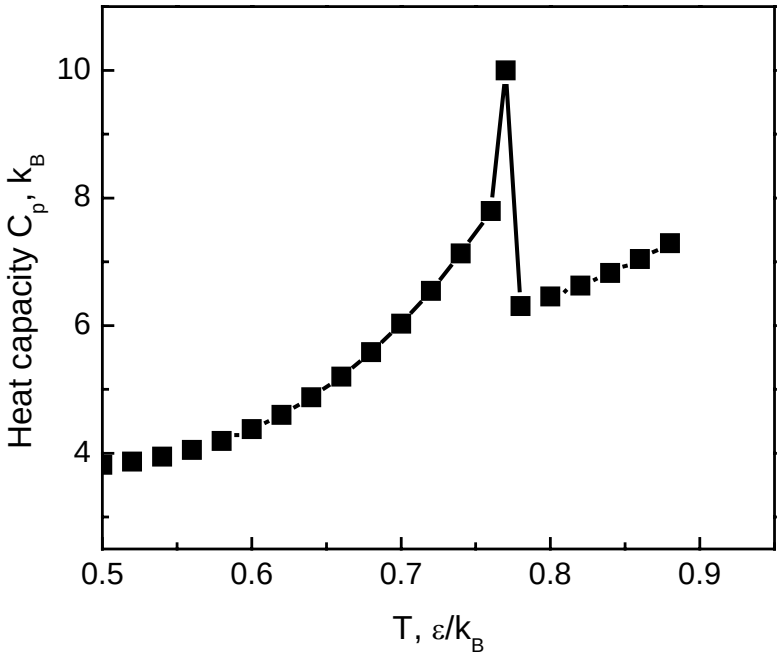

Figure 7.27. The heat capacity as a function of temperature. The melting occurs at the discontinuous point.

7.4.3. Bond-Orientational Order

The first-order transition is always associated with the order to disorder or disorder to order transition. Therefore, from the structural change, one also can determine the order of a transition. The pair distribution function (PDF) or radial distribution function (RDF) can be used for investigating the structure of materials. In Chapter 2, we have calculated the pair distribution function (PDF) at different temperatures. However, the PDF only shows the numbers of atoms in a set of spherical shells from which the structure is determined. Unfortunately, different structures may have the same number of nearest neighbors. For example, a central atom with 12 nearest neighbors can form fcc, hcp or icosahedral structures [164]. It has been found that in a supercooled liquid the icosahedral order is predominant [164]. However, the PDF cannot differentiate fcc and icosahedral structures.

A more accurate method for determining these structures is the "bond-orientational order" method that is proposed by Nelson *et al*. [164,165]. Rintoul and Torquato [166,167] have used this method in the glass transition and obtained some results that cannot be determined by PDF method. The details of the bond-orientational order method are described as follows.

Suppose a central atom connects to all its nearest neighbors via a set of spatial bonds. One then assigns the value

$$Q_{lm}(\vec{r}) \equiv Y_{lm}[\theta(\vec{r}),\ \phi(\vec{r})] \tag{7.2}$$

to each bond oriented in a direction $\vec{r}$, where $Y_{lm}[\theta(\vec{r}),\ \phi(\vec{r})]$ are the spherical harmonics, and $\theta(\vec{r})$ and $\phi(\vec{r})$ are the polar angles of a bond in the spherical coordinate,

and m is an integer number between $-l$ and l. If $Q_{lm}(\vec{r})$'s are averaged over all the bonds, one can get an average quantity,

$$\overline{Q}_{lm} \equiv \frac{1}{N_b}\sum_{i=1}^{N_b} Q_{lm}(\vec{r}_i)\,, \tag{7.3}$$

where N_b is the total number of bonds. For a given l and m, $\overline{Q}_{lm}$ changes if the coordinate system is rotated. To get a rotationally invariant quantity, one can define a new quantity Q_l and the third-order invariant W_l, as shown by

$$Q_l \equiv \left(\frac{4\pi}{2l+1}\sum_{m=-1}^{l}\left|\overline{Q}_{lm}\right|^2\right)^{1/2}, \tag{7.4}$$

and

$$W_l \equiv \sum_{\substack{m_1,m_2,m_3 \\ m_1+m_2+m_3=0}} \begin{pmatrix} l & l & l \\ m_1 & m_2 & m_3 \end{pmatrix} \times \overline{Q}_{lm_1}\overline{Q}_{lm_2}\overline{Q}_{lm_3}\,, \tag{7.5}$$

where the coefficients $\begin{pmatrix} l & l & l \\ m_1 & m_2 & m_3 \end{pmatrix}$ are the Wigner 3j symbols [168]. The normalized value of W_l is a sensitive quantity of different orientational symmetries,

$$\hat{W}_l \equiv \frac{W_l}{\left(\sum_{m=-1}^{l}\left|\overline{Q}_{lm}\right|^2\right)^{3/2}}\,. \tag{7.6}$$

The bonds are defined by connecting an atom to its nearest neighbors. In order to define the nearest neighbors, one can define a cutoff radius. Usually this cutoff radius is the distance at which the PDF has its first minimum value [164]. All atoms inside this sphere are considered as nearest neighbors.

For the cubic symmetry, the first nonzero Q_l is Q_4; For the icosahedral symmetry, the first nonzero Q_l is Q_6; For random systems and isotropic fluid, Q_l is zero for any $l > 0$ [164]. For the solid-to-liquid transition, we will focus on $l = 4$ and $l = 6$. Nelson *et al.* [164] plotted a graph of quadratic invariants Q_l and third-order invariants W_l for different symmetries. It is a good table for checking the invariants Q_l and W_l for different structures.

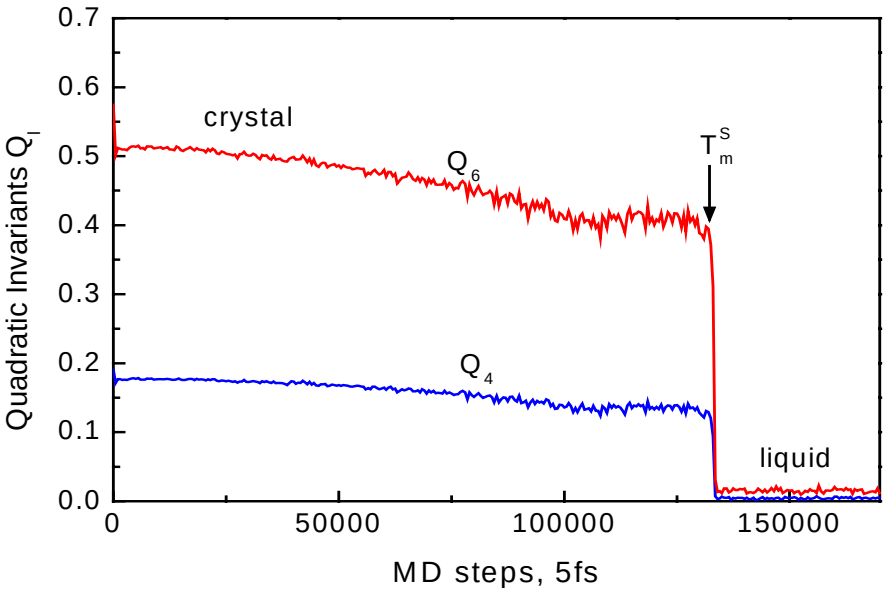

Figure 7.28. The quadratic invariants Q_4 and Q_6 as functions of time during the melting. Both Q_4 and Q_6 drop to zero at the superheating limit, indicating the melting is an order-to-disorder transition.

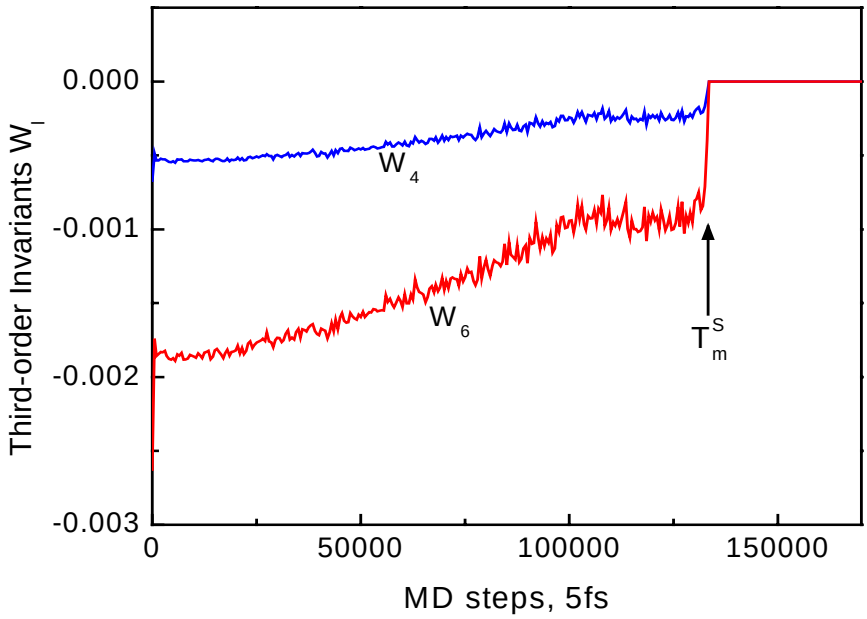

Figure 7.29. The third-order invariants W_4 and W_6 as functions of time during the melting. Both W_4 and W_6 jump to zero when melting occurs.

Figures 7.28 and 7.29 show the quadratic invariants Q_4 and Q_6 and the third-order invariants W_4 and W_6 as functions of time during the melting respectively. For a perfect fcc crystal, Q_4=0.19, Q_6=0.57, $W_4 = -6.72\times10^{-4}$, and $W_6 = -2.63\times10^{-3}$ [164]. At the beginning of the simulation, the calculated values are close to these ideal values, indicating the initial structure of the sample is fcc. As the temperature increases, the thermal fluctuations generate some defects. As a result, the values of these invariants deviate from the ideal values. At the critical temperature but before melting occurs, the quadratic invariants are Q_4=0.13 and Q_6=0.41, and the third-order invariants are $W_4 = -2.5\times10^{-4}$ and $W_6 = -0.93\times10^{-3}$, indicating that the structure is still close to the

fcc symmetry. After melting occurs, all of the four invariants Q_4, Q_6, W_4, and W_6 jump to zero very quickly, indicating the system is totally in a random order. Unlike the icosahedral order has been found as a transient order during the supercooling process, we did not find any intermediate order during the melting at superheating. From Figures 7.28 and 7.29, we can find that the order-to-disorder transition is very obvious. Therefore, we conclude that the melting at superheating is a first-order transition.

7.4.4. Symmetry Parameter

The order-to-disorder transition also can be characterized by the symmetry parameter. In this work, we define three symmetry parameters (*S*x, *S*y, *S*z) which are the sums of bond vectors of the first nearest neighbors in *X*, *Y*, and *Z* directions respectively,

$$S_\alpha = \frac{1}{N}\sum_{i=1}^{N}[\frac{1}{M}(r_a^j - r_\alpha^i)], \qquad (7.7)$$

where α represents one of three Cartesian coordinates, *N* is the total number of atoms in the system, and *M* is the number of the nearest neighbor atoms of the *i*th atom, r_α^i is the coordinate of the central *i*th atom in α direction, and r_a^j is the coordinate of the *j*th nearest neighbor in α direction. For a perfect fcc crystal, the symmetric bond vectors cancel with each other. Thus, three symmetry parameters are equal to zero. Due to the aggregated defects at high temperatures, the symmetry parameters have small values. For disordered state, the symmetry parameters should have very large values. Figure 7.30 shows that the evolution of the symmetry parameters in *X*, *Y*, and *Z* directions during the melting process. Clearly, the symmetry parameters in three directions behave similarly. The symmetry parameters have small values at low temperatures and increase with the

increasing temperature. After melting occurs, the crystal loses its symmetry. Therefore the symmetry parameters increase rapidly. From Figure 7.30, we also can conclude that the order-to-disorder transition is very fast and distinct during the melting at the superheating. Therefore, the melting should be a first-order transition.

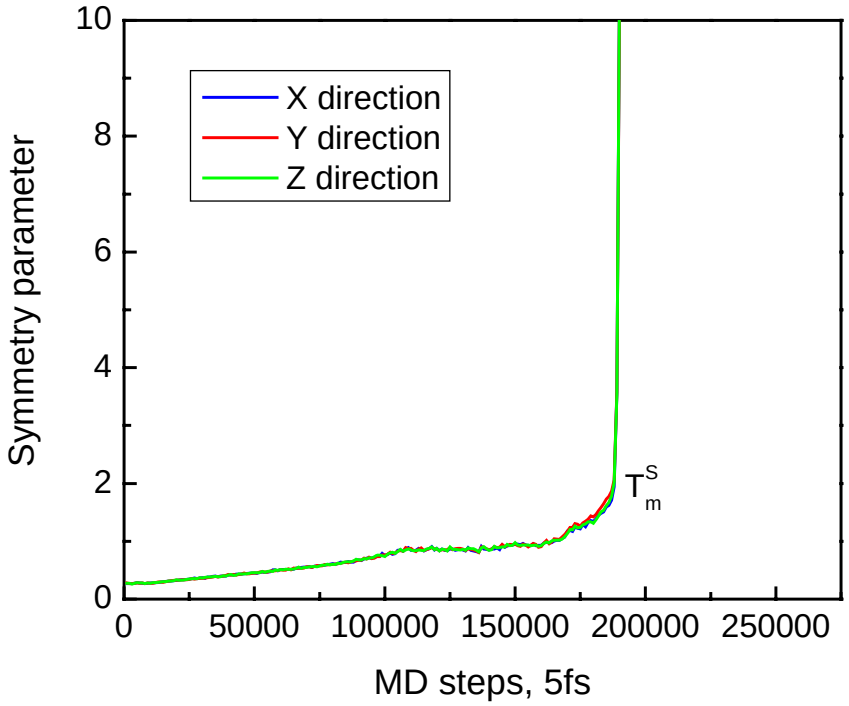

Figure 7.30. The symmetry parameters in X, Y, and Z directions. The rapid increase of the symmetry parameters indicates the crystal loses its symmetry.

7.5. Discussion and Conclusions

In this chapter, we discussed the homogeneous melting mechanism at the upper limit of melting at superheating. It seems that most predominant theories are not entirely correct. Born shear instability theory is incomplete because the shear modulus does not vanish at temperatures close to the upper limit of superheating. The Lindemann vibrational instability fails to predict melting in the isothermal heating method, because the mean square displacements can be very large without melting. The interstitial melting is elusive because the minimum nearest neighbor distance in our simulation is at least 14% larger than the distance between an atom and an octahedral site in an fcc crystal. The entropy instability may not be entirely correct because the melting at superheating is a first-order transition rather than a second-order transition.

Since the heating rate is usually very fast in either laser irradiation experiments or computer simulations, the thermodynamic relaxation of atoms is suppressed. It may be this reason that causes various catastrophes of melting. However, if one uses the isothermal heating method as we did in this work, the melting at superheating occurs at a temperature 3% below that in the conventional gradual heating method. At this temperature, melting does not occur instantaneously. Before melting occurs, there is a long period in which the system is in the crystal state. Some atoms are found to jump to their neighboring sites in a collective way, which forms the ring diffusion. The diffusion causes the instability to the superheated crystal. This is a real thermodynamically driven nucleation process that cannot be found in the gradual heating method. We have found two types of diffusion loops: close loop and open loop. After the close loop forms, all atoms in the loop vibrate around their new equilibrium sites and become new crystal

atoms. Thus, the close loop does not cause the instability to the system. In the open loop, the head atom jumps to a new atomic site and leaves a vacancy. At the same time, the tail atom has not finished the jump yet. Thus the head and tail atoms can cause the instability to the crystal. When the number of open loops accumulates to a critical number, the melting occurs. This critical number of the open loops has a finite-size effect: it increases with the increasing system size. However, this finite-size effect can be reduced if the critical number is scaled with the system size. We find that the critical density of the open loops at melting, which is the ratio of critical number of open loops to the system size, is about 0.5%-1% for different size systems.

REFERENCES

[1] D. A. Porter and K. E. Easterling, Phase Transformations in Metals and Alloys, 2nd ed., Chapman & Hall, London (1992).

[2] J. Frenkel, Kinetic Theory of Liquids, Oxford University Press, New York (1946).

[3] D. P. Woodruff, The Solid-Liquid Interface (Cambridge University Press, London, 1973).

[4] D. Turnbull, J. Appl. Phys. 21, 1022 (1950).

[5] D. Turnbull, R. E. Cech, J. Appl. Phys. 21, 804 (1950).

[6] D. Turnbull, J. Chem. Phys. 20, 411 (1952).

[7] R.W. Cahn, Nature 273, 491 (1978).

[8] J. W. M. Frenken and J. F. van der Veen, Phys. Rev. Lett. 54, 134 (1985).

[9] P. Stoltze, J. K. Norskov and U. Landman, Phys. Rev. Lett. 61, 440 (1988).

[10] J. Daeges, H. Gleiter and J. H. Perepezko, Phys. Lett. A 119, 79 (1986).

[11] K. Sokolowski-Tinten et al., Phys. Rev. Lett. 87, 225701 (2001).

[12] B. Rethfeld, K. Sokolowski-Tinten, and D. von der Linde, Phys. Rev. B 65, 92103 (2002).

[13] M. P. Allen and D. J. Tildesley, Computer simulation of liquids, Oxford University Press, New York (1987).

[14] K. Lu and Y. Li, Phys. Rev. Lett. 80, 4474 (1998).

[15] M. Born, J. Chem. Phys. 7, 591 (1939).

[16] F. A. Lindemann, Physik. Zeitschr. 11, 609 (1910).

[17] Z. H. Jin et al., Phys. Rev. Lett. 87, 55703 (2001).

[18] J. H. Wang et al., Physica A 240, 396 (1997).

[19] H. J. Fecht and W. L. Johnson, Nature 334, 50 (1988).

[20] J. L. Tallon, Nature 342, 658 (1989).

[21] W. Kauzmann, Chem. Rev. 43, 219-256 (1948).

[22] V. I. Motorin and S. L. Musher, J. Chem. Phys. 81, 465 (1984).

[23] S. N. Luo et al., Phys. Rev. B 68, 134206 (2003).

[24] S. Williamson, G. Mourou, and J. C. M. Li, Phys. Rev. Lett. 52, 2364 (1984).

[25] S. N. Luo, A. Strachan, and D. C. Swift, J. Chem. Phys. 120, 11640 (2004).

[26] D. K. Chokappa and P. Clancy, Molec. Phys. 61, 617 (1987).

[27] P. R. ten Wolde, M. J. Ruiz-Montero and D. Frenkel, J. Chem. Phys. 104, 9932 (1996).

[28] T. Koishi et al., J. of Non-crystalline solids, 312-314, 332 (2002).

[29] S. Auer and D. Frenkel, Nature 409, 1020 (2001).

[30] J. Q. Broughton and G. H. Glimer, J. Chem. Phys. 84, 5759 (1986).

[31] K. F. Kelton, A. L. Greer, D. M. Herlach, and D. Holland-Moritz, MRS Bulletin 29, 940 (2004).

[32] J. J. Hoyt, M. Asta and A. Karma, Phys. Rev. Lett., 86, 5530 (2001).

[33] F. Spaepen, Solid State Physics (Academic Press, Inc., Boston) 47, 1-32 (1994).

[34] J. Q. Broughton, G. H. Gilmer and K. A. Jackson, Phys. Rev. Lett. 49, 1496 (1982).

[35] H. A. Wilson, Philos. Mag. 24, 118 (1912).

[36] J. Frenkel, Phys. Z. Sowjetunion 1, 498 (1932).

[37] D. Turnbull and B. G. Bagley, in Treatise on Solid State Chemistry, edited by N. B. Hannay, (Plenum Press, New York, 1975), Vol. 5, pp513-554.

[38] E. Burke, J. Q. Broughton, and G. H. Gilmer, J. Chem. Phys. 89, 1030 (1988).

[39] C. J. Tymczak and J. R. Ray, Phys. Rev. Lett. 64, 1278 (1990).

[40] H. L. Tepper and W. J. Briels, J. Chem. Phys. 115, 9434 (2001)

[41] H. E. A. Huitema, M. J. Vlot, and J. P. van der Eerden, J. Chem. Phys. 111, 4714 (1999).

[42] M. S. Gulam Razul et al., Mol. Phys. 103, 1929 (2005).

[43] J. L. Walker, reported by B. Chalmers, Principles of solidification (Wiley, New York, 1964), pp. 114-116.

[44] P. H. Bucksbaum and J. Bokor, Phys. Rev. Lett. 53, 182 (1984).

[45] J. Z. Tischler, B. C. Larson, and D. M. Mills, App. Phys. Lett. 52, 1785 (1988).

[46] J. Y. Tsao, M. J. Aziz, M. O. Thompson, and P. S. Peercy, Phys. Rev. Lett. 56, 2712 (1986).

[47] M. O. Thompson et al., App. Phys. Lett. 42, 445 (1983).

[48] G. J. Galvin et al., Phys. Rev. B 27, 1079 (1983).

[49] J. Y. Tsao, S. T. Picraux, P. S. Peercy, and M. O. Thompson, Appl. Phys. Lett. 48, 278 (1986).

[50] C. A. MacDonald, A. M. Malvezzi, and F. Spaepen, J. Appl. Phys. 65, 129 (1989).

[51] J. M. Howe and H. Saka, MRS Bulletin 29, 951 (2004).

[52] J. F. van der Veen and H. Reichert, MRS Bulletin 29, 958 (2004).

[53] J. G. Dash, Rev. Mod. Phys. 71, 1737-1743 (1999).

[54] J. Erlebacher, M. J. Aziz, A. Karma, N. Dimitrov, and K. Sleradzkl, Nature 410, 450-453 (2001).

[55] P. M. Agrawal, L. M. Raff, and R. Komanduri, Phys. Rev. B 72, 125206 (2005).

[56] P. M. Agrawal, B. M. Rice, and D. L. Thompson, J. Chem. Phys. 118, 9680 (2003).

[57] G. F. Velardez, S. Alavi, and D. L. Thompson, J. Chem. Phys. 120, 9151 (2004).

[58] J. Solca, A. J. Dyson, G. Steinebrunner, and B. Kirchner, J. Chem. Phys. 108, 4107 (1998).

[59] J. F. Lutsko, D. Wolf, S. R. Phillpot, and S. Yip, Phys. Rev. B 40, 2841 (1989).

[60] B. J. Siwick, J. R. Dwyer, R. E. Jordan, and R. J. Dwayne Miller, Science 302, 1382 (2003).

[61] X. M. Bai and M. Li, J. Chem. Phys. 124, 124707 (2006).

[62] X. M. Bai and M. Li, J. Chem. Phys. 122, 224510 (2005).

[63] X. M. Bai and M. Li, J. Chem. Phys. 123, 151102 (2005).

[64] X. M. Bai and M. Li, Phys. Rev. B 72, 052108 (2005).

[65] X. M. Bai and M. Li, submitted to Phys. Rev. Lett., in review.

[66] X. M. Bai and M. Li, Nano Lett. 6, 2284 (2006).

[67] H. C. Andersen, J. Chem. Phys. 72, 2384 (1980).

[68] M. Parrinello and A. Rahman, J. Appl. Phys. 52, 7182 (1981).

[69] S. Nose, Mol. Phys. 52, 255 (1984).

[70] M. S. Daw and M. I. Baskes, Phys. Rev. B 29, 6443 (1984).

[71] S. M. Foiles, M. S. Daw, and M. I. Baskes, Phys. Rev. B 33, 7983 (1986).

[72] P. Erhart, N. Juslin, O. Goy, K. Nordlund, R. Muller and K. Albe1, J. Phys.: Condens. Matter 18, 6585 (2006).

[73] M. S. Sprik, R. W. Impey, and M. L. Klein, Phys. Rev. B 29, 4368 (1984).

[74] M. Parrinello and A. Rahman, J. Chem. Phys. 76, 2662 (1982).

[75] P. J. Fay and J. R. Ray, Phys. Rev. A, 46, 4645 (1992).

[76] M. Karimi and H. Yates, J. R. Ray, T. Kaplan and M. Mostoller, Phy. Rev. B, 58, 6019 (1998).

[77] J. R. Ray and A. Rahman, J. Chem. Phys. 80, 4423 (1984).

[78] J. R. Ray, M. C. Moody and A. Rahman, Phys. Rev. B 32, 733(1985).

[79] M. Karimi, G. Stapay, T. Kaplan and M. Mostoller, Modelling Simul. Mater. Sci. Eng. 5, 337 (1997).

[80] R. J. Wolf, K. A. Mansour, M. W. Lee and J. R. Ray, Phys. Rev. B 46, 8027 (1992).

[81] R. A. Johnson, Phys. Rev. B, 6, 2094 (1972).

[82] J. F. Nye, Physical Properties of Crystals-Their Representation by Tensors and Materials, Page 134, Oxford University Press, New York (1985).

[83] V. V. Brazhkin and A. G. Lyapin, Phys. Rev. Lett. 78, 2493 (1997).

[84] R. L. Davidchack and B. B. Laird, Phys. Rev. Lett. 85, 4751 (2000).

[85] M. Asta, J. J. Hoyt, and A. Karma, Phys. Rev. B 66, 100101 (2002).

[86] D. W. Marr and A.P. Gast, Phys. Rev. E 47, 1212 (1993).

[87] W. A. Curtin, Phys. Rev. B. 39, 6775 (1989).

[88] F. Spaepen, Mater. Sci. Eng. A 178, 15 (1994).

[89] S. Liu, R. E. Napolitano and R. Trivedi, Acta Mater. 49, 4271 (2001).

[90] D. Kashchiev, Nucleation: Basic Theory with Applications (Butterworth-Heinemann, Oxford, 2000).

[91] U. Gasser, E. R. Weeks, A. Schofield, P. N. Pusey, and D. A. Weitz, Science 292, 258 (2001).

[92] C. Kittel, Introduction to Solid State Physics, 7th ed., (John Wiley & Sons, New York,1996).

[93] J. R. Morris and X. Y. Song, J. Chem. Phys. 119, 3920 (2003).

[94] R. Agrawal and D. A. Kofke, Mol. Phys. 85, 43 (1995).

[95] Y. C. Shen and D. W. Oxtoby, J. Chem. Phys. 104, 4233 (1996).

[96] J. M. Leyssale, J. Delhommelle and C. Millot, J. Am. Chem. Soc. 126, 12286 (2004).

[97] W. Z. Ostwald, Z. Phys. Chem. 22, 289 (1897).

[98] Y. C. Shen and D. W. Oxtoby, Phys. Rev. Lett. 77, 3585 (1996).

[99] P. R. ten Wolde, M. J. Ruiz-Montero, and D. Frenkel, Phys. Rev. Lett. 75, 2714, (1995).

[100] K. F. Kelton, Solid State Phys. 45, 75 (1991).

[101] K. F. Kelton and A. L. Greer, Phys. Rev. B 38, 10089 (1988).

[102] R. L. Davidchack and B. B. Laird, J. Chem. Phys., 118, 7651 (2003).

[103] S. Auer and D. Frenkel, Nature 409, 1020 (2001).

[104] J. A. Barker and D. Henderson, J. Chem. Phys. 47, 4714 (1967)

[105] D. W. M. Marr, J. Chem. Phys. 102, 8283 (1995).

[106] W. J. Boettinger, S. R. Coriell, A. L. Greer, A. Karma, W. Kurz, M. Rappaz, and R. Trivedi, Acta Mater. 48, 43 (2000), and the references therein.

[107] K. K. Koo, R. Ananth, and W. N. Gill, Phys. Rev. A 44, 3782 (1991).

[108] M. Muschol, D. Liu, and H. Z. Cummins, Phys. Rev. A 46, 1038 (1992).

[109] A. Cacciuto, S. Auer, and D. Frenkel, J. Chem. Phys. 119, 7467 (2003).

[110] P. R. ten Wolde and D. Frenkel, J. Chem. Phys. 109, 9901 (1998).

[111] R. McGraw and A. Laaksonen, J. Chem. Phys. 106, 5284 (1997).

[112] D. Wu, L. Granasy, and F. Spaepen, MRS Bulletin 29, 945 (2004).

[113] Y. J. Kim, B. E. Wyslouzil, G. Wilemski, J. Wolk, and R. Strey, J. Phys. Chem. A 108, 4365 (2004).

[114] J. Wolk and R. Strey, J. Phys. Chem. B 105, 11683 (2001).

[115] S. M. Kathmann and B. N. Hale, J. Phys. Chem. B 105, 11719 (2001).

[116] Y. Miyazawa and G. M. Pound, J. Cryst. Growth 23, 45 (1974).

[117] G. R. Wood and A. G. Walton, J.Appl. Phys. 41, 3027 (1970).

[118] J. D. Eshelby, Solid State Physics 3, 79 (Academic Press, New York, 1956).

[119] M. J. Haye and C. Bruin, J. Chem. Phys. 100, 556 (1994).

[120] K. Koga, X. C. Zeng, and A. K. Shchekin, J. Chem. Phys. 109, 4063 (1998).

[121] D. R. Uhlmann, J. Non-cryst. Solids, 41, 347 (1980).

[122] E. A. Brener et al., Phys. Rev. Lett. 82, 1506 (1999).

[123] R. F. Wood and G. E. Jellison, Semiconductors and Semimetals: Pulsed Laser Processing of Semiconductors 23, 166-246 (Academic Press, New York, 1984).

[124] M. Koenig, et. al. Nucl. Fusion 44, S208 (2004).

[125] V.I. Tarzhanov, Shock Waves 9, 307 (1999).

[126] J.W. Herman and H.E. Elsayed-Ali, Phys. Rev. Lett. 69, 1228 (1992).

[127] K. A. Jackson, in Treatise on Solid State Chemistry, edited by N. B. Hannay, (Plenum Press, New York, 1975), Vol. 5, pp 233-282.

[128] J. Q. Broughton and G. H. Gilmer, J. Chem. Phys. 84, 5749 (1986).

[129] M. S. Gulam Razul, J. G. Hendry, and P. G. Kusalik, J. Chem. Phys. 123, 204722 (2005).

[130] P. M. Richards, Phys. Rev. B 38, 2727 (1988).

[131] E. Johnson, Science 296, 477 (2002).

[132] S. E. Donnelly, R. C. Birtcher, C. W. Allen, I. Morrison, K. Furuya, M. Song, K. Mitsuishi, and U. Dahmen, Science 296, 507 (2002).

[133] A. Williams, R. Moss, and P. Harrowell, J. Chem. Phys. 99, 3998 (1993).

[134] D. W. Oxtoby and P. R. Harrowell, J. Chem. Phys. 96, 3834 (1992).

[135] H. E. A. Huitema, B. van Hengstum, and J. P. van der Eerden, J. Chem. Phys. 111, 10248 (1999).

[136] J. D. Honeycutt and H. C. Andersen, J. Phys. Chem. 90, 1585 (1986).

[137] L. D. Landau and E. M. Lifshitz, Statistical Physics, 3rd ed. (Pergamon, New York 1980), Pt. 1, pp. 333-345.

[138] J. Eisenmenger and I. K. Schuller, Nature Mater. 2, 437 (2003).

[139] http://www.ioffe.rssi.ru/SVA/NSM/Semicond/Si/thermal.html (Accessed September 26,2006).

[140] J. B. Hannon, S. Kodambaka, F. M. Ross, and R. M. Tromp, Nature (London) 440, 69 (2006).

[141] P. R. Couchman and W. A. Jesser, Nature (London) 269, 481 (1977).

[142] J. Q. Broughton and G. H. Gilmer, J. Chem. Phys. 84, 5741 (1986).

[143] D. Benielli, N. Bergeon, H. Jamgotchian, B. Billia, and Ph. Voge, Phys. Rev. E 65, 051604 (2002).

[144] K. Morishige, H. Iwasaki, Langmuir 19, 2808 (2003).

[145] A. Schreiber, I. Ketelsen, G. H. Findenegg, Phys. Chem. Chem. Phys. 3, 1185 (2001).

[146] W. Fan and X. G. Gong, Phys. Rev. B 72, 064121 (2005).

[147] M. Forsblom and G. Grimvall, Nature Mater. 4, 388 (2005).

[148] M. Forsblom and G. Grimvall, Phys. Rev. B 72, 054107 (2005).

[149] F. Lund, Phys. Rev. Lett. 69, 3084 (1992).

[150] A. V. Granato, Phys. Rev. Lett. 68, 974 (1992).

[151] C. Reichhardt, C. J. Olson, R. T. Scalettar, and G. T. Zimanyi, Phys. Rev. B 64, 144509 (2001).

[152] Y. Zhou and X. Jin, Phys. Rev. B 71, 224113 (2005).

[153] L. Burakovsky, D. L. Preston, and R. Silbar, Phys. Rev. B 61, 15011 (2000).

[154] L. Gomez, A. Dobry, Ch. Geuting, H. T. Diep, and L. Burakovsky, Phys. Rev. Lett. 90, 095701 (2003).

[155] F. Delogu, J. Phys. Chem. B 109, 15291 (2005).

[156] L. E. Reichl, A Modern Course in Statistical Physics, University of Texas Press, Austin (1980).

[157] R. M. J. Cotterill and J. U. Madsen, Nature 288, 467 (1980).

[158] D. K. Chokappa and P. Clancy, Molec. Phys. 61, 597 (1987).

[159] J. P. Hansen and L. Verlet, Phys. Rev. 184, 151 (1969).

[160] J. M. Ziman, Principles of the Theory of Solids, 2nd ed., page 65, Cambridge University Press, London (1972).

[161] A. B. Belonoshko, N. V. Skorodumova, A. Rosengren, and B. Johansson, Phys. Rev. B 73, 012201 (2006).

[162] J. R. Morris and X. Y. Song, J. Chem. Phys. 116, 9352 (2002).

[163] K. Sokolowski-Tinten et al., Nature 422, 287 (2003).

[164] P. J. Steinhardt, D. R. Nelson and M. Ronchetti, Phys. Rev. B 28, 784 (1983).

[165] D. R. Nelson and J. Toner, Phys. Rev. B 24, 363 (1981).

[166] M. D. Rintoul and S. Torquato, Phys. Rev. Lett. 77, 4198 (1996).

[167] M. D. Rintoul and S. Torquato, J. Chem. Phys. 105, 9258 (1996).

[168] L. D. Landau and E. M. Lifshitz, Quantum Mechanics, 2nd ed., p. 401, Oxford ; New York : Pergamon Press (1977).